University of Turin

Department of Earth Sciences

UNIVERSITÀ
DI TORINO

Doctoral School of Science and Innovative Technologies

Ph.D. Program in Earth Sciences XXXIV Cycle

Thermal remote sensing of volcanic activity by using Sentinel-2 and Landsat-8: an improvement of the MIROVA system.

Thesis' author: **Francesco Massimetti**

Tutor: **Diego Coppola**

Co-Tutors: **Marco Laiolo, Corrado Cigolini**

PhD Programme Co-ordinator: Francesco Dela Pierre

Academic years: 2018/2019, 2019/2020, 2020/2021

Code of scientific discipline: GEO/08

Declaration of Authorship

I, Francesco Massimetti, declare that this thesis titled, “Thermal remote sensing of volcanic activity by using Sentinel-2 and Landsat-8: an improvement of the MIROVA system.” and the work presented in it are my own. I confirm that:

- This work was done wholly or mainly while in candidature for a research degree at this University.
- This thesis is the product of my own work. All assistance received in preparing this thesis and the sources used have been acknowledged. This thesis has not been submitted at any other university.
- Where I have consulted the published work of others, this is always clearly attributed and cited.
- Where I have quoted from the work of others, the source is always given.

Francesco Massimetti

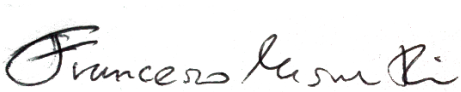

Torino, 18/10/2022

Abstract

Volcanoes are places of heat transfer from Earth's interior to the surface, and this heat relates to the volcano activity and brings information about the ongoing volcanic status. Studying thermal signals provides fundamental insights into volcanic behaviors, and represents a crucial parameter for comprehensively monitoring volcanoes. Thermal satellite remote sensing is one of the available tools to effectively, safely, and in-depth detect, track, and forecast eruptive activity, delivering critical information to volcano observatories and reducing eruption-related hazards. This thesis aims to explore the potential of Infrared high-spatial-resolution satellite images to study and monitor active volcanoes from a global perspective and to enhance the thermal detection and analysis of the MIROVA thermal monitoring system, based on MODIS images. The recent availability of SENTINEL-2 MSI and LANDSAT-8 OLI satellite images with spatial resolutions of 20-30 meters/pixel in the Short Wave Infrared allows to integrate the MODIS dataset, with a moderate spatial resolution of 1 km in the Middle Infrared, and to enrich the quality and quantity of information on thermal activity emitted by volcanoes. Particularly, high-spatial-resolution images allow more detailed spatial information of volcanic thermal features, detecting subtle thermal anomalies and precursors before eruptions, and understanding which volcanic process the heat emission is related to. The multispatial and multisensory thermal approach proposed in this work aims to define in space and time the thermal emissions sourced by a variety of volcanic phenomena occurring at low-viscosity and high-viscosity volcanoes. A new algorithm is developed for detecting and counting hotspots using MSI-S2 and OLI-L8 SWIR images with a global applicability purpose, showing coherent results to heat flux measured by MODIS and indicating a complementary usage of moderate and high-spatial-resolution imagery to characterize volcanic activity more effectively. Multicraters' open vent activity is investigated at Stromboli and Etna volcanoes to track emissions during Strombolian activity, study thermal budgets over long-term periods, and measure heat flux produced by single vents. Dome-forming eruptions at Láscar, Sabancaya, and Shiveluch volcanoes are studied to explore what qualitative and quantitative analysis of thermal features could reveal about lava dome dynamics, and the potential of multi-platform thermal data to monitor processes occurring at lava domes. Finally, a fully automated near real-time monitoring architecture, analyzing MSI-S2 and OLI-L8 images at ca. 120 volcanoes worldwide, is built to be implemented in the MIROVA MODIS-based tool, enriching the thermal surveillance offered by the system with new outcomes beneficial for volcano observatories and civil protection agencies, and contributing to developing a modern and multisensory volcano-devoted thermal monitoring system. The results here are significant for the whole volcanological community, strengthening the global volcano monitoring perspective and offering a tool to better understand the evolution of volcanic episodes and their associated hazards.

Contents

Chapter 1

1. Introduction

1. BACKGROUND

Volcanoes are not only evidence of how Earth is a dynamic planet but are highly fascinating to humans and bring many economic, agricultural, and social benefits to human life (Sigurdsoon, 2015). Luckily, much of the time, volcanoes are not an unsustainable danger because they erupt not so frequently or because communities have adapted to eruptions (Brown et al., 2015a). Nevertheless, living nearby a volcano means an ever-present threat, considering that volcanic eruptions can cause loss of life and livelihoods, damage to facilities, stress to fragile environments and populations displacing, as well as have global impacts by upsetting climate, businesses, and air travel (Hooper et al., 2012; Loughlin et al., 2015). In fact, since 1600, about 280.000 fatalities have been recorded because of volcanic activity, and the number of deadly episodes has been growing as more people live in areas of vulnerability to volcanic hazards, particularly in less developed countries (Witham, 2005; Auker et al., 2013). In this regard, over 800 million people live within 100 km of a Holocene volcano, and about 30 million people within 10 km (Brown et al., 2015b). All these facts indicate how volcanic activity could pose severe hazards.

There are about 1400 volcanoes considered active worldwide (Siebert, 2011), with ~70 of those erupting every year (Loughlin et al., 2015). Due to different reasons, such as costs and difficulties in maintaining instrumentation in volcanic contexts operative, up to 45% of Holocene volcanoes are not monitored (Brown et al., 2015b), and less than 10% are monitored routinely (Ferrucci et al., 2012), meaning that about 90% of potential volcanic hazards do not have a dedicated observatory and are either monitored occasionally or not monitored at all. Moreover, some devasting eruptions occurred as unexpected after high quiescence intervals in volcanoes considered dormant or extinct, thus in a context poorly monitored, such as the Chaitén (Chile) eruption in 2008 after ca. 100 years of quiescence (Major & Lara, 2009), and Pinatubo (Philippines) 1991 Plinian eruption, after 500 years of volcanic sleeping (Newhall & Punongbayan, 1996). Some recent eruptive crises of more famous volcanoes demonstrate how lacking monitoring capabilities could have dramatic consequences, such as the Fuego (Guatemala) 2018 eruption, with at last hundreds of deaths caused by pyroclastic flows (Global Volcanism Program, 2018), at the Anak Krakatoa (Indonesia) 2018 sector collapse, causing a tsunami resulting in 430 fatalities on close shores (Walter et al., 2019), or the small explosive

event in 2019 on the touristic Whakaari Island (New Zealand) that killed 22 people between tourists and guides (Global Volcanism Program, 2020a). Volcanic eruptions, even if produce minor physical injuries to people, could have devastating effects on the global economy and communities, as recent events also show: the spring 2010 eruption of Eyjafjallajökull (Iceland), with the closure of airports in Europe and an overall economic damage of ~5 billion (Oxford Economics, 2010); the eruption of Taal volcano (Philippines) in 2020, inducing the evacuation of ~460.000 people (Global Volcanism Program, 2020b); the paroxysmal phase at Stromboli (Italy) during summer 2019, which reshaped the touristic influx to the island (Knafou, 2019); the Nyiragongo (DRC) effusive eruption of May 2021, with 32 people died and ca. 1,000 homes destroyed (Boudoire et al., 2022); the eruption at Cumbre Vieja (Canary Islands, Spain) in 2021, with 12 km^2 of territory and hundreds of hectares of plantations buried by lava flows (Civico et al., 2022); the VEI 5 explosion at Hunga Tonga–Hunga Ha'apai (Tonga) volcano in January 2022, as the largest eruption of the 21st century, affecting with tsunami-waves several shorelines along the Pacific rim, caused 90 million of dollars in damages in Tonga (around 18.5% of Tonga's GDP; Terry et al., 2022; World Bank, 2022). These eruption case studies, a few among many possible ones, and their knock-on effects demonstrated that the hazards posed by volcanic activity are still relevant today both for regions close to volcanoes and globally, but highlight at the same time the critical role that should have monitoring actions.

Eruptions are often preceded by some precursory signals possibly indicating a state of unrest, such as changes in seismic activity, ground deformation, gas, ash, and thermal emissions (Newhall, 2000; Sparks, 2012; Phillipson et al., 2013; Pallister & McNutt, 2015; Reath et al., 2019a; Girona et al., 2021). Volcano monitoring, considered the continuous analysis of numerous parameters that describe the state of a volcano, is the best way to recognize signs of changes to provide early warnings and short-term forecasting of a future eruption (Sparks, 2003; Tilling, 2008). But, constantly monitoring all potentially active volcanoes is a challenge, logistically and economically (Brown et al., 2015a). Looking for signs of unrest, detecting the eruption's onset, and tracking the evolution over time of volcanic activity are fundamental requisites to warning of catastrophes. Still, they cannot be achieved by ground-based techniques alone (Poland et al., 2020). In this gap, satellite remote sensing provides a wealth of observations of critical value, mainly when ground-based monitoring is limited or lacking and in unsafe contexts, and offers the opportunity for continuous long-term measurements of volcanic activity, essential to establish background levels of activity and enhance the understanding of volcanic processes on broader time scales of analysis (Reath et al., 2019a; Valade et al., 2019). Naturally, satellite remote sensing arrives at remote and inaccessible

volcanoes too, and imagery can survey almost the entire Earth's land surface or areas hundreds of kilometers wide, providing complete coverage of volcanic regions (Furtney et al., 2018; Pritchard et al., 2018; Reath et al., 2019b). In other words, improved monitoring potentials of volcanic activity are possible to reach by utilizing available satellite detection resources, measuring ground deformation, gas and aerosol emissions, and thermal anomalies (i.e., Bally, 2012; Biggs et al., 2014; Wright, 2016; Carn et al., 2017; Coppola et al., 2020; Poland et al., 2020). To give an idea of the effectiveness of space-based techniques, estimates found that 78% of all volcanoes that erupted since 1978 showed at least one typology of a satellite-detected anomaly among surface change, SO2 emission, or thermal signals indicative of volcanic unrest (Furtney et al., 2018). Additionally, satellite monitoring techniques of diverse geophysical, geochemical, and morphological parameters that characterize volcanic activity allow to integrate different data and reach a more comprehensive overview of volcanic processes, with a multi-sensor perspective to contribute to global volcano monitoring strategies (Furtney et al., 2018; Reath et al., 2019a; Valade et al., 2019).

2. THERMAL SATELLITE REMOTE SENSING: DEVELOPMENTS AND LIMITS

Thermal data represent one of the crucial parameters for comprehensively monitoring volcanoes. This is because volcanic activity transfers heat from the subsurface to the surface, and measuring this heat provides insights into the physical processes governing volcanic activity (Figure 1; Oppenheimer, 1998; Harris, 2013). The activity observed could be viewed as the expression of diverse thermal emitting phenomena with different thermal sources: low-temperature phenomena (< 100°C), such as crater lakes, low-temperature fumaroles, cooling pyroclastic flows, and cooling lava flows; or high-temperature phenomena (> 100°C), like high-temperature fumaroles, active lava flows or lava lakes, erupting vents exposing magmatic materials, hot inner cores of lava domes (see Oppenheimer et al., 1993; Harris & Stevenson, 1997; Harris, 2013; Blackett, 2017, Coppola et al., 2020). All these processes are not strictly separated but take part together, gradually transitioning from one to the other. Those processes are manifested as "anomalies," "thermal signatures," or "volcanic thermal features," consisting of spatial elements with temperature deviating from the background of the surrounding, having variable sizes and spatial features, and whose nature is linked to volcanic processes (Figure 1 & 2; Oppenheimer, 1993; Harris, 2013; Davies et al., 2010; Way et al., 2022). Of course, a thermal signature's characteristics (i.e., intensity, dimension, spatial distribution, temporal persistency) may significantly vary in space and time. They can be different because of the distinct source processes cited above. It is intuitive to think that, for example, a km-long basaltic lava flow will be expressed differently by a cooling viscous lava dome with hot cracks on its

surface in terms of related thermal signature, which exactly represents the challenge that must face the volcanic thermal remote sensing approach.

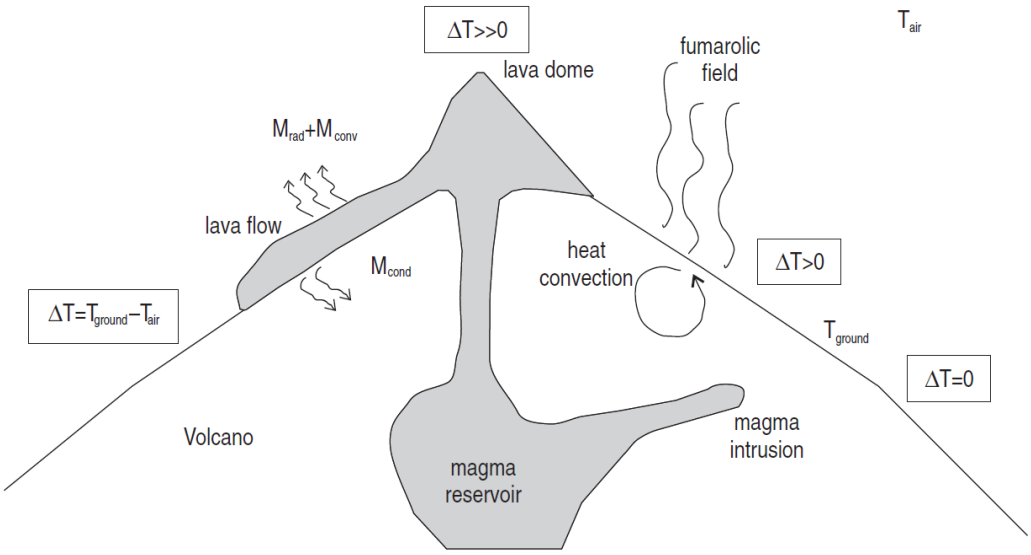

Figure 1 *– Simplified representation of primary sources of thermal emission that can be detected by a satellite. With a heat supply from depth, such as a magmatic intrusion or rising, thermal emissions related to a temperature deviation from the background of the surrounding could appear on surfaces due, for example, to a lava flow emplacement, a lava dome growing, or a fumarolic field (from Harris, 2013).*

In the last decades, thermal data from satellites with Infrared (IR, measurement within the 0.7 to 20 μm waveband; Harris, 2013) sensors have been effectively used to investigate a wide range of volcanic phenomena. Among others, the main applications of thermal satellite data have been to identify thermal precursors (Dehn et al., 2002; Pieri & Abrams, 2005), measure effusive/extrusive rates (Harris et al., 1998; Coppola et al., 2015), estimate magma budgets (Francis et al., 1993; Coppola et al., 2019), track high-temperature fumaroles (Harris & Stevenson, 1997) and forecast the end of effusive eruptions (Coppola et al., 2017; Ripepe et al., 2017; for an exhaustive review of the most important outcomes in the discipline, see Harris, 2013; Ramsey et al., 2022).

IR sensors are distinguished based on their spatial resolutions and revisit frequency. Harris, 2013 categorized three main classes of IR sensors: GOES (Geostationary Operational Environmental Satellite: 4-km pixels, 15-min cadence), AVHRR (Advanced Very-High-Resolution Radiometer: 1-km pixel; 6-h cadence), and TM (Thematic Mapper: 60-m pixel; 16-day cadence). At the same time, sensors are classified also based on spectral characteristics, such as the number of available bands and the saturation values that determine their range of use (see Harris, 2013). All these features are vital to assessing the strength to detect thermal volcanic emissions adequately and determining the diverse applications using IR in volcanological disciplines, including monitoring.

The recent technological developments in the field of Earth Observation, with newly available sensors, each own with its spatial-temporal and spectral features and processing techniques (Steffke & Harris, 2011), have made thermal remote sensing further evolve, especially as a tool for improving real-time monitoring systems (Ramsey & Harris, 2013). Indeed, several volcanic hot-spot detection systems have been developed to detect and quantify volcanic thermal features and volcanogenic heat flux, with the main operational goals to assess the presence of precursor signals of eruption and to follow eruptive crises providing information for volcanic hazard assessment to observatories and protection agencies (see Coppola et al., 2020). In other terms, satellite thermal monitoring has reached a level of maturity that should be considered at the same level as more conventional monitoring approaches based on degassing, seismicity, and deformation parameters (Poland et al., 2020).

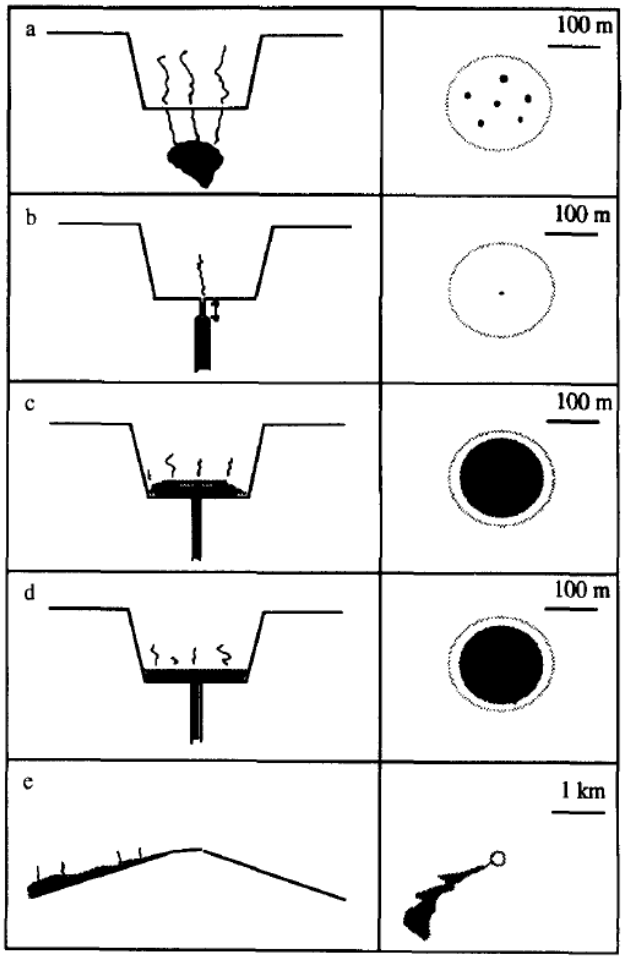

Figure 2 *– Examples of the main volcanic thermal signals tracked using thermal remote sensing (Oppenheimer et al., 1993). The right column illustrates the representative spatial extension of the associated signatures. (a) fumaroles; (b) an open vent containing magma; (c) an active lava dome; (d) an active lava lake; (e) an active lava flow.*

Nevertheless, no satellite mission is dedicated explicitly to monitoring volcanoes from space. The current systems use sensors with spatial, temporal, and spectral resolutions in principle aimed at non-volcanological Earth Observations (Ramsey et al., 2022). This leads to a series of

shortcomings for the InfraRed sensing, related to the temporal-spatial-spectral resolution trade-off, or the "too short blanket" paradox (Figure 3; Blackett, 2017), where volcanic activity, which is wildly variable in space, time, and intensity, cannot be in-depth monitored if we consider only one type of sensor or imagery product. For example, in the case of a prolonged and fast-evolving effusion of fresh lava from the Kilauea volcano (Hawaii, USA), the high-temporal revisit frequency of up to four images per day of the Moderate Resolution Imaging Spectroradiometer Sensors (MODIS) is optimal to monitor through time the evolution of the effusion. However, for a short and rapid explosive event produced by the Shiveluch volcano (Kamchatka, Russia) or for a detailed dimensional analysis of thermal features related to the different craters on the top of the Stromboli volcano (Sicily, Italy), MODIS spatial resolution of 1 km/pixel, in the Middle Infrared (MIR) bands, is too coarse or its relatively high temporal resolution may be inadequate, resulting in such possibly no detection. As summarized by Hochberg et al., 2015 and reported by Blackett, 2017, "There is no current thermal infrared sensor that combines multiple bands needed for temperature-emissivity separation, a sub-100 m spatial resolution, and a frequent repeat interval with global coverage, which are necessary to answer a wide range of Earth science studies related to surface composition, hydrology, and volcanology". Therefore, in response to this need and waiting for a sensor with adequate characteristics for optimal characterization of volcanic thermal activity, one of the possible approaches to enrich the thermal volcanic investigation and to improve the monitoring potentialities of monitoring systems is to combine and join different IR sensors, taking advantage of the recent availability of new thermal satellite imagery.

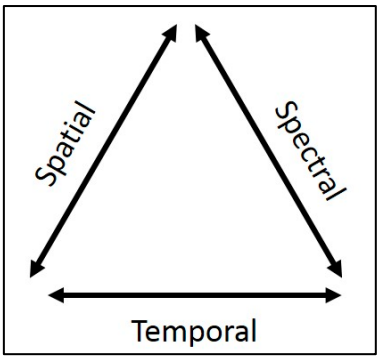

Figure 3 *- The trade-off between spatial, spectral, and temporal resolution for IR Earth observation imagery. A high spectral resolution sensor must compromise spatial or temporal resolution or vice versa (Blackett, 2017).*

Thus, even though the moderate temporal resolution of MODIS is crucial for volcano monitoring (Harris, 2013), its spatial resolution prevents the retrieval of precise spatial information from hot targets (Figure 4). In this regard, the Short Wave InfraRed (SWIR) high-spatial-resolution sensors, with detail of 20 – 30 meters per pixel, such as the Multispectral

Instrument (MSI) and the Operational Land Imager (OLI), carried on SENTINEL-2 (S2) and LANDSAT-8 (L8) platforms and launched by the European Space Agency (ESA) and National Aeronautics and Space Administration (NASA) respectively, can be crucial to face this shortcoming and relevant to move toward a multisensory approach in the field of thermal satellite sensing of volcanic activity (Marchese et al., 2019; Massimetti et al., 2020).

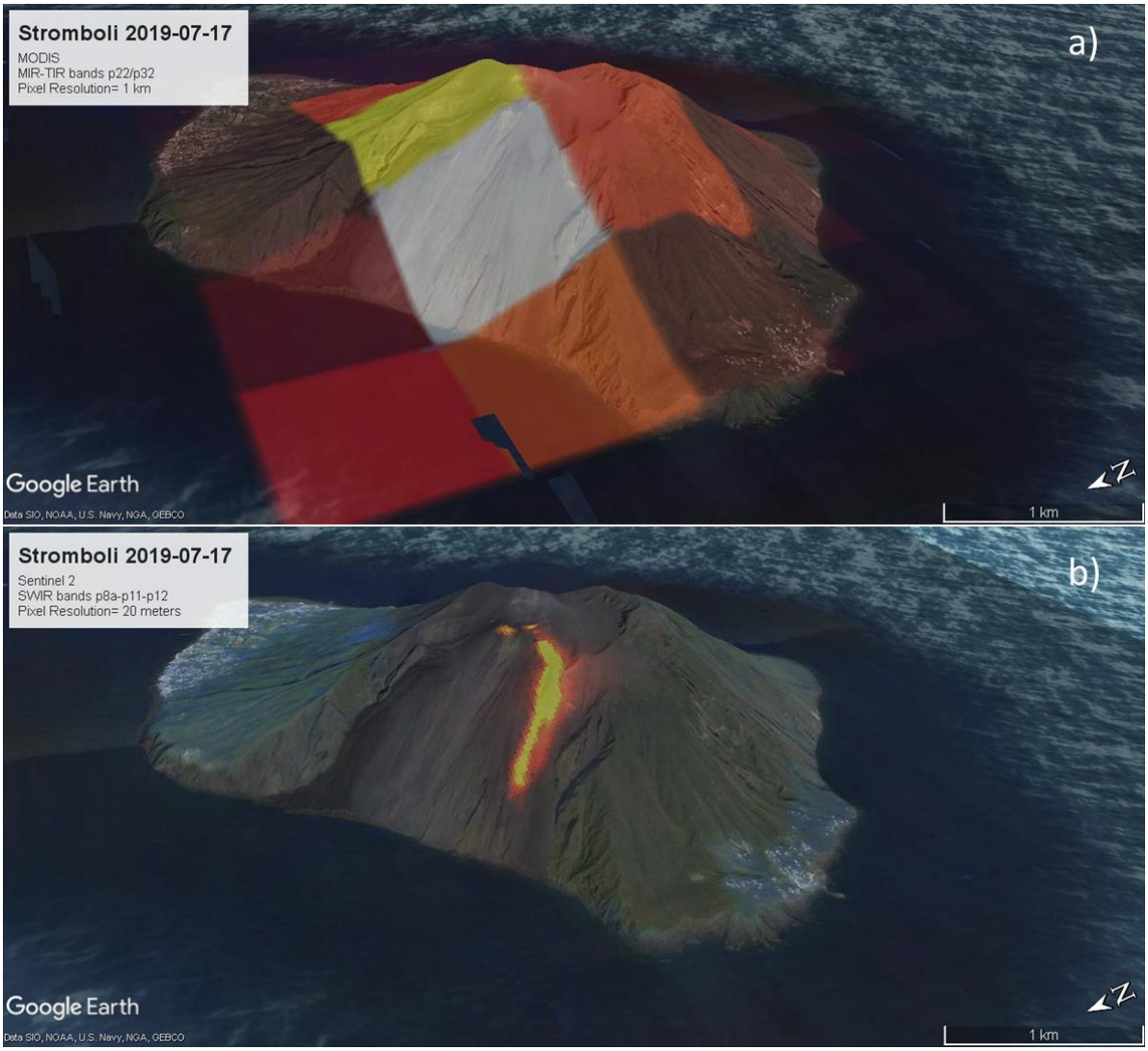

Figure 4 *- Examples of different thermal signatures related to the same volcanic process, an emplacement of a lava flow on Stromboli during July 2019, detected by (a) MODIS and (b) MSI S2 images (projected on Google Earth software) in the MIR and SWIR region, with a pixel resolution of 1 km and 20 meters, respectively. As is possible to observe, the spatial information that can be retrieved from the images is enormously different.*

3. THE MIROVA SYSTEM: STRENGTHS AND IMPROVEMENT

A satellite thermal volcanic monitoring system aims to detect the presence of thermal signals and monitor their changes in space, time, and intensity precisely and rapidly. All the algorithms developed to detect hot spots (Steffke & Harris, 2011; Harris, 2013) work to recognize anomalous pixel(s) based on a definition of a specific thermal threshold that separates from the background. The outcome provided could include *i*) IR anomalous images (in diverse spectral

regions of the electromagnetic spectrum, such as SWIR, ShortWave InfraRed 1.1 to 3.0 μm, MIR, Middle InfraRed 3.0 to 5.0 μm, and TIR, Thermal InfraRed 8 to 15 μm, Harris, 2013); *ii*) measurement of intensity using a specific metric, in terms of heat flux (Volcanic Radiative Power, VRP; Wooster et al., 2003; Coppola et al., 2016), the number of hot pixels or hot area exposed (Massimetti et al., 2020), and "excess of radiance" ΔL_{HOT}, or "excess of temperature" ΔT_{HOT} than the background (Wright et al., 2004; Gouhier et al., 2016); *iii*) time-series of the parameters measured in a specific time window of hours, days or years.

Among the numerous system available, the MIROVA (Middle InfraRed Observations of Volcanic Activity) represents a primary resource in the actual panorama of thermal satellite monitoring of volcanoes (Coppola et al., 2016; 2020). MIROVA was born as a small pilot project at the Department of Earth Sciences at the University of Torino, in collaboration with the University of Florence and supported by the Italian Department of Civil Protection (DPC). The project's first steps were to monitor the thermal heat flux of the Italian volcanoes of Stromboli and Etna. Years by years, and using the global potentialities of the MODIS sensor (on board NASA Terra and Aqua satellites since 1999 and 2002, respectively), the project developed to monitor a higher number of volcanoes worldwide. Indeed, combining a spatial resolution of 1 km at 3.959 μm (Middle InfraRed wavelength), with temporal coverage of up to 4 images per day (at equator latitudes), and an elevated sensitivity to detect low-power thermal anomalies, MIROVA moved steps toward applications of near real-time global monitoring of active volcanoes. Nowadays, the system daily routinely quantifies thermal emissions at a global scale for 220 active volcanoes worldwide, freely disseminating data and results to several observatories and civil protection agencies through a dedicated website (http://www.mirovaweb.it/) with a series of static graphical outputs for any monitored volcano, including MIR images, VRP quantification, and time-series (Coppola et al., 2020). According to the use of thermal data by volcano observatories, these products give information about the presence or absence of thermal anomalies, the intensity of the thermal emission, the location of the hotspot, and, indirectly, tracking changes in the thermal output, about eruptive evolution and trends. Additionally, the MIROVA system provides higher-level post-processed products such as lava effusion rates for specific eruptions and requests from observatories (i.e., Coppola et al., 2019). Together with other systems based on MODIS MIR analysis, such as MODVOLC (http://modis.higp.hawaii.edu/; Wright et al., 2004; 2016), the MIROVA system is currently one of the most used satellite-based monitoring systems for volcanic activity (Coppola et al., 2020). The recent work of Coppola et al., 2020, "*Thermal Remote Sensing for Global Volcano Monitoring: Experiences From the MIROVA System*" perfectly depicts the efficiency of the

system, showing the role that the thermal data provided had in detecting the transition from ordinary to critical state (volcanic unrest; Laiolo et al., 2017; Cigolini et al., 2018; Coppola et al., 2022), to forecast eruptions (Coppola et al., 2017; Ripepe et al., 2017) and to depict trends of heat fluxes and volumes erupted during an eruptive crisis (Coppola et al., 2012, 2019; Laiolo et al., 2019). All these results have also been achieved in collaboration and support of the monitoring actions of several volcano observatories worldwide, enhancing the evaluation of associated hazards (Coppola et al., 2020). Also, the research discusses the limits of the system and the requirements to improve the quality, distribution, and interpretation of the data, particularly in the light of the experience collected in recent years by the volcanological community and the challenges to face in the next future for a developed satellite monitoring system. Among these limits, it is possible to find:

i) evaluation of image quality to check the effects of clouds, environment, and viewing geometry conditions;

ii) improving image spatial resolution, considering the too broad 1 km pixel size of the MODIS-MIR imagery;

iii) making thermal data available and downloadable in near real-time on the website.

These steps are vital to achieving the main aim to constrain the volcanic thermal signatures better and improve monitoring potentialities (Coppola et al., 2020). The integration of multiple IR thermal satellite data with various spatial, temporal, and spectral features is suggested as the one central solution to overcome the presented limits and to make MIROVA more exhaustive as a monitoring tool, providing a complete view of events by tracing their evolution both in time and in space and reaching deeper insight into the volcanic activity in progress (Coppola et al., 2020). The SWIR MSI SENTINEL-2 and OLI LANDSAT-8 new generation of thermal high-spatial-resolution sensors, open the door to better constrain thermal anomalies quantitatively and qualitatively, and represents one of the better-suited answers in the panorama of available IR sensors for this purpose.

4. AIMS AND STRUCTURE OF THIS THESIS

The general objective of this thesis is to explore and implement the MIROVA potentialities in terms of thermal detection and analysis of volcanic activity by using new InfraRed sensors. This means enhancing the overall set and nature of satellite thermal observations and the operational real-time monitoring system. This implementation has been carried out with the integration of the SWIR sensors MSI SENTINEL-2 and OLI LANDSAT-8 available since 2015 and 2013, respectively, with a higher spatial resolution of 20-30 meters. The other use of the

high-spatial-resolution thermal datasets, in comparison with the MODIS-derived ones initially processed by the MIROVA algorithm, has the final aim to reach the best technical approach and scientific accuracy to define in space and time the thermal emissions produced by a variety of volcanic phenomena occurring at low-viscosity and high-viscosity volcanoes. In this research path, a series of research questions were addressed:

- *What can SWIR high spatial resolution imagery add to measuring volcanic thermal parameters and studying volcanic activity?*
- *Which is the volcanic heat source responsible for the thermal heat flux measured by the MODIS sensor?*
- *Are there potential thermal "precursors" of eruptive unrest, upcoming eruptions, or changes in the long-term volcanic behavior in low- and high-viscosity volcanoes detectable by SWIR sensors?*
- *Are SWIR high spatial resolution useful for volcano monitoring from a global perspective, and what can they add to the already existing MIROVA system potentials?*

These questions trace different lines of research, both theoretical and technical: on one side, the investigation focuses on the integration of thermal metrics derived by MODIS, such as the volcanogenic heat flux (Volcanic Radiative Power, VRP), and by MSI S2 and OLI L8, as the hot area exposed (Number of Hot Pixels), and its strength to study volcanic activity; on the other, concentrated on the technical improvement of the MIROVA platform with the new satellite-sourced data, in terms of algorithm development and test, downloading and processing architecture, and web development. These research fronts could be summarized in three main steps:

1. Develop and validate a hotspot detection algorithm to recognize thermal anomalies at a global scale by using MSI SENTINEL-2 and OLI LANDSAT-8 images, and build the architecture to automize the process, from download to archiving;
2. Explore the potentialities and effectiveness of high-spatial-resolution thermal images to study a variety of volcanic activities, such as:
    a. Open vent and Strombolian multicraters sourced activity at Stromboli and Etna volcanoes (Italy);
    b. Dome-forming eruptions at Láscar (Chile), Sabancaya (Peru), and Shiveluch (Russia) presenting an overview of thermal satellite investigation at high-viscosity and more explosive volcanic behavior;
3. Building an automated near real-time monitoring system based on the analysis of SWIR signals of MSI SENTINEL-2 and OLI LANDSAT-8, implementing the MIROVA

website with additional web pages freely accessible to disseminate new quantitative and qualitative information, such as SWIR-based images, time-series, and downloadable database to the volcanological community.

According to the above-mentioned thesis aims, carried throughout a 3-year period, the work is presented in different chapters structured as autonomous research articles (Chapters 2, 3, and 4), some of them based on peer-reviewed publications and presentations in international conferences. In this thesis, only the most relevant results are presented and resumed, with the aim to present a linear and logical research path through the different case studies and themes covered. Nonetheless, the list of all my publications as first author and co-author is shown in Chapter 5.1 (see below), with the intention of allowing the reader to delve into some issues that, for necessity of synthesis could not be presented here in the thesis.

Chapter 2 is a first-author publication of the candidate (see Massimetti et al., 2020) and represents the central methodological part of this thesis, with the title "***Volcanic Hot-Spot Detection Using SENTINEL-2: A Comparison with MODIS–MIROVA Thermal Data Series"***. The chapter represents the published article in March 2020 on *Remote Sensing* without any modification. Here, the hotspot detection algorithm developed for the SWIR MSI SENTINEL-2 data with a 20-meter resolution (and applicable in the same way to OLI LANDSAT-8, with 30m resolution) is presented in all its logical, spatial, and statistical steps. The algorithm detects hot-spot-contaminated pixels (Number of Hot Pixels) for several types of volcanic activities. The accuracy performances are demonstrated, underlining its robustness to be applied globally. The results are compared with the VRP heat flux data derived from MODIS-MIR images processed by the MIROVA algorithm, showing the correlation between the two thermal signals. The results indicate the multi-sensor approach's benefits, combining high- and moderate-resolution images, and present also the success of the hotspot algorithm as an implementation of thermal surveillance to the MIROVA and MOUNTS monitoring systems. The algorithm results received great attention by volcanological community, and has led me to be involved in several publications using SWIR high resolution images. This chapter represents the first step of the Ph.D. course, where the first and partially the second research questions are addressed.

In Chapter 3, titled "***Quantifying thermal emission from open vent multicraters system using a multisensory space-based approach: Stromboli and Etna case studies***", the results of the eight years (2013 – 2021) multisensory investigation of Stromboli and Etna thermal open-vent activity are presented, combining MODIS, MSI-S2 and OLI-L8 data in the MIR and SWIR

spectral regions, respectively. High-spatial-resolution potentials are applied to map variations of Strombolian activity, measure the different active vents' thermal budgets, and estimate heat flux values produced by single craters, using a fitting method between the Volcanic Radiative Energy retrieved by MODIS and the Thermal Index by SENTINEL-2 and LANDSAT-8. Results are interpreted in the framework of volcanic behavior observed in recent years by Stromboli and Etna, indicating long-term changes in the thermal budgets in connection with the increase of explosivity and possibly revealing variations in the magmatic supply rate. The chapter represents the second step in investigating volcanic phenomena occurring at low-viscosity volcanoes and answers several research questions listed above, from the potentialities of high-resolution-spatial monitoring to the effectiveness of SWIR signals in detecting long-term changes in volcanic behavior. The result here shown on Stromboli and Etna thermal activity have been presented in an Oral Session at the AGU Fall Meeting 2021 (Massimetti et al., 2021b).

In Chapter 4, titled "***Thermal Signatures at Lava Domes: an overview comparison using multi-sensor and multi-spatial thermal IR satellites***" a multisensory and multiyear approach using MODIS, VIIRS, MSI SENTINEL-2, and OLI LANDSAT-8 is applied to study the thermal signatures of three dome-forming eruptions at Láscar, Sabancaya, and Shiveluch volcanoes. The chapter gives an overview of the potential of using multi-platform data to explore volcanic processes typically occurring at lava domes, such as cyclicity in activity, the transition from unrest to eruptive phase, growing and destructive dynamics, and explosive activity. The chapter represents the second step in investigating volcanic phenomena occurring at high-viscosity volcanoes and answers both the second and third of the research questions, from understanding the volcanic source responsible for thermal emissions to using SWIR signals for recognizing the transition from ordinary to eruptive phases. The results here shown are part of two peer-reviewed articles I was co-author: for the Sabancaya, Coppola et al., 2022 "*Shallow magma convection evidenced by excess degassing and thermal radiation during the dome-forming Sabancaya eruption (2012–2020)"*, published on *Bulletin of Volcanology*, for the Shiveluch, Shevchenko et al., 2021 "*Constructive and Destructive Processes During the 2018–2019 Eruption Episode at Shiveluch Volcano, Kamchatka, Studied From Satellite and Aerial Data"* published on *Frontiers in Earth Sciences*. For the Láscar, results have been partially presented in the Physics of Volcanoes 2021 Workshop POV-7 with the title "*Overview of Láscar's recent activity as monitored by different observation platforms: multi-years thermal cyclicity as seen from space during the 2013-2020 eruptive episode"* (Massimetti et al., 2021a).

Chapter 5, titled ***"Monitoring applications and implementation of the Mirova system"***, summarizes the main results using the high-spatial-resolution images from SENTINEL-2 and LANDSAT-8 satellites in monitoring applications and implementations made to the MIROVA system. We take two recent eruptions occurred in Italy, at Etna in December 2018 and Stromboli in July-August 2019, to show how SWIR data could be relevantly used to support the management efforts of eruptive crises by the Italian Civil Protection Department. All the features of the automated hot-spot monitoring architecture based on the SWIR imagery are explained, showing its application to about 120 volcanoes worldwide and presenting the additional features brought to the MIROVA website in terms of data dissemination, improving the thermal outcomes available, and thus moving one step beyond toward a modern thermal multisensory volcano-devoted monitoring system.

In Chapter 6, a summary of the main conclusions of the Thesis is reported. In addition, starting from the results achieved during the doctoral course, some future perspectives and next steps are briefly outlined.

5. LIST OF PUBLICATIONS

Here, is presented a list of all publications in which I have participated as an author or co-author (from the newest to the oldest) during the Ph.D. The list presents diverse volcanological research themes and methodologies. The variety of topics covered is representative of the different collaborations undertaken during these 3 years of Ph.D. thesis, and is mainly the result of a constant and intense research work with the monitoring group of MIROVA of University of Torino, and LGS of University of Firenze and University of Palermo. Indeed, a significant part of the work and time devoted to the Ph.D. path, has been also employed in operational monitoring aspects, with the development of research and monitoring tools applicable from local to global scale, and the participation to several volcanic crisis management efforts about Italian volcanoes of Stromboli and Etna.

- Coppola, D., Laiolo, M., Campus, A., **Massimetti, F.**, 2022. Thermal unrest of a fumarolic field tracked using VIIRS imaging bands: The case of La fossa crater (Vulcano Island, Italy). *Front. Earth Sci.*, 10:964372. https://doi.org/10.3389/feart.2022.964372
- Gouhier, M., Pinel, V., Belart, J.M.C., De Michele, M., Proy, C., Tinel, C., Berthier, E., Guéhenneux, Y., Gudmundsson, M.T., Óskarsson, B.V., Gremion, S., Raucoules, D., Valade, S., **Massimetti, F.**, Bjorn, O., 2022. CNES-ESA satellite contribution to the operational monitoring of volcanic activity: The 2021 Icelandic eruption of Mt. Fagradalsfjall. *J. Appl. Volcanol.*, 11, 10. https://doi.org/10.1186/s13617-022-00120-3

- Boulesteix, T., Legrand, D., Taquet, N., Coppola, D., Laiolo, M., Valade, S., **Massimetti, F.**, Caballero-Jiménez, G., Campion, R, 2022. Modulation of Popocatépetl's activity by regional and worldwide earthquakes. *Bull. Volcanol.*, 84, 80, https://doi.org/10.1007/s00445-022-01584-2
- Laiolo, M., Delle Donne, D., Coppola, D., Bitetto, M., Cigolini, C., Della Schiava, M., Innocenti, L., Lacanna, G., La Monica, F.P., **Massimetti, F.**, Pistolesi, M., Silengo, M.C., Aiuppa, A., Ripepe, M., 2022. Shallow magma dynamics at open-vent volcanoes tracked by coupled thermal and SO2 observations. *Earth Planet. Sci. Lett.*, 594, 117726. https://doi.org/10.1016/j.epsl.2022.117726
- Campus, A., Laiolo, M., **Massimetti, F.**, Coppola, D., 2022. The Transition from MODIS to VIIRS for Global Volcano Thermal Monitoring. *Sensors*, 22, 1713. https://doi.org/10.3390/s22051713
- Coppola, D., Valade, S., Masias, P., Laiolo, M., **Massimetti, F.**, et al., 2022. Shallow magma convection evidenced by excess degassing and thermal radiation during the dome-forming Sabancaya eruption (2012–2020). *Bull. Volcanol.*, 84, 16. https://doi.org/10.1007/s00445-022-01523-1
- Aiuppa, A., Bitetto, M., Delle Donne, D., La Monica, F., Tamburello, G., Coppola, D., Della Schiava, M., Innocenti, L., Lacanna, G., Laiolo, M., **Massimetti, F.**, Pistolesi, M., Silengo, C., Ripepe, M., 2021. Volcanic CO2 tracks the incubation period of basaltic paroxysms. *Sci. Adv.*, 17 (7(38)). https://doi.org/10.1126/sciadv.abh0191
- Coppola, D., Laiolo, M., **Massimetti, F.** et al., 2021. Thermal remote sensing reveals communication between volcanoes of the Klyuchevskoy Volcanic Group. *Sci. Rep.*, 11, 13090. https://doi.org/10.1038/s41598-021-92542-z
- Shevchenko, A.V., Dvigalo, V.N., Zorn, E.U., Vassileva, M.S., **Massimetti, F.**, Walter, T.R., Svirid, I.Y., Chirkov, S.A., Ozerov, A.Y., Tsvetkov, V.A., Borisov, I.A., 2021. Constructive and Destructive Processes During the 2018–2019 Eruption Episode at Shiveluch Volcano, Kamchatka, Studied From Satellite and Aerial Data. *Front. Earth Sci.*, 9:680051. https://doi.org/10.3389/feart.2021.680051
- Ripepe, M., Lacanna, G., Pistolesi, M., Silengo, M.C., Aiuppa, A., Laiolo, M., **Massimetti, F.**, Innocenti, L., Della Schiava, M., Bitetto, M., La Monica, F.P., Nishimura, T., Rosi, M., Mangione, D., Ricciardi, A., Genco, R., Coppola, D., Marchetti, E., Delle Donne, D., 2021. Ground deformation reveals the scale-invariant conduit dynamics driving explosive basaltic eruptions. *Nat. Commun.*, 12, 1683. https://doi.org/10.1038/s41467-021-21722 -2
- Plank, S., **Massimetti, F.**, Soldati, A., Hess, K.U., Nolde, M., Martinis, S., Dingwell D.B., 2021. Estimates of lava discharge rate of 2018 Kīlauea Volcano, Hawai'i eruption using multi-sensor satellite and laboratory measurements, *Int. J. Remote Sens.*, 42:4, 1492-1511. https://doi.org/10.1080/01431161.2020.1834165
- **Massimetti F.**, Coppola D., Laiolo M., Valade S., Cigolini C., Ripepe M. (2020). Volcanic Hot-Spot detection using SENTINEL-2: A comparison with MODIS-MIROVA thermal data series. *Remote Sens.*, 12 (5), 820. https://doi.org/10.3390/rs12050820

- Coppola D., Laiolo M., Cigolini C., **Massimetti F.**, Delle Donne D., Ripepe M, Arias H., Barsotti S., Parra C.B., Riky G. , Cevuard S., Chigna G., Chun C., Garaebiti E., Gonzales D., Griswold J., Juarez J., Lara L.E., López C.M., Macedo O., Mahinda C., Ogburn S.E., Prambada O., Ramon P., Ramos D., Peltier A., Saunders S., De Zeeuw - Van Dalfsen E., Varley N., William R. (2020). Thermal remote sensing for global volcano monitoring: Experiences from the MIROVA system. *Front. Earth Sci.*, https://doi.org/10.3389/feart.2019.00362
- Walter T.R., Haghshenas Haghighi M., Schneider F.M., Coppola D., Motagh M., Saul J., Babeyko A., Dahm T., Troll V.R., Tilmann F., Heimann S., Valade S., Triyono R., Khomarudin R., Kartadinata N., Laiolo M., **Massimetti F.**, Gaebler P., 2019. Complex hazard cascade culminating in the Anak Krakatau sector collapse. *Nat. Commun.*, 10 (1), 1-11. https://doi.org/10.1038/s41467-019-12284-5
- Coppola D., Laiolo M., **Massimetti F.**, Cigolini C., 2019. Monitoring endogenous growth of open-vent volcanoes by balancing thermal and SO2 emissions data derived from space. *Sci. Rep.*, 9 (1), 9394. https://doi.org/10.1038/s41598-019-45753-4
- Valade S., Ley A., **Massimetti F.**, D'Hondt O., Laiolo M., Coppola D., Loibl D., Hellwich O., Walter T.R., 2019. Towards Global Volcano Monitoring Using Multisensor Sentinel Missions and Artificial Intelligence: The MOUNTS Monitoring System. *Remote Sens.*, 11 (13), 1528. https://doi.org/10.3390/rs11131528
- Laiolo M., Ripepe M., Cigolini C., Coppola D., Della Schiava M., Genco R., Innocenti L., Lacanna G., Marchetti E., **Massimetti F.**, Silengo M.C., 2019. Space- and Ground-Based Geophysical Data Tracking of Magma Migration in Shallow Feeding System of Mount Etna. *Remote Sens.*, 11 (10), 1182. https://doi.org/10.3390/rs11101182
- Laiolo M., **Massimetti F.**, Cigolini C., Ripepe M., Coppola C., 2018. Long-term eruptive trends from space-based thermal and SO2 emissions: a comparative analysis of Stromboli, Batu Tara and Tinakula volcanoes. *Bull. Volcanol.*, 80, 68. https://doi.org/10.1007/s00445-018-1242-0
- Coppola D., Laiolo M., Franchi A., **Massimetti F.**, Cigolini C., Lara L.E., 2017. Measuring effusion rates of obsidian lava flows by means of satellite thermal data. *J. Volcanol. Geotherm. Res.*, 347, 82-90. https://doi.org/10.1016/j.jvolgeores.2017.09.003

6. BIBLIOGRAPHY

Auker, M.R., Sparks, R.S.J., Siebert, L., Crosweller, H.S. and Ewert, J., 2013. A statistical analysis of the global historical volcanic fatalities record. Journal of Applied Volcanology, 2(1): 2. https://doi.org/10.1186/2191-5040-2-2

Bally, P., 2012. Scientific and technical memorandum of the international forum on satellite EO and geohazards. European Space Agency Publication, 21–23, 170.

Biggs, J., Ebmeier, S. K., Aspinall, W. P., Lu, Z., Pritchard, M. E., Sparks, R. S. J., & Mather, T. A., 2014. Global link between deformation and volcanic eruption quantified by satellite imagery. Nature Communications, 5(1), 3471. https://doi.org/10.1038/ncomms4471

Boudoire, G., Calabrese, S., Colacicco, A. et al., 2022. Scientific response to the 2021 eruption of Nyiragongo based on the implementation of a participatory monitoring system. Sci Rep 12, 7488. https://doi.org/10.1038/s41598-022-11149-0

Blackett, M., 2017. An overview of infrared remote sensing of volcanic activity. J. Imaging 3 (2), 13. https://doi.org/10.3390/jimaging3020013

Brown, S.K., Loughlin, S.C., Sparks, R.S.J., Vye-Brown, C., Barclay, J., Caldera, E., Cottrell, E., Jolly, G., Komorowski, J.-C., Mandeville, C., Newhall, C.G., Palma, J.L., Potter, S., Valentine, G., 2015a. Global volcanic hazard and risk. In: Loughlin SC, Sparks RSJ, Brown SK, Jenkins SF, Vye-Brown C (eds) Global Volcanic Hazards and Risk. Cambridge University Press, pp. 81–172. https://doi.org/10.1017/CBO9781316276273.004

Brown. S.K., Auker, M.R., Sparks, R.S.J., 2015b. Populations around Holocene volcanoes and development of a population exposure index. In: Loughlin SC, Sparks RSJ, Brown SK, Jenkins SF, Vye-Brown C (eds) Global Volcanic Hazards and Risk. Cambridge University Press, pp. 223–232. https://doi.org/10.1017/CBO9781316276273.006

Carn, S.A., Fioletov, V.E., McLinden, C.A., Li, C., Krotkov, N.A., 2017. A decade of global volcanic SO2 emissions measured from space. Scientific Reports, 7(1), 44095. https://doi.org/10.1038/srep44095

Cigolini, C., Coppola, D., Yokoo, A. et al., 2018. The thermal signature of Aso Volcano during unrest episodes detected from space and ground-based measurements. Earth Planets Space 70, 67. https://doi.org/10.1186/s40623-018-0831-7

Civico, R., Ricci, T., Scarlato, P. et al.,2022. High-resolution Digital Surface Model of the 2021 eruption deposit of Cumbre Vieja volcano, La Palma, Spain. Sci Data 9, 435. https://doi.org/10.1038/s41597-022-01551-8

Coppola, D., Piscopo, D., Laiolo, M., Cigolini, C., Delle Donne, D., Ripepe, M., 2012. Radiative heat power at Stromboli volcano during 2000–2011: Twelve years of MODIS observations. J. Volcanol. Geotherm. Res., 215–216, 48–60. https://doi.org/10.1016/j.jvolgeores.2011.12.001

Coppola, D., Macedo, O., Ramos, D., Finizola, A., Delle Donne, D., Del Carpio, J., et al., 2015. Magma extrusion during the Ubinas 2013–2014 eruptive crisis based on satellite thermal imaging (MIROVA) and ground-based monitoring. J. Volcanol. Geotherm. Res. 302, 199–210. https://doi.org/10.1016/j.jvolgeores.2015.07.005

Coppola, D., Laiolo, M., Cigolini, C., Delle Donne, D., Ripepe, M. 2016. Enhanced volcanic hot-spot detection using MODIS IR data: Results from the MIROVA system. Geol. Soc. Lond. Spec. Publ. 2016, 426, 181–205. https://doi.org/10.1144/SP426.5

Coppola, D., Ripepe, M., Laiolo, M., Cigolini, C., 2017. Modelling satellite-derived magma discharge to explain caldera collapse. Geology, 45(6), 523–526. https://doi.org/10.1130/G38866.1

Coppola, D., Barsotti, S., Cigolini, C., Laiolo, M., Pfeffer, M., Ripepe, M., 2019. Monitoring the time-averaged discharge rates, volumes and emplacement style of large lava flows by using MIROVA system: The case of the 2014-2015 eruption at Holuhraun (Iceland). Ann. Geophys., 61, 52. https://doi.org/10.4401/ag-7749

Coppola, D., Laiolo, M., Cigolini, C., Massimetti, F., Delle Donne, D., Ripepe, M., Arias, H., Barsotti, S., Parra, C.B., Centeno, R.G., Cevuard, S., Chigna, G., Chun, C., Garaebiti, E., González, D., Griswold, J., Juarez, J., Lara, L.E., López, C.M., Macedo, O., Mahinda, C., Ogburn, S., Prambada, O., Ramon, P., Ramos, D., Peltier, A., Saunders, S., de Zeeuw-van Dalfsen, E., Varley, N., William, R., 2020. Thermal remote sensing for global volcano monitoring experiences from the Mirova system. Front Earth Sci 7. https://doi.org/10.3389/feart.2019.00362

Coppola, D., Valade, S., Masias, P. et al., 2022. Shallow magma convection evidenced by excess degassing and thermal radiation during the dome-forming Sabancaya eruption (2012–2020). Bull Volcanol 84, 16. https://doi.org/10.1007/s00445-022-01523-1

Davies, A.G., Keszthelyi, L.P., Harris, A.J.L., 2010. The thermal signature of volcanic eruptions on Io and Earth,. JVGR 194, 75–99. https://doi.org/10.1016/j.jvolgeores.2010.04.009

Dehn, J., Dean, K. G., Engle, K., & Izbekov, P., 2002. Thermal precursors in satellite images of the 1999 eruption of Shishaldin Volcano. Bulletin of Volcanology, 64(8), 525–534. https://doi.org/10.1007/s00445-002-0227-0

Delgado, F., Poland, M., Biggs, J., Ebmeier, S., Sansosti, E., Lundgren, P., et al., 2019. lessons learned from the ceos volcano pilot in latin american and the ongoing volcano demonstrator project. Geophys. Res. Abstr. 21, EGU2019 – EGU14981.

Ferrucci, F., Prata, F., Amelung, F., Bawden, G., Biggs, J., Briole, P., Del Negro, C., Eineder, M., Jordan, C., Loughlin, S., Puglisi, G., Bianchi, M., Tait, S., Theys, N., Schneider, D., Norbury, D., 2012. Perspectives concerning satellite EO and geohazard risk management: volcanic hazards. In: Bally, P. (Ed.)The International Forum on Satellite EO and Geohazards, The Santorini Conference, 21–23 May 2012. European Space Agency, Santorini, Greece https://doi.org/10.5270/esa-geo-hzrd-2012

Francis, P., Oppenheimer, C., Stevenson, D., 1993. Endogenous growth of persistently active volcanoes. Nature 366, 554–557. https://doi.org/10.1038/366554a0

Girona, T., Realmuto, V. & Lundgren, P., 2021. Large-scale thermal unrest of volcanoes for years prior to eruption. Nat. Geosci. 14, 238–241. https://doi.org/10.1038/s41561-021-00705-4

Global Volcanism Program, 2018. Report on Fuego (Guatemala) (Crafford, A.E., and Venzke, E., eds.). Bulletin of the Global Volcanism Network, 43:8. Smithsonian Institution. https://doi.org/10.5479/si.GVP.BGVN201808-342090

Global Volcanism Program, 2020a. Report on Whakaari/White Island (New Zealand) (Krippner, J.B., and Venzke, E., eds.). Bulletin of the Global Volcanism Network, 45:2. Smithsonian Institution. https://doi.org/10.5479/si.GVP.BGVN202002-241040

Global Volcanism Program, 2020b. Report on Taal (Philippines) (Krippner, J.B., and Venzke, E., eds.). Bulletin of the Global Volcanism Network, 45:6. Smithsonian Institution. https://doi.org/10.5479/si.GVP.BGVN202006-273070

Gouhier, M.; Guéhenneux, Y.; Labazuy, P.; Cacault, P.; Decriem, J.; Rivet, S., 2016. HOTVOLC: A web-based monitoring system for volcanic hot spots. Geol. Soc. Lond. Spec. Publ., 426, 223–241. https://doi.org/10.1144/SP426.31

Harris, A., 2013. Thermal Remote Sensing of Active Volcanoes: A User's Manual. Cambridge, MA: Cambridge university press. https://doi.org/10.1017/CBO9781139029346

Harris, A.J.L., Stevenson, D.S., 1997. Thermal observations of degassing open conduits and fumaroles at Stromboli and Vulcano using remotely sensed data. Journal of Volcanology and Geothermal Research, 76(3-4), 175–198. https://doi.org/10.1016/s0377-0273(96)00097-2

Harris, A.J.L., Flynn, L.P.; Keszthelyi, L., Mouginis-Mark, P.J., Rowland, S.K., Resing, J.A., 1998. Calculation of lava effusion rates from Landsat TM data. Bull. Volcanol., 60, 52–71. https://doi.org/10.1007/s004450050216

Hochberg, E.J.; Roberts, D.A.; Dennison, P.E.; Hulley, G.C. Special issue on the Hyperspectral infrared Imager (HyspIRI): Emerging science in terrestrial and aquatic ecology, radiation balance and hazards. Remote Sens. Environ. 2015, 167, 1–5. https://doi.org/10.1016/j.rse.2015.06.011

Hooper, A., Prata, F., Sigmundsson, F., 2012. Remote sensing of volcanic hazards and their precursors. Proc. IEEE 100 (10), 2908–2930. https://doi.org/10.1109/JPROC.2012.2199269

Knafou, R., « Stromboli or Russian roulette tourism », 2019, mis en ligne le 30 mars 2020, consulté le 29 juillet 2022. http://journals.openedition.org/viatourism/4829

Jay, J.A., Welch, M., Pritchard, M.E., Mares, P.J., Mnich, M.E., Melkonian, A.K., Aguilera, F., Naranjo, J.A., Sunagua, M., Clavero, J., 2013. Volcanic hotspots of the central and southern Andes as seen from space by ASTER and MODVOLC between the years 2000 and 2010. Geol. Soc. Lond. Spec. Publ. 380 (1), 161–185. https://doi.org/10.1144/SP380.1.

Laiolo, M., Coppola, D., Barahona, F., Benítez, J. E., Cigolini, C., Escobar, D., et al., 2017. Evidences of volcanic unrest on high-temperature fumaroles by satellite thermal monitoring: the case of Santa Ana volcano, El Salvador. J. Volcanol. Geotherm. Res. 340, 170–179. https://doi.org/10.1016/j.jvolgeores.2017.04.013

Laiolo, M., Ripepe, M., Cigolini, C., Coppola, D., Della Schiava, M., Genco, R., Innocenti, L., Lacanna, G., Marchetti, E., Massimetti, F., Silengo, M.C., 2019. Space- and Ground-Based Geophysical Data Tracking of Magma Migration in Shallow Feeding System of Mount Etna Volcano. Remote Sens., 11, 1182. https://doi.org/10.3390/rs11101182

Loughlin, S.C., Vye-Brown, C., Sparks, R.S.J., Brown, S.K., Barclay, J., Calder, E., Cottrell, E., Jolly, G., Komorowski, J.-C., Mandeville, C., et al., 2015. An introduction to global volcanic hazard and risk. In Global Volcanic Hazards and Risk; Cambridge University Press: Cambridge, UK; pp. 1–80. ISBN 9781316276273.

Major, J., Lara, L. 2013. Overview of Chaitén Volcano, Chile, and its 2008-2009 eruption. Andean Geology 40 (2): 196-215. https://dx.doi.org/10.5027/andgeoV40n2-a01

Marchese, F., Genzano, N., Neri, M., Falconieri, A., Mazzeo, G., Pergola, N., 2019. A Multi-Channel Algorithm for Mapping Volcanic Thermal Anomalies by Means of Sentinel-2 MSI and Landsat-8 OLI Data. Remote Sens., 11, 2876. https://doi.org/10.3390/rs11232876

Massimetti, F., Coppola, D., Laiolo, M., Valade, S., Cigolini, C., Ripepe, M., 2020. Volcanic Hot-Spot Detection Using SENTINEL-2: A Comparison with MODIS–MIROVA Thermal Data Series. Remote Sens 12: 820. https://doi.org/10.3390/rs12050820

Massimetti, F., Bredemeyer, S., Bravo, C.G., Franco, L.M., Coppola, D., Laiolo, M., Walter, T., 2021a. Overview of Láscar's recent activity as monitored by different observation platforms: multi-years thermal cyclicity as seen from space during the 2013-2020 eruptive episode. PHYSICS OF VOLCANOES 2021 WORKSHOP POV-7. 9-10 March, 2021 http://www.volcanotectonics.de/PoV-2021_program.pdf

Massimetti, F., Coppola, D., Laiolo, M., Campus, A., Cigolini, C., Ripepe, M., 2021b. Quantifying thermal emissions from multiple craters in active volcanoes: a multisensory satellite approach on Stromboli and Etna (Italy) case studies. AGU Fall Meeting 2021, held in New Orleans, LA, 13-17 December 2021, id. V33C-03. 2021AGUFM.V33C..03M

Newhall, C. G., Costa, F., Ratdomopurbo, A., Venezky, D. Y., Widiwijayanti, C., Win, N. T. Z., et al., 2017. WOVOdat – an online, growing library of worldwide volcanic unrest. J. Volcanol. nd Geotherm. Res. 345, 184–199. https://doi.org/10.1016/j.jvolgeores.2017.08.003

Newhall C G, Punongbayan R S (eds), 1996. Eruptive history of Mount Pinatubo. Quezon City, Philippines: Philippine Inst Volc Seism, and Seattle: Univ Wash Press, 1126 p.

Newhall, C. G. (2000). Volcano warnings. In Encyclopedia of Volcanoes (pp. 1–85). New York: Academic Press.

Oppenheimer, C., 1998. Review article: Volcanological applications of meteorological satellites. Int. J. Remote Sens. 19, 2829–2864. https://doi.org/10.1080/014311698214307

Oppenheimer, C., Rothery, D.A., Francis, P.W., 1993. Thermal distributions at fumarole fields - implications for infrared remote-sensing of active volcanos. J. Volcanol. Geotherm. Res. 55 (1–2), 97–115. https://doi.org/10.1016/0377-0273(93)90092-6

Oxford Economics (2010). The economic impacts of air travel restrictions due to volcanic ash. Report. Abbey House, Oxford.

Pallister, J., McNutt, S. R., 2015. "Synthesis of volcano monitoring," in The Encyclopedia of Volcanoes, 2nd Edn, ed. H. Sigurdsson, (Cambridge, MA: Academic Press), 1151–1171. doi: https://doi.org/10.1016/B978-0-12-385938-9.00066-3

Phillipson, G., Sobradelo, R., Gottsmann, J., 2013. Global volcanic unrest in the 21st century: An analysis of the first decade. J. Volcanol. Geotherm. Res., 264, 183–196. https://doi.org/10.1016/j.jvolgeores.2013.08.004

Pieri, D., Abrams, M., 2005. ASTER observations of thermal anomalies preceding the April 2003 eruption of Chikurachki volcano, Kurile Islands, Russia. Remote Sensing of Environment, 99(1–2), 84–94. https://doi.org/10.1016/j.rse.2005.06.012

Poland, M.P., Lopez, T., Wright, R. et al. 2020. Forecasting, Detecting, and Tracking Volcanic Eruptions from Space. Remote Sens Earth Syst Sci 3, 55–94. https://doi.org/10.1007/s41976-020-00034-x

Pritchard, M. E., Biggs, J., Wauthier, C., Sansosti, E., Arnold, W. D., Delgado, F., et al., 2018. Towards coordinated regional multi-satellite InSAR volcano observations: results from the latin America pilot project. J. Appl. Volcanol. 7:5. https://doi.org/10.1186/s13617-018-0074-0

Ramsey, M. S., Harris, A. J. L., 2013. Volcanology 2020: how will thermal remote sensing of volcanic surface activity evolve over the next decade? (invited review article). J. Volcanol. Geotherm. Res., 249, 217–233. https://doi.org/10.1016/j.jvolgeores.2012.05.011

Ramsey, M.S., Harris, A.J.L., Watson, I.M., 2022. Volcanology 2030: Will an orbital volcano observatory finally become a reality? Bull. Volcanol., 84, 6. https://doi.org/10.1007/s00445-021-01501-z

Reath, K., Pritchard, M., Poland, M., Delgado, F., Carn, S., Coppola, D., et al., 2019a. Thermal, deformation, and degassing remote sensing time series (CE 2000–2017) at the 47 most active volcanoes in Latin America: Implications for volcanic systems. Journal of Geophysical Research: Solid Earth, 124, 195– 218. https://doi.org/10.1029/2018JB016199

Reath, K., Pritchard, M., Moruzzi, S., Alcott, A., Coppola, D., Pieri, D., 2019b. The AVTOD (ASTER Volcanic Thermal Output Database) Latin America archive. J. Volcanol. Geotherm. Res. 376, 62–76. https://doi.org/10.1016/j.jvolgeores.2019.03.019

Ripepe, M., Pistolesi, M., Coppola, D., Delle Donne, D., Genco, R., Lacanna, G., et al., 2017. Forecasting effusive dynamics and decompression rates by magmastatic model at open-vent volcanoes. Scientific Reports, 7(1), 3885. https://doi.org/10.1038/s41598-017-03833-3

Shevchenko, A.V., Dvigalo, V.N., Zorn, E.U., Vassileva, M.S., Massimetti, F., Walter, T.R., Svirid, I.Y., Chirkov, SA, Ozerov, A.Y., Tsvetkov, V.A., Borisov, I.A., 2021. Constructive and Destructive Processes During the 2018–2019 Eruption Episode at Shiveluch Volcano, Kamchatka, Studied From Satellite and Aerial Data. Front. Earth Sci. 9:680051. https://doi.org/10.3389/feart.2021.680051

Siebert, L., Simkin, T., Kimberly, P., 2011. Volcanoes of the World, 3rd ed.; University of California Press: Berkley, CA, USA. ISBN: 9780520268777. https://www.ucpress.edu/book/9780520268777/volcanoes-of-the-world.

Sigurdsson, H., 2015. Volcanoes in art. The Encyclopedia of Volcanoes, 1321–1343. https://doi.org/10.1016/b978-0-12-385938-9.00077-8

Sparks, R., 2003. Forecasting volcanic eruptions. Earth and Planetary Science Letters, 210(1-2), 1–15. https://doi.org/10.1016/S0012-821X(03)00124-9

Sparks, R.S.J., Biggs, J., Neuberg, J.W., 2012. Geophysics. Monitoring volcanoes. Science, 335, 1310–1311. https://doi.org/10.1126/science.1219485

Steffke, A.M., Harris, A.J.L., 2011. A review of algorithms for detecting volcanic hot spots in satellite infrared data. Bull. Volcanol. 73, 1109–1137. https://doi.org/10.1007/s00445-011-0487-7

Terry, J.P., Goff, J., Winspear, N. et al., 2022. Tonga volcanic eruption and tsunami, January 2022: globally the most significant opportunity to observe an explosive and tsunamigenic submarine eruption since AD 1883 Krakatau. Geosci. Lett. 9, 24. https://doi.org/10.1186/s40562-022-00232-z

Tilling, R. I., 2008. The critical role of volcano monitoring in risk reduction. Adv. Geosci. 14, 3–11. https://doi.org/10.5194/adgeo-14-3-2008

Valade, S., Ley, A., Massimetti, F., D'Hondt, O., Laiolo, M., Coppola, D., Loibl, D., Hellwich, O., Walter, T.R., 2019. Towards Global Volcano Monitoring Using Multisensor Sentinel Missions and Artificial Intelligence: The MOUNTS Monitoring System. Remote Sens., 11, 1528. https://doi.org/10.3390/rs11131528

Way, L., Pritchard, W.E., Wike, L., Reath, K., Gunawan, H., Prambada, O., Syahbana, S., 2022. Detection of thermal features from space at Indonesian volcanoes from 2000 to 2020 using ASTER. J. Volcanol. Geotherm. Res., 430, 107627. https://doi.org/10.1016/j.jvolgeores.2022.107627

Walter, T.R., Haghshenas Haghighi, M., Schneider, F.M., Coppola, D., Motagh, M., Saul, J., Babeyko, A., Dahm, T., Troll, V.R., Tilmann, F., Heimann, S., Valade, S., Triyono, R., Khomarudin, R., Kartadinata, N., Laiolo, M., Massimetti, F. and Gaebler, P., 2019. Complex hazard cascade culminating in the Anak Krakatau sector collapse. Nature Communications, 10(1): 4339. https://doi.org/10.1038/s41467-019-12284-5

Witham, C.S., 2005. Volcanic disasters and incidents: A new database. Journal of Volcanology and Geothermal Research, 148(3): 191-233. https://doi.org/10.1016/j.jvolgeores.2005.04.017

Wooster, M.J., Zhukov, B., Oertel, D., 2003. Fire radiative energy for quantitative study of biomass burning: Derivation from the BIRD experimental satellite and comparison to MODIS fire products. Remote Sens. Env., 86, 83–107. https://doi.org/10.1016/S0034-4257(03)00070-1

Wright, R., Flynn, L.P., Garbeil, H., Harris, A.J.L., Pilger, E. MODVOLC: Near-real-time thermal monitoring of global volcanism., 2004. J. Volcanol. Geotherm. Res., 135, 29–49. https://doi.org/10.1016/j.jvolgeores.2003.12.008

Wright, R., 2016. MODVOLC: 14 years of autonomous observations of effusive volcanism from space. Geological Society, London, Special Publications, 426(1), 23–53. https://doi.org/10.1144/SP426.12

World Bank, 2022. The January 15, 2022 Hunga Tonga-Hunga Ha'apai eruption and tsunami, Tonga: Global rapid post disaster damage estimation (GRADE) report. International Bank for Reconstruction and Development / The World Bank, Washington DC, p 42.

Chapter 2

2. Volcanic Hot-Spot Detection Using SENTINEL-2: A Comparison with MODIS–MIROVA Thermal Data Series

Massimetti Francesco[1]; Coppola Diego[1,2]; Laiolo Marco[1,2]; Valade Sébastien [3,4]; Cigolini Corrado[1,2]; Ripepe Maurizio[5]

1 – Dipartimento di Scienze della Terra, Università di Torino, V. Valperga Caluso 35; 10125 Torino, Italy;

2 –NATRISK: Centro Interdipartimentale sui Rischi Naturali in Ambiente Montano e Collinare, Università di Torino, Largo Paolo Braccini, 2, 10095, Grugliasco (TO), Italy;

3 – Dep. Computer Vision & Remote Sensing, Technische Universität Berlin, 10587 Berlin, Germany;

4 – GFZ German Research Centre for Geosciences, Telegrafenberg, 14473 Potsdam, Germany;

5 – Dipartimento di Scienze della Terra, Università di Firenze, V. G. La Pira 4; 50121 Firenze, Italy;

Abstract

In satellite thermal remote sensing, the new generation of sensors with high-spatial resolution SWIR data opens the door to an improved constraining of thermal phenomena related to volcanic processes, with strong implications for monitoring applications. In this paper, we describe a new hot-spot detection algorithm developed for SENTINEL-2/MSI data that combines spectral indices on the SWIR bands 8a-11-12 (with a 20-meter resolution) with a spatial and statistical analysis on clusters of alerted pixels. The algorithm can detect hot-spot-contaminated pixels (S2Pix) in a wide range of environments and for several types of volcanic activities, showing high accuracy performances of about 1% and 94% in averaged omission and commission rates, respectively, underlining strong reliability on a global scale. The S2-derived thermal trends, retrieved at eight key-case volcanoes, are then compared with the Volcanic Radiative Power (VRP) derived from MODIS (Moderate Resolution Imaging Spectroradiometer) and processed by the MIROVA (Middle InfraRed Observation of Volcanic Activity) system during an almost four-year-long period, January 2016 to October 2019. The presented data indicate an overall excellent correlation between the two thermal signals, enhancing the higher sensitivity of SENTINEL-2 to detect subtle, low-temperature thermal signals. Moreover, for each case we explore the specific relationship between S2Pix and VRP showing how different volcanic processes (i.e., lava flows, domes, lakes and open-vent activity) produce a distinct pattern in terms of size and intensity of the thermal anomaly. These promising results indicate how the algorithm here presented could be applicable for volcanic monitoring purposes and integrated into operational systems. Moreover, the combination of high-resolution (S2/MSI) and moderate-resolution (MODIS) thermal timeseries constitutes a breakthrough for future multi-sensor hot-spot detection systems, with increased monitoring capabilities that are useful for communities which interact with active volcanoes.

1. INTRODUCTION

Satellite thermal remote sensing is a key discipline to study and monitor recent and ongoing volcanic activity. This role arises from several pioneering studies demonstrating how volcanogenic heat, measured in the InfraRed wavelengths (IR; 0.7–20 μm), is strictly related to the activity of volcano itself (i.e., Gawarecki, et al., 1965; Yokoyama, 1972; Francis, 1979;

Oppenheimer, 1998). In the last decades, space-based thermal data have been used to investigate a wide spectrum of volcanic phenomena, in particular lava-flow-forming eruptions (Harris & Baloga, 2009; Wright & Flynn, 2003], lava lakes' dynamic (Francis et al., 2003; Aiuppa et al., 2018), extrusion of lava domes (Oppenheimer et al., 1993; Wener et al., 2017), mechanisms driving effusive dynamics (Ripepe et al., 2017; Coppola et al., 2017) and magma budgets (D'Aleo et al., 2018; Coppola et al., 2019), as well as to track high-temperature fumaroles (Harris & Stevenson, 1997; Mia et al., 2017; Cigolini et al., 2018). Nowadays, thermal signals from volcanoes can be investigated by using new sensors and processing algorithms, and such advancements will continue to make thermal remote sensing an expanding field, whose techniques represent a safe and low-cost tool for improving volcano comprehension (Ramsey & Harris, 2013). Fundamental parameters, such as the location, size and temperature of the hot target(s), the radiant flux and the time-averaged lava discharge rates (TADR) can be estimated from IR remote sensing and delivered to research centers, observatories and protection agencies that are in charge of volcano monitoring (Harris et al., 2017; Coppola et al., 2019). The thermal signature (i.e., intensity, dimension, spatial distribution and temporal persistency) of these volcanic phenomena may vary in space and time, because of the distinct source processes and conditions at which the hot source (magma/gas) is exposed at the surface. Thus, different kinds of volcanic activities could be expressed by a wide spectrum of thermal signals, with some being more explicit, such as a fresh lava body exposed to surface, others more cryptic, such as a highly viscous lava dome or a hot-degassing surface (Blackett, 2017). The prompt interpretation of the thermal signature is a challenge, particularly for volcano monitoring and real-time assessment of hazardous scenarios.

In the last decade, several automated detection systems of volcanic IR signal have been developed, most of which use the Middle InfraRed/Thermal InfraRed region (MIR, 3.44–4.13 mm; TIR, 8.6–12.2 mm) to extract the radiances emitted by a hot body (Wright et al., 2004; Ganci et al., 2016; Gouhier et al., 2016; Coppola et al., 2016). The widespread use of MIR is mainly because the integrated temperature of the lava surfaces (from 200 to 1200 °C) produces an emission peak at these wavelengths and strongly increases spectral radiance in a pixel if compared with other spectral wavelengths (Wright et al., 2002; Harris, 2013). Particularly, MODIS sensor (Moderate-Resolution Imaging Spectroradiometer, on-board NASA Terra and Aqua satellites since 1999 and 2002, respectively) has been highly utilized in the last 20 years for thermal volcanic observation. This sensor is characterized by two useful bands for volcanic hot-spot detection, located in MIR and TIR respectively, by a moderate spatial resolution in the IR bands (1 km), and by regular overpasses providing up to four images per day considering

both sensors (Rothery et al., 2005). Several algorithms have been developed to automatically detect the presence of thermal anomalies based on MODIS data, each one with its own advantages and drawbacks, mainly related to variabilities in spatial–temporal–spectral resolution and temperature saturation limits (see Steffke & Harris, 2011). Among all, MODVOLC (Wright et al., 2002) and MIROVA (Coppola et al., 2016) are probably the most used in real-time volcanic monitoring (Coppola et al., 2019).

Even though the moderate temporal resolution of MODIS (four data per day) is crucial for volcano monitoring, its spatial resolution (1 km) is too coarse for detailed analysis of volcanic hot spots and prevents to retrieve accurate spatial information from hot targets. Instead, high-spatial-resolution sensors (< 120 meters pixel size), such as the recent Multispectral Instrument (MSI) and the Operational Land Imager (OLI), carried on SENTINEL-2 (Marchese et al., 2018; Valade et al., 2019) and LANDSAT-8 (Blackett, 2014; Mia et al., 2017, 2018) platforms, respectively, or the older ASTER (Advanced Spaceborne Thermal Emission and Reflection) sensor (Ramsey, 2016; Reath et al., 2019), can prove crucial to tackle this. Indeed, smaller pixel size allow a higher detail of observation and measurement, yet with the drawback that higher-resolution IR sensors can saturate and have low temporal resolution for several days (Blackett, 2017). The NASA's LANDSAT program has a long history of satellite volcanic thermal studies since the 1980s, and it has been the centerpiece of high-spatial-resolution volcanic-hot-spot analysis from space (Harris, 2013 and reference therein). The 2013 launch of LANDSAT-8 (OLI and TIRS onboard instruments), with spatial resolution of 100 m in TIR and 30 m in VIS-NIR-SWIR (Visible 0.4 to 0.7 μm/Near InfraRed 0.7 to 1.1 μm/Shortwave InfraRed SWIR 1.1 to 3.0 μm; Harris, 2013) provides a continuation of the LANDSAT program (Blackett, 2014). In any case, its revisit frequency of 16 days poses a major limit to characterize volcanic activity with an adequate temporal resolution.

In this regard, the recent launches of the Copernicus SENTINEL-2A and -2B platforms provide an additional tool to improve high-resolution thermal monitoring of unrest and eruptive dynamics, possibly on a global scale. Even if SENTINEL-2 was mainly designed for agriculture, forests, land consumption, coastlines evolution and risks mapping applications (Drusch et al., 2012), its usage has high potentials for volcanic studies. In fact, the availability of 13 bands, particularly of SWIR channels for detection of thermal emission by hot bodies, a revisit frequency of maximum five days and a spatial resolution of 20 m/pixel in the SWIR bands, make SENTINEL-2 data excellent to detect small high-temperature thermal anomalies and to retrieve relevant spatial information (e.g., location, size and shape) from active hot targets, improving potentialities both for volcanic scientific research and monitoring. Moreover,

the compatibility between the SENTINEL-2 MSI and LANDSAT-8 OLI sensors in spectral calibration and spatial resolutions, particularly in NIR and SWIR regions, allows the scientific community to use the two datasets synergistically, possibly improving and developing volcanic thermal investigations. Nevertheless, because of their recent availability, the SENTINEL-2 (hereafter S2) thermal dataset is partially still under-investigated in volcanological studies: a few works started to use these images, mainly for studying qualitatively a specific eruption or volcanic phase (Laiolo et al., 2019; Plank et al., 2019a,b), mapping lava flows (Corradino et al., 2019) or as a comparison dataset to calculate pixel-integrated temperatures or to infer thermal model of a specific volcanic phenomena (Aufaristama, 2018; Gray et al., 2019).

Anyway, some relevant SWIR fires-devoted hot-spot-detection algorithms, using high-spatial resolution data (LANDSAT-8 and SENTINEL-2), are available (i.e., Murphy et al., 2016; Giglio et al., 2008; Schroeder et al., 2016; Roteta et al., 2019), stating an increasing interest for these imagery products in last years. Moreover, recently, Marchese and co-authors (2019) tested an easy multichannel algorithm based on NIR and SWIR analysis, with valuable results on mapping volcanic hot spots in different volcanic contexts, using both SENTINEL-2 and LANDSAT-8 imagery. However, as far as we know, no operationally systems use these existing high-resolution SWIR-based algorithms for volcanic monitoring tasks and, in addition, no multi-years and continuous analysis have been carried out to combine these algorithms results with automated and web-based hot-spot volcanic detection systems, or to compare hot-spot-related data with key volcanic parameters.

Here, we present a new volcano-dedicated contextual hot-spot-detection algorithm for SENTINEL-2 MSI data, based on SWIR bands analysis, with the aim to precisely locate and quantify the number of thermally anomalous pixels in a variety of volcanic eruptive phenomena. The algorithm analyzes the TOA (Top of the Atmosphere) reflectance of the 12–11–8A bands, improving the hot pixel detection method with a contextual threshold based on a statistical distribution of each thermally anomalous clusters. We tested the reliability of this algorithm by comparing the number of thermally anomalous pixels detected by S2 data with the Volcanic Radiative Power (VRP, in Watt) timeseries provided by the global MIROVA system (Coppola et al., 2016), based on an MIR analysis of MODIS satellite images, at different worldwide volcanoes (Figure 1) during a period of almost four years, between January 2016 –October 2019. More than 2200 S2 images were visually inspected in order to quantitively assess both the algorithm efficiency to sense thermal volcanic activity and the capacity to avoid false alerts, proving its reliability to be applied as a tool on a global scale. Hence, we explore the potential of the integration between moderate- and high-spatial-resolution images, providing exceptional

constrains in terms of distribution, persistence and extent of hot targets, and, in turn, insights to better understand the thermal signals and the related volcanic source processes.

The algorithm represents a volcano-devoted enhancement adopting, as a starting point and solid reference, the HOTMAP detection method (Murphy et al., 2016). But it fully differs, since here the algorithm is developed applying spatial and statistical criteria, reaching an improved care to detect hot pixels on volcanic environments, especially when disturbing effects (i.e., clouds coverage, diffraction spikes, blurring and thermal halo) affect the detection precision and possibly induce to sense non-volcanic-related hot pixels. The algorithm we developed is specifically focused to detect the size (number of hot pixels) and location of volcanic hot thermal anomalies with high accuracy, in order to provide useful and reliable information about thermal signals related to ongoing volcanic activity. In this regard, we preferred to avoid calculation of pixel-integrated temperature or radiant fluxes, because the SWIR bands at a high spatial resolution (such as ASTER and OLI/LANDSAT-8 sensors) offer smaller pixels and a more sensitivity to detect hot magmatic features (200–1200 °C), and thus saturated over high-temperature targets (fires, volcanoes), since a hot surface constitutes a greater part of pixel footprint (Blackett et al., 2011, 2017). In fact, some previous works on fire detection, using SWIR wavelengths, reported common saturation issues, leading to counterfeit DN pixel values and artificial radiances conversions, thereby hindering accurate quantitative analyses (Murphy et al., 2016; Giglio et al., 2008; Schroeder et al., 2016).

This is one of the first works, even if embryonic, to specifically design a volcano thermal-detection algorithm. using S2 high-resolution imagery, tested on several different volcanic cases through a multi-year-long analysis. Moreover, it is the first attempt to compare the two different thermal signals derived from SENTINEL-2 MSI and MODIS sensors on volcanic environments. The algorithm was developed in order to be applicable for volcanic-monitoring purposes at a global scale and to be integrated into thermal space-based systems, such as MIROVA, and in multiparametric applications. In this respect, the algorithm here presented works operationally nowadays on MOUNTS (Monitoring Unrest from Space, http://www.mounts-project.com/home; Valade et al., 2019), a multiparametric monitoring satellite system combining SAR, UV and IR analysis, using SENTINEL constellation. The final goal of this work is to demonstrate the validity of the here-proposed detection algorithm for the SENTINEL-2 high-resolution data (and possibly exportable on LANDSAT-8 imagery), with the aim to provide to the volcanological community—from single researcher to volcanic observatories and monitoring centers—a useful and solid tool to evaluate the presence and size of active hot spot, to detect possible volcanic precursor thermal signals, and to track the thermal

and spatial evolution of active volcanic portions, such as single vents, fumaroles fields or lava bodies.

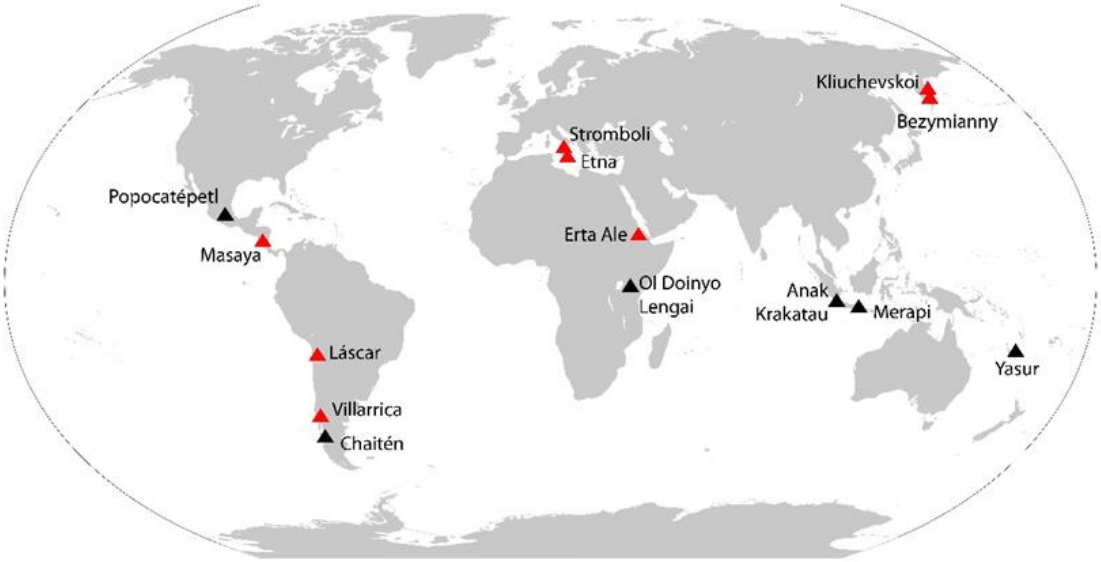

Figure 1 *- Geographic locations of volcanoes investigated in this work. With black triangles are indicated examples of algorithm applications presented in this work; with red triangles the case studies on which MSI SENTINEL-2 and MODIS–MIROVA 2016–2019 timeseries are here shown.*

2. PRODUCTS AND METHODS

2.1. SENTINEL-2 Products

The SENTINEL-2 mission consists of the two platforms, 2A and 2B, launched in June 2015 and March 2017, respectively, by the European Space Agency (Copernicus program). They are located at 786 km altitude and placed in the same sun-synchronous polar orbit at 180° from each other (ESA Sentinel Online, https://sentinel.esa.int/web/sentinel/missions/sentinel-2). The Multispectral Instrument (MSI) onboard captures multispectral images at 13 different bands, spanning from visible (VIS) to short-wave infrared (SWIR) wavelengths, with spatial resolution of 10, 20 and 60 m (Table 1). The revisit time, considering both orbiting platforms, spans from 5 days at equator latitudes to 2–3 days at midlatitudes (Li & Roy, 2017). The SENTINEL-2 constellation provides coherence with LANDSAT-type image data, contributing to ongoing multispectral observation (Li & Roy, 2017; ESA Sentinel Online). Here, we used the SENTINEL-2 Level-1C products, composed of 100 x 100 km^2 tiles (or granules) orthorectified in UTM/WGS84 projection, where the radiometric data are furnished in Top of Atmosphere (TOA) reflectances (ρ), together with the conversion parameters for radiances calculation.

Band number	Resolution (m)	Central wavelength (μm)	Purpose
Band 1	60	0.443	Aerosol detection
Band 2	10	0.490	Blue
Band 3	10	0.560	Green
Band 4	10	0.665	Red
Band 5	20	0.705	Vegetation classification
Band 6	20	0.740	Vegetation classification
Band 7	20	0.783	Vegetation classification
Band 8	10	0.842	Near Infrared
Band 8a	20	0.865	Vegetation classification (NIR/SWIR)
Band 9	60	0.945	Water vapor
Band 10	60	1.375	SWIR - Cirrus
Band 11	20	1.610	SWIR
Band 12	20	2.190	SWIR

Table 1 *- Wavebands of MSI sensor onboard of SENTINEL-2 satellites.*

2.2. Data Access

SENTINEL-2 data are originally distributed by the ESA Copernicus Open Access Hub (https://scihub.copernicus.eu/dhus/#/home) and in the past years, other visualization and storage platforms came out, which can be of great help to whoever takes the first steps to manage satellite data. Amongst these, the cloud storage service of Amazon Web Service S3 (AWS-S3) hosts SENTINEL-2 data, which are added regularly, usually within few hours after they are available on Copernicus OpenHub. One of the advantages of this service (AWS-S3) consists in the possibility to download just single bands of interest, instead of the entire SENTINEL-2 L1C product, greatly reducing the amount of data to be downloaded for specific applications. By considering three bands with 20 m of resolution, as used by the here-proposed algorithm, this opportunity allows us to reduce the data volume from ~ 600 MB (full SENTINEL-2 Level-1C size) to that of the three downloaded bands (i.e., less than ~100 MB). Conversely, it is important to point out that, since summer 2018, this service has imposed a pay request for each download ($0.05–$0.09 per GB, AWS Documentation; roughly, less than $1 for a one-year thermal monitoring, using the three SWIR bands per volcano). After downloading the bands of interest in JPEG 2000 format and the supporting metadata files (Granule_Metadata_File and Product_Level_Metadata containing respectively the geometric/satellite and sensing data), granules products are cropped in a mask of 10 km size (501×501 pixel), centered on the coordinates of each volcano summit of interest. For consistency with the MIROVA system (see Coppola et al., 2016), we used the Global

Volcanism Program volcano database (Global Volcanism Program, 2013a) as a reference for both volcano names and coordinates.

2.3. Hot-Spot Algorithm

According to several authors (Murphy et al., 2016; Giglio et al., 2008; Schroeder et al., 2016), for the hot-spot detection during daytime, SWIR reflectances are preferred to radiances because (i) they are normalized to the incoming solar radiation, reducing the effects of Earth–sun–satellite geometry; and (ii) they allow for better compatibility between different satellite sensors (SENTINEL-2 MSI and LANDSAT-8 OLI, mainly), making the algorithm easily exportable to other sensors (Murphy et al., 2016). The presented algorithm is based on the analysis on the TOA reflectances of three bands in the SWIR regions, ρ8a (865 nm), ρ11 (1610 nm) and ρ12 (2190 nm), all having a 20 m pixel size resolution (Figure 2). These bands are chosen because the nearest to higher wavelengths, and falling in the SWIR region, extremely sensitive to radiations from very hot surfaces (e.g., fires and fresh lava; Blackett, 2017). In addition, the selected S2 bands are the equivalent of bands 7-6-5 OLI LANDSAT-8 sensor, previously used for fires detection (Murphy et al., 2016; Giglio et al., 2008; Schroeder et al., 2016). The algorithm is essentially divided into three main steps focused in detecting all the hot-spot-contaminated pixels present in the analyzed image (Figure 3). In the first step, a series of logical test is used to identify pixels potentially contaminated by hot spots. The second step calculates a Thermal Index (hereby considered a proxy of the pixel integrated temperature) for each alerted pixel and group the adjacent pixels into distinct clusters. In the third step, each cluster is analyzed spatially and statistically in order to reduce effects of thermal halo, diffractions spikes or "blurring" (adjacency effects, i.e., the scattering of light reflected from the nearby land into the sensor's field of view, due to contrast between a target pixel and its neighborhood; Sterckx et al., 2015).

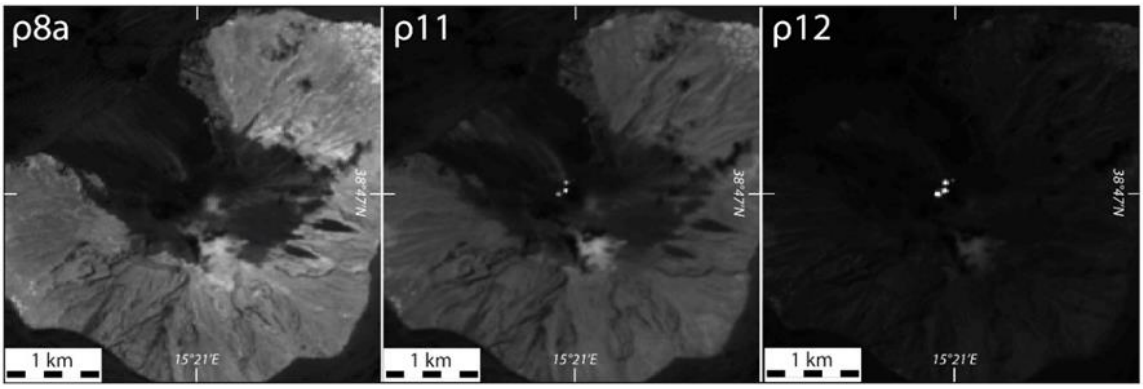

Figure 2 *- SENTINEL-2 images of ρ8a (865 nm), ρ11 (1610 nm) and ρ12 (2190 nm) bands in grayscale colors, over Stromboli summit volcano, 12/07/2018. The three separated thermal anomalies, particularly evident in the 11 and 12 bands, are related to the three main summit craters of Stromboli.*

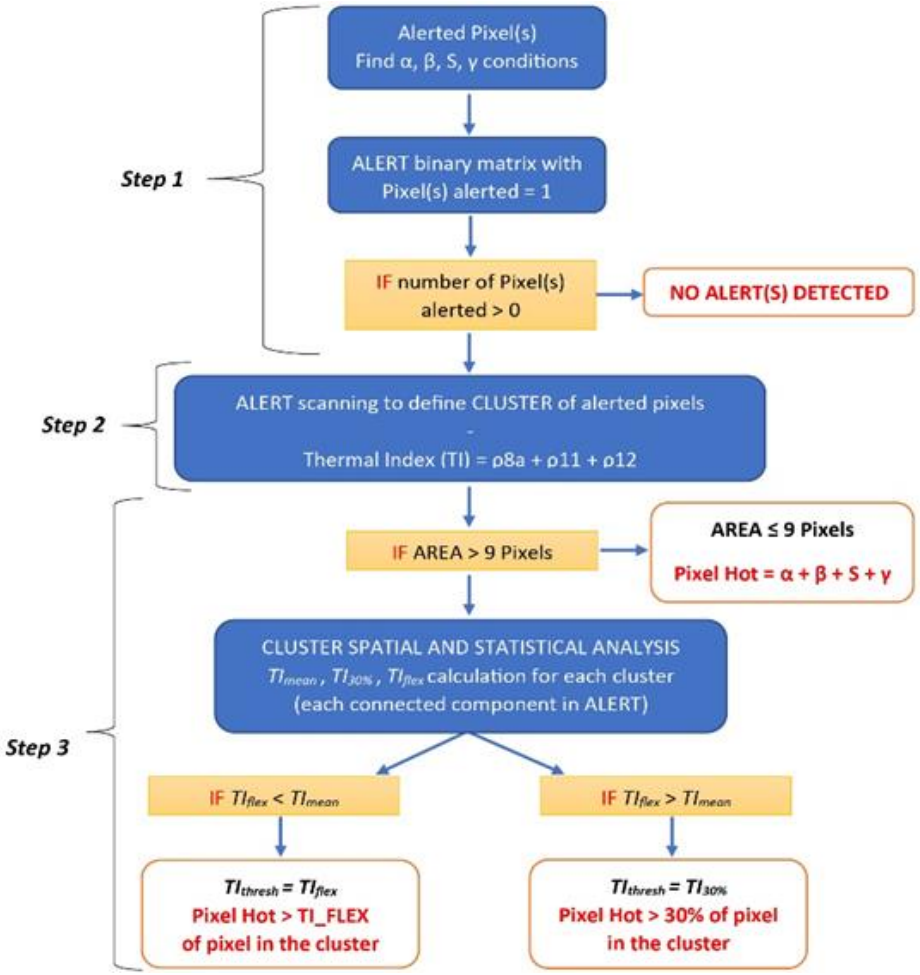

Figure 3 *- Flowchart of the algorithm. In blue boxes are the conceptual steps; in yellow, the logical conditions; and in red, the results. On left side, the three main steps of the algorithm are indicated.*

2.3.1. Step 1: Spectral Principles

This initial step is an implementation of the *Hotmap* algorithm (Murphy et al., 2016), developed to detect hot-spot-contaminated pixels within OLI-LANDSAT 8 daytime images. Accordingly, hot-spot-contaminated pixels are individuated by using reflectance ratios and single-band thresholds grouped to define four distinct logical tests, named α, β, *S* and γ:

$$\alpha = \left[\left(\left(\frac{\rho_{12}}{\rho_{11}}\right) \geq 1.4\right) \& \left(\left(\frac{\rho_{12}}{\rho_{8a}}\right) \geq 1.2\right) \&(\rho_{12} \geq 0.15)\right] \quad (1)$$

$$\beta = \left\{\left[\left(\left(\frac{\rho_{11}}{\rho_{8a}}\right) \geq 2\right) \&(\rho_{11} \geq 0.5) \&(\rho_{12} \geq 0.5)\right]\right\} \quad (2)$$

$$S = \{[(\rho_{12} \geq 1.2) \&(\rho_{8a} \leq 1)] or [(\rho_{11} \geq 1.5) \&(\rho_{8a} \geq 1)]\} \quad (3)$$

$$\gamma = \{(\rho_{12} \geq 1) \&(\rho_{11} \geq 1) \&(\rho_{8a} \geq 0.5)\} \&(surrounded\ by\ \alpha\ or\ \beta) \quad (4)$$

A pixel fulfilling at least one of these tests is flagged as hot-spot-contaminated and is taken into account during the further steps.

In this procedure, we keep the original *Hotmap* approach, where tests α and β are designed to (i) reveal very few false alarms and detect at least one hot "warm" pixel (α condition), and (ii) identify "hot" pixels (β condition). However, we modified the band ratios' thresholds in order to better avoid false alarms over highly reflective surfaces (i.e., clouds and dry soils): parameters α and β are structured in a first-ratio portion (ρ12 must be 40% and 20% greater than ρ11 and ρ8a for α, respectively; ρ11 twofold of ρ8a for β) and in minimal conditions in the three bands, to avoid too-low reflectances in bands 12, 11 and 8a.

In addition, we added two other conditions which allow us to consider pixels having α and/or β corrupted by saturation of bands 12 and 11 (*S* condition), as well as very reflective pixels (γ condition), surrounded by other alerted pixels (satisfying α and β). The thresholds for *S* test condition represent the saturation values, retrieved empirically by analyzing the limits of reflectance values for the SWIR bands in different volcanic thermal active bodies. The γ condition triggers just the very hot detected pixels, which are placed into an area surrounded by α and β parameters; this is necessary to detect pixels located in the inner part of very-high-radiance-emitting events (such as large lava flows or very thermally active lava lakes) otherwise discarded by the previous tests. It should be noted that some single-band thresholds in condition *S* and γ are higher than 1: this condition is necessary since specular effect on land surface and clouds can lead to reflectance values of S2 higher than 1 (ESA Sentinel Online). The spectral thresholds proposed for Step 1 are derived by using an empirical approach, starting with those band ratios proposed by previous hot-spot-detection systems (Murphy et al., 2016) and testing on different volcanic cases (as shown later) the best achievable combination both to avoid non-volcanic false alarms and to detect low thermal anomalies. The output of Step 1 is thus a logical matrix named ALERT (composed by 0 and 1), having the same dimension of the S2 cropped image (501×501 pixel), and containing all the pixels classified as alerted (with value = 1). If the ALERT matrix is composed only by zeros, no alerted pixels are found.

2.3.2. Step 2: Thermal Index

The ALERT mask is scanned in order to group all adjacent pixels potentially alerted into distinct clusters, identified as each connected component in the binary image. As explained above, it is not practical to use the spectral radiances to accurately calculate the area or integrated temperature the sub-pixel hot emitter because, over volcanic targets, the bands 12

and 11 are often saturated. For this reason, in this work, we introduced an empirical Thermal Index (TI), defined as the sum of the reflectance recorded in bands 8, 11 and 12:

$$Thermal\ Index\ (TI) = \rho 8a + \rho 11 + \rho 12 \quad (5)$$

Here, the TI is considered to be a proxy for the pixel integrated temperature, based on the assumption that increasing the size or temperature of the sub-pixels' hot target will produce an increase in the reflectance values and hence in the TI. This Thermal Index is calculated for all the pixels alerted during Step 1. Each cluster is then analyzed separately from the others during the Step 3.

2.3.3. Step 3: Spatial and Statistical Principles

Step 3 consists in the spatial and statistical analysis of TI values, applied to each cluster identified in Step 2 (see scheme in Figure 2). The aim of this step is to remove, or at least reduce, the number of alerted pixels caused by "blurring", diffraction spikes and/or halo effects, which in some cases distort the effective spatial pattern of the anomaly and cause an evident increase in the size of the alerted clusters (i.e., excess of hot area, which may occur in presence of clouds or large thermal anomalies), especially in case of intense thermal anomalies.

Due to their small size, all clusters composed by less or equal than 9 pixels (3×3 box) are considered unaffected by the above-described effects and are immediately classified as hot-spot-contaminated, independently on the TI values. This condition allows us to detect and keep unchanged small-size thermal anomalies associated to hot degassing cracks or eventually occurring at the beginning of a renovated volcanic activity phase (i.e., Figure 4a–d). For instances, fumaroles at Chaitén lava dome (Chile, Global Volcanism Program, 2013b) are perfectly localized by our algorithm, which detect several small (< 9 pixels) clusters composed by α-triggered warm pixels only (Figure 4 a,b). Instead, glowing inside the main vent of Anak Krakatau Island (Indonesia, Global Volcanism Program, 2013c) triggered a central hot pixel (β condition) and a surrounding perimeter of eight warm pixels (α condition), related to a new Strombolian activity producing incandescence and grey plumes at the beginning of the eruptive phase culminating with the December 2018 island flank collapse (Figure 4c,d; see Walter et al., 2019). These cases definitively reveal the meaning of the 9 pixels threshold, working as a minimal criterion to detect thermal signals produced by a very hot and localized source, with a hotter core extending heat in the nearby area of at least of eight pixels. As discussed later, this feature proves to be extremely useful to detect volcanic precursor thermal signals and/or weak but persistent hot spots.

If the cluster is composed of more than 9 pixels, the algorithm applies an investigation of the frequency distribution of TI values (see flow chart in Figure 3 and Figures 5a and 6a). In particular, it calculates the arithmetic mean of TI (TI_{mean}), the 30th percentile of TI ($TI_{30\%}$), and recognizes the value of max departure of the observed distribution from the normal one (TI_{flex}), for each cluster. The frequency distribution plot of the Thermal Index allows us to observe how the different pixels are thermally distributed and where the observed distribution diverges from the theoretical normal one (Figures 5a and 6a). The purpose of this step is to automatically recognize the lower tail of the observed thermal distribution, by defining a "flex" threshold where the distribution of hottest pixels in the cluster moves from the less hot pixels. This analysis allows us to automatically recognize the colder pixels in the lower tail of the TI distribution, which we ascribe to the thermal halo or "blurring effects" surrounding the real hot spots. These pixels are detected by defining a contextual TI threshold (TI_{thres}), which varies from cluster to cluster, depending on the analyzed TI distribution and according to the following conditions:

$$TI_{thresh} = TI_{flex} \quad (for\ TI_{flex} < TI_{mean}) \tag{6}$$

$$TI_{thresh} = TI_{30\%} \quad (for\ TI_{flex} > TI_{mean}) \tag{7}$$

where TI_{flex} is the TI value exhibiting the largest difference between the observed and the theoretical normal distribution (Figure 5a).

We define the two conditions expressed in *(6)* and *(7)*, because the clear presence of a single sharp flex in the distribution of a thermal cluster able to cut the lower emitting pixels is not unequivocal in all cases. This could be mainly due to a limited extension of the hot body, which may bring to a complex thermal distribution with different potential "flexes" (Figure 6), or to masking effects of thermal anomalous region by clouds/plume presence. Indeed, the process could lead to the definition of a too-high thermal flex, which does not differentiate the lower tail but the higher one (see Figure 6a). In these cases, where the $TI_{flex} > TI_{mean}$ (*Equation 7*) in the cluster (green dotted line and black line respectively in Figure 6a), we choose a conservative and fixed solution, setting TI_{thresh} at the 30th percentile of thermal distribution ($TI_{30\%}$, yellow dotted line in Figure 6a). This threshold is set empirically because we observed in lots of thermal distribution cases, particularly those related to limited extended lava bodies, that the 30% simulates a good fitting cut in the divergency between the lower tail and the normal theoretical distribution (cross between blue pixels distribution and the normal theoretical distribution black dotted line Figure 6a).

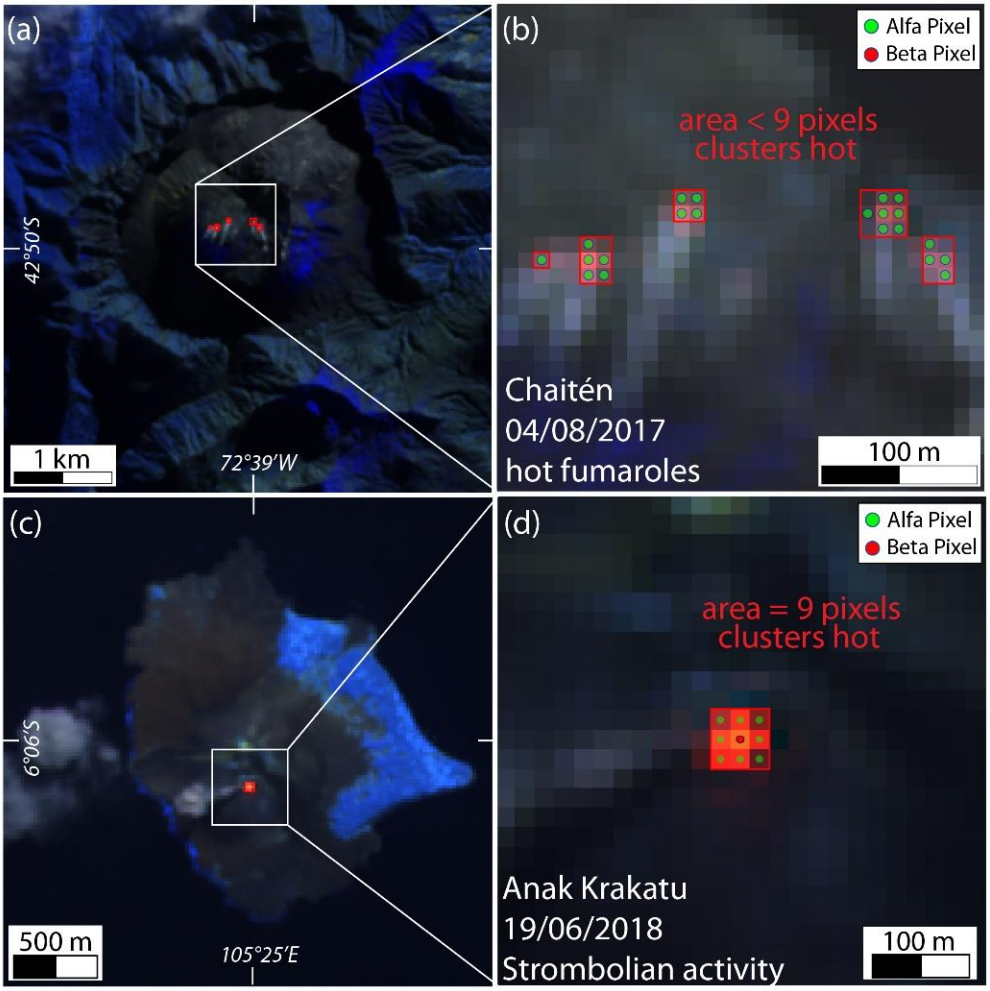

Figure 4 *- Nine pixels threshold. (a) Algorithm application on Chaitén volcano, the 04/08/2017; (b) red boxes represent the bounding box of each alerted cluster and isolated the hot fumaroles; (c) algorithm application on Anak Krakatau volcano, 19/06/2018; (d) red box represent the bounding box of the alerted cluster and isolated the hot-spot pixels related to Strombolian activity. With green and red dots, hot pixels triggered by α and β conditions, respectively.*

The benefit of the frequency distribution analysis is that it does not act as a single threshold over the entire image, but works with a contextual filter based on the thermal distribution of each cluster itself. This means that, for instance, the threshold value for a high thermal anomaly produced by a widespread lava flow will not be the same as the one related to a breakout over an active lava-tube, to hot-degassing fumaroles fields or to hot materials at the surface of a growing lava dome. The discarding process of lower anomalous pixels based on the flex definition cuts the colder boundaries surrounding the hotter core and defines a more-fitting shape of thermal anomalies, as shown in Figures 5b and 6b (where white represents the alerted pixels discarded; green and red are the α-triggered and β-triggered conditions pixels, respectively).

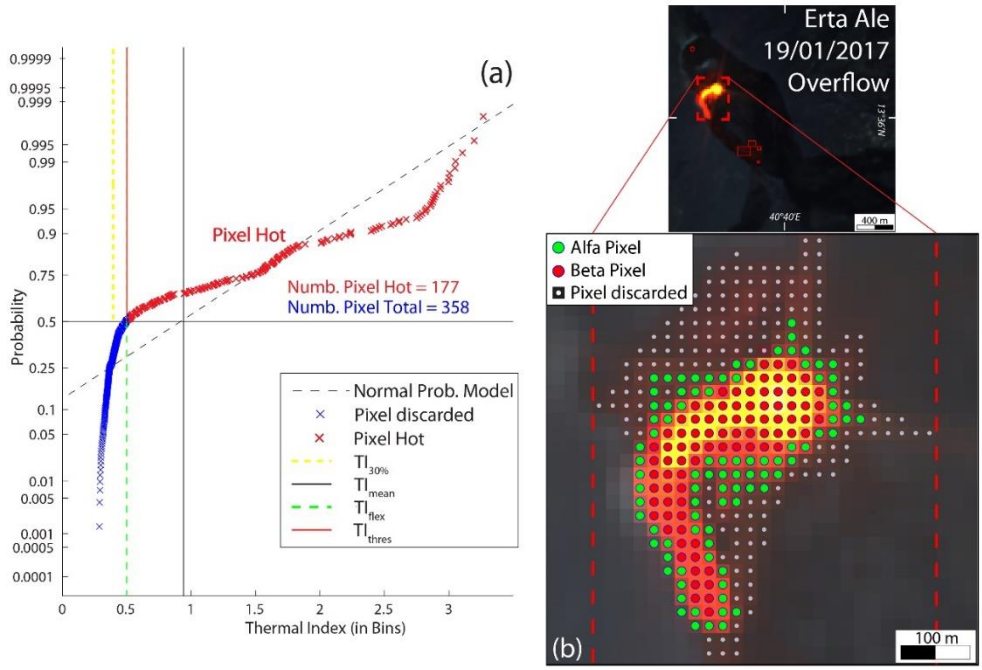

Figure 5 *- Algorithm application on Erta Ale (Global Volcanism Program, 2013d) lava flow case, 19/01/2017. (a) Normal Probability Distribution plot of the Thermal Index (TI) of the analyzed cluster. In red and blue, hot selected and discarded pixels. Dotted black, solid black, dotted yellow, dotted green and red lines represent, respectively, the theoretical normal distribution model, TI_{mean}, TI_{flex}, $TI_{30\%}$ and TI_{thres} hot threshold, fitting with the TI_{flex} in this case. (b) SENTINEL-2 RGB (12-11-8a) image zoomed over cluster analyzed; in green, red and withe, alfa-triggered, beta-triggered and discarded pixels; respectively.*

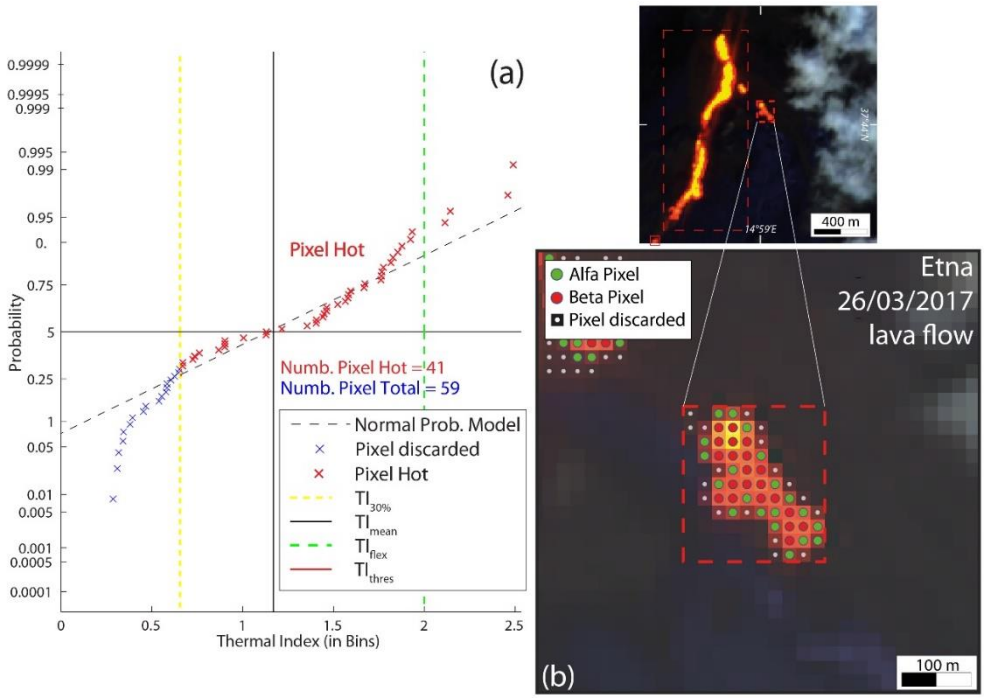

Figure 6 *- Algorithm application on Etna (Global Volcanism Program, 2013e) lava flow small portion, 26/03/2017. (a) Normal Probability Distribution plot of the Thermal Index (TI) of the analyzed cluster. In red and blue, hot selected and discarded pixels. Dotted black, solid black, dotted yellow, dotted green and red lines represent, respectively, the theoretical normal distribution model, TI_{mean}, TI_{flex}, $TI_{30\%}$ and TI_{thres} hot threshold, fitting with the TI_{flex} in this case. (b) SENTINEL-2 RGB (12-11-8a) image zoomed over cluster analyzed; in green, red and withe, alfa-triggered, beta-triggered and discarded pixels; respectively.*

The differentiated-steps procedure described above was designed to work on a wide spectrum of volcanic activity, from hot fumaroles to lava domes, lava flows and lava lake. It has a high sensitivity to low, small thermal anomalies, which is extremely useful to detect both volcanic precursor signals and/or weak persistent hot spots. It is also able to effectively isolate the hottest pixels in wider clusters, discarding anomalous pixels alerted by thermal halo or clouds refraction effects. In this regard, Figure 7 displays two explicit cases to show how the algorithm works overall and its potential for volcanological purposes.

A small-sized light-brown plume, probably of volcanic origin, overlays the anomalies triggered by summit Strombolian activity at Stromboli volcano (Global Volcanism Program, 2013f) during January 2018. The presence of this semitransparent cloud affects the thermal detection, because it produces a halo effect, expanding the possible hot-spotted pixels (Figure 7a). The contextual algorithm here proposed recognizes a clear TI_{flex} in the thermal distribution of the cluster and excludes all pixels interested by cloud reflections, thus precisely isolating the hottest portion of the cluster, mainly colored with yellow to orange and bright red tones (Figure 7c). Figure 7b shows the performance of the Hotmap algorithm (Murphy et al., 2016), which overestimates by about 4 times the hot area detected by our algorithm (Figure 7c).

The strong thermal anomalies occurring over the Yasur's pyroclastic cone (Global Volcanism Program, 2013g), composed by two distinct active vents, indicate a sustained Strombolian activity or spatter producing incandescent bombs as far as the crater rim, underscoring the hazardous nature of get closer to the volcano summit (Figure 7d). The extremely powerful heat-release affects the MSI sensor and induces it to produce a "cross-shaped" thermal effect, called diffraction spikes, with four arms radiating from the bright volcanic sources in the SENTINEL-2 image. We noticed that these artifacts occurred commonly in very energetic and saturating thermal anomalies. As we can see in Figure 7e,f, the here-proposed contextual algorithm, compared to *Hotmap* algorithm, reduces the number of hot pixels related to these diffraction wings, detecting hot materials just into the two crater areas. Therefore, the concurrence of both spatial and statistical filters (Step 3 in the algorithm) particularly allowed to exclude hot-spot pixels not directly related to the volcanic hot spot (i.e., clouds coverage) or triggered by instrument optics effects combined to intense thermal emissions (i.e., diffraction spikes). This enhancement is extremely relevant for monitoring purposes, particularly for automated system applications, since pixels affected by halo effects might have been wrongly interpreted as hot materials emplacing outside the summit crater terrace of Stromboli or the Yasur crater rim, with relevant implications for hazard assessment.

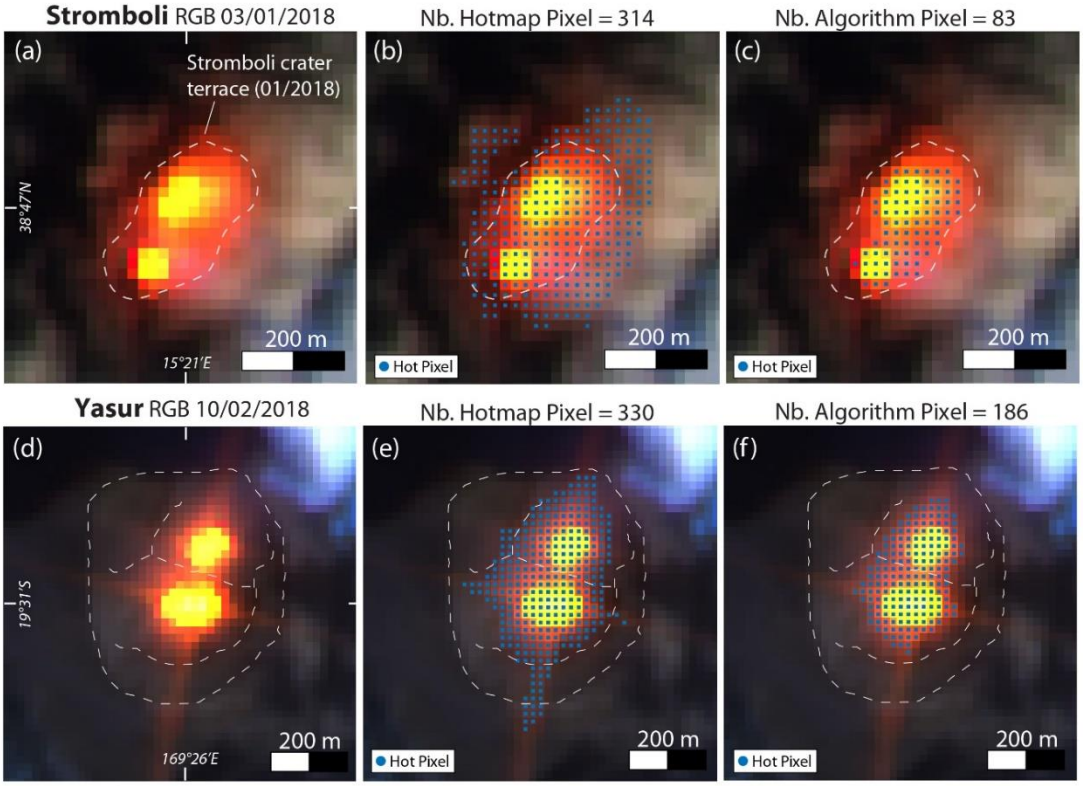

Figure 7 *- Application of the algorithm and comparison with Hotmap. (a) SENTINEL-2 MSI RGB (12-11-8a) image, over Stromboli crater summit area (roughly delimitated with a white dotted line by Google Earth analysis), 03/01/2018; (b) Application of Hotmap algorithm; (c) this work's hot-spot algorithm; (d) SENTINEL-2 MSI RGB (12-11-8a) image, over summit crater of the Yasur pyroclastic cone, composed by the northern and southern vents (roughly delimitated with white dotted lines by Google Earth analysis), 10/02/2018; (e) application of Hotmap algorithm; (f) this work hot-spot algorithm. Blue dots mark the hot detected pixels by the respective algorithms.*

3. RESULTS

The reliability of the algorithm described above was tested on several different volcanoes, first by quantitively evaluating the algorithm performance to detect thermal anomalies and to avoid false alerts, and then by comparing the number of hot pixels detected by the algorithm with MODIS-derived radiant-heat-flux timeseries. Here, we present the results of these analysis.

We investigated eight volcanoes case studies, located in very different geographic contexts and characterized by four exemplary end-members volcanic heat sources: lava flows, lava lake, lava domes and open-vents. The eight case studies are examined from the 1st January 2016 to 1st October 2019 timespan: Kliuchevskoi (Kamchatka peninsula, Russia; Global Volcanism Program, 2013h) and Etna (Sicily island, Italy; Global Volcanism Program, 2013e) for lava-flow activity, Erta Ale (Afar region, Ethiopia; Global Volcanism Program, 2013d) and Masaya (Nicaragua; Global Volcanism Program, 2013i) for lava-lake activity, Stromboli (Sicily island, Italy; Global Volcanism Program, 2013f) and Villarrica (Chile; Global Volcanism Program, 2013j) for open-vent activity in low-viscosity systems, and Bezymianny (Kamchatka peninsula, Russia; Global Volcanism Program, 2013k) and Láscar (Chile; Global Volcanism Program,

2013l) as lava-dome type with high-viscosity lavas extruded (cf. with Figure 1). The algorithm is therefore tested on a wide variety of volcanic systems, in order to assess its performance and limits in detecting various thermal sources. Because the chosen volcanoes show persistent but variable activity, we tested the reliability of this latter on detecting transitions between different eruptive styles over time. Regardless, geographical locations of the volcanoes are variable (Figure 1), with diverse contributions of weather conditions and cloud-coverage effects.

3.1 S2 Algorithm Evaluation

The hot-spot-detection algorithm has the main aim to detect the most of thermal anomalies produced by volcanic activity, by minimizing errors related to false alerts, which is crucial to performing operationally over a global scale. To define when a pixel is volcanologically alerted or not is not a univocal concept (Murphy et al., 2016), and this kind of analysis brings a certain degree of subjectivity and relativity. In this section, we present the performance of the proposed S2 algorithm based on the visual inspection all the SENTINEL-2 images, for a total of 2.211 products, acquired during the January 2016 to October 2019 period, over the abovementioned eight volcanic case studies.

According to our visual inspection, we classify all the "alerting conditions" in the following ways:

- True volcanic alert: a pixel anomaly detected by the algorithm which is expressly and visually related to volcanic activity (hot degassing, lava body exposed, hot eruptive materials exposed and possibly confirmed by literature or consistent with the background knowledge of volcano activity) and that shows a visible thermal glowing (from dark-red to bright-white in color);
- Fires or anthropogenic alert: a pixel anomaly detected by the algorithm expressly and visually related to wildfire occurrence and/or located near of human-settled areas (usually these latter anomalies could be far from the source of volcanic activity, show dark-red tonalities and have a very small areal extent of 1–2 pixels);
- False alert: a pixel anomaly detected by the algorithm, visually related to cloud coverage, secondary cloud fringes and reflections effects over hot sources (also volcanic), blurring, high-reflectivity effects of land/sea surfaces;
- S2-MSI-derived false alert: a pixel anomaly detected by the algorithm and visually triggered by abnormal colored pixels related to stripe artifacts of the MSI sensor.

Notably, one "alerting condition", as defined above, cannot exclude the occurrence in the same S2 image of one or more others "alerting condition(s)", so that different kinds of alerts could take place concurrently. For a successful detection, the algorithm must detect a true volcanic alert, and this capability underlines the reliability of the algorithm to recognize thermal volcanic activity. On the contrary, the algorithm inaccuracy is expressed by how many false alerts have been counted in the overall number of alerts detected. In Table 2, we summarize the evaluation results.

In the upper part of the table, results about detection capabilities of the algorithm are presented. The successful detection percentages (sixth column in upper part of Table 2) show high values for all the case studies, with percentages spanning between ca. 85% and 97% (Bezymianny and Kliuchevskoi as minimum, Masaya as maximum case studies), highlighting the excellent algorithm accuracy on sensing thermal volcanic activity. The main controlling factor appears to be the weather conditions, with the only two percentages below 90% related to the Russian Kamchatka's volcanoes, located at high-latitudes and with a robust cloud cover contribution. Particularly at Bezymianny and Etna, the algorithm missed diverse still visible volcanic hot spot due to a commonly thick cloud coverage, in first case mainly, and to persistent white steam and degassing over summit vents, partially hiding hot anomalous pixels. Notably, fire/human-induced alerts are excluded from this analysis, because they do not represent volcanogenic thermal anomalies, but nevertheless they are not considered as false, because they are likewise triggered by hot-spot sources, thermally comparable with volcano-related ones. Understandably, fires/human alerts are commonplace in Etna and Stromboli, where fires are likely and human activities are located on the volcano's slopes, and Masaya, where the nearby villages surrounding Masaya city fall into 5 km from volcano crater.

In the second part of the table, false-detection amounts per volcano are listed, distinguished between false alerts and MSI artifacts. Algorithm false detection percentages (second column in lower part of Table 2) exhibit generally extreme low values, spanning from no fake alerts to 3.45%, with the two higher percentages are to be found on Etna and Kliuchevskoi. In some case studies (e.g., Erta Ale, Masaya, Villarrica and Láscar), no false alerts are detected, and this is mostly due to absence of cloud coverage and its related disturbing effects. Higher percentages of false detection occur if we also consider fake effects induced by artifact on MSI detector sensing. These effects, known as "spectral response non-uniformity" (ESA, 2020), consist in oblique soft-edged darker or brighter stripes near the detector margins, that induce localized irregular spectral response and anomalous pixel colors, some of that of red tones. Particularly, fake anomalous pixels are produced when stripes interact with clouds coverage, and this issue

is more noticeable still in Etna and Kliuchevskoi cases and absent in ones with cloud-free conditions. These artifacts are tiles and sensor dependent and for that reason does not show the same occurrence in the geographical areas of volcanic case studies analyzed. The evaluation results summarized in Table 2 indicate an overall great reliability of the S2 algorithm here presented for working on a global-scale level, considering the eight different volcanic case studies and their variabilities in thermal activity and geographical location. The remarkable successful detection percentages underline the high sensitivity of the algorithm to detect different thermal hot-spot sizes and natures. Moreover, if we do not consider the MSI-related artifacts, which are not dependent by how algorithm works and neither avoidable nor finally resolvable by our application, false-detection occurrence has certainly low frequencies. Expectedly, the most affecting factor algorithm turns out to be the cloud-cover-related effects, both in true- and false-alerts detection.

3.2 SENTINEL-2 and MODIS–MIROVA Timeseries Comparison

Here, we show the almost four-year-long timeseries comparison between the number of hot pixels, S2Pix, detected by the algorithm application on SENTINEL-2 MSI images and the Volcanic Radiative Power elaborated by the MIROVA system on MODIS data, in order to explore the accuracy of the algorithm to detect and track volcanic thermal activity.

MIROVA is an automated global hot-spot-detection system based on the near-real-time processing of infrared MODIS–MIR data (http://www.mirovaweb.it/; Coppola et al., 2016). Its thermal algorithm incorporates spectral and spatial filters, providing an accurate sensitivity to lower thermal anomalies. It gives a quantification of the Volcanic Radiative Power (heat flux, in Watt) through a hybrid algorithm based on MIR radiance data analysis (~ 3.9 μm) recorded at the moderate spatial resolution of 1 km per pixel of MODIS satellites images. MIROVA currently monitors over 220 volcanoes, providing real-time post-processed products, such as lava effusion rates, in support to eruptive crisis management (Coppola et al., 2020). Figures 8–11 show the heat flux in Watt calculated by MIROVA system (on the left y scale, with blue stem, from 10^5 W to 10^{10} W), and the number of hot pixels S2Pix detected by the new algorithm (on the right y scale, with red dots, from 1 to 10,000) on the eight volcanic case studies. No atmospheric correction was performed on S2-MSI and MODIS images here presented, in order to evaluate the purest detection capabilities. The MODIS dataset is filtered to exclude images with poor viewing geometry (Zenith > 40°) and possible deformation effects of the projected thermal anomalies (see Coppola et al., 2016). The MIR method (Wooster et al., 2003) applied by MIROVA to MODIS images detects the thermal flow radiated from the surfaces with T >

500 K solely and return the VRP with a standard error of 30%. VRP values represent just the thermal output of high-temperature features, produced by the arrival of magma at the surface or at very shallow levels; Coppola et al., 2020).

VOLCANO	S2 Images[1]	Algorithm Alerts[2]	Algorithm Volcanic Alerts[3]	True Volcanic Alerts[4]	Missed Volcanic Alerts[5]	Successful Detection (%)[6]	Fires / Anthropogenic Alerts[7]
ETNA	417	275	259	270	11	95.92%	7
KLIUCHEVSKOI	337	29	25	29	4	86.21%	0
ERTA ALE	207	190	190	197	7	96.44%	0
MASAYA	166	124	117	120	3	97.50%	16
STROMBOLI	243	134	128	132	4	96.96%	7
VILLARRICA	337	184	183	186	3	98.38%	1
BEZYMIANNY	338	126	118	137	19	86.13%	0
LÁSCAR	166	116	116	120	4	96.66%	0

	False Alerts			
VOLCANO	Algorithm False Alerts[8]	Algorithm False Detection (%)[9]	S2-MSI derived False Alerts[10]	False Detection All (%)[11]
ETNA	8	2.91%	22	10.91%
KLIUCHEVSKOI	1	3.45%	3	13.78%
ERTA ALE	0	-	0	-
MASAYA	0	-	2	1.61%
STROMBOLI	2	1.49%	0	1.49%
VILLARRICA	0	-	0	-
BEZYMIANNY	1	0.79%	7	6.34%
LÁSCAR	0	-	0	-

Table 2 *- Results of evaluation of the SENTINEL-2 hot-spot algorithm. 1N. images analyzed; 2N. images with at least one alert detected by the algorithm; 3N. images with at least one true volcanic alert detected by the algorithm; 4N. images with at least one true volcanic alert; 5N. images with at least one true volcanic alert missed by the algorithm; 6Percentage of successful detections = (Algorithm volcanic alerts / True volcanic alerts) * 100; 7N. images with at least one fire/human-related alert detected by the algorithm; 8N. images with at least one false alert detected by the algorithm. 9Percentage of false detections = (Algorithm false alerts / Algorithm alerts) * 100; 10N. images with at least one false alert related to S2-MSI sensor artifacts detected by the algorithm; 11Percentage of false detections considering also the S2-MSI derived false alerts = ((Algorithm false alerts + S2-MSI derived false alerts) / Algorithm alerts) * 100.*

The comparison with MIROVA data is therefore relevant for the S2 algorithm proposed here, because both aim to detect the hottest portion, directly related to the ascent of magmatic fluids subaerially exposed. The first measures the volcanogenic heat flux, and the second measures the number of hot pixels, i.e., the radiant emitting hot area.

Lava flows represent the most prominent example of volcanic heat sources detectable by satellite, as depicted in Figure 8a–h, showing Etna and Kliuchevskoi volcanoes.

In the case of Etna, whose thermal activity varied by several orders of magnitude during the analyzed period (Figure 8a), it is possible to observe how the detected S2Pix follow the VRP

thermal trend with high accuracy and mimic its general trend. In fact, there is a strong correspondence between the two analyzed thermal signals, both during the so-called "low thermal regime", related to Strombolian and degassing activity at the summit craters (characterized by VRP < 10^8 W (cf. Laiolo et al., 2019) and S2Pix < ~100, Figure 8c), and during the "high thermal regime" related to high-sustained Strombolian activity or major lava effusion phases (Figure 8b,d and yellow bands in Figure 8a, characterized by VRP > 10^8 W and S2Pix > 100). Even if energetic events such as summit overflows or fountaining episodes at Etna are generally short-lived, each peak detected by MIROVA is also constrained by S2Pix hot pixels detections, also thanks to 2–3 days of revisit time of SENTINEL-2 above Etna.

Kliuchevskoi volcano is another good example of lava flow-forming eruption, with an excellent correlation between MODIS and S2 related thermal signals, despite the high latitude and strong cloud coverage in the region. In this case, the main thermal activity was recorded between March and November 2016, with a rising trend related to an increased lava effusion from the summit craters (max VRP > 10^9 W, S2Pix >1000; Figure 8e,f,g). A sharp drop in the thermal activity tracked by MODIS and S2 marked the end of the eruptive phase on November 2016, and it was followed by a month-long slow decline of thermal emissions detected by MIROVA (VRP < 10^6 W; Figure 8h). Despite the low revisit frequency at these latitudes, spanning from 5 to 10 days, the effusive phase and its increasing trend was well detected by the algorithm, with a growing number of detections from hundreds to a peak of ~ 1200 S2Pix (Figure 8e). Afterward, the lack of a continuous satellite acquisition and the more sporadic thermal activity of Kliuchevskoi makes the S2 data sparse, although sporadic hot spots were detected during short-lived, low-level resuming phases (May–June 18 and July–August 19; Figure 8e,h).

Lava-lake cases are represented by Erta Ale and Masaya volcanoes, as shown in Figure 9a–h. Erta Ale volcano is well-known for its long-lived lava-lake activity hosted within one (or two) summit pit-crater(s) (Barnie et al., 2016). However, since January 2017, a large flank eruption (still ongoing at the time of this writing), has produced lava flows, with an estimated area of at least 26 km^2, in June 2019 (Moore et al., 2019). Considering the drastic change in the eruptive style, the consistency between MIROVA and S2 thermal signals is remarkable both in terms of recorded intensity and trends (Figure 9a). The correlation between the two signals is very high both during the lava-lake activity (before January 2017; Figure 9b), with S2Pix < 100 and VRP < 10^8 W, except some overflows, as well as during the lava flows' production (after January 2017; Figure 9c/d), with a peak phase in S2Pix (max > 1000 pix.) and VRP (> 10^9 W). Some S2Pix values are underestimated due to cloud coverage that partially masked the satellite sensor detection (S2Pix ~ 10, visual inspection of those data). Moreover, a series of short-lived

overflows occurred during the second half of 2016 and the beginning of the effusive eruption on 22 January 2017 (VRP > 7000 MW) were not detected by S2. This clearly highlights the limitations of this system in detecting short-lived yet very intense events. The high number of S2 hot-spot detections and the strong correlation observed with VRP values are even favored by the good atmospheric conditions in this African area, with a very low number of cloudy periods and, thus, optimal conditions satellite observations.

A similar behavior can be seen in the Masaya case study (Figure 9e), where a persistent thermal output has been detected by MIROVA since the resumption of the lava lake in December 2015 (Aiuppa et al., 2018). Here the S2Pix (generally between 10 to 200 pixels) maintains a good overall match with VRP (~ 10^7 – 10^8 W), tracking the formation and rise of the lava lake until March 2017 (Figure 9e,f,g), followed by a gentle decline until now; notwithstanding, the S2 hot spots appear more scattered and, in some cases, seems to be higher to the corresponding VRP (Figure 9e). This discrepancy could be partially due to (i) a greater influence of cloud coverage in scattering, masking or, at times, increasing of hot spots due to reflection effects by low and thin clouds (blurring effects not completely removed), and (ii) an inner variability in thermal output emission of the Masaya lava-lake system, with different energetic phases related to a rapid fluid dynamic behavior rather than a more stable and slower surface observable at Erta Ale, as testified by some works on Masaya lava-lake dynamics (see Pering et al., 2019 and references therein).

Open-vent activity case studies are represented by Stromboli and Villarrica volcanoes, in Figure 10a–h. Both cases present interesting results, considering that open vents volcanoes should be characterized highly variable activities, with continuous gas emissions, mild explosive behavior and with the magma column top often visible and considered as the last portion of the shallow plumbing system (Rose et al., 2013). At Stromboli, our algorithm detects almost persistent thermal anomalies associated to the continuous but variable Strombolian activity (May–August 2017, December 2017, January 2018) as inferred by MIROVA-derived VRP (Figure 10a). The S2Pix and the VRP show excellent agreement during effusive activity (July–August 2019, Figure 10d), with the threshold of ~ 50 MW (see Coppola et al., 2012), or 50 S2Pix, representing the transition between Strombolian and effusive regimes (summit overflows and/or flank effusions, in Figure 10a as yellow bands and Figure 10d). During periods of weak Strombolian activity the high sensitivity of our algorithm to very low thermal emissions (January–March 2016) is testified by few hot pixels almost continuously detected (S2Pix < 10), with no or weak MIROVA thermal anomalies (VRP ~ 10^6 W; Figure 10b,c). It is also clear how the thermal

signal produced by Strombolian open-vent activity results in a variability in the hot area detected by S2, spanning from a limited S2Pix < 10 to a dozen of hot-spots.

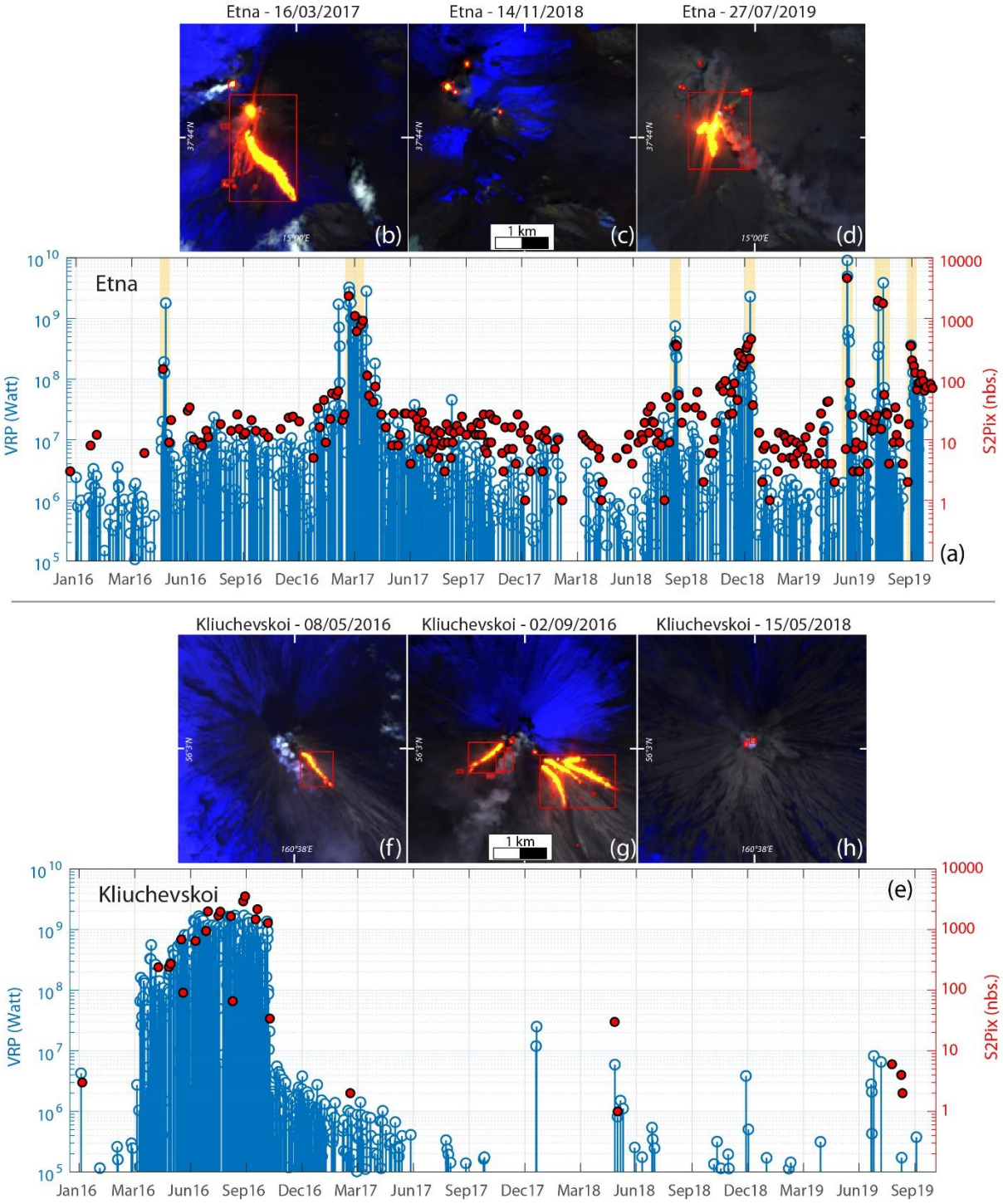

Figure 8 *- S2Pix and VRP–MIROVA thermal comparison on Etna and Kliuchevskoi lava-flow-type case studies. In (a,e), y-logarithmic timeseries. With blue stem on left y-axis, MIROVA VRP heat flux in Watt, with red dots on right y-axis the S2Pix. With yellow pale fields, major effusive phases are indicated for Etna case. In (b,c,d), images, particulars of thermal emissions and volcanic activity over Etna summit. In (f,g,h), particulars of thermal emissions and lava flows over Kliuchevskoi summit area.*

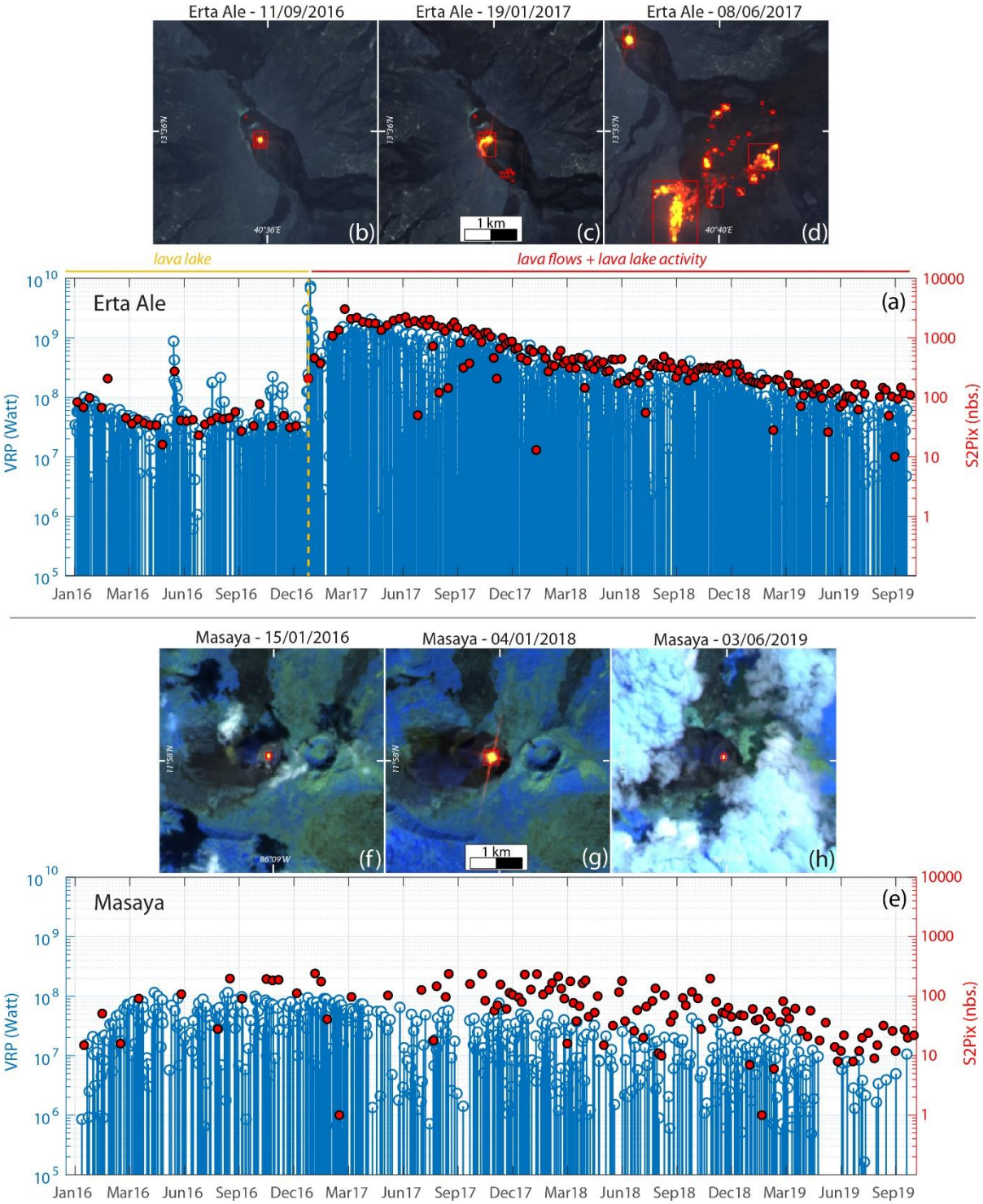

Figure 9 *- S2Pix and VRP–MIROVA thermal comparison on Erta Ale and Masaya lava-lake-type case studies. In (a,e), y-logarithmic timeseries. With blue stem on left y-axis, MIROVA VRP heat flux in Watt; with red dots on right y-axis, the S2Pix. Yellow dotted line in Figure 9a distinguishes the lava-lake activity to the lava-flows periods at Erta Ale. In (b,c,d), particulars of thermal emissions and lava flows over Erta Ale area. In (f,g,h), particulars of thermal emissions and lava-lake activity of Masaya.*

At Villarrica volcano, the MIROVA VRP measurements indicate persistent thermal emissions with values comprised between 10^7 and 10^8 W (Figure 10e–h), with variations in the volcanic heat flux probably related to the fluctuations of the lava level and intensity of Strombolian activity (Palma et al., 2008). Until December 2017, the S2 algorithm successfully recognizes this thermal trend, with a variable hot-spots number, from a few hot pixels to S2Pix > 100, that nicely fit the VRP trend (Figure 10e). Afterward, the VRP shows at least two major cycles of decreasing and increasing thermal emission (Figure 10e). In relation to these cycles, the S2Pix appears quite stable with a value around 10 pix., whilst they also track the higher thermal emitting phases of June-September 2018 (Figure 10g) and of September 2019. This suggests that, during the lowering phases, the area occupied by the thermal anomaly remains roughly constant (i.e., the bottom of the crater), while the thermal flux decreases greatly, in response to the lowering of the effective temperature of the hot target.

A similar behavior is thus found in these two open vent cases, with a strict correlation between VRP–S2Pix during major activity phases and the sensibility to recognize hot emitting area by S2 even when VRP clearly decreases.

Considering the lava-dome activity types, or more generally open-vents activity with high-viscosity magmas (Rose et al., 2013), we analyze Bezymianny and Láscar volcanoes, in Figures 11a–h. During the analyzed timespan, Bezymianny activities consist of sustained fumarolic emissions, periodically interrupted by phases of lava-dome growth, strong explosions and eventually by extrusion viscous lava flows (11a–d). This variability is well represented by VRP data, showing a "thermal baseline" (VRP < 10^7 W), and peaks in thermal flux occurring when lava domes/flows or hot pyroclastic deposits are exposed on the volcano summit and flanks (Figure 11a–d). This activity is well tracked also by the S2Pix, which follows the same overall trend, with particularly good accuracy during the higher activity phases (i.e., peak 16 March 2019, with ~ $7*10^8$ W of VRP and S2Pix = 515, where hot material is dispersed over the top of volcano and surrounding slopes Figure 11d). During lower thermal emission periods or decreasing phase, such as after a strong explosion occurred in June 2017 (Figure 11b), the S2Pix agrees with the overall VRP trend, but with a clear dispersion due to the high cloud coverage in the region.

Instead, over Láscar dome volcano, we find an extremely stable and persistent thermal signal, partially owed to excellent weather conditions in that area, detected by both MIROVA and S2 algorithm. Here, the S2Pix mimics very well the VRP trend both in the 2016–2017 phase, (with

a VRP < 10^7 W and a S2Pix < 10 pixels; Figure 11e), and during phases of increased thermal activity, as occurred from November 2018 (Figure 11h). It is interesting to note that, during the first half of 2018, no thermal activity was detected by either of the systems (Figure 11g). Moreover, the S2 algorithm was able to detect the sharp rise in the thermal signal produced by Láscar lava dome during October to November 2018 (from S2Pix ~ 3 to S2Pix > 20 pixels; Figure 11h).

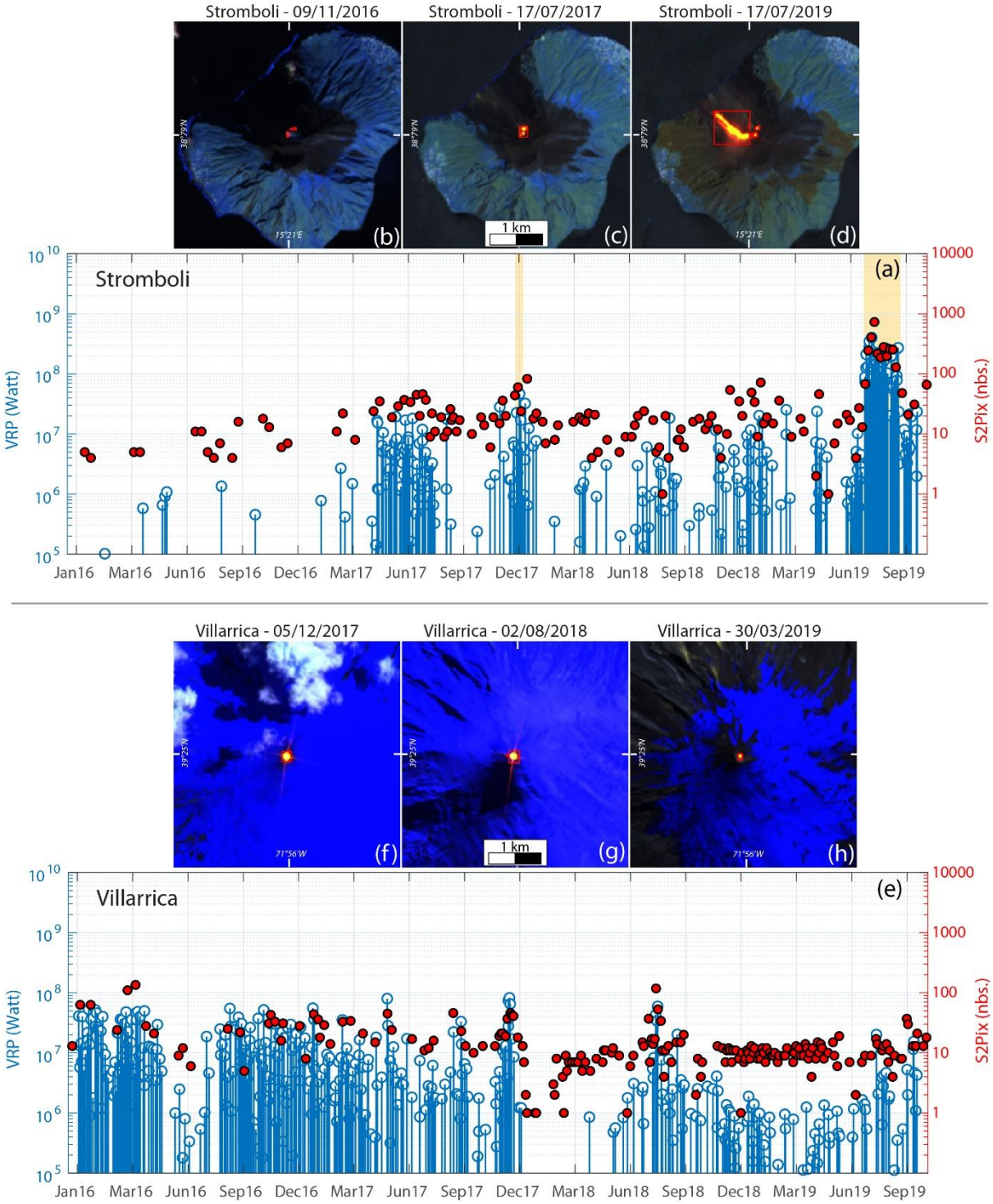

Figure 10 *- S2Pix and VRP–MIROVA thermal comparison on Stromboli and Villarrica open-vent-type case studies. In (a,e) y-logarithmic timeseries. With blue stem on left y-axis, MIROVA VRP heat flux in Watt; with red dots on right y-axis the S2Pix. With yellow fields, major effusive and overflows phases are indicated for Stromboli case. In (b,c,d), particulars of thermal emissions and Strombolian to lava flow activity over Stromboli. In (f,g,h), particulars of thermal emissions and open-vent activity of Villarrica.*

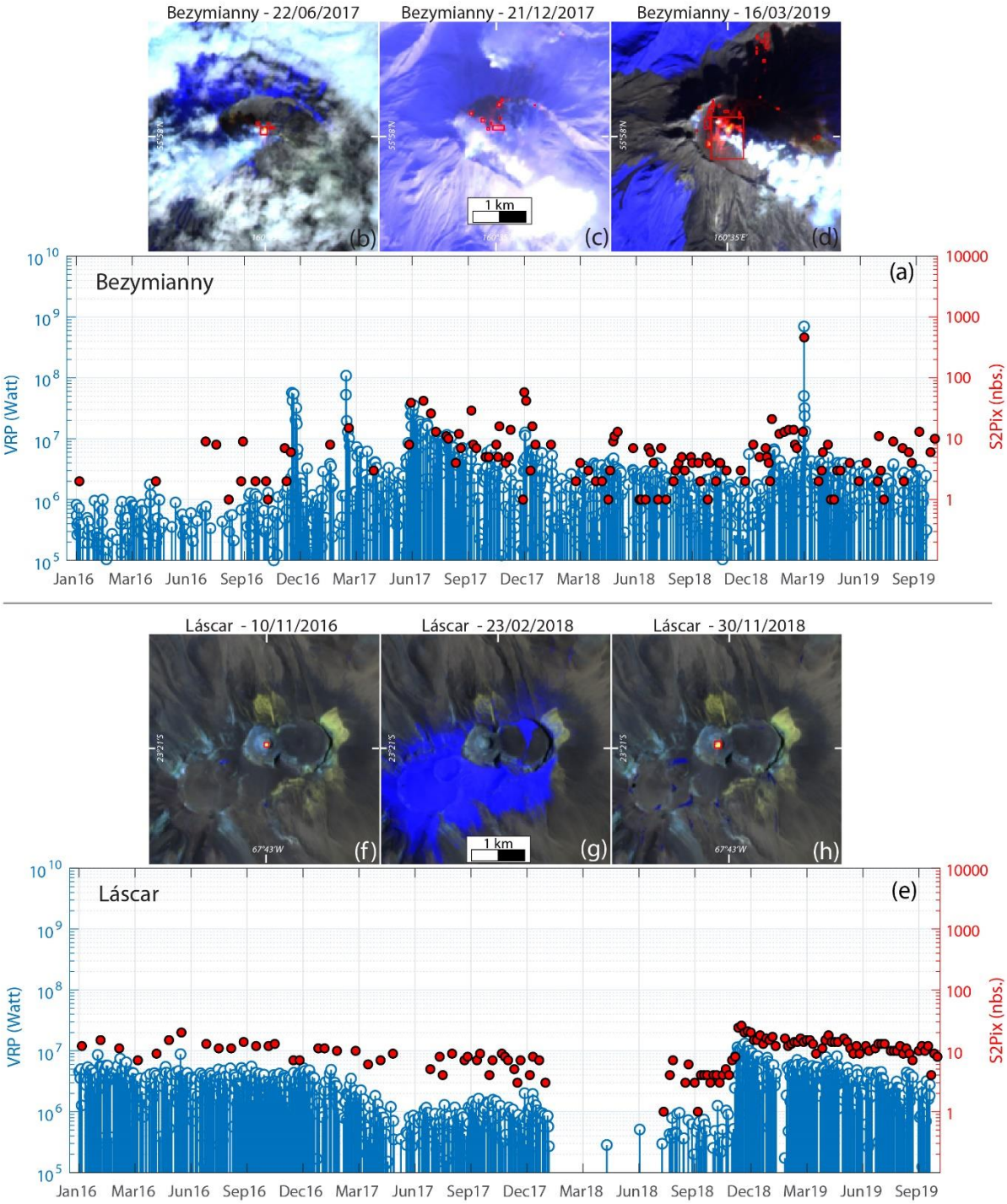

Figure 11 *- S2Pix and VRP–MIROVA thermal comparison on Bezymianny and Láscar lava-dome-type case studies. In (a,e), y-logarithmic timeseries. With blue stem on left y-axis, MIROVA VRP heat flux in Watt; with red dots on right y-axis, the S2Pix. In (b,c,d), particulars of thermal emissions and lava dome activity over Bezymianny summit area. In (f,g,h), particulars of thermal emissions and dome activity of Láscar.*

4. DISCUSSION

The relationship between the number of S2 pixels and the VRP heat flux provides important information on the thermal structure of sources and related volcanic processes at the origin of the anomalies detected by SENTINEL-2 MSI and MODIS. For each of the eight cases described above, we selected only the cloud-free S2 images (through visual inspection), and we considered the maximum VRP recorded by MODIS images (filtered data with Zenith angle < 40°) in a time window of ± 24 hours, from each S2 acquisition. This allowed us to associate the S2Pix to a VRP value measured almost simultaneously, limiting the discrepancies due to sudden changes in activity or cloud cover. The aim is to compare the two best satellite images, acquired when the hot spots and the heat flux should represent and measure the same thermal volcanogenic process. This kind of analysis was similarly applied by some authors to test the correlation between MODIS and other thermal satellite related signals (i.e., ASTER; see Reath et al., 2019). In order to evaluate the correlation between SENTINEL-2 and MODIS–MIROVA data, we examined the eight precedent cases by comparing the intensity of the heat flux produced (VRP) and the hot area responsible for that thermal radiation (S2Pix).

In Figure 12, we plotted the S2Pix as a function of the corresponding VRP, with dashed lines representing "isotherm" curves (from 10^5 to 10^8 W/S2Pix). Considering that VRP represents the radiant flux in Watt and the S2Pix is a proxy of the hot area, the region of the plot where the observed data fall is an indicator of the temperature of the source, which is useful to assess the thermal behavior of the investigated volcanic phenomena. In this regard, for each case, we modeled the relationship (red lines in Figure 12) according to the following equation:

$$logVRP = A(logS2Pix) + B \quad (8)$$

where A and B are the slope (Watt per pixel) and intercept (minimum radiant power for one alerted S2 pixel) of the model. According to *(8)*, the isotherm curves in the graphs have A = 1.

Beginning from volcanoes dominated by lava flows, we observe how the relationship is represented by data that follow an isotherm trend and linearly grow in area and heat flux produced. Even if the numbers of the useful data are strikingly different, both Etna and Kliuchevskoi show this similar behavior (Figure 12a,b). In particular, for Etna, the distribution of the data is representative both of Strombolian (major clustering about 10 - 100 S2Pix and 10^6 - 10^8 W) and effusive activity, with major hot pixels (100 - 1000 S2Pix) and VRP (> 10^8 W). This fits with what is expected for the thermal signal of a lava flow: the higher the area occupied by the hot body is, the greater the radiative power is (Coppola et al., 2016). Kliuchevskoi cluster has a lower number of data points (few cloud free images) and is more

dispersed, but it is strictly related to the effusion phase described in Figure 8e, where the VRP–S2Pix combination detects the rising in thermal signal and the consecutive decline following the cessation of lava-flow feeding.

At lava lakes, two different behaviors are observed at Erta Ale and Masaya (Figure 12c,d). This results from the fact that Erta Ale dataset is composed of two different eruptive styles and associated thermal regimes (cf. Figure 9a). A first regime of lava-lake thermal emission only is characterized by a lower VRP/S2Pix ratio and some higher VRP—lower S2Pix points associated to overflow events. Conversely, the higher thermal regime is related to the large effusive phase (reaching S2Pix > 10^2 and VRP > 10^8 W) and is represented by the dense cluster with isothermal behavior, not by chance, as in Etna and Kliuchevskoi cases (Figure 12a-d). Masaya shows a different thermal behavior, with data clustered in the same region, around S2Pix ~ 10^2 and 10^7 W < VRP < 10^8 W, and not aligned along an isotherm. This feature suggests the presence of a thermal source (the lava lake), essentially confined within the deep crater, with very limited variations in both the hot area and the heat flux.

Lava dome examples draw clusters in the lower leftmost portion of the plots (Figure 12e,f), thus indicating small-size anomalies with an overall low heat radiation involved in dome-forming eruptions, such as degassing, surface cracks on the dome body, collapse events or extrusion phases. The Bezymianny volcano exhibits thermal behavior with most detections having a VRP < 10^7 W and S2Pix < 20, except for a few points related to explosive events or post-explosive exposure of hot ejecta (Figure 12e). Láscar displays two well-clustered point clouds, the first being sparser, around ~ 10^6 W, and the second being denser, with a VRP up to 10^7 W (Figure 12f), that in turn represent the two thermal regimes already observed in the timeseries (Figure 11e). The overall distribution seems partly to cut the isotherms, indicating that periods of higher heat flux are not accompanied by a proportional increase in the hot area exposed.

At open-vent systems, we observe the most scattered distributions among the case studies. Both Stromboli and Villarrica seem to draw a trend with a sharp increase in heat flux, from about 10^5 to VRP > 10^8 W, still maintaining a relatively small amount of hot area exposed, generally with S2Pix < 10^2 (Figure 12g,h). Only a few detections at Stromboli seem to represent a “isothermal” linear relationship between VRP and S2Pix, that are in fact related to an effusive phase occurred during July–August 2019 (cf. with Figure 10a). This behavior could represent an inner character of open-vent volcanoes, where an intensification in the VRP could be related to the increase in the convective dynamics in the upper portion of the magma column, inducing a rising of the

magma column level and an increase in vent(s) temperature (Coppola et al., 2012; 2020), while retaining a hot area quite constant.

These considerations allow us to outline some key points about the algorithm here proposed and its reliability in the detection of volcanic hot spots. First of all, we observe that the SENTINEL-2 hot-spots number has a high correlation with MIROVA analysis ($R^2 > 0.8$), particularly in low-viscous lava flows cases (i.e., Etna, Erta Ale and Kliuchevskoi; Figure 12a,b,c), where hot emitting bodies have the possibility to expand over large areas, to emit greater amount of heat flux and, thus, to trigger the sensitivity both of MODIS and MSI/S2 detectors, even though theirs spectral, spatial and revisit time differences. Conversely, a diverse relationship takes place, when the heat source is partially morphologically constrained, and when the radiative processes are colder or more subtle to detect.

If the number of hot pixels cannot grow due to morphological constrain, the relationship necessarily diverges from an isotherm behavior and become more steep (increasing A parameter in *Equation 8*). This occurs particularly at open-vent systems (i.e., Masaya, Villarrica and, in part, Stromboli examples; Figure 12d,g,h) where changes in the heat flux measured by MIROVA ($A > 1$) are not accompanied by the same evident variations in the hot area exposed to the atmosphere (the vent(s)). Thus, the increasing/decreasing in A value could, in turn, be useful to prove a variability in the temperature, and the consequent emitted heat flux, of the volcanic source.

When the emitter has a small size dimension, such as for lava domes, the VRP/S2Pix distribution substantially falls in the lower left region of the plots, indicating a clear colder thermal behavior, as testified by Bezymianny and Láscar cases. The points distribution can extend to higher VRP and higher S2Pix (following a more linear rule) only during major extrusive phases (Figure 12e,f) or in correspondence of pyroclastic flows produced generally after strong explosions. Therefore, the proposed analysis turns out to be a useful approach to explore the thermal behavior and evolution of the volcanic processes. Accordingly, the different correlations observed and the relative values of R^2 and the occurrence of a linearity between VRP and S2Pix (A parameter) indicate variable relationships between temperature and hot area of volcanic hot emitting body. It is correct and meaningful, from a volcanological point of view, that the amount of VRP produced by a lava dome through hot fumaroles and that of an expanding lava flow by radiation, for examples, have a different related number of hot pixels and thus a different extension of the thermal source. This discrepancy represents the variation in temperature, and we suggest that this method of analysis could be potentially used to explore

and classify the thermal signals of a variety of volcanic activities by space-based methods. The comparison between the number of hot pixels detected and the MIROVA signal is thus relevant to both validate the S2 algorithm detection capability and to infer useful insights about volcanic processes and their thermal features.

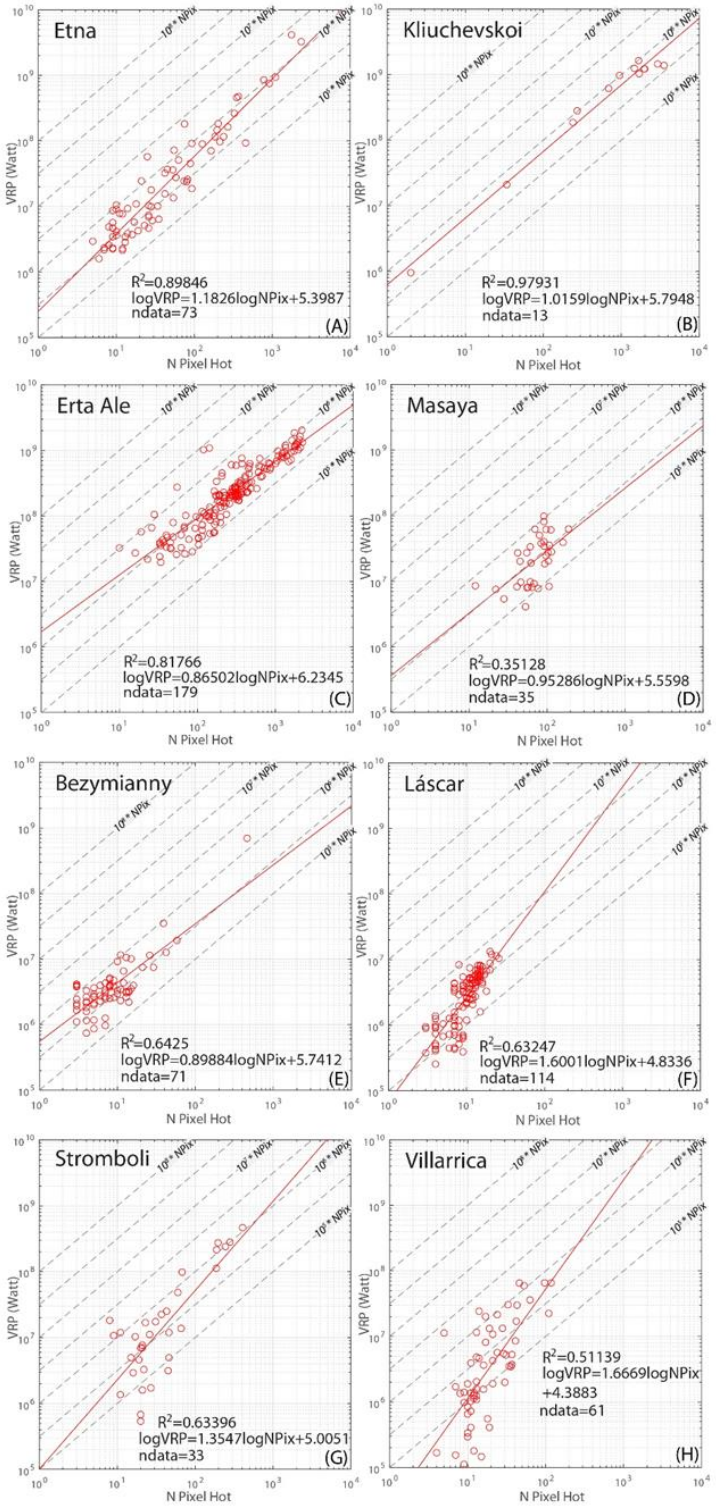

Figure 12 *- Log graphs for volcanic cases analyzed, (A–H). On y-axis, VRP (Watt); on x-axis S2Pix, the number of hot pixels. In each graph, red dots represent the closest SENTINEL-2 and MIROVA data, in an interval of ± 24 h from each S2 cloudy free acquisition; the red line represents the best fit regression for the data. R^2 values, fitting line equation and number of data are reported.*

5. STRENGTHS AND LIMITS

5.1 High-Spatial-Resolution Sensitivity

The most important advantage of SENTINEL-2 MSI imagery products is the high spatial resolution they offer. This feature strongly affects the detection capability and marks a sharp improvement compared to the moderate spatial resolution imagery, such as MODIS. In fact, sensors with higher spatial resolution are more skillful to sense small hot targets, because they cover a bigger proportion of the field of view of the detector element (Murphy et al., 2016). Detecting small thermal anomalies, minor volcanic events or changes in the locations of subtle hot targets could be extremely useful to notice thermal precursor signals and/or variations in weak but persistent hot spots. Here, we show two examples that clearly reflect this proficiency.

In Figure 13, timeseries of SENTINEL-2 S2Pix and MIROVA VRP are presented, for Merapi (Java Island and Indonesia; Global Volcanism Program, 2013m) and Ol Doinyo Lengai (Tanzania, Global Volcanism Program, 2013n) volcanoes. Merapi is the most active Indonesian volcano, located ~ 25 km from the densely populated town of Yogyakarta, and hosts in a 200 meters deep crater, a growing basaltic–andesitic dome regularly disrupted by explosions (up to VEI 4 level) causing pyroclastic flows (Pallister et al., 2013). Notably, an explosive eruption in 2010 killed about 300 people in the southern area of the volcanic edifice (Surono et al., 2012).

Ol Doinyo Lengai (OL) volcano is famous for its unique active carbonatite volcanism, producing fluid and low temperature (495–590 °C) natrocarbonatite lavas (Dawson et al., 1995). Its recent summit thermal features included fumaroles, open vents, or small-scale cooling lava from pools or hornitos (Vaughan et al., 2008). Some works already focused on the thermal analysis of OL activity using MODIS imagery, illustrating the limitations of original MODVOLC algorithm to routinely detect the low-intensity thermal anomalies [Vaughan et al., 2008, Kervyn et al., 2008] and underlining that these restrictions are mainly due to low temperatures, small area extents and low effusion rates of Ol Doinyo Lengai flows.

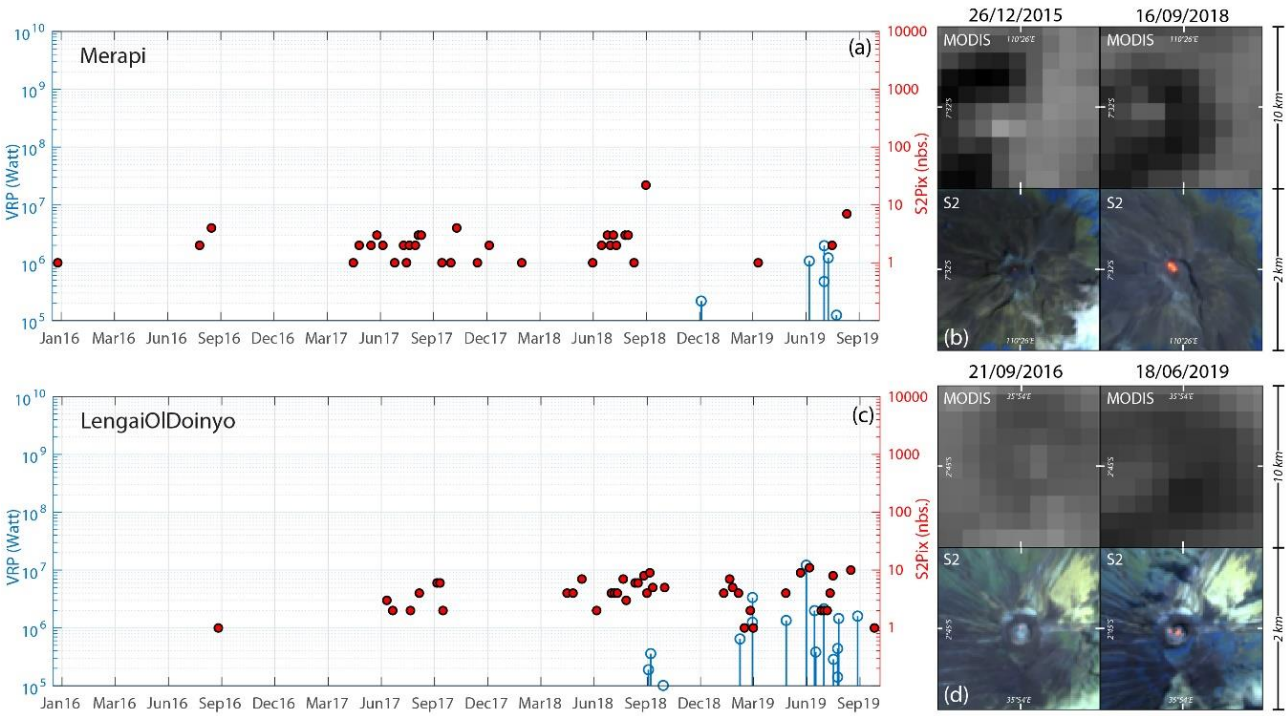

Figure 13 *- SENTINEL-2 and MIROVA thermal comparison. Case studies of Merapi and Ol Doinyo Lengai. In (a,c), logarithmic timeseries. With blue stem on left y-axis, MIROVA VRP heat flux in Watt, with red dots on right y-axis S2Pix. In (b,c), composition images, particulars of NTI–MODIS zoomed maps from MIROVA (see Coppola et al., 2016) are reported on top side, SENTINEL-2 MSI RGB (12-11-8a bands analysis) zooms are reported on the bottom side. The MODIS and SENTINEL-2 MSI images are taken in the same day acquisition and with the closest timing (hours or minutes) available between the acquisitions.*

Our analysis shows that the MSI-S2 20 m resolution images allow the detection of low thermal hot spots at these two volcanoes, otherwise undetected by MODIS 1 km resolution images (Figure 13). At Merapi (Figure 13a), the algorithm detected very low thermal anomalies (S2Pix = 1) since January 2016 and discontinuous but frequent hot spots during all 2017-2018 (max. S2Pix = 20, the 16/09/2018), when MIROVA system did not detect any (Figure 13b). The first MODIS anomaly is measured during December 2018 (very low < 10^6 W), followed during June–August 2019 by sporadic low anomalies (max. $2*10^6$ W). In the analyzed period, the SENTINEL-2 SWIR thermal signal precedes by at least two years the first MIROVA detection, giving regarding the thermal activity persistence and locations during the dome evolution.

Similarly, at Ol Doinyo Lengai, the first SENTINEL-2 detection occurs in September 2016 and is followed by several others hot-spot detections, between 1 < S2Pix < 10, during June–September 2017, April–October 2018 (Figure 13c). Notably, the first thermal activity was detected by MIROVA in September 2018 and then intermittently during 2019 (Figure 13c,d). Here, too, the first SENTINEL-2 hot spot anticipated by almost two years the MIROVA detections, demonstrating the sensitivity of the algorithm to detect the small, low-temperature signals produced by the OL volcano.

Despite the lack of the thermally sensitive MIR bands of MODIS, the advantages using the high-spatial-resolution SWIR wavelengths to detect very hot surfaces are thus outstanding, because any hot spot will most likely cover a major portion of a SWIR pixel, resulting in a clear thermal signal detected.

These two examples demonstrate the improved ability of the proposed algorithm, to detect small and low thermal emissions which are undetected by systems like MIROVA. This ability is of great interest in order to identify possible thermal precursors at explosive and high-risk volcanoes, such as Merapi. Moreover, the low temperature lavas of Ol Doinyo Lengai shows the ability of the proposed algorithm to successfully detect volcanic thermal anomalies in a very wide variety of volcanic settings.

5.2 Reflection Effects and False Anomalies

Due to the high sensitivity of the algorithm to detect subtle and low-temperature thermal anomalies, some issues arise in specific cases, generally related to clouds. One of the most difficult cases is when dense and cirrus clouds partially overlap and/or surround volcanogenic-heat-emission sources. Cirrus clouds are thin and semitransparent, able to create thermal halo when covering the heat source. As demonstrated beforehand (see Section 2.3; Figure 7a–c), the proposed contextual algorithm isolates the hottest part of the triggered cluster, which is falsely enlarged by the thermal halo.

In the case of dense clouds covering intense thermal radiations, strong reflection, along with diffraction effects, may occur. In Figure 14a,b, a SENTINEL-2 RGB image of Nyiragongo lava-lake volcano (DR Congo, Global Volcanism Program, 2013o) in the 8a-11-12 bands is shown, with the relative hot pixels triggered in the α and β conditions by the algorithm. The combined effect of the strong thermal emission produces a “cross-shaped” diffraction spike, and the presence of dense clouds is striking. Here, pixels obscured by clouds become deep red by approaching lava lake because of the sharp reflection and are triggered, mainly by the α condition, as hot pixels by the algorithm (Figure 14b). Moreover, the powerful thermal emission of Nyiragongo lava lake generates an enlargement of the apparent hot area, even when not covered directly by clouds, due to diffraction spike effect on MSI sensor (cf. Figure 7d–f). These pixels are also recognized as hot and alerted by the α condition. Though the thermal emission by Nyiragongo lava lake is not an artifact (the relative measured MIROVA heat flux is about $7*10^8$ W), the result clearly overestimates the hot area dimension (Figure 14b). This issue results from the high sensitivity set for the α condition, that, however, as previously demonstrated, allows the detection of low thermal signal. Overall, the main aim being to offer

a volcanic global applicable algorithm, able to detect hot spots, including hot-fumaroles and low-temperatures lavas, entails that partial overestimation can occur in specific settings, such as Nyiragongo. A possible solution is to use the SENTINEL-2 clouds mask (ESA Sentinel Online. Technical Guides) or to apply a more restrictive thermal algorithm just for a specific volcanic setting, for example limiting the detection to β condition triggered pixels in order to isolate the hottest portion of the detected hot area.

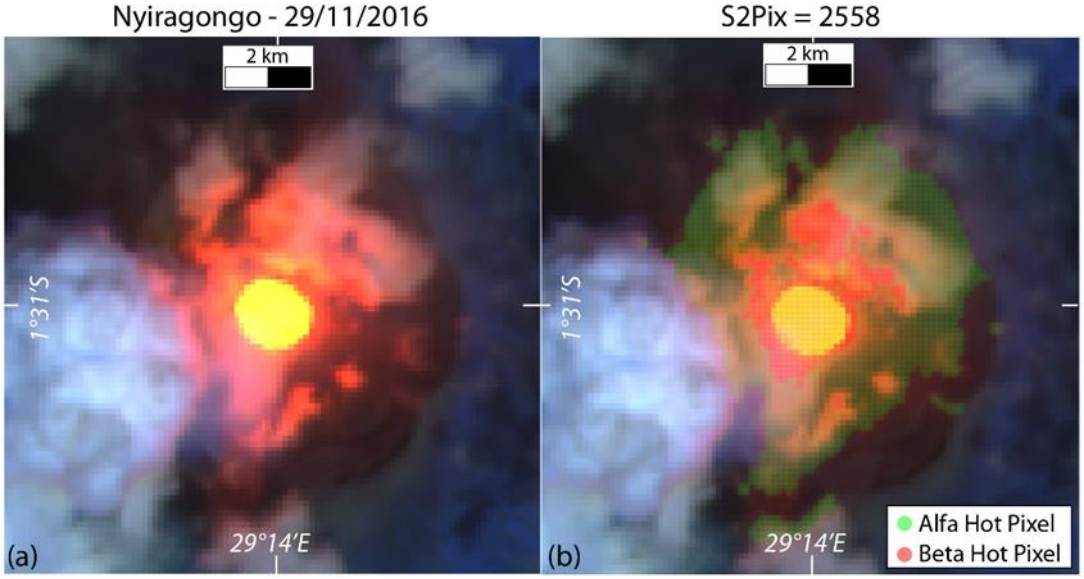

Figure 14 *- Limits of algorithm detection. (a) SENTINEL-2 RGB image (12-11-8a bands analysis), over Nyiragongo lava-lake volcano, 29/11/2016; (b) application of detection algorithm at the same image, in which green area represent the α-triggered pixels and red area represent the β-triggered pixels.*

6. CONCLUSIONS AND PERSPECTIVES

We developed a new algorithm for detecting, locating and counting hot thermal anomalies in volcanic environments, with a global applicability, using SENTINEL-2 satellites images. The algorithm is based on a multispectral hybrid approach, whereby SWIR bands 12, 11 and 8a are spectrally, spatially and statistically elaborated, in order to enhance the presence of subpixel hot spots, with a spatial resolution of 20 meters that represents, nowadays, a remarkable profit for volcanic studies.

To explore the algorithm efficiency, the S2-derived number of hot pixel (S2Pix), detected at eight different volcanoes, was compared with the Volcanic Radiative Power (VRP) recorded by the MODIS–MIROVA thermal dataset. The results demonstrate an extremely coherent match in a variety of volcanic settings, involving hot bodies of various temperatures, spatial extent and typology. The match is particularly striking for wide intense thermal emissions such as lava flows, and more generally proves to give complementary information about thermal volcanic status, even if some limitations are still present mainly due to clouds coverage disturbs.

Moreover, we have not confined our analysis to MSI SENTINEL-2 SWIR and MODIS–MIROVA MIR trend comparisons, but we explored what these correlations, between number of hot pixels detected (hot area) and the heat flux, could decrypt about thermal features related to different volcanic processes.

Significantly, the algorithm presented here is, as far we know, the first SENTINEL-2 multispectral based volcanic thermal detection process that runs operationally. In fact, the algorithm is part of the multiplatform MOUNTS volcanic monitoring system online since the beginning of 2018 (http://www.mounts-project.com/home; Valade et al., 2019). This system uses the SENTINEL constellation (-1, -2 and -5P) to retrieve and display key parameters volcano monitoring timeseries, such as deformation, heat anomalies and SO2 flux, in near real time.

In this work, we demonstrated, through an almost four-year-long investigation of eight case studies, how SENTINEL-2 thermal signal analysis can enhance the study and monitoring of several volcanic processes, including lava-flow morphometric evaluations, extrusion phases and growing dynamics of lava domes, lava-lake pulsations, fumarolic activity, multiple active craters thermal activity, thermal precursors and new hot spots' presence, or periods of magma column rising in open-vent volcanoes.

A future perspective for monitoring purposes is to build an integration of the two thermal datasets, joining both the high-spatial-resolution potentialities of MSI SENTINEL-2 and high temporal resolution of MODIS data processed by the MIROVA system, in order to provide a specifically devoted product for the volcanic thermal activity characterization. In Figure 15, an example is provided with an application to Popocatépetl volcano (Mexico, Global Volcanism Program, 2013p). The two SENTINEL-2 RGB images allow to visualize the thermal anomaly location and status into the crater, with a double zoom visualization 2 x 2 km and 10 x 10 km and immediate estimation of the number of hot pixels and maximum distance from the summit of volcano, while the plots on short (two months) and long (two years) timespan allow to evaluate the thermal activity and to track the evolution of hot area exposed and heat flux radiated. The two RGB S2 images with a different detail level, the number hot pixels and the heat flux produced by volcanic activity, summarized in a near real-time produced output, can provide an easy-to-understand product, rich of relevant qualitative (location and presence of hot spot) and quantitative (heat flux, hot area exposed) information both on the past and current thermal activity state of volcanoes.

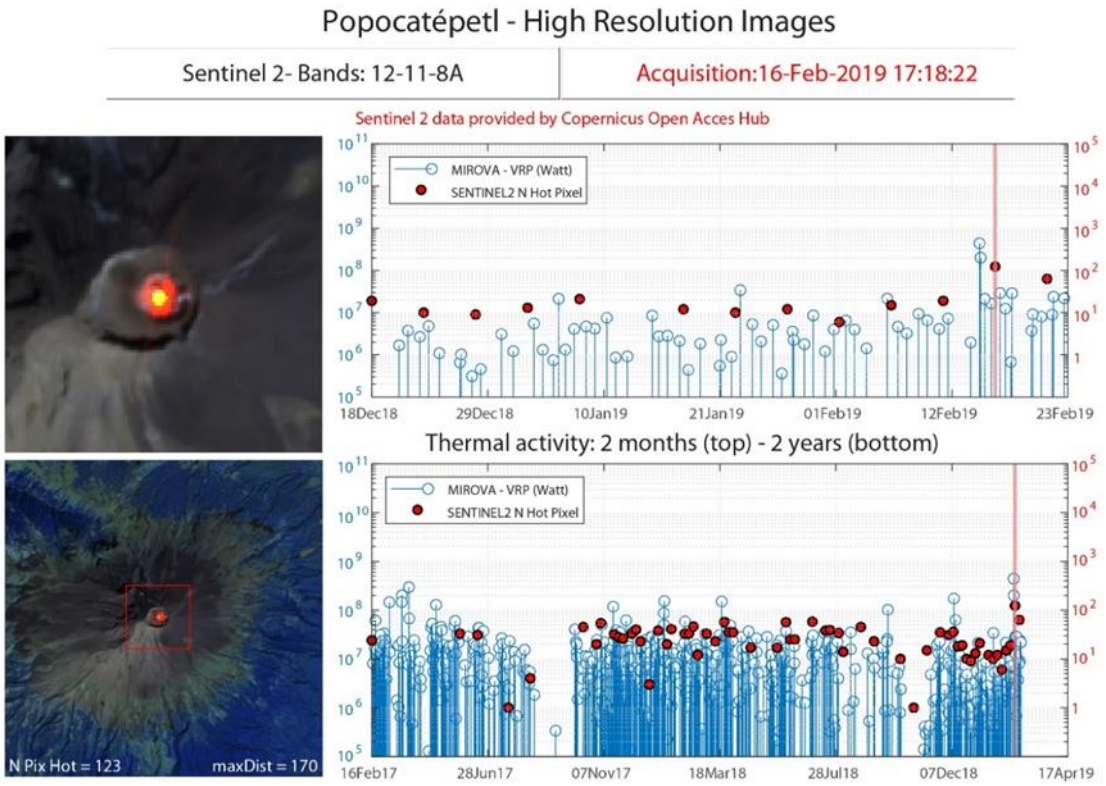

Figure 15 *- Model of output integration of SENTINEL-2 MSI and MODIS–MIROVA thermal data on Popocatépetl volcano. Left panels show the SENTINEL-2 RGB (bands 12, 11 and 8a). On the top-left, a 2 x 2 km zoomed-in view over crater area; on the bottom-left, a 10 x 10 granule with an estimation of the number of hot pixels and the maximum distance of hot pixels from the volcano summit (Global Volcanism Program, 2013p). On the right, two thermal y-logarithmic timeseries, two months and two years on the top and bottom respectively, with MIROVA thermal flux in Watt, blue stems, and S2Pix in red dots.*

Considering the SENTINEL-2 global coverage, and the possible improvement by integrating the LANDSAT 8 OLI data (with 30 m/pixel resolution in the NIR/SWIR bands), a similar output of that exposed in Figure 15, could be produced over the most active volcanoes with a global scale and with a revisit time of a few days. These outputs could be made available to observatories, monitoring centers and local authorities, in order to improve already existing monitoring systems and to contribute to the thermal surveillance of volcanic activity, as already partially suggested by some recent attempts [Coppola et al., 2020; Massimetti et al., 2018).

The current availability of satellite sensors with InfraRed detection capabilities in diverse wavelengths (MIR, TIR and SWIR) gives the possibility to characterize and monitor volcanic activity with an unprecedent level of detail. The MSI SENTINEL-2 multichannel thermal detection algorithm proposed here, even if represents a first-stage effort, and its correlation with MODIS–MIROVA analysis, fits into this view and aims to contribute to the monitoring and understanding of volcanic activity on a global scale.

7. BIBLIOGRAPHY

Aiuppa, A., de Moor, J.M., Arellano, S., Coppola, D., Francofonte, V., Galle, B., Giudice, G., Liuzzo, M., Mendoza, E., Saballos, A., et al. 2018. Tracking formation of a lava lake from ground and space: Masaya volcano (Nicaragua), 2014–2017. Geochem. Geophys. Geosyst., 19, 496–515. https://doi.org/10.1002/2017GC007227

Aufaristama, M., Hoskuldsson, A., Jonsdottir, I., Ulfarsson, M.O., Erlangga, I.G.D., Thordarson, T., 2019. Thermal model of lava in Mt. Agung during December 2017 episodes derived from Integrated SENTINEL 2A and ASTER remote sensing datasets. In Proceedings of the IOP Conference Series: Earth and Environmental Science; Padjadjaran Earth Dialogues, International Symposium on Geophysical Issues 2–4 July 2018, Bandung, Indonesia; IOP Publishing: 2019; Volume 311, p. 012016. http://dx.doi.org/10.1088/1755-1315/311/1/012016

AWS S3. Registry of Open Data on AWS. Available online: https://registry.opendata.aws/ (accessed on November 2019).

AWS Documentation. Requester Pays Buckets. Available online: https://docs.aws.amazon.com/AmazonS3/latest/dev/RequesterPaysBuckets.html (accessed on November 2019).

Barnie, T.D., Oppenheimer, C., Pagli, C., 2016. Does the lava lake of Erta`Ale volcano respond to regional magmatic and tectonic events? An investigation using Earth Observation data. Geol. Soc. Lond. Spec. Publ., 420, 181–208. https://doi.org/10.1144/SP420.15

Blackett, M., 2014. Early Analysis of Landsat-8 Thermal Infrared Sensor Imagery of Volcanic Activity. Remote Sens., 6, 2282-2295. https://doi.org/10.3390/rs6032282

Blackett, M., 2017. An overview of infrared remote sensing of volcanic activity. J. Imaging 3 (2), 13. https://doi.org/10.3390/jimaging3020013

Blackett, M., Wooster, M.J., 2011. Evaluation of SWIR-based methods for quantifying active volcano radiant emissions using NASA EOS-ASTER data. Geomat. Nat. Haz. Risk 2:1, 2, 51–78. https://doi.org/10.1080/19475705.2010.541501

Cigolini, C., Coppola, D., Yokoo, A. et al., 2018. The thermal signature of Aso Volcano during unrest episodes detected from space and ground-based measurements. Earth Planets Space 70, 67. https://doi.org/10.1186/s40623-018-0831-7

Coppola, D., Piscopo, D., Laiolo, M., Cigolini, C., Delle Donne, D., Ripepe, M., 2012. Radiative heat power at Stromboli volcano during 2000–2011: Twelve years of MODIS observations. J. Volcanol. Geotherm. Res., 215–216, 48–60. https://doi.org/10.1016/j.jvolgeores.2011.12.001

Coppola, D., Laiolo, M., Cigolini, C., Delle Donne, D., Ripepe, M. 2016. Enhanced volcanic hot-spot detection using MODIS IR data: Results from the MIROVA system. Geol. Soc. Lond. Spec. Publ. 2016, 426, 181–205. https://doi.org/10.1144/SP426.5

Coppola, D., Ripepe, M., Laiolo, M., Cigolini, C., 2017. Modelling satellite-derived magma discharge to explain caldera collapse. Geology, 45, 523–526. https://doi.org/10.1130/G38866.1

Coppola, D., Laiolo, M., Massimetti, F., Cigolini, C., 2019. Monitoring endogenous growth of open-vent volcanoes by balancing thermal and SO2 emissions data derived from space. Sci. Rep., 9, 9394. https://doi.org/10.1038/s41598-019-45753-4

Coppola, D., Laiolo, M., Cigolini, C., Massimetti, F., Delle Donne, D., Ripepe, M., Arias, H., Barsotti, S., Parra, C.B., Centeno, R.G., Cevuard, S., Chigna, G., Chun, C., Garaebiti, E., González, D., Griswold, J., Juarez, J., Lara, L.E., López, C.M., Macedo, O., Mahinda, C., Ogburn, S., Prambada, O., Ramon, P., Ramos, D., Peltier, A., Saunders, S., de Zeeuw-van Dalfsen, E., Varley, N., William, R., 2020. Thermal remote sensing for global volcano monitoring experiences from the Mirova system. Front Earth Sci 7. https://doi.org/10.3389/feart.2019.00362

Copernicus Open Access Hub. Available online: https://scihub.copernicus.eu/dhus/#/home (accessed on December 2019).

Corradino, C., Ganci, G., Cappello, A., Bilotta, G., Hérault, A., Del Negro, C., 2019. Mapping Recent Lava Flows at Mount Etna Using Multispectral Sentinel-2 Images and Machine Learning Techniques. Remote Sens., 11, 1916. https://doi.org/10.3390/rs11161916

D'Aleo, R., Bitetto, M., Delle Donne, D., Coltelli, M., Coppola, D., McCormick Kilbride, B., Pecora, E., Ripepe, M., Salem, L.C., Tamburello, G., et al. Understanding the SO2 Degassing Budget of Mt Etna's Paroxysms: First Clues from the December 2015 Sequence. Front. Earth Sci. 2018, 6, 239. https://doi.org/10.3389/feart.2018.00239

Dawson, J.B., Keller, J., Nyamweru, C., 1995. Historic and Recent Eruptive Activity of Oldoinyo Lengai. In: Bell, K., Keller, J. (eds) Carbonatite Volcanism. IAVCEI Proceedings in

Volcanology, vol 4. Springer, Berlin, Heidelberg. https://doi.org/10.1007/978-3-642-79182-6_2

Drusch, M., Del Bello, U., Carlier, S., Colin, O., Fernandez, V., Gascon, F., Hoersch, B., Isola, C., Laberinti, P., Martimort, P., 2012. Sentinel-2: ESA's optical high-resolution mission for GMES operational services. Remote Sens. Env., 120, 25–36. https://doi.org/10.1016/j.rse.2011.11.026

ESA Sentinel Online. Missions, SENTINEL 2. Available online: https://sentinel.esa.int/web/sentinel/missions/sentinel-2 (accessed on December 2019).

ESA Sentinel Online. User Guides. Sentinel-2 MSI. Available online: https://sentinel.esa.int/web/sentinel/user-guides/sentinel-2-msi (accessed on December 2019).

ESA Sentinel Online. User Guides. Sentinel-2 MSI. S2-MSI Document Library. Sentinel-2 L1C Data Quality Report Issue 48 (February 2020). Available online: https://sentinel.esa.int/documents/247904/685211/Sentinel-2_L1C_Data_Quality_Report (accessed on January 2020).

ESA Sentinel Online. Technical Guides. Sentinel-2 MSI. Cloud Masks. Available online: https://sentinel.esa.int/web/SENTINEL/technical-guides/SENTINEL-2-msi/level-1c/cloud-masks (accessed on January 2020).

Francis, P.W, 1979. Infra-red techniques for volcano monitoring and prediction—A review. J. Geol. Soc. Lond., 136, 355–359. https://doi.org/10.1144/gsjgs.136.3.0355

Francis, P., Oppenheimer, C., Stevenson, D., 1993. Endogenous growth of persistently active volcanoes. Nature 366, 554–557. https://doi.org/10.1038/366554a0

Ganci, G., Bilotta, G., Cappello, A., Hérault, A., Del Negro, C., 2016. HOTSAT: A multiplatform system for the satellite thermal monitoring of volcanic activity. Geol. Soc. Lond. Spec. Publ., 426, 207–221. https://doi.org/10.1144/SP426.21

Gawarecki, S.J., Lyon, R.J.P., Nordberg, W., 1965. Infrared spectral returns and imagery of the Earth from space and their application to geological problems. Sci. Technol. Ser. Am. Astron. Soc., 4, 13–33.

Giglio, L., Csiszar, I., Restás, Á., Morisette, J.T., Schroeder, W., Morton, D., Justice, C.O., 2008. Active fire detection and characterization with the advanced spaceborne thermal emission

and reflection radiometer (ASTER). Remote Sens. Env., 112, 3055–3063. https://doi.org/10.1016/j.rse.2008.03.003

Global Volcanism Program, 2013a. Volcanoes of the World, v. 4.8.6. Venzke, E (ed.). Smithsonian Institution. Downloaded 02 Mar 2020. https://doi.org/10.5479/si.GVP.VOTW4-2013

Global Volcanism Program, 2013b. In Volcanoes of the World; Chaitén (358041), Vision 4.8.5; Venzke, E., Ed.; Smithsonian Institution: 2013; doi:10.5479/si.GVP.VOTW4-2013. Available online: https://volcano.si.edu/volcano.cfm?vn=358041 (accessed on December 2019).

Global Volcanism Program, 2013c. In Volcanoes of the World; Krakatau (262000), Vision 4.8.5.; Venzke, E., Ed.; Smithsonian Institution: 2013; doi:10.5479/si.GVP.VOTW4-2013. Available online: https://volcano.si.edu/volcano.cfm?vn=262000 (accessed on December 2019).

Global Volcanism Program, 2013d. In Volcanoes of the World; Erta Ale (221080), Vision 4.8.5.; Venzke, E., Ed.; Smithsonian Institution: 2013; doi: 10.5479/si.GVP.VOTW4-2013. Available online: https://volcano.si.edu/volcano.cfm?vn=221080 (accessed on December 2019).

Global Volcanism Program, 2013e. In Volcanoes of the World; Etna (211060), Vision 4.8.5.; Venzke, E., Ed.; Smithsonian Institution: 2013; doi:10.5479/si.GVP.VOTW4-2013. Available online: https://volcano.si.edu/volcano.cfm?vn=211060 (accessed on December 2019).

Global Volcanism Program, 2013f. In Volcanoes of the World; Stromboli (211040), Vision 4.8.5.; Venzke, E., Ed.; Smithsonian Institution: 2013; doi:10.5479/si.GVP.VOTW4-2013. Available online: https://volcano.si.edu/volcano.cfm?vn=211040 (accessed on December 2019).

Global Volcanism Program, 2013g. In Volcanoes of the World; Yasur (341090), Vision 4.8.5.; Venzke, E., Ed.; Smithsonian Institution: 2013; doi:10.5479/si.GVP.VOTW4-2013. Available online: https://volcano.si.edu/volcano.cfm?vn=341090 (accessed on December 2019).

Global Volcanism Program, 2013h. In Volcanoes of the World; Klyuchevskoy (300260), Vision 4.8.5.; Venzke, E., Ed.; Smithsonian Institution: 2013; doi:10.5479/si.GVP.VOTW4-2013. Available online: https://volcano.si.edu/volcano.cfm?vn=300260 (accessed on December 2019).

Global Volcanism Program, 2013i. In Volcanoes of the World; Masaya (344100), Vision 4.8.5.; Venzke, E., Ed.; Smithsonian Institution: 2013; doi:10.5479/si.GVP.VOTW4-2013. Available online: https://volcano.si.edu/volcano.cfm?vn=344100 (accessed on December 2019).

Global Volcanism Program, 2013j. In Volcanoes of the World; Villarrica (357120), Vision 4.8.5.; Venzke, E., Ed.; Smithsonian Institution: 2013; doi:10.5479/si.GVP.VOTW4-2013. Available online: https://volcano.si.edu/volcano.cfm?vn=357120 (accessed on December 2019).

Global Volcanism Program, 2013k. In Volcanoes of the World; Bezymianny (300250), Vision 4.8.5.; Venzke, E., Ed.; Smithsonian Institution: 2013; doi:10.5479/si.GVP.VOTW4-2013. Available online: https://volcano.si.edu/volcano.cfm?vn=300250 (accessed on December 2019).

Global Volcanism Program, 2013l. In Volcanoes of the World; Láscar (355100), Vision 4.8.5.; Venzke, E., Ed.; Smithsonian Institution: 2013; doi:10.5479/si.GVP.VOTW4-2013. Available online: https://volcano.si.edu/volcano.cfm?vn=355100 (accessed on December 2019).

Global Volcanism Program, 2013m. In Volcanoes of the World; Merapi (263250), Vision 4.8.5.; Venzke, E., Ed.; Smithsonian Institution: 2013; doi:10.5479/si.GVP.VOTW4-2013. Available online: https://volcano.si.edu/volcano.cfm?vn=263250 (accessed on December 2019).

Global Volcanism Program, 2013n. In Volcanoes of the World; Ol Doinyo Lengai (222120), Vision 4.8.5.; Venzke, E., Ed.; Smithsonian Institution: 2013; doi:10.5479/si.GVP.VOTW4-2013. Available online: https://volcano.si.edu/volcano.cfm?vn=222120 (accessed on December 2019).

Global Volcanism Program, 2013o. In Volcanoes of the World; Nyiragongo (223030), Vision 4.8.5.; Venzke, E., Ed.; Smithsonian Institution: 2013; doi:10.5479/si.GVP.VOTW4-2013. Available online: https://volcano.si.edu/volcano.cfm?vn=223030 (accessed on December 2019).

Global Volcanism Program, 2013p. In Volcanoes of the World; Popocatépetl (257100), Vision 4.8.5.; Venzke, E., Ed.; Smithsonian Institution: 2013; doi:10.5479/si.GVP.VOTW4-2013. Available online: https://volcano.si.edu/volcano.cfm?vn=257100 (accessed on December 2019).

Gouhier, M., Guéhenneux, Y., Labazuy, P., Cacault, P., Decriem, J., Rivet, S., 2016. HOTVOLC: A web-based monitoring system for volcanic hot spots. Geol. Soc. Lond. Spec. Publ., 426, 223–241. https://doi.org/10.1144/SP426.31

Gray, D.M., Burton-Johnson, A., Fretwell, P.T., 2019. Evidence for a lava lake on Mt. Michael volcano, Saunders Island (South Sandwich Islands) from Landsat, Sentinel-2 and ASTER satellite imagery. J. Volcanol. Geotherm. Res., 379, 60–71. https://doi.org/10.1016/j.jvolgeores.2019.05.002

Harris, A., 2013. Thermal Remote Sensing of Active Volcanoes: A User's Manual. Cambridge, MA: Cambridge university press. https://doi.org/10.1017/CBO9781139029346

Harris, A.J.L., Stevenson, D.S., 1997. Thermal observations of degassing open conduits and fumaroles at Stromboli and Vulcano using remotely sensed data. J. Volcanol. Geotherm. Res., 76, 175–198. https://doi.org/10.1016/S0377-0273(96)00097-2

Harris, A., Baloga, S., 2009. Lava discharge rates from satellite-measured heat flux. Geophys. Res. Lett. 36, L19302. https://doi.org/10.1029/2009GL039717

Harris, A.J.L., Villeneuve, N., Di Muro, A. et al., 2017. Effusive crises at Piton de la Fournaise 2014–2015: a review of a multi-national response model. J Appl. Volcanol. 6, 11. https://doi.org/10.1186/s13617-017-0062-9

Kervyn, M., Ernst, G.G.J., Harris, A.J.L., Belton, F., Mbede, E., Jacobs, P., 2008. Thermal remote sensing of the low-intensity carbonatite volcanism of Oldoinyo Lengai, Tanzania. Int. J. Remote Sens., 29, 6467–6499. https://doi.org/10.1080/01431160802167105

Laiolo, M., Ripepe, M., Cigolini, C., Coppola, D., Della Schiava, M., Genco, R., Innocenti, L., Lacanna, G., Marchetti, E., Massimetti, F., Silengo, M.C., 2019. Space- and Ground-Based Geophysical Data Tracking of Magma Migration in Shallow Feeding System of Mount Etna Volcano. Remote Sens., 11, 1182. https://doi.org/10.3390/rs11101182

Li, J., Roy, D.P., 2017. A Global Analysis of Sentinel-2A, Sentinel-2B and Landsat-8 Data Revisit Intervals and Implications for Terrestrial Monitoring. Remote Sens., 9, 902. https://doi.org/10.3390/rs9090902

Marchese, F., Neri, M., Falconieri, A., Lacava, T., Mazzeo, G., Pergola, N., Tramutoli, V., 2018. The Contribution of Multi-Sensor Infrared Satellite Observations to Monitor Mt. Etna (Italy) Activity during May to August 2016. Remote Sens., 10, 1948. https://doi.org/10.3390/rs10121948

Marchese, F., Genzano, N., Neri, M., Falconieri, A., Mazzeo, G., Pergola, N., 2019. A Multi-Channel Algorithm for Mapping Volcanic Thermal Anomalies by Means of Sentinel-2 MSI and Landsat-8 OLI Data. Remote Sens., 11, 2876. https://doi.org/10.3390/rs11232876

Massimetti, F., Coppola, D., Laiolo, M., Cigolini, C., Ripepe, M., 2018. First comparative results from SENTINEL-2 and MODIS-MIROVA volcanic thermal dataseries. In Proceedings of the CoV10 IAVCEI General Assembly, Naples, Italy, 2–7 September 2018.

Mia, M.B., Fujimitsu, Y., Nishijima, J., 2017. Thermal Activity Monitoring of an Active Volcano Using Landsat 8/OLI-TIRS Sensor Images: A Case Study at the Aso Volcanic Area in Southwest Japan. Geosciences, 7, 118. https://doi.org/10.3390/geosciences7040118

Mia, M.B., Fujimitsu, Y., Nishijima, J., 2018. Monitoring of Thermal Activity at the Hatchobaru–Otake Geothermal Area in Japan Using Multi-Source Satellite Images—With Comparisons of Methods, and Solar and Seasonal Effects. Remote Sens., 10, 1430. https://doi.org/10.3390/rs10091430

Moore, C., Wright, T., Hooper, A., Biggs, J., 2019. The 2017 eruption of Erta 'Ale Volcano, Ethiopia: Insights into the shallow axial plumbing system of an incipient mid-ocean ridge. Geochem. Geophys. Geosyst., 20, 5727–5743. https://doi.org/10.1029/2019GC008692

Murphy, S.W., de Souza Filho, C.R., Wright, R., Sabatino, G., Pabon, R.C., 2016. HOTMAP: Global hot target detection at moderate spatial resolution. Remote Sens. Env., 177, 78–88. https://doi.org/10.1016/j.rse.2016.02.027

Oppenheimer, C., 1998. Volcanological applications of meteorological satellites. Int. J. Remote Sens., 19, 2829–2864. https://doi.org/10.1080/014311698214307

Oppenheimer, C., Francis, P.W., Rothery, D.A., Carlton, R.W., Glaze, L.S., 1993. Infrared image analysis of volcanic thermal features: Láscar Volcano, Chile, 1984–1992. J. Geophys. Res. Solid Earth, 98, 4269–4286. https://doi.org/10.1029/92JB02134

Pallister, J.S., Schneider, D.J., Griswold, J.P., Keeler, R.H., Burton, W.C., Noyles, C., Newhall, C.G., Ratdomopurbo, A., 2013. Merapi 2010 eruption—Chronology and extrusion rates monitored with satellite radar and used in eruption forecasting. J. Volcanol. Geotherm. Res., 261, 144–152. https://doi.org/10.1016/j.jvolgeores.2012.07.012

Palma, J.L., Calder, E.S., Basualto, D., Blake, S., Rothery, D.A., 2008. Correlations between SO2 flux, seismicity, and outgassing activity at the open vent of Villarrica volcano, Chile. J. Geophys. Res., 113, B10201. https://doi.org/10.1029/2008JB005577

Pering, T.D., Ilanko, T., Wilkes, T.C., England, R.A., Silcock, S.R., Stanger, L.R., Willmott, J.R., Bryant, R.G., McGonigle, A.J.S., 2019. A Rapidly Convecting Lava Lake at Masaya Volcano, Nicaragua. Front. Earth Sci., 6, 241. https://doi.org/10.3389/feart.2018.00241

Plank, S., Walter, T.R., Martinis, S., Cesca, S., 2019a. Growth and collapse of a littoral lava dome during the 2018/19 eruption of Kadovar Volcano, Papua New Guinea, analyzed by multi-sensor satellite imagery. J. Volcanol. Geotherm. Res., 388, 106704. https://doi.org/10.1016/j.jvolgeores.2019.106704

Plank, S., Marchese, F., Filizzola, C., Pergola, N., Neri, M., Nolde, M., Martinis, S., 2019b. The July/August 2019 Lava Flows at the Sciara del Fuoco, Stromboli–Analysis from Multi-Sensor Infrared Satellite Imagery. Remote Sens., 11, 2879. https://doi.org/10.3390/rs11232879

Ramsey, M.S. Synergistic Use of Satellite Thermal Detection and Science: A Decadal Perspective Using ASTER. Geol. Soc. Spec. Publ. 2016, 426, 115–136. https://doi.org/10.1144/SP426.23

Ramsey, M. S., Harris, A. J. L., 2013. Volcanology 2020: how will thermal remote sensing of volcanic surface activity evolve over the next decade? (invited review article). J. Volcanol. Geotherm. Res., 249, 217–233. https://doi.org/10.1016/j.jvolgeores.2012.05.011

Reath, K., Pritchard, M., Moruzzi, S., Alcott, A., Coppola, D., Pieri, D., 2019. The AVTOD (ASTER Volcanic Thermal Output Database) Latin America archive. J. Volcanol. Geotherm. Res. 376, 62–76. https://doi.org/10.1016/j.jvolgeores.2019.03.019

Ripepe, M., Pistolesi, M., Coppola, D., Delle Donne, D., Genco, R., Lacanna, G., et al., 2017. Forecasting effusive dynamics and decompression rates by magmastatic model at open-vent volcanoes. Scientific Reports, 7(1), 3885. https://doi.org/10.1038/s41598-017-03833-3

Rose, W.I., Palma, J.L., Delgado Granados, H., Varley, N., 2013. Open-vent volcanism and related hazards: Overview. Geol. Soc. Lond. Spec. Publ., 498, 7–13. https://doi.org/10.1130/2013.2498(00)

Roteta, E., Bastarrika, A., Padilla, M., Storm, T., Chuvieco, E., 2019. Development of a Sentinel-2 burned area algorithm: Generation of a small fire database for sub-Saharan Africa. Remote Sens. Env., 222, 1–17. https://doi.org/10.1016/j.rse.2018.12.011

Rothery, D., Coppola, D., Saunders, C., 2005. Analysis of volcanic activity patterns using MODIS thermal alerts. Bull Volcanol 67, 539–556. https://doi.org/10.1007/s00445-004-0393-3

Schroeder, W., Oliva, P., Giglio, L., Quayle, B., Lorenz, E., Morelli, F., 2016. Active fire detection using landsat-8/OLI data. Remote Sens. Env., 185, 210–220. https://doi.org/10.1016/j.rse.2015.08.032

Steffke, A.M., Harris, A.J.L., 2011. A review of algorithms for detecting volcanic hot spots in satellite infrared data. Bull. Volcanol. 73, 1109–1137. https://doi.org/10.1007/s00445-011-0487-7

Sterckx, S., Knaeps, S., Kratzer, S., Ruddick, K., 2015. SIMilarity Environment Correction (SIMEC) applied to MERIS data over inland and coastal waters. Remote Sens. Env., 157, 96–110. https://doi.org/10.1016/j.rse.2014.06.017

Surono, M., Jousset, P., Pallister, J., Boichu, M., Buongiorno, M.F., Budisantoso, A., Costa, F., Andreastuti, S., Prata, F., Schneider, D., et al., 2012. The 2010 explosive eruption of Java's Merapi volcano—A '100-year' event. J. Volcanol. Geotherm. Res., 241, 121–135. https://doi.org/10.1016/j.jvolgeores.2012.06.018

Valade, S., Ley, A., Massimetti, F., D'Hondt, O., Laiolo, M., Coppola, D., Loibl, D., Hellwich, O., Walter, T.R., 2019. Towards Global Volcano Monitoring Using Multisensor Sentinel Missions and Artificial Intelligence: The MOUNTS Monitoring System. Remote Sens., 11, 1528. https://doi.org/10.3390/rs11131528

Vaughan, R.G.; Kervyn, M.; Realmuto, V.; Abrams, M.; Hook, S.J. Satellite measurements of recent volcanic activity at Oldoinyo Lengai, Tanzania. J. Volcanol. Geotherm. Res. 2008, 173, 196–206. https://doi.org/10.1016/j.jvolgeores.2008.01.028

Walter, T.R., Haghshenas Haghighi, M., Schneider, F.M. et al., 2019. Complex hazard cascade culminating in the Anak Krakatau sector collapse. Nat Commun 10, 4339. https://doi.org/10.1038/s41467-019-12284-5

Werner, C., Kern, C., Coppola, D., et al., 2017. Magmatic degassing, lava dome extrusion, and explosions from Mount Cleveland volcano, Alaska, 2011–2015: Insight into the continuous nature of volcanic activity over multi-year timescales. J. Volcanol. Geotherm. Res., 337, 98-110. https://doi.org/10.1016/j.jvolgeores.2017.03.001

Wooster, M.J., Zhukov, B., Oertel, D., 2003. Fire radiative energy for quantitative study of biomass burning: Derivation from the BIRD experimental satellite and comparison to MODIS fire products. Remote Sens. Env., 86, 83–107. https://doi.org/10.1016/S0034-4257(03)00070-1

Wright, R., Flynn, L., Garbeil, H., Harris, A.J.L., Pilger, E., 2002. Automated volcanic eruption detection using MODIS. Remote Sens. Env., 82, 135–155. https://doi.org/10.1016/S0034-4257(02)00030-5

Wright, R., Flynn, L.P., 2003. On the retrieval of lava-flow surface temperatures from infrared satellite data. Geology, 31, 893–896. https://doi.org/10.1130/G19645.1

Wright, R., Flynn, L.P., Garbeil, H., Harris, A.J.L., Pilger, E. MODVOLC: Near-real-time thermal monitoring of global volcanism., 2004. J. Volcanol. Geotherm. Res., 135, 29–49. https://doi.org/10.1016/j.jvolgeores.2003.12.008

Yokoyama, I. Heat and mass transfer through volcanoes. Riv. Ital. Geofis. 1972, 21, 165–169.

Chapter 3

3. Quantifying thermal emission from open vent multicraters system using a multisensory space-based approach: Stromboli and Etna case studies

Abstract

Volcanic space-based thermal remote sensing is broadening its limits with the availability of new sensors with different temporal and spatial resolutions. Open-vent activity is characterized by constantly active magmatic processes, which source a significant amount of heat from vents and feed mild explosive activity, lava flows, and thermal emissions. The conjunction of InfraRed satellite analysis with different features, leads to continuous, homogenous, and multispatial constraints of thermal activity, representing a significant improvement to better monitoring and understanding of dynamics of open-vent behaviors. In this work, we investigate eight years of thermal activity (2013-2021) of Stromboli and Etna volcanoes (Sicily, Italy), two iconic open vent volcanoes exhibiting permanent thermal signals, combining data acquired by MODIS (Moderate Resolution Imaging Spectroradiometer, with 1 km/pixel) and high-spatial-resolution sensors SENTINEL-2 MSI (Multi-Spectral Instrument) and LANDSAT-8 OLI (Operational Land Imager) with 20/30 m/pixel, in the Middle and Short Wave Infrared spectral regions, respectively. We focused our analysis during periods of ordinary thermal activity, excluding emissions related to lava flows, effusions, paroxysms, and major explosions. The multisensory approach allows to (i) map variations of thermal emissions position in summit areas, (ii) calculate thermal budgets of different vents, and (iii) estimate heat flux values produced by single craters, comparing the Volcanic Radiative Power (VRP, in Watt) and the Volcanic Radiative Energy (VRE, in Joule) measured by MIR-MODIS with the Thermal Index parameter recorded by SWIR analysis using S2 and L8 datasets. Thermal analysis is compared with the most important eruptive events that recently occurred at Stromboli and Etna: thermal observations are in accord with the occurrence of higher intensities events such as effusion, explosion, and paroxysms, indicating a closed link between explosivity and long-term thermal budgets in the shallow feeding systems. At Stromboli, a marked change in the overall thermal budget from craters since 2017 is in evident connection with the increase of explosivity suffered by the shallow magmatic system; at Etna, the new paroxysm phase started in late 2020, is interpreted as the culmination of a long-lasting thermal rising trend at South-East sector and after months of reduced emissions at Central Craters, with a markable agreement with the increase in the seismic release. Remarkably, using multiple space-based InfraRed datasets, we can perform a multiyear quantification of heat fluxes from every single crater on Stromboli and Etna, which represents a great improvement for monitoring purposes, with a possible dedicated space-based algorithm able to track in near real-time the heat flux produced by vents and the thermal budget on multicraters contexts.

1. INTRODUCTION

Open-vent volcanoes are systems with constantly active magmatic processes, resulting in eruptive patterns lasting for a long period (Vergniolle & Métrich, 2021). Even though a unique definition of open-vent systems is not straightforward, it is possible to state that open-vent behavior should exhibit a persistency of activity, magma-free surface exposure, continuous

degassing, background seismicity, and thermal emissions (Rose et al., 2013). In this view, open vent volcanoes are significant emitters of heat (Francis et al., 1993; Kazahaya et al., 1994; Harris & Stevenson, 1997a; Wright et al., 2015; Coppola et al., 2020), even more at low-viscosity systems (e.g., basalt to basaltic andesite), where magma efficiently arrives at the surface, feeding mild explosive activity and lava flows, and sourcing thermal emissions (Harris & Stevenson, 1997a; Rose et al., 2013). Open-vent behavior also shows peculiar aspects because these volcanoes often exhibit a bimodal pattern, with a milder and regular activity interrupted by violent and unexpected explosions (Houghton & Gonnermann, 2008; Rose et al., 2013; Vergniolle & Métrich, 2021). This behavior testifies for the importance of having continuous and in-depth monitoring of geophysical, geochemical, and thermal parameters acquiring solid long-term datasets of the baseline activity, thus having a reliable volcanological interpretation of any sign of deviation from the normal behavior (Sparks, 2003; Philipson et al. 2013; Reath et al., 2019). This implies, in other terms, improving capabilities to forecast eruptive unrest in these volcanic contexts (Chaussard et al., 2013; Phillipson et al., 2013; Valade et al., 2016; Coppola et al., 2019).

One of the parameters in understanding volcanoes is thermal data (Sparks et al., 2012; Harris, 2013; Pallister & McNutt, 2015; Bonny & Wright, 2017; Reath et al., 2019; Coppola et al., 2020). Thermal anomalies are features that provide information about the state of volcanoes (Yokoyama, 1972; Francis, 1979; Wright & Pilger, 2008; Harris, 2013; Coppola et al., 2020). Thermal investigations benefit from space-based data, allowing a homogeneous dataset to be acquired over time. Even in well-monitored volcanoes, satellite thermal observations provide invaluable information on the evolution of the eruption, reducing human risks and costs associated with direct observations, and offering a frequent and long-term dataset than other remote-sensed techniques, for example, UAVs and airborne methods (Laiolo et al., 2019; Valade et al., 2019; Coppola et al., 2020; Poland et al., 2020). The availability of higher spatial resolution images with pixel resolution <90 m (Harris, 2013; Blackett et al., 2017; Ramsey et al., 2022) sign a further improvement in space-based thermal monitoring, making it possible to localize the position of eruptive vents and to characterize the contribution of different sectors inferring magnitude and spatial information of thermal emissions (Mia et al., 2018; Cigolini et al., 2018; Marchese et al., 2018; Laiolo et al., 2019; Plank et al., 2019; Massimetti et al., 2020). In this view, studying thermal features at crater scale could be highly relevant to volcanological research and monitoring purposes, giving insights into various parameters such as magma depth, thermal flux, and mapping vents distribution (Harris & Stevenson, 1997b). Indeed, open vent volcanoes are prone to modifications in vent location, number, and position because of the

interplay between various eruptive dynamics and intensities (Rose et al., 2013; Salvatore et al., 2018; Simons et al., 2020); in some contexts, this leads to the presence of multiple active craters setting – i.e., Stromboli and Etna (Italy), Yasur (Vanuatu), Erta Ale (Ethiopia). The multi-crater feature means more complexity rather than a single emitting vent, such as some low-viscosity open vents volcanoes such as Kilauea (Hawaii, USA), Villarrica (Chile), or Masaya (Nicaragua) (Rose et al., 2013). Multiple vents in proximity pose challenges to discriminating emissions and characterizing activity (Pering et al., 2020) because different vents could show diverse eruptive styles, as testified by Stromboli (see Ripepe et al., 2008) and Etna (see Andronico et al., 2021). Notably, the sudden occurrence of highly explosive phenomena such as lava fountains (Etna; Corsaro et al., 2015; Calvari et al., 2018; Andronico et al., 2021), abrupt paroxysmal explosions (Stromboli; Barberi et al., 1993; Rosi et al., 2013; Pioli et al., 2014; Bevilacqua et al., 2020; Ripepe et al., 2021) sourced from summit craters, and flank effusions (Acocella & Neri, 2003; Neri et al., 2011; Barberi et al., 2009; Ripepe et al., 2017) pose significant risks (Rosi et al., 2013; Andronico et al., 2015; Bonaccorso et al., 2016; Giordano & De Astis, 2021). In this view, parametrizing patterns of activity at the vent scale can give relevant information, among others, on shallow conduit dynamics (Giberti et al., 1992) such as on source mechanisms of explosive activity (Ripepe & Marchetti, 2002; Chouet et al., 2003; McGreger & Lees, 2004; Salvatore et al., 2018), on degassing processes (Tamburello et al., 2012), on eruptive dynamics (Ripepe et al., 2008; Cannata et al., 2011) and hazard mitigation (Johnson et al., 2018; Ripepe et al., 2018).

Here, we investigate the thermal features of the Stromboli and Etna volcanoes (Sicily, southern Italy), two of the most iconic volcanoes worldwide, exhibiting continuous thermal emissions (Giberti et al., 1992; Andronico & Lodato, 2005; Ripepe et al., 2005; Allard et al., 2006; Harris et al., 2011; Rosi et al., 2013; Coppola et al., 2016). These volcanoes have been the subject of extensive work characterizing their thermal activity through thermal satellite methods (see Gaonac'h et al., 1994; Harris & Stevenson, 1997b; 2011; Coppola et al., 2012; Wright et al., 2015; Laiolo et al., 2019; Plank et al., 2019; Calvari et al., 2021 and references therein). Nevertheless, multiyear analysis of thermal activity is only demonstrated in a few papers (cf. Coppola et al., 2016; Ganci et al., 2016; Marchese et al., 2019; Massimetti et al., 2020). Moreover, a long-lasting quantification of thermal emission produced by single craters at these open-vent volcanoes has never been performed so far. Recently, a few attempts have been made to qualitatively distinguish activity at crater scale using diverse satellites for single eruption (i.e., Marchese et al., 2018, Laiolo et al., 2019) or short periods (i.e., Marchese et al., 2021),

while older investigations integrated ground and space-based techniques to map and quantify heat emissions at crater extent (Harris & Stevenson, 1997a).

We analyzed almost eight years of activity of Stromboli and Etna volcanoes, from April 2013 to July 2021, focusing our analysis during the period of ordinary thermal activity, excluding emissions related to lava flows, effusions, paroxysms, and major explosions. We used a satellite-based multisensory approach exploiting the potential of various spatial resolutions: a combination of MODIS (Moderate Resolution Imaging Spectroradiometer), MSI SENTINEL-2 (MultiSpectral Instrument), and OLI LANDSAT-8 (Operational Land Imager) images have been analyzed in the InfraRed (IR) wavelengths to *i*) map variations of the position of thermal emissions in summit areas; *ii*) calculate thermal budgets of different sectors; *iii)* estimate heat flux values produced by single craters. We firstly explore the Volcanic Radiative Power (in Watt) and Thermal Index parameters during ordinary activity and the distinguished thermal behavior of single craters of Stromboli and Etna. Then we compared the Volcanic Radiative Energy (in Joule) measured by MODIS with the Thermal Index parameter recorded by MSI SENTINEL-2 and OLI LANDSAT-8 images; through this relationship, we can retrieve the heat flux produced by single vents. Using the pixel spatial resolution of 20/30 meters offered by the MSI and OLI sensors, it is possible to constrain thermal signature at a crater scale, otherwise impossible with MODIS. This approach allows us to analyze how thermal signature varied in the recent years on Stromboli and Etna, tracking changes in summit areas, and quantitively measure how craters have released thermal energy. Moreover, we compared the thermal dataset with the most important eruptive events in the last eight years, interpreting thermal patterns related to changes in volcanic activity.

Integrating satellite thermal data from various sensors allows precise, safe, and repeatable measurements and monitoring of open-vent systems characterized by thermal emission. Detecting thermal changes is crucial in contexts characterized by many vents persistently active, such as Stromboli and Etna. This information, combined with the stream of geophysical and geochemical data available from the ground-based network, could be used as a valuable supplement even at-well monitored volcanoes, offering, on the one hand, a thermal baseline of reference and, on the other, indicating signs of thermal variation, precious for monitoring applications and risk reduction.

2. VOLCANIC CONTEXTS

2.1 Stromboli

Stromboli volcano (Sicily, Italy, 924m a.s.l., Figure 1) is globally known for its regular, millennial long-lasting, and mild explosive "Strombolian" activity, also termed "ordinary" (Mercalli 1907; Rosi et al., 2000). This activity is characterized by moderate explosions ejecting bombs, black scoria, lapilli, and ash, occurring every 10–20 min from summit craters and accompanied by degassing (Barberi et al., 1993; Ripepe et al., 2008). The feeding mechanism is thought to be a steady-state convective regime within the magmatic conduit, where a gas-rich magma ascends, degases, crystalizes, and overturns downwards (Allard et al., 2008; Aiuppa et al., 2010), with most of the magma remaining unerupted and only a small portion responsible of summit mild explosions. Although this mechanism is defined as steady, with an averaged magma supply rate of 0.1–0.5 m3/s (Burton et al., 2007), activity is highly variable even over a daily scale, with gas flux fluctuations promoting changes in magma level in the conduit, inducing variability in explosive frequency and thermal emission (Ripepe et al., 2008; Aiuppa et al., 2010). A sharp deviation from the "ordinary" activity is marked by more violent events, such as major to paroxysmal explosions and episodic effusive eruptions, which pose hazards for local villagers, tourists, and scientists (Barberi et al., 1993; Rosi et al., 2013; Ripepe et al., 2008; 2021). One of the last "non-ordinary" periods occurred in July-August 2019, when two paroxysms hit the island, causing one fatality, producing small tsunamis, and marking the begging and end of a two-month-long effusion sourced from summit craters (Aiuppa et a., 2021; Giordano and De Astis, 2021; Ripepe et al., 2021; Laiolo et al., 2022).

Strombolian activity occurs from a variable number of vents concentrated within a crater terrace at 780 m a.s.l. located in the upper part of the Sciara del Fuoco scar (a collapsed sector delimited by a horseshoe-scarp, Rosi et al., 2013; Fig. 1b). Vents are clustered in three main sectors named by convention NorthEast (NE), Central (C) and SouthWest (SW) craters (Fig. 1c) aligned along a NE-SW elongated trend explained by the location of a feeder dike (Ripepe et al., 2008; Tibaldi et al., 2008; Rosi et al., 2013). Indeed, geophysical investigations show that explosive activity at craters is linked to a common shallow source (Harris et al., 1996; Ripepe et al., 2005); however, the vent's location, size, and geometry may change over time, also due to strong effects of major explosive and paroxysm events, up to the possibility of a collapse of the whole crater terrace (Calvari et al., 2014; Schmid et al., 2021). The three Stromboli's sectors generally have different behaviors; "puffing" activity (short gas bursts associated with small infrasonic pulses), is typically present at one vent at once and mainly at the Central crater, representing

the expression of magmatic continuous degassing; short and frequent explosions are associated with NE crater, while longer bursts, typically ash-rich, are produced from SW sector (Ripepe et al., 2008). Also, the amplitude of thermal radiation shows systematic variabilities, indicating a common link of craters to the shallow variations of magma level (Ripepe et al., 2008; Coppola et al., 2012). At Stromboli, the origin of thermal radiation is composed by a different contribution between explosions, degassing, material ejected (incandescent scoriae and bombs), all sourced by magma inside the active vents (Harris & Stevenson, 1997a; Ripepe et al., 2008; Marchetti et al., 2009). Still, the latter source is the most relevant in the thermal budget from the crater terrace, related to the fluctuation of the magma level inside the conduit, as shown by Coppola et al., 2012; the same authors identified a thermal heat flux threshold of ~ 50 MW (by MODIS MIR analysis) as the transition from Strombolian to effusive regimes, thus indicating that "ordinary" mild-explosive activity, excluding lava flows and major explosive events, should be comprised in values below ~ 50 MW.

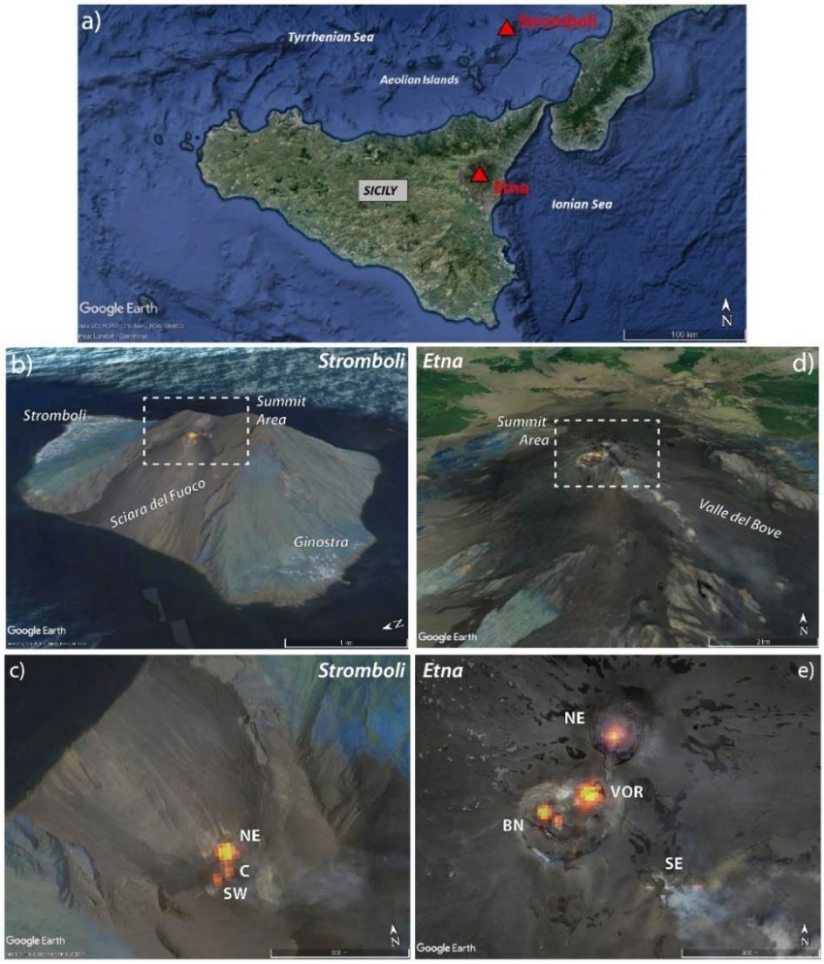

Figure 1 *– Geographical setting of volcanoes analyzed. a) Localization of Stromboli and Etna volcanoes on Google Earth (GE); b) Stromboli island, by S2 – MSI Swir image of 12/07/2017 projected on GE; c) focus on the summit area and localization of craters at Stromboli; d) Etna summit edifice, by S2 – MSI Swir image of 25/09/2019 projected on GE; e) focus on the summit area and localization of craters at Etna.*

2.2 Etna

Mt. Etna (Sicily, Italy, Fig. 1a) is one of the most persistent active volcanoes in the world, erupting nearly every year (Allard et al., 2006; Corsaro et al., 2017; Andronico et al., 2021), and one of the most intensely monitored of the planet (Bonaccorso et al., 2004; Patanè et al., 2013; Ripepe et al., 2018). Etna is a basaltic stratovolcano whose activity ranges from lava flows to Plinian eruptions (Guest, 1982; Coltelli et al., 2000). It shows mild to sustained Strombolian activity, gas emissions, periodic fountaining, and paroxysmal events, sometimes associated with lava flows, sourced from summit craters. Instead, when magma reaches the surface through radial fissures opened along volcano slopes, flank eruptions feed lava flows, with occurrence of years (Branca & De Carlo, 2005; Corsaro et al., 2017). Those effusive eruptions represent the primary hazard source in the event of distal eruptive fissures, with lava flows reaching inhabited areas and infrastructures (Del Negro et al., 2013; Bonaccorso et al., 2016). Etna has changed its shape in the last century with a growing number of its summit craters: to date, Voragine (VOR, oldest), North East (NE), Boccanuova (BN, then joined to VOR, also referred to as "Central craters" CC) and South East (SE) are the main four sectors, ranging between ~3000 at the base up to 3357, the new highest value of the SE crater reached during 2021 (Del Negro et al., 2013; Acocella et al., 2016; Neri et al., 2017; INGV-OE, 2021a; Fig. 1d-e). In this description, the New South East crater (NSE), formed at the base of SE in late 2007, has grown progressively until today leading to a disappearance of morphological differences with the SE cone; for this reason, the New South East crater is included as terminology in the apparatus of the South East sector (INGV-OE, 2020a; Andronico et al., 2021). The continuous open vent activity of Etna and its high variability, fed by degassed magma stored at a superficial level and rising through the central conduits (Corsaro et al., 2017), progressively change the morphology of the summit area and craters, shifting the source of activity (Acocella et al., 2016). Several paroxysmal events recently occurred at Etna's summit craters (Andronico et al., 2021; Marchese et al., 2021). Starting from January 2011 until December 2015, paroxysmal activity became more intense, with >50 episodes characterized by lava fountains (LF) mainly from NSEC and VOR, preceded by an increase of Strombolian activity and accompanied only by short-lived lava flows (Benchke et al., 2014; Ganci et al., 2018; Calvari et al., 2018; Andronico et al., 2021). The last decade was marked by a few effusive eruptions not accompanied by lava fountain activity (see Andronico et al., 2021); the most relevant occurred in December 2018 with the opening of an eruptive fissure at the base of the SEC and accompanied by a seismic crisis (Laiolo et al., 2019; Calvari et al., 2020).

After a long-steady mild Strombolian activity, intra-crater lava overflows sourced by SE and VOR, respectively, and about 18 months of eruptive pause (Marchese et al., 2021), Etna exhibited in December 2020 episodes of strong Strombolian activity alternating with short-lived lava fountains. Then, in February 2021, a violent eruptive sequence started, characterized by spectacular lava fountains from the SE sector, with heights of a few km and eruptive columns up to 11 km above sea level (Andronico et al., 2021; Calvari et al., 2021; Marchese et al., 2021). This paroxysmal lava fountain sequence has been active for all of 2021, at the beginning (February – April) at intervals of ca. 2–2.5 days (Marchese et al., 2021), then decreasing to a broader time rate (Andronico et al., 2021). The last event at the time of writing, counted as the 52° paroxysm since February 2021, occurred the 23 October 2021 with the production of a 2km long lava flow and small pyroclastic flows on the eastern SE flank (INGV-OE, 2021b). These events, possibly producing an ash fallout up to ~40 kg/m^2, have a substantial impact on aviation, road viability, roof stability, agriculture, and waters (Calvari et al., 2021 and references therein). This sharp reactivation of paroxysms activity arises after an overall inflation pattern of the volcanic edifice and a general increase in seismicity since summer 2020 (INGV-OE, 2020b), indicating a resumption of pressurization in the magmatic system (De Gori et al., 2021). Lava fountains erupted from the SE crater in this last phase, which seemed to be fed by a new primitive magma rich in gas, (INGV, 2021c).

The South East crater is the main character in the last year of Etna activity and the primary source of Strombolian to lava fountain activity (Behncke et al., 2006). Persistence and magnitude of eruptions migrated progressively in the last decade toward the SE direction due to a preferential structural pattern NE-SW oriented related to the overall north-east flank instability of the volcano (Acocella et al., 2016; Urlaub et al., 2018). Moreover, more than 90% of paroxysmal events, lava fountains, and high Strombolian activity periods started in 2011 have been sourced by the SE sector (from SE and NSE craters, considering the previous discrimination; see Andronico et al., 2021).

Focusing on thermal space-based methods, relevant works studied, for example, the volumetric output between magma volume supplied to the system and volume erupted during effusive eruptions and cycles (Harris et al., 2011; Coppola et al., 2019), or mapped the lava flows products and calculated lava volumes from effusion and fountains (Acocella et al., 2016; Calvari et al., 2018; Ganci et al., 2018). A first study proposed by Marchese et al., 2021 and using a different combination of high-resolution thermal satellites calculated thermal emissions related to LF episodes in 2021 and mapped thermal anomalies at crater scale on the summit

area of Etna. Notably, although Etna's activity shows complex multicraters dynamics with impulsive activity shifting to paroxysmal behavior as described above, no studies have been performed to quantify thermal emissions through time at scale of single scale and build a thermal baseline useful to interpret signs of lava fountains occurrence.

3. METHODOLOGY AND DATASET

3.1 Satellite Sensors and Metrics

We used a combination of InfraRed satellite sensors and volcano-devoted thermal algorithms to extract qualitative and quantitative information from images composed of MODIS, MSI SENTINEL-2, and OLI LANDSAT-8 (Figure 2). We briefly explain the main features of sensors, the processing techniques, and the thermal metrics. Moreover, to compare the results with the main volcanic events that recently occurred at Stromboli and Etna, we used data from the permanent monitoring network operated by the Laboratory of Experimental Geophysics (LGS) of the University of Florence (http://lgs.geo.unifi.it/) at Stromboli (Ripepe et al., 2009; Valade et al., 2016) and the Early-Warning operating system at Etna (Ripepe et al., 2018). In addition, we used the catalog of the major effusive eruptions mainly producing lava deposits at Etna furnished by Andronico et al., 2021.

3.1.1 MODIS-MIROVA VRP

MODIS sensor was launched in 1999 and then in 2002 on NASA's satellites Terra and Aqua and has a moderate spatial resolution of 1 km in the Middle InfraRed (MIR: 3.0 - 5.0 μm). It offers the main advantage of having a high revisit frequency, up to 4 times per day at low latitudes, which makes it appropriate for volcanic monitoring (Wright et al., 2002; Ramsey & Harris, 2013; Coppola et al., 2016). MODIS dataset has been analyzed through the hot spot detection algorithm of MIROVA, based on MIR radiance analysis (3.9 μm), quantifying the Volcanic Radiative Power (heat flux, in Watt) produced at magmatic temperatures (thermal radiation from surfaces with T > 500 K; Fig. 2a). MIROVA has become a global volcanic thermal monitoring system based on the near-real-time processing of MODIS imagery, delivering crucial information worldwide about the thermal state of volcanoes (http://www.mirovaweb.it/; Coppola et al., 2020). MIROVA data are integrated into the monitoring network of LGS to provide to Department of Civil Protection (DPC) daily/weekly reports on Stromboli and Etna activities; heat fluxes, effusion rates, and erupted volume data by MIROVA are helpful information given to Volcano Risk section of DPC during eruptive crisis.

We used two parameters from MODIS images: the VRP (Volcanic Radiative Power, in Watt) and the Volcanic Radiative Energy (VRE, in Joule), obtained by integrating the VRP values over time. VRP is calculated by using the MIR method (Wooster et al., 2003), for the MODIS hot-spot contaminated pixels detected, as follows:

$$VRP = \Delta L_{MIR} \cdot 1.97 \times 10^7 \cdot A_{PIX} \qquad (1)$$

where A_{PIXEL} is the pixel size of 1 km^2 for the MODIS MIR image, the constant 1.97 x 10^7 represents the Wooster's empirical coefficient to fit the linear relationship existing between MIR radiance and radiative power among 600 and 1600 K temperatures, and ΔL_{MIR} is the excess of MIR radiance of the alerted pixel/s and background. The VRP parameter expresses the heat flux in Watt (W) as the measurement of the area of the hot volcanic source having an effective radiating temperature higher than 600 K (see Coppola et al., 2016 for details).

VRE is calculated starting from VRP, by applying a trapezoidal rule of integration over time, as follows

$$VRE\ (t)\ = \int_{t0}^{t} VRP\ dt \approx \frac{1}{2} \sum_{n=2}^{N} (\ t_n - t_{n-1})(VRP_n + VRP_{n-1}) \qquad (2)$$

where t_0 and t are the beginning and end of the VRP MODIS dataset (April 2013 – July 2021), or possibly of any other discrete period of integration, N is the number of VRP data points, n is the nth measurement of VRP, t_n - t_{n-1} is the time spacing between each consecutive pair of VRP points. The summing operation starts from n=2 because VRE is calculated since the second VRP point; otherwise, for n=1, VRE would be equal to 0. The VRE function in time is a fundamental parameter since it allows to study thermal energy emitted during activity. It has been used to analyze effusive eruptions because it is directly correlated to the volume of erupted lava (see Coppola et al., 2013).

3.1.2 SENTINEL 2, LANDSAT 8, and THERMAL INDEX

SENTINEL-2 MultiSpectral Instrument (S2) and LANDSAT-8 Operational Land Imager (L8) represent recent space-based tools launched in June 2015/ March 2017 (SENTINEL-2A & -2B) by the European Space Agency (ESA), and in February 2013 by National Aeronautics and Space Administration (NASA), respectively. They have a spatial resolution of 20-30 meters/pixel in Short Wave InfraRed (SWIR: 1.1 - 3.0 μm) wavelengths, but a revisit time that spans between a few days for SENTINEL-2 (2-3 to 5 days) to weeks for LANDSAT-8 (8 to 16 days) depending on latitude and overlap between different swaths. We analyzed the SWIR TOA

(Top of Atmosphere) reflectances in the ρ12 (2.19 μm), ρ11 (1.61 μm), and ρ8A (0.86 μm) bands for the S2 MSI and the ρ7 (2.11–2.29 μm), ρ6 (1.57–1.65 μm), and ρ5 (0.85–0.88 μm) bands for the L8 OLI applying a recently proposed automated hybrid hotspot detection algorithm, based on fixed ratios and contextual statistical analysis (see Chapter 2 for details; Fig. 2b-c). The algorithm detects the number of "hot" pixels and allows to study of the Hot Area (in m^2) exposed as recorded by each SWIR S2 and L8 image. Considering only the hot spotted pixels recognized by the algorithm is possible to derive the Thermal Index parameter, calculated as follows:

$$TI = \rho\ 2.2\ \mu m\ +\ \rho\ 1.6\ \mu m\ +\ \rho\ 0.8\ \mu m \qquad (3)$$

where ρ are the TOA SWIR reflectances in the three bands analyzed, both for S2 (ρ12+ ρ11+ ρ8A) and L8 (ρ5 + ρ6+ ρ7). Thermal Index is an empirical and adimensional parameter considered a proxy for the pixel integrated temperature (Massimetti et al., 2020) and has been successfully used to study volcanogenic thermal emission in SWIR bands (Laiolo et al., 2019; Shevchenko et al., 2021). As we did for the VRP and VRE, we calculated the cumulative Thermal Index to evaluate the thermal budget over time of the different craters studied by applying a trapezoidal rule of integration over time as follows:

$$cumTI\ (t) = \int_{t0}^{t} TI\ dt \approx \frac{1}{2}\sum_{n=2}^{N}(\ t_n - t_{n-1})(TI_n + TI_{n-1}) \qquad (4)$$

where t_0 and t are the beginning and end of the Thermal Index S2/L8 dataset (April 2013 – July 2021), or possibly of any other discrete period of integration, N is the number of TI data points, n is the nth measurement of TI, t_n - t_{n-1} is the time spacing between each consecutive pair of TI points. The cumulative Thermal Index parameter represents a valuable element of comparison to study the thermal balance between the active vents, able to highlight significant thermal variations.

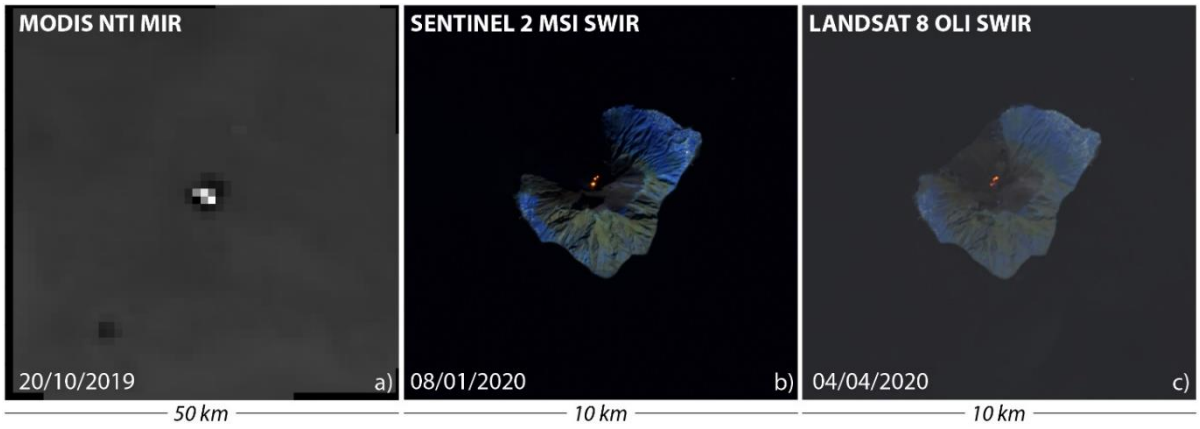

Figure 2 *– Image examples on Stromboli of dataset utilized in this work. a) MODIS NTI Middle InfraRed image; b) SENTINEL-2 MSI Short Wave InfraRed image; c) LANDSAT-8 OLI Short Wave InfraRed image.*

3.1.3 SENTINEL 2 and LANDSAT 8 Thermal Profiles

We used S2 and L8 high-resolution thermal datasets to build thermogram profiles in time over summit areas of the Stromboli and Etna volcanoes. We take every Thermal Index map of our dataset during the 2013 – 2021 period with at least one hot pixel, and sum them for each column or row, depending on the point of observation if north-south or west-east oriented, obtaining one single vector. Each Thermal Index acquisition thus consists of a single column, then juxtaposed and interpolated with the time to get a thermal profile representing the thermal spatial variation in the analysis period. We focused the spatial analysis on a box on the top of volcanoes of 1 km for Stromboli and 1.6 km for Etna, leaving out farther locations of thermal anomalies, and indicating the leading positions of craters. This approach was already proposed to study thermal anomalies evolution on open vents (Laiolo et al., 2019) and lava dome volcanic activity (Shevchenko et al., 2021; Coppola et al., 2022), permitting to distinguish the different craters in terms of persistence and to observe the thermal contribute of each defined sector.

3.2 Data filtering and Errors

To study the thermal budget of Stromboli and Etna, we chose to compare only thermal satellite data related to "ordinary" activity produced by summit craters, thus excluding all acquisitions related to highly explosive and effusive events. Using the reports from the LGS of the University of Florence, we filtered out MODIS, S2, and L8 datasets for Stromboli acquisitions related to lava overflows, flank effusions, major explosions, and paroxysms. For Etna, we exclude paroxysms, lava fountains events, summit lava flows, and flank effusions.

The multiple satellite thermal dataset has been filtered. The VRP-MODIS dataset has been cleaned as follows, (*i*) keeping out images with unfavorable viewing geometry (Zenith > 40°),

avoiding deformation effects of the projected thermal anomalies, (*ii*) selecting only nighttime images, and (*iii*) alerts with a maximum distance of 2 km from volcano summit (for fires or anthropogenic heat sources; see Coppola et al., 2020). The S2-L8 imagery has been visually inspected for a total of 1816 products to assess the quality of images and discard thermal halo, diffractions spikes, or blurring effects (see Massimetti et al., 2020). Notably, the three SWIR sensors used have different functionality times; L8 was launched in February 2013, S2A, and S2B in June 2015 and March 2017. This means that the sampling rate of SWIR acquisition grows in our analysis period as the number of images for time unit, possibly inducing bias, apparent thermal changes not related to actual changes in the source thermal signal, or undersampling until the complete coverage by the three satellites. Anyway, the trapezoidal cumulative method applied in *(2)* and *(4)* leading to VRP and cumTI parameters, integrates the different revisit frequencies of satellite overpasses and the time intervals between acquisitions, canceling the effects of asynchrony of the three SWIR satellite sensors used. All the algorithms used here are subject to limitations. VRP estimation suffers from a standard error of ±30% associated with the MIR method applied by the MIROVA algorithm (Coppola et al., 2016). The hotspot detection algorithm used for S2 and L8 shows an overall estimate of up to 4% in detecting false alerts (cf. Massimetti et al., 2020). In dealing with satellite-based thermal remote sensing, various factors may contribute to increasing uncertainty or lead to false thermal signals: the presence of meteorological and volcanic clouds, satellite viewing geometry, fires, or anthropogenic heat sources, may add a higher uncertainty to the single-point validity. We partially overcome these issues through filtering and visual inspection of our dataset (see above) and making our analysis to a long-time period of more than eight years, assessing the quality of the data comparison over the long term rather than on a single point.

3.3 Region of Interest Analysis

To study the thermal anomalies with a crater scale of details, we take advantage of the spatial resolution of the S2 and L8 imagery. The 20-30 meters/pixel resolution allows discriminating the different crater sectors and the extension of their thermal signal (Figure 3). We looked at the Cumulative Maps of the Thermal Index parameter during the 2013-2021 timespan of analysis, where the more persistent and thermally active sources are highlighted, excluding both feeble and very energetic but not time-continuous thermal sources. We confine the different sectors in regions of interest (ROI), creating masks including the hot pixels, throughout a comparison between morphological constraints, visible by DEMs products of summit areas, and visual inspection of thermal SWIR RGB images (Fig. 3). Indeed, at Stromboli, we apply a

box of 4x4 or 5x3, with same dimensions, for the three main vent sectors of North-East, Central, and South-West (Fig. 3b). At Etna, this is not applicable, because of the variety of volcanic thermal intensities produced by the craters (Fig. 3e). Here, we qualitatively mark the limits of the North-East, Bocca Nuova and Voragine, and South-East sectors, including the hotter portion represented by the pixels with white and brighter colorations (cf. Massimetti et al., 2020, α pixels considered with high reflectances values).

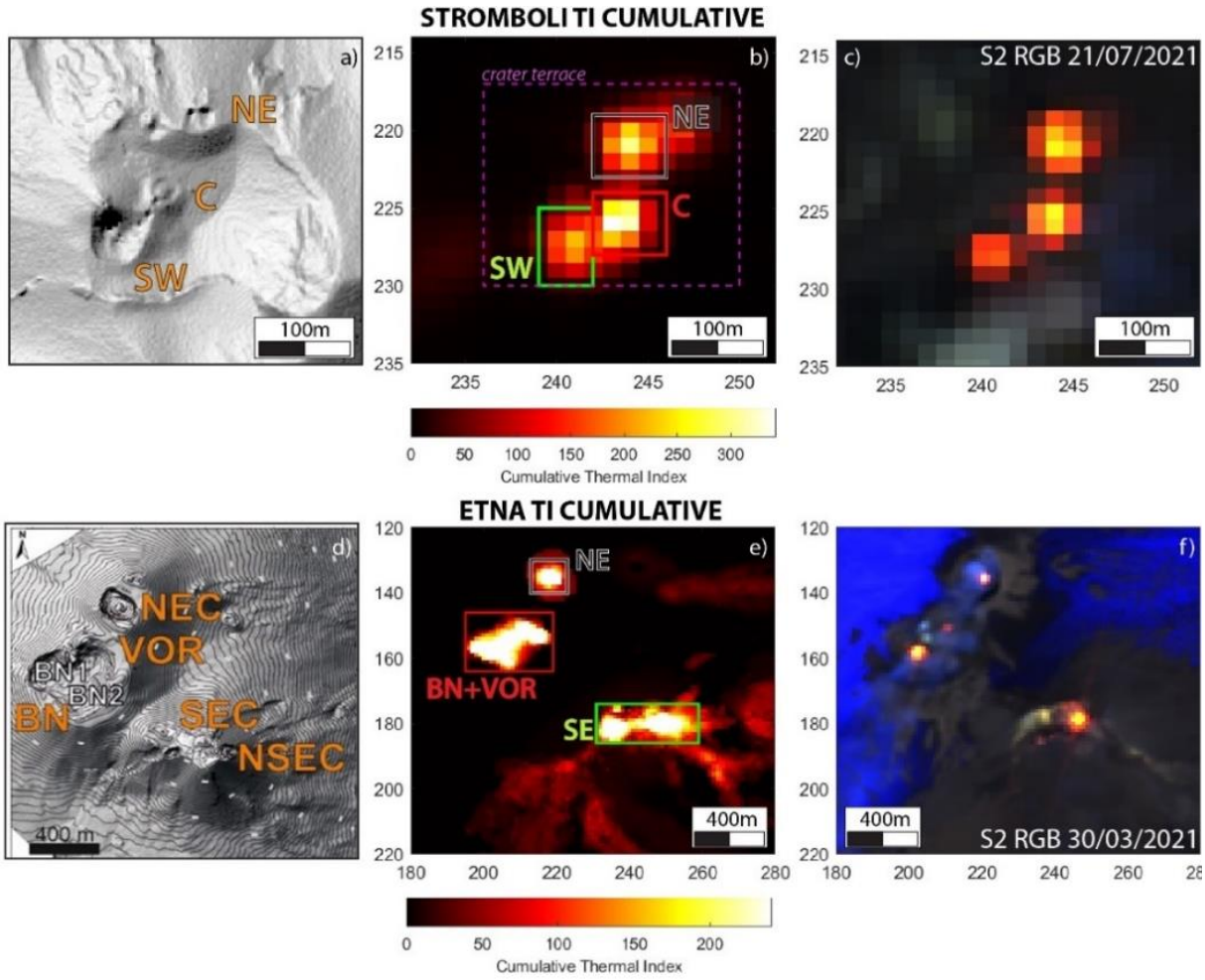

Figure 3 – *a) DEM of Stromboli terrace; b) Cumulative Thermal Index Map over Stromboli's terrace, depicting the three primary thermal sources related to the three main sectors; c) S2 RGB example image on Stromboli; d) DEM of Etna summit area, from Neri et al., 2017; e) Cumulative Thermal Index Map over Etna summit area, depicting the four main thermal sources related to the four main sectors; f) S2 RGB example image on Etna*

4. RESULTS

Here we present the results derived by the thermal analysis of the MODIS, S2, and L8 dataset on Stromboli and Etna, in the period April 2013 – July 2021, in terms of i) VRP and Thermal Index and ii) the Cumulative Thermal Index subdivided for the different craters and iii) the Thermal Profiles.

4.1 Stromboli

4.1.1 VRP and Thermal Index Time Series

The VRP and Thermal Index time series of Stromboli are shown in Figure 4, with a linear scale. Notably, the values of the plots are referred only to the thermal emission from the crater terrace on Stromboli, excluding any other thermal source. To clarify the nature of the investigated dataset, in Fig. 4a, we plotted in blue the VRP sourced by crater terrace and in pale gray the VRP related to the overall thermal activity, including effusions, that occurred in 2014 and 2019, for example. As already stated in the 3.2 Section, the Thermal Index time series (Fig. 4b) should be interpreted considering that the SWIR satellites had different functionality times; this means that thermal signals should be partially undersampled until the complete time coverage by the three space-based sensors. Stromboli VRP and Thermal Index show two similar behaviors; in the first part of the timespan of analysis, between April 2013 till the middle of 2017, TI is at very low values, never reaching values > 50, and this is reflected by VRP never reaching values above 20 MW (excluding single peak before August 2014 effusive peak). Thermal emissions from the crater terrace at Stromboli are thus very weak and non-constant. Since May 2017, VRP and TI parameters show an increase in magnitude and density: thermal emissions have become more consistent with several acquisitions with TI > 50 and VRP above 20 MW. Even in period of minor thermal emission, such as in 2018, TI shows a low but continuous signal.

Periods with higher thermal output occurred in December 2017, between November 2018 and January 2019, during the summer 2019 crisis, and the following months, in August 2020. In these periods, thermal emission often reaches values with TI > 100 and VRP up to 40 MW. Overall, the change in thermal activity on the crater terrace from mid-2017 is evident from both MIR and SWIR sensors, reaching the highest values during the post-effusive 2019 period and indicating a sharp change in thermal emission and related activity of Stromboli. In addition, the similar trends depicted by the MODIS and S2-L8 indicate that different functionality time of SWIR images does not affect the detection of the unadulterated thermal output of Stromboli.

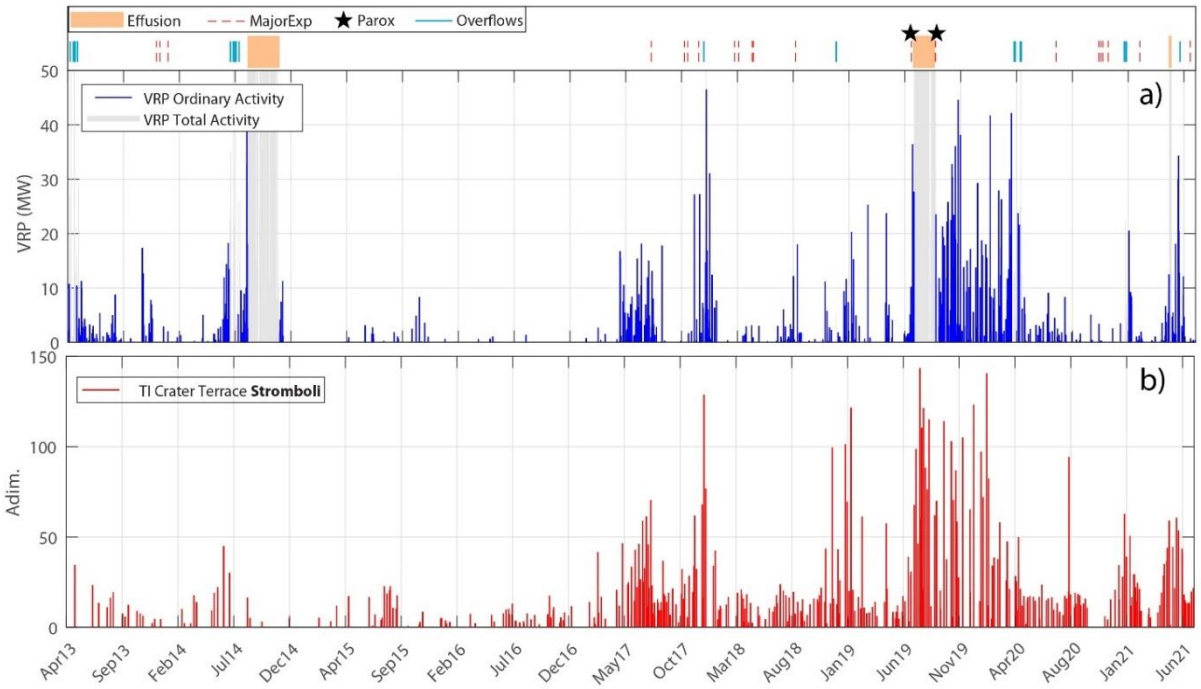

Figure 4 *- VRP (a) and Thermal Index (from crater terrace, b) time-series at Stromboli. The code bar above indicate period of effusion (in orange), major explosions (red dotted bars), overflows events (blue bars) and paroxysms (black stars).*

4.1.2 Cumulative Craters Thermal Index Time Series

Stromboli shows an almost balanced thermal budget between the three crater sectors in the first years of analysis, between 2013 and 2017 (Fig. 5). The Central crater displays a faster growth in thermal emissions preceding the effusive crisis of August – November 2014 (pale orange field in Fig. 5). It then becomes constant and stable in the following years in all the sectors. A sharp increase in the cumTI is observable from March 2017, mainly driven by NE and secondarily by the Central crater. Notably, the NE curve shows a "stepwise trend", likely indicating periods of higher emissions and relatively following calm, while the Central crater shows a more stable and constant-growing pattern. The SW sector also experiences an increase in cumTI but is less pronounced than the other craters.

The 2019 summer effusive crisis marks an apparent rise in thermal emissions from the SW sector. After that rising until April 2020, thermal emissions from SW almost dramatically decrease, with a cumTI pattern almost flat, indicating near-zero thermal emissions. The cumTI gap between NE and C partially widens, with the NE curve showing the last step in January 2021 and the Central crater being almost stable.

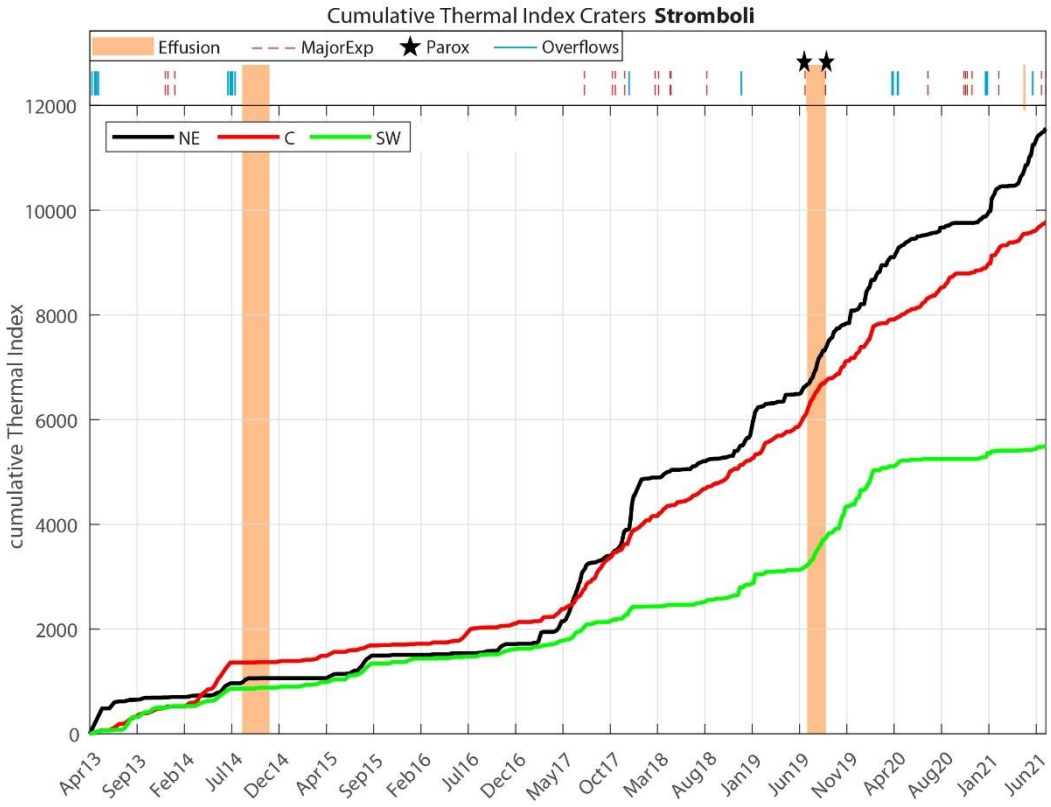

Figure 5 *– Cumulative Thermal Index time-series on Stromboli divided for each crater. Orange fields indicate effusive eruptions, red dotted bars major explosions, blue bar overflows events and black stars indicate paroxysms.*

4.1.3 Thermal Profiles

At Stromboli, anomalies during 2013-2021 became more intense and present since May 2017, as is possible to notice from profiles in Figures 6a-6b, with an increasing presence of yellow shades over time. Indeed, before this date, emissions were rare and with low intensities (dark tone reds), often localized on the SW sector, and mainly related to the 2014 effusive eruption, with anomalies spreading northward (Fig. 6a) because of lava flow emplacement on northern portions of the Sciara del Fuoco sector. Later, anomalies became more intense and frequent, with TI peaks of yellowish tones in both northern and southern portions of the crater terrace in January 2018 and 2019, with relevance to the NE crater as a thermal source. The effusive crisis of summer 2019 produced higher thermal emission, mainly scattering towards Sciara del Fuoco area due to lava flows production, and an intense period of sustained thermal activity mainly sourced by the SW sector with anomalies prone to expand outside the crater terrace, primarily westward and northward, until 2020. Interestingly, anomalies diminished and migrated toward the north and central portions of the terrace after this period, with a temporary reduction of emissions in the SW sector for large parts of the 2020 year (Fig. 6a – 6b). NE and C craters

became the major emitters, the first sourcing expansions of anomalies toward the north and feeding short effusive events during the first half of 2021.

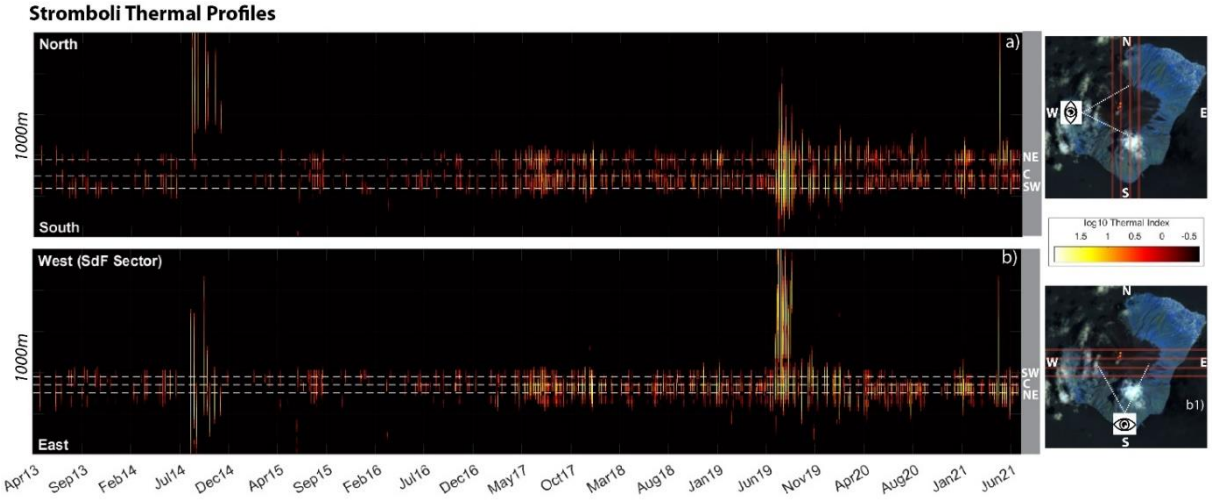

Figure 6 – *Thermal profile over Stromboli summit area, north-south (a – a1) and west-east (b – b1) oriented. The profiles are produced by stacking each SENTINEL-2 and LANDSAT-8 SWIR image in the two main directions. The main positions of the three Stromboli craters are marked with white dotted lines on the profiles.*

4.2 Etna

4.2.1 VRP and Thermal Index Time Series

The VRP and Thermal Index time series of Etna are shown in Figure 7, with a linear scale. As for the Stromboli case, values refer only to the thermal emission coming from the volcano's summit area, excluding other thermal sources. In Fig. 7a, we plotted with blue VRP sourced by summit craters and pale gray VRP related to the overall thermal activity, including summit lava flows, flank effusions, and paroxysms (from Andronico et al., 2021). As previously stated, the Thermal Index time series (Fig. 7b) should be interpreted considering that the SWIR satellites had different functionality times. At Etna, thermal emissions show a variable trend, showing a marked increase in the last period since 2019. In the first years of analysis, emissions remain sporadic and low, with VRP generally below 40 MW with occasional peaks up to 80-90 MW and TI stable under values of 100. Emissions are mainly clustered around earlier or later effusive eruptions or paroxysms occurrences, such as January – April 2014 eruption or October 2013 and December 2015 fountaining events (see Andronico et al., 2021), when TI reaches values above 300. Summit craters show an increase in thermal emissions around the effusive crisis of March – April 2017 both in VRP and TI, with anomalies reaching a TI_{max} over 300 and lots of VRP values by little below 40 MW, and a denser occurrence rate from June 2016 till March 2018. Then, the thermal behavior appears more impulsive and energetic: TI > 400 and

VRP up to 100 MW peaks in several phases, such as December 2018 and February 2020, within periods of high and constant thermal activity. In the last year of analysis, thermal activity remains very high, with a background level of TI ~ 50 and peaks of over 600 TI ca., and VRP values sourced by summit activity reaching values up to 100 MW ca., particularly during October 2020 – February 2021; this phase of rising and very high thermal emissions is preceding the sequence of paroxysms taking place from February 2021. Subsequently, thermal anomalies from summit craters, while remaining present with values around 20 TI and VRP < 40 MW, clearly decrease until July 2021.

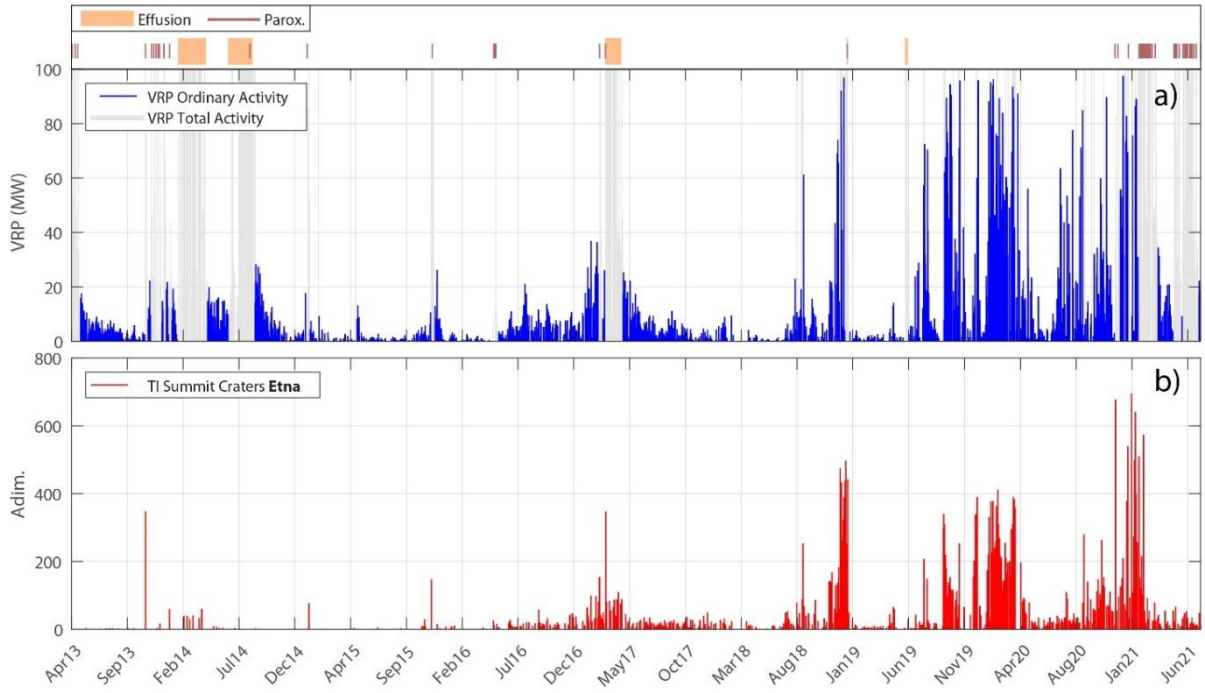

Figure 7 *- VRP (a) and Thermal Index (from summit craters, b) time-series at Etna. The code bar above indicate period of effusion (in orange) and occurrence of paroxysms (in red bars).*

4.2.2 Cumulative Craters Thermal Index Time Series

At Etna, the cumTI curves for each summit sector have different patterns (Figure 8). Until 2017, the SE sector's leading actor grew through two steps, particularly during the first effusive eruption of 2014 and in less degree before the minor eruption of March – April 2017. Instead, NE and BN+VOR craters exhibit low thermal magnitudes. However, these sectors started a rapid increase from the end of 2016 to the beginning of 2017, leveling the thermal contribution of the SE sector in May 2017. After that, thermal emissions from BN+VOR sectors became predominantly, with a slight rise in December 2018 and a steep increase in cumTI between October 2019 and April 2020. Similarly, the SE crater had a thermal growth before the December 2018 eruption and then a stable period until the beginning of 2020, when a slow but

consistent increase in cumTI became steeper until February 2021. In this scenario, NE is a lower thermal emitter sector, although it has shown an evident but less steep rise since October 2019. In the last months of analysis, the SE sector shows the most pronounced growth compared to the other craters.

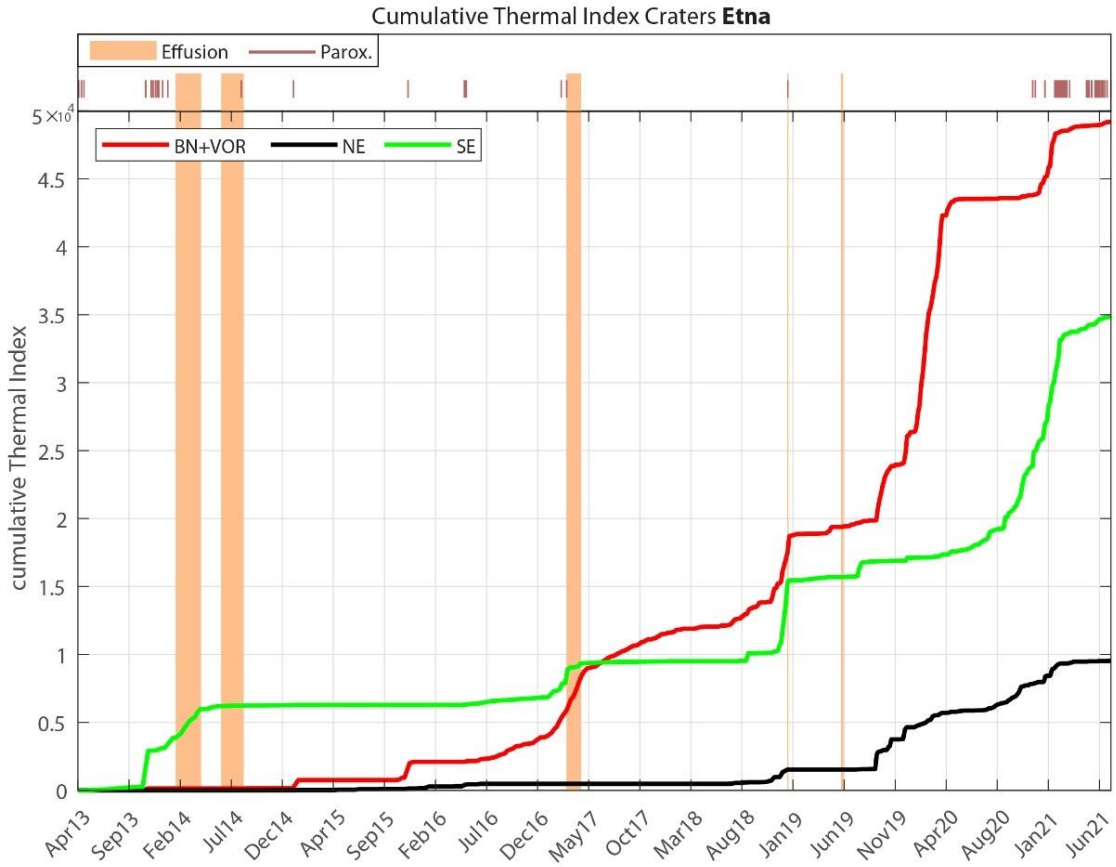

Figure 8 *- Cumulative Thermal Index time-series on Etna divided for each sector. Pale fields indicate effusive eruptions, red bars indicate paroxysms.*

4.2.3 Thermal Profiles

Etna's thermal profile appears relatively disordered and rich in intense thermal events (Figure 9). Craters' locations are only wholly reported on the N-S profile because, in the other W-E orientation, the positions of craters are partially overlapped due to the projection method. Until spring 2016, Etna thermal activity seemed to be sporadic and related nearly to small effusive and overflows events mainly from the SE sector and at NE crater. Thermal activity was confined stably at BN/VOR and partially at the SE sector in 2016 – 2017. Starting from the summer of 2018, thermal emissions partially resumed at the NE crater and intensified from BN+VOR and SE sectors, ending in the December 2018 short effusive event. A high thermal phase due to intracrater overflows in the BN and VOR craters occurs between 2019-2020, in conjunction

with a thermal increase in the SE sector and a regular occurrence of hotspots at NE. From mid-2020, activity decreases at Central Craters and increases in spatial extent and TI magnitude at SE. The pattern changed with paroxysm phase in 2021, with the lava fountains events (white stripes in the TI profiles) dominating the profile. During this phase, it is possible to observe an apparent decrease in thermal emissions from all the summit sectors, particularly with VOR and NE almost switched off from a thermal point of view.

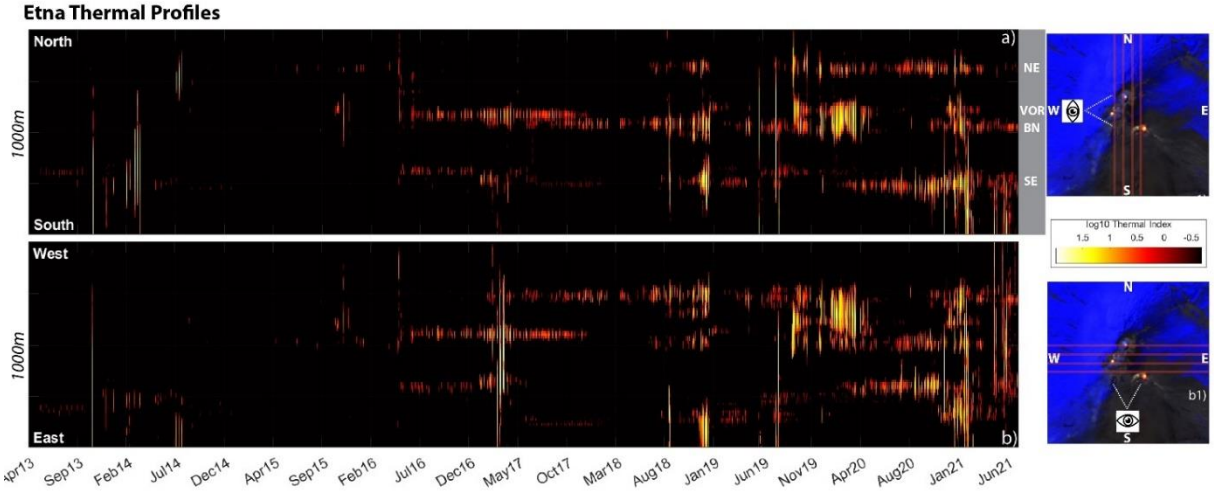

Figure 9 - *Thermal profile over Etna summit area, north-south (a – a1) and west-east (b – b1) oriented. The profiles are produced by stacking each SENTINEL-2 and LANDSAT-8 SWIR image in the two main directions. The main positions of Etna's craters are marked with white dotted lines on the profiles.*

5. DISCUSSION

5.1 Volcanic Radiative Energy and Thermal Index fitting

Our results demonstrate that the high-spatial-resolution feature of SWIR sensors OLI and MSI allows studying the thermal evolution of craters at Stromboli and Etna, depicting a complex interplay between thermal emissions and the behavior of each active sector. The Thermal Index parameter is a useful proxy to study the thermal activity produced by open-vent volcanoes. Nevertheless, its nature as a dimensionless parameter makes it unusable for quantification of thermal activity so far. This brings to the question of how to use Thermal Index to quantify heat flux and thermal energy produced from single craters at Stromboli and Etna. We rely on the MODIS MIR dataset to answer this topic and use the Thermal Index as a quantitative parameter to quantify thermal emissions. Indeed, as we already introduced, the use of MODIS imagery in the Middle InfraRed analysis allows us to get, through the MIROVA algorithm, a quantification of the heat flux and the thermal energy, VRP, and VRE, respectively, produced by volcanic activity. The VRE is the result of the radiation of active thermal bodies such as lava surfaces or gas/heat emitted by lava bodies (Coppola et al., 2020), and the trapezoidal rule of integration

calculates it over time of each VRP measurement during a certain period of analysis (see Method section). We compare the Volcanic Radiative Energy emitted only during ordinary activity with the cumulative Thermal Index released just by the crater terrace portion for Stromboli and by the summit craters of Etna. The choice to isolate this thermal dataset is motivated by our intention to focus the comparison on the long-time thermal budgets of different craters, excluding all those high energetic (effusions, flank eruptions, and fountains) and very short in time (paroxysms, major explosions) events that could make thermal data less homogeneous and therefore the comparison less accurate. Indeed, the different revisit frequencies of sensors used could create discrepancies with some events not recorded by all satellites.

In Figure 10, we compare VRE and cumulative Thermal Index, averaged on a weekly window. At Stromboli (Fig. 10a), thermal emissions from the whole crater terrace have sharply increased since March 2017, with an analogous behavior displayed by the two parameters, except a minor discrepancy related to a small step during the summer of 2014 with MODIS VRE exceeding the cumTI. Afterwards, the trends remain paired and diverging after the summer 2019 eruptive crisis, with VRE overcoming again the cumTI, related to the monthly-long thermal effects after the effusive crisis of that period (Laiolo et al., 2022) and the different revisit frequency of the satellites used. At Etna (Fig. 10c), the two trends follow the same pattern generally, with VRE higher than cumTI between 2013-2019, when SWIR thermal emissions paired VRE in correspondence to the short but highly thermal energetic eruption of December 2019. After that, thermal emissions have grown approximately evenly. The comparison between VRE and cumTI is relevant for two main reasons. Firstly, the two parameters came from the same logical operation, so that a cumulative sum over time of a specific thermal signal: in the case of VRP, which is originally a heat flux measurement in Watt, this is expressed in terms of emitted energy VRE in Joule, or other words as *Watt * time*; for the Thermal Index, which is an empirical parameter, the cumTI result is a proxy of how much "SWIR" thermal magnitude has been released in a certain period, so expressed as *Thermal Index * time*. Secondly, this comparison shows that the thermal energy produced by ordinary activity at Stromboli and Etna and recorded over time by MIR and SWIR satellite sensors, detected adequately employing devoted algorithms and filtered, is comparable in terms of trends and magnitude. These two essential considerations open the path to finding a model to predict the thermal energy released by volcanic activity through a relationship between VRE and cumTI. Figures 10b-10d show the results of a linear regression model, where cumulative VRE is plotted against cumulative Thermal Index. Here, we apply a linear fitting over the data with excellent agreement results

(coefficient of determination $R^2 = 0.982$ for Stromboli and $R^2 = 0.983$ for Etna, Fig. 10b-10d), indicating a predictable behavior of VRE using the Thermal Index value. The relationships are in a direct comparison of the two parameters through a linear rule. The equation showing this relationship is as follows:

$$VRE_{SWIR} = m * cumTI + k \quad (5)$$

where *m* is the best-fit linear coefficient resulting from the linear fit ($m = 2.4*10^5$ for Stromboli, $m = 2.6*10^5$ for Etna; Fig. 10), and *k* is a constant value from the linear equation. VRE_{SWIR} is expressed in *Watt*s* and *cumTI* in *TI*s* (or *Adim*s*), considering that TI is dimensionless. Mainly, the *m* coefficient represents the model able to link the radiative energy with the SWIR signals and embodies the comparable behavior between VRE and Thermal Index.

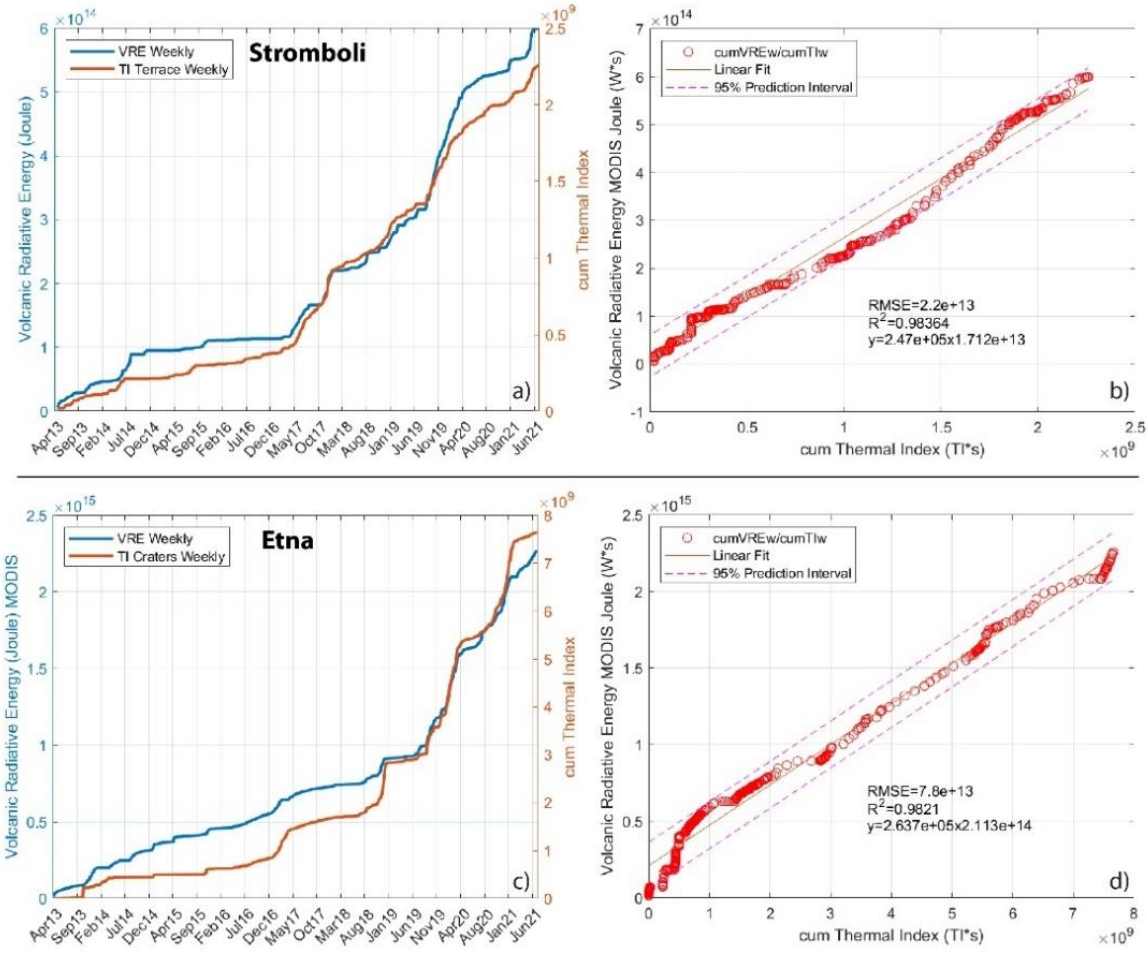

Figure 10 *– a) Plot YY of Volcanic Radiative Energy (Joule) from MODIS MIR (weekly avg.) in blue, and cumulative Thermal Index from Stromboli crater terrace (weekly avg.) in orange; b) Linear fitting (on 95% prediction interval) of VRE vs. CumTI on Stromboli; c) Plot YY of Volcanic Radiative Energy (Joule) from MODIS MIR (weekly avg.) in blue, and cumulative Thermal Index from Etna summit craters (weekly avg.) in orange; d) Linear fitting (on 95% prediction interval) of VRE vs. CumTI on Etna.*

5.2 Craters Heat Flux

The model found through a linear relationship between Volcanic Radiative Energy and Thermal Index allow us to make another step forward; indeed, if we consider the equation *(5)*, which expresses the linear relationship between SWIR and MIR thermal signals throughout the cumTI and VRE parameters respectively, we can easily revise it on a crater scale of study, as:

$$VRE_{SWIR\ crater} = m * cumTI_{crater} + k \qquad (6)$$

where TI_{crater} and $VRE_{SWIR\ crater}$ are, respectively, the cumulative Thermal Index parameter and the Volcanic Radiative Energy emitted only by a single crater of analysis. Since VRP and VRE are related following (see Coppola et al. 2013):

$$VRE = VRP\ * t \qquad (7)$$

we can easily obtain heat flux values at single crater scale applying to our dataset the following equation:

$$VRP_{SWIR\ crater} = VRE_{SWIR\ crater}/t \qquad (8)$$

where the $VRP_{SWIR\ crater}$ and the $VRE_{SWIR\ crater}$ are the heat flux in Watt and the thermal energy in Joule emitted by a single crater or sector of analysis. The result achieved has the perspective, as far as we know for the first time, of constantly measuring the heat flux by satellite methods over a long time of analysis (in this case of almost eight years) produced by volcanic activity at the different craters of Stromboli and Etna volcanoes.

Figure 11 shows the VRP_{SWIR} heat flux time-series of each Stromboli crater. In a general picture, the NE crater has the most impulsive nature, with peaks of VRP_{SWIR} up to 20 MW and a poorly constrained thermal behavior, with a wide distribution of heat flux without a clear maximum, starting from very low (VRP_{SWIR} < 0.5 MW) and with most values between 1 to 3 MW. Mean VRP_{SWIR} values at the NE crater are the highest among the three sectors. On the contrary, the Central crater shows a well-constrained thermal behavior, with a unimodal distribution around a VRP_{SWIR} = 2.5 MW, reflecting a steady process as the source of thermal emissions. By comparison, the SW sector has the lowest thermal output (mean VRP_{SWIR} heat flux of 2 MW), with the higher activity focused during and following the 2019 eruption. These measurements trace well the dynamics of Stromboli activity. If we refer to Coppola et al., 2012, the sum of the three craters' *VRP* heat flux resides below the ca. 50 MW, which is the threshold transition from Strombolian to the effusive regime, and it stays in accord with the Stromboli shallow system heat loss, estimated between 7 – 23 MW (Harris & Ripepe, 2007). Moreover, heat fluxes

derived by SWIR-MIR comparison here agree with the type of products and activity explained at Stromboli (Landi et al., 2011), where the Central sector tends to host "puffing", and thus more stable, regular, and continuous thermal emissions. In contrast, lateral vents such as the NE crater preferentially hosts Strombolian explosions, expressed with a more variable and discontinuous thermal output. As argued by Ripepe et al. 2008, convection mechanisms and the structure of the shallow system explain why puffing activity is more often stable in the Central crater and only temporarily migrates towards terrace edges due to a drift of the convection cell centroid. Finally, Figure 11 clearly shows the thermal emission at Stromboli's craters during the effusion of summer 2019, even if effectively sourced only by the SW sector (Plank et al., 2019; Laiolo et al., 2022; Giordano & De Astis, 2021), grow noticeably at all three craters, indicating a common higher thermal source probably linked to an uprising of magma level within conduits and affecting all crater terrace (Coppola et al., 2012; Laiolo et al., 2022).

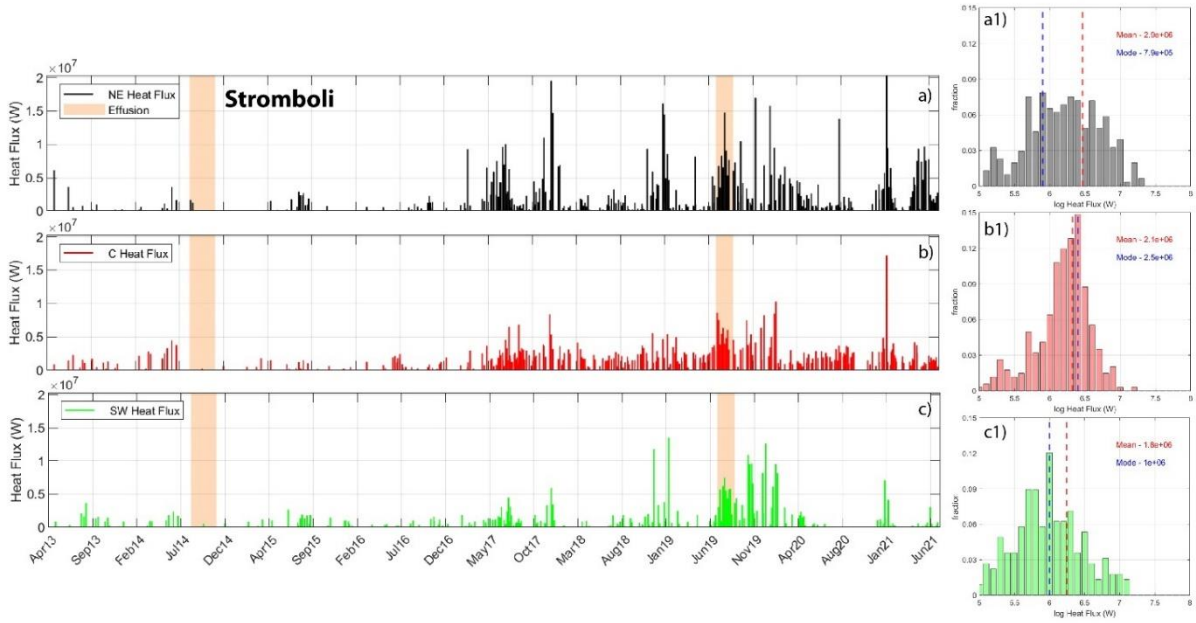

Figure 11 *– VRP_{SWIR} Heat flux (Watt) from Stromboli craters, a) North East, b) Central, and c) South West. In a1), b1), and c1) are reported the histogram diagrams in logarithmic scale for each crater, with VRP_{SWIR} Mean and Mode Heat Flux values in red and blue, respectively.*

At Etna, the three craters show distinct heat flux patterns in the last eight years (Figure 12). The NE sector displays lower thermal signals, with VRP_{SWIR} emissions mostly comprised during the 2019 – 2021 period and with a mean of ca. 6 MW (Fig. 12a – 12a1). The distribution plot shows a weakly unimodal behavior, with a poor occurrence of anomalies of VRP_{SWIR} > 10 MW. Otherwise, the central craters (BN+VOR) at Etna dominate over time the overall thermal budget (Fig. 12b). VRP_{SWIR} values from BN+VOR appear the most continuous and stable in the last during 2013 – 2021, although a temporary lack of emissions during 2020, with more frequent

VRP_{SWIR} heat flux values around 2.5 MW but mean values reaching 12 MW (Fig. 12b1); these values, express the attitude of central craters to be emitters of both small and moderate thermal emissions likely related of activity spanning from low Strombolian and degassing to higher-sustained activity. SE thermal behavior, instead, seems to be more deeply related to effusive periods, showing periods of emissions before and during the occurrence of effusive eruption (February 2014, March 2017, December 2018; Fig. 12c). Heat flux values are more sporadic rather than Central craters, and regularly and stably increased from 2020 till the first part of 2021, becoming the primary thermal emitter sector in the last two years of analysis.

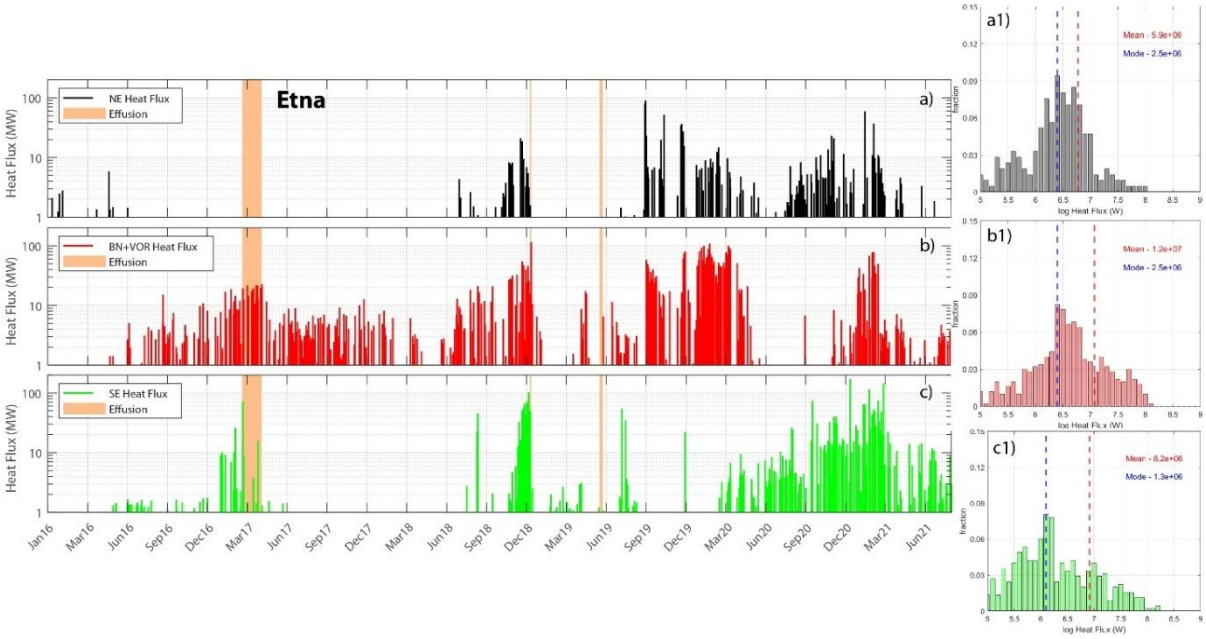

Figure 12 *- VRP_{SWIR} Heat flux (Watt) from Etna summit sectors, a) North East, b) BoccaNuova + Voragine (Central Craters), and c) South East. In a1), b1), and c1) are reported the histogram diagrams in logarithmic scale for each crater, with Mean and Mode VRP_{SWIR} Heat Flux values in red and blue, respectively.*

VRP_{SWIR} distribution is wider at SE (VRP_{SWIR} mode ca. 1.3 MW and VRP_{SWIR} mean ca. 8 MW, Fig. 12c1), lacking a clear unimodal peak but also indicating the capability of ordinary activity at SE to reach values higher than 100 MW and sourcing a variable type of volcanic activity. In a general view of the three craters, thermal anomalies related to ordinary activity rose before the paroxysm phase started in the first months of 2021 and then partially reduced after February 2021, when the paroxysm phase started (Andronico et al., 2021). Notably, the beginning of the paroxysmal phase at Etna concentrated thermal emission production by a very hot thermal source, such as lava flows and ejecta deposition on South-East volcano flanks after the occurrence of lava fountains. Here we focus the analysis only on the summit vents so that we do not record the emissions related to fountains and hot ejecta on flanks. This feature suggests a concurring reduction of thermal emission from summit vents during the paroxysms phase

between February – July 2021. This is valid considering not only the single data (which could be eventually affected by the satellite not recording the Strombolian rising phase before the starting of a lava fountain) but the last month of our period of analysis, in which thermal emission at all craters decreased in magnitude and frequency.

5.3 Volcanological and Hazards Implications

Open vents volcanism characterized by mild activity can rapidly evolve towards more energetic phenomena. This behavior can occur at Stromboli and Etna with violent explosions, lava fountains, or opening of lateral vents. The persistence of thermal emissions during regular activity gives us an important parameter to detect and possibly interpret deviations in volcanic behavior that can lead to major changes and eruption onset. A multisensory satellite-based monitoring effort, able to give a continuous thermal dataset with high-spatial accuracy at crater's scale and to build time-series usable as a reference, is a tool to improve understanding of how open vents behavior as Stromboli and Etna work. Notably, heat flux data shown above offer a quantification of thermal emissions produced by single craters or summit areas. These measurements could be placed in context with other geophysical parameters and volcanological data to understand how thermal emissions are related to shallow volcanic dynamics.

At Stromboli, the increased heat flux emitted by the crater terrace in the first part of 2017, marks the beginning of a new volcanic phase. In the Figure 13a, VRE_{SWIR} in Joule (Equation *5* and *6*), for each sector and crater terrace overall, is reported with the occurrence of the main "not-ordinary" events between April 2013 – July 2021. These events have been recorded by the LGS monitoring network (http://lgs.geo.unifi.it), and signed as a major explosion, paroxysms, summit overflows and effusive eruption (Rosi et al., 2013). Major and paroxysm explosions differ from regular Strombolian types by eruptive masses, ejecta heights, mass discharge rate, and distinct magma properties (Ripepe et al., 2021 and references therein). The rising of thermal emissions from crater terraces started around March/May 2017, mainly driven by the NE contribution. This increase precedes of some months the occurrence of the first major explosion in July 2017 after years of major explosion quiescence since 2014, and in a general view, seems to open the door to a new higher energetic stage suffered by Stromboli activity, with several explosions (Fig. 13a, marked with pale yellow). In other words, the rising thermal emission seems closely related to the resumption of a marked explosivity behavior at Stromboli since 2017. This is even more explicit if we consider the cumulative number of explosions, shown in Fig. 13b. We argue that, in a general picture, this correlation could be due to the consequences of a new and long-lasting rising in the level of magma column after the flank effusion of 2014

and the emptying of shallow portions of the conduit (Ripepe et al., 2017), reflecting in a slow but constant recovery of thermal emissions from summit vents and new predisposition of the shallow system to fed more energetic explosive events, as occurred from 2017 onwards. This mechanism was already depicted, even if at a shorter scale of months, before the 2014 effusion onset, when an increase in thermal emissions by craters coupled with a progressive transition of a higher explosive regime (> rate and amplitude of explosions) related to shallowing of magma column (VLP seismic source migration toward the surface; see Valade et al., 2016). Moreover, a direct relationship between moderate explosive activity at Stromboli, responsible for VLP seismic signals, and thermal radiance emissions by craters sourcing explosions has been already proved (Chouet et al., 2003; Marchetti & Ripepe, 2005; Ripepe et al., 2021). These remarks could be of great relevance for hazards implication at Stromboli, highlighting thermal signals as a critical parameter to track possible signs of system unbalance and monitoring changes in explosive rate and activity.

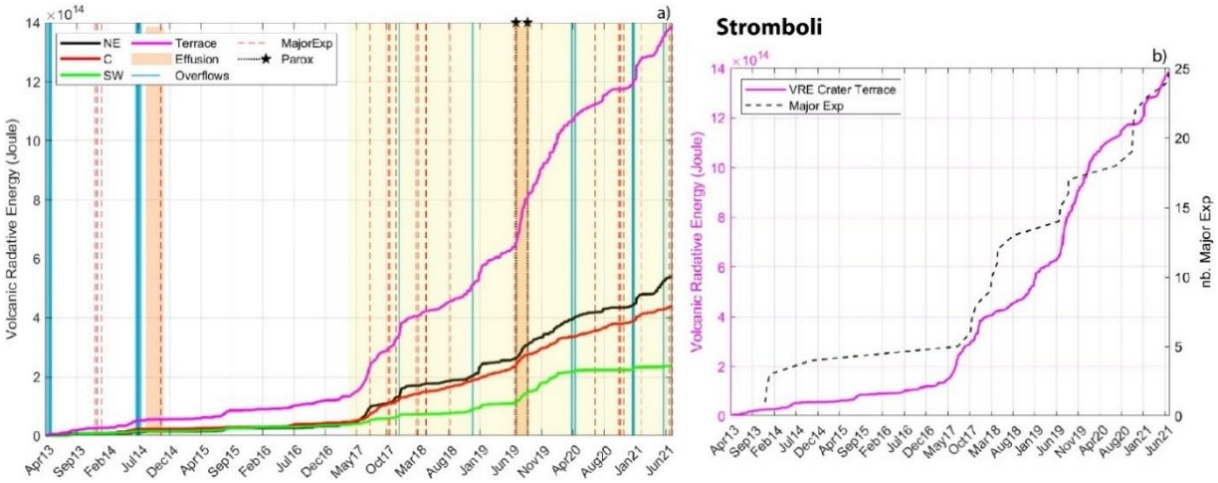

Figure 13 *– a) Volcanic Radiative Energy (Joule) at Stromboli by SWIR sensors, divided for single vents and overall crater terrace. In the pale yellow field, the period of increasing thermal emissions. With red dotted lines, Major Explosions; blue bars, Overflows, black dotted lines with stars Paroxysms, with pale orange field effusive periods. b) Comparison between Volcanic Radiative Energy (Joule) emitted by crater terrace at Stromboli and cumulative occurrence rate of Major Explosions.*

At Etna, a complex behavior took place in 2019 – 2021, with a marked increase of thermal activity sourced by summit craters, as is possible to notice from the cumulative TI graph (Fig. 8) and Thermal Profile (Fig. 9). A new phase of intense activity characterized by paroxysms and lava fountains started in December 2020 and became more regular from February 2021 (Calvari et al., 2021). In Figure 14, we focused on this period. Starting from September 2019, after a small eruption originating from the low slopes of the SE cone in May - June 2019, the activity was constrained mainly at NE and Central craters, with Strombolian explosions and

intra-crater lava overflows at VOR, concurrently with a period of minor thermal emission at SE. A shift occurred in the first months of 2020 when the thermal balance partially reversed, indicating the slow and constant resumption of thermal activity at SE and a period of cessation of thermal signals from BN+VOR, and a reduction from NE. This pattern is visible even from a spatial point of view with a shifting of thermal hotter source through the Thermal Profile (Fig. 9a). South-Est sector seems to display a gradual waxing phase leading to the beginning of the new paroxysm phase. The thermal activity sharply rises at NE and CC from September 2019 and the fast resumption of thermal signals in December 2020 too (see Fig. 8), are in perfect agreement with a sharp increase in seismic release, both deep ($z \geq 12$ km) and shallow ($z \leq 3$ km, see De Gori et al., 2021); the authors explain this increase with a possible new accumulation of magma in the shallower residing reservoir feeding craters activity. The growing trend in heat flux emitted by the SE crater, up to value $VRP_{SWIR} > 10^8$ MW, could likely represent the surface expression of a slow and continuous increase in magma supply within the upper portions of shallower reservoirs and related conduits. Indeed, this is not the first time that thermal activity rising at craters at Etna before major events such as paroxysms, overflows, and effusive crisis is interpreted as the consequence of upward migration of the active magma column, promoting a concurrent boost in summit explosive activity: this happened on a monthly scale for the December 2018 eruption and its previous stages (Laiolo et al., 2019), and or a shorter scale of days before the sequence of paroxysms at VOR, between November – December 2015 (Corsaro et al., 2017). Moreover, considering that in our period of analysis of 2013 – 2021 have occurred other several paroxysm sequences in 2013 (different stages), December 2015, and May 2016 (see Andronico et al., 2021), it is interesting to note that only in the last stage started in 2021 we have such prominent thermal emission rising, reaching heat flux values $VRP_{SWIR} > 10^8$ MW, then other phases. This remarkable if considering the general picture about paroxysmal events at Etna investigations, which indicate an overall increase in geophysical (seismic energy) and volcanic parameters (heights and volume of lava fountains) related to paroxysm events from 2000 until now (Andronico et al., 2021; Calvari et al., 2021).

6. CONCLUSIONS

In this work, we showed how integrating multiple satellite sensors, in this case of the SWIR MSI SENTINEL-2 and OLI LANDSAT-8 ones, with the MODIS MIR dataset improves the studying capabilities of thermal signals emitted by open vents activity. The conjunction of InfraRed moderate and higher spatial analysis opens the door to a more precise and denser analysis of how thermal emissions variate over time and space in a context such as Stromboli

and Etna, where thermal anomalies are almost continuously present. This allows studying with a crater scale of detail the thermal signals produced by every sector and tracking it over time. Moreover, the proposed work displays an important consistency between the SWIR Thermal Index parameter (S2&L8) and the Thermal Energy (MODIS) emitted during ordinary activity by Stromboli and Etna. Following this relationship, this is the first time that a multiyear quantification of heat fluxes from every crater is shown on these volcanoes. This outcome firstly depicts a diverse thermal behavior of every single vent, confirmed by previous ground-based observation and studies; secondly, it could be of great

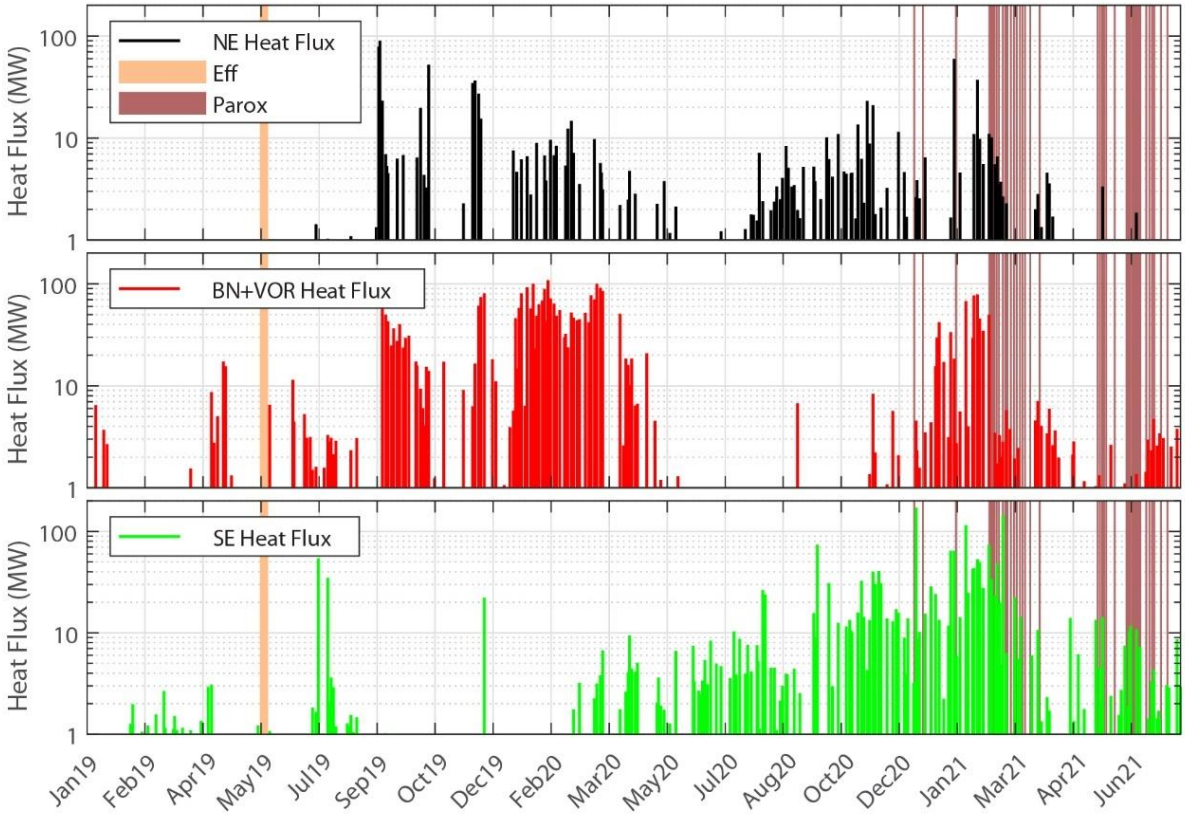

Figure 14 *- VRP_{SWIR} Heat flux (Watt) from Etna summit sectors between January 2019 – July 2021, a) North East, b) BoccaNuova + Voragine (Central Craters), and c) South East. Pale orange and red-colored bars indicate effusive periods and Paroxysms events.*

importance for monitoring purposes, with a possible dedicated space-based algorithm able to track in near real-time the heat flux produced by vents and the thermal budget on multicraters contexts.

In addition, we found that the thermal dataset is in tight accord with the occurrence of higher intensities events such as effusion, explosion, and paroxysms, likely testifying to a long-term change in the magmatic supply rate in the shallow feeding balance and, more generally, in shallow eruptive dynamics. At Stromboli, in our opinion, it is of great interest to observe how

changes in the overall thermal budget from the crater terrace since 2017 are in evident connection with the increase of explosivity suffered by the shallow magmatic system in the last year; at Etna, the new ongoing Paroxysm phase started in December 2020 – February 2021, arrives at the end of a long-lasting thermal rising trend at South-East sector and after months of reduced emissions at Central Craters, with a markable agreement with the increase in the seismic release.

7. BIBLIOGRAPHY

Acocella, V., Behncke, B., Neri, M., and D'Amico, S., 2003. Link between major flank slip and eruptions at Mt.Etna (Italy). Geophys. Res. Lett. 30, 2286. https://doi.org/10.1029/2003GL018642

Acocella, V., Neri, M., Behncke, B., Bonforte, A., DelNegro, C, Ganci, G., 2016. Why Does a Mature Volcano Need New Vents? The Case of the New Southeast Crater at Etna. Front. Earth Sci. 4:67. https://doi.org/10.3389/feart.2016.00067

Aiuppa, A., Bertagnini, A., Métrich, N., Moretti, R., Di Muro, A., Liuzzo, M., Tamburello, G., 2010. A model of degassing for Stromboli volcano. Earth Planet Sci Lett 295 (1–2): 195–204 https://doi.org/10.1016/j.epsl.2010.03.040

Aiuppa, A., Bitetto, M., Delle Donne, D., La Monica, F., Tamburello, G., Coppola, D., Della Schiava, M., Innocenti, L., Lacanna, G., Laiolo, M., Massimetti, F., Pistolesi, M., Silengo, C., Ripepe, M., 2021. Volcanic CO2 tracks the incubation period of basaltic paroxysms. Sci. Adv.17 (7(38)). https://doi.org/10.1126/sciadv.abh0191

Allard, P., Behncke, B., D'Amico, S., Neri, M., Gambino, S., 2006. Mount Etna 1993–2005: anatomy of an evolving eruptive cycle. Earth Sci. Rev. 78, 85–114. https://doi.org/10.1016/j.earscirev.2006.04.002.

Allard, P., Aiuppa, A., Burton, M., Caltabiano, T., Federico, C., Salerno, G., La Spina, A., 2008. Crater gas emissions and the magma feeding system of Stromboli volcano. In: Calvari, S., Inguaggiato, S., Puglisi, G., Ripepe, M., Rosi, M. (Eds.), Learning from Stromboli: AGU Geophysics Monograph Series, 182, pp. 65–80. Washington DC. https://doi.org/10.1029/182GM07

Andronico, D., Lodato, L., 2005. Effusive activity at Mount Etna Volcano (Italy) during the 20th Century: a contribution to volcanic hazard assessment. Nat. Hazards 36, 407–443. https://doi.org/10.1007/s11069-005-1938-2.

Andronico, D., Scollo, S., Cristaldi, A., 2015. Unexpected hazards from tephra fallouts at Mt Etna: the 23 November 2013 lava fountain. J. Volcanol. Geotherm. Res. 304, 118–125. https://doi.org/10.1016/j.jvolgeores.2015.08.007

Andronico, D.; Cannata, A.; Di Grazia, G.; Ferrari, F., 2021. The 1986–2021 paroxysmal episodes at the summit craters of Mt. Etna: Insights into volcano dynamics and hazard. Earth Sci. Rev., 220, 103686. https://doi.org/10.1016/j.earscirev.2021.103686

Barberi, F., Rosi, M., Sodi, A. 1993. Volcanic hazard assessment at Stromboli based on review of historical data. Acta Vulcanologica, 3, 173–187.

Barberi, F., Civetta, L., Rosi, M., Scandone, R. 2009. Chronology of the 2007 eruption of Stromboli and the activity of the Scientific Synthesis Group. Journal of Volcanology and Geothermal Research, 182, 123–130. https://doi.org/10.1016/j.jvolgeores.2008.09.019

Behncke, B., Neri, M., Pecora, E. et al., 2006. The exceptional activity and growth of the Southeast Crater, Mount Etna (Italy), between 1996 and 2001. Bull Volcanol 69, 149–173. https://doi.org/10.1007/s00445-006-0061-x

Behncke, B., Branca, S., Corsaro, R.A., De Beni, E., Miraglia, L., Proietti, P., 2014. The 2011–2012 summit activity of Mount Etna: birth, growth and products of the new SE crater. J. Volcanol. Geotherm. Res. 270, 10–21. https://doi.org/10.1016/j.jvolgeores.2013.11.012

Bevilacqua, A., Bertagnini, A., Pompilio, M. et al., 2020. Major explosions and paroxysms at Stromboli (Italy): a new historical catalog and temporal models of occurrence with uncertainty quantification. Sci Rep 10, 17357. https://doi.org/10.1038/s41598-020-74301-8

Blackett, M., Wooster, M.J., 2011. Evaluation of SWIR-based methods for quantifying active volcano radiant emissions using NASA EOS-ASTER data. Geomat. Nat. Haz. Risk 2:1, 2, 51–78. https://doi.org/10.1080/19475705.2010.541501

Bonaccorso, A., Calvari, S., Coltelli, M., Del Negro, C., and Falsaperla, S. (eds.)., 2004. "Mt. Etna: volcano laboratory," in American Geophysical Union, Geophysical Monograph Series, v. 143:350. DOI:10.1029/GM143

Bonaccorso, A.; Calvari, S.; Boschi, E., 2016. Hazard mitigation and crisis management during major flank eruptions at Etna volcano: Reporting on real experience. Geol. Soc. Lond. Spec. Publ., 426, 447–461. https://doi.org/10.1144/SP426.4

Bonny, E., Wright, R., 2017. Predicting the end of lava flow-forming eruptions from space. Bull Volcanol 79, 52. https://doi.org/10.1007/s00445-017-1134-8

Branca, S., Carlo, P.D., 2005. Types of eruptions of Etna volcano AD 1670–2003: implications for short-term eruptive behaviour. Bull Volcanol 67, 732–742. https://doi.org/10.1007/s00445-005-0412-z

Burton, M.R., Mader, H.M., Polacci, M., 2007. The role of gas percolation in quiescent degassing of persistently active basaltic volcanoes. Earth Planet Sci Lett 264(1): 46-60 https://doi.org/10.1016/j.epsl.2007.08.028

Calvari, S., Bonaccorso, A., Madonia, P. et al., 2014. Major eruptive style changes induced by structural modifications of a shallow conduit system: the 2007–2012 Stromboli case. Bull Volcanol 76, 841. https://doi.org/10.1007/s00445-014-0841-7

Calvari, S., Cannavò, F., Bonaccorso, A., Spampinato, L., Pellegrino, A.G., 2018. Paroxysmal Explosions, Lava Fountains and Ash Plumes at Etna Volcano: Eruptive Processes and Hazard Implications. Front. Earth Sci. 6:107. https://doi.org/10.3389/feart.2018.00107

Calvari, S., Bilotta, G., Bonaccorso, A., Caltabiano, T., Cappello, A., Corradino, C., Del Negro, C., Ganci, G., Neri, M., Pecora, E., et al., 2020. The VEI 2 Christmas 2018 Etna Eruption: A Small But Intense Eruptive Event or the Starting Phase of a Larger One? Remote Sens., 12, 905. https://doi.org/10.3390/rs12060905

Calvari, S., Bonaccorso, A., Ganci, G., 2021. Anatomy of a Paroxysmal Lava Fountain at Etna Volcano: The Case of the 12 March 2021, Episode. Remote Sens., 13, 3052. https://doi.org/10.3390/rs13153052

Cannata, A., Sciotto, M., Spampinato, L., Spina, L., 2011. Insights into explosive activity at closely-spaced eruptive vents using infrasound signals: example of Mt. Etna 2008 eruption. J Volcanol Geotherm Res 208:1–11. https://doi.org/10.1016/j.jvolgeores.2011.09.003

Cigolini, C., Coppola, D., Yokoo, A. et al., 2018. The thermal signature of Aso Volcano during unrest episodes detected from space and ground-based measurements. Earth Planets Space 70, 67. https://doi.org/10.1186/s40623-018-0831-7

Chaussard, E., Amelung, F., Aoki, Y., 2013. Characterization of open and closed volcanic systems in Indonesia and Mexico using InSAR time series. J Geophys Res Solid Earth 118:1–13. https://doi.org/10.1002/jgrb.50288

Chouet, B., Dawson, P., Ohminato, T., Martini, M., Saccorotti, G., Giudicepietro, F., De Luca, G., Milana, G., Scarpa, R., 2003. Source mechanisms of explosions at Stromboli volcano, Italy, determined from moment-tensor inversions of very-long-period data. Journal of Geophysical Research 108 (B1), 2019. https://doi.org/10.1029/2002JB001919

Coltelli, M., Del Carlo, P., Vezzoli, L., 2000. Stratigraphic constraints for explosive activity in the past 100 ka at Etna Volcano, Italy. International Journal of Earth Sciences, 89(3), 665–677. https://doi.org/10.1007/s005310000117

Coppola, D., Piscopo, D., Laiolo, M., Cigolini, C., Delle Donne, D., Ripepe, M., 2012. Radiative heat power at Stromboli volcano during 2000–2011: Twelve years of MODIS observations. J. Volcanol. Geotherm. Res., 215–216, 48–60. https://doi.org/10.1016/j.jvolgeores.2011.12.001

Coppola, D., Laiolo, M., Piscopo, D., Cigolini, C., 2013. Rheological control on the radiant density of active lava flows and domes. J. Volcanol. Geotherm. Res.249, 39–48. https://doi.org/10.1016/j.jvolgeores.2012.09.005

Coppola, D., Laiolo, M., Cigolini, C., Delle Donne, D., Ripepe, M. 2016. Enhanced volcanic hot-spot detection using MODIS IR data: Results from the MIROVA system. Geol. Soc. Lond. Spec. Publ. 2016, 426, 181–205. https://doi.org/10.1144/SP426.5

Coppola, D., Laiolo, M., Massimetti, F., et al., 2019. Monitoring endogenous growth of open-vent volcanoes by balancing thermal and SO2 emissions data derived from space. Sci Rep 9, 9394 (2019). https://doi.org/10.1038/s41598-019-45753-4

Coppola, D., Laiolo, M., Cigolini, C., Massimetti, F., Delle Donne, D., Ripepe, M., Arias, H., Barsotti, S., Parra, C.B., Centeno, R.G., Cevuard, S., Chigna, G., Chun, C., Garaebiti, E., González, D., Griswold, J., Juarez, J., Lara, L.E., López, C.M., Macedo, O., Mahinda, C., Ogburn, S., Prambada, O., Ramon, P., Ramos, D., Peltier, A., Saunders, S., de Zeeuw-van Dalfsen, E., Varley, N., William, R., 2020. Thermal remote sensing for global volcano monitoring experiences from the Mirova system. Front Earth Sci 7. https://doi.org/10.3389/feart.2019.00362

Coppola, D., Valade, S., Masias, P. et al., 2022. Shallow magma convection evidenced by excess degassing and thermal radiation during the dome-forming Sabancaya eruption (2012–2020). Bull Volcanol 84, 16. https://doi.org/10.1007/s00445-022-01523-1

Corsaro, R.A., Andronico, D., Behncke, B., Branca, S., Caltabiano, T., Ciancitto, F., Cristaldi, A., De Beni, E., La Spina, A., Lodato, L., et al., 2017. Monitoring the December 2015 summit eruptions of Mt. Etna (Italy): Implications on eruptive dynamics. J. Volcanol. Geotherm. Res., 341, 53–69. https://doi.org/10.1016/j.jvolgeores.2017.04.018

De Gori, P., Giampiccolo, E., Cocina, O. et al., 2021. Re-pressurized magma at Mt. Etna, Italy, may feed eruptions for years. Commun Earth Environ 2, 216. https://doi.org/10.1038/s43247-021-00282-9

Del Negro, C., Cappello, A., Neri, M., Bilotta, G., Hérault, A., Ganci, G., 2013. Lava flow hazards at Etna volcano: constraints imposed by eruptive history and numerical simulations. Scientific Reports - Nature 3:3493. http://dx.doi.org/10.1038/srep03493

Francis, P.W, 1979. Infra-red techniques for volcano monitoring and prediction—A review. J. Geol. Soc. Lond., 136, 355–359. https://doi.org/10.1144/gsjgs.136.3.0355

Francis, P., Oppenheimer, C., Stevenson, D., 1993. Endogenous growth of persistently active volcanoes. Nature 366, 554–557. https://doi.org/10.1038/366554a0

Ganci, G., Bilotta, G., Cappello, A., Hérault, A., Del Negro, C., 2016. HOTSAT: A multiplatform system for the satellite thermal monitoring of volcanic activity. Geol. Soc. Lond. Spec. Publ., 426, 207–221. https://doi.org/10.1144/SP426.21

Ganci, G., Cappello, A., Bilotta, G., Herault, A., Zago, V., Del Negro, C., 2018. Mapping Volcanic Deposits of the 2011–2015 Etna Eruptive Events Using Satellite Remote Sensing. Front. Earth Sci. 6:83. https://doi.org/10.3389/feart.2018.00083

Gaonac'h, H., Vandemeulebrouck, J., Stix, J., Halbwachs, M., 1994. Thermal infrared satellite measurements of volcanic activity at Stromboli and Vulcano. Journal of Geophysical Research, 99(B5), 9477–9485. https://doi.org/10.1029/93JB02392

Giberti, G., Jaupart, C., Sartoris, G., 1992. Steady-state operation of Stromboli volcano, Italy: constraints on the feeding system. Bull. Volcanol., 54: 535-541. https://doi.org/10.1007/BF00569938

Giordano, G., De Astis, G., 2021. The summer 2019 basaltic Vulcanian eruptions (paroxysms) of Stromboli. Bull. Volcanol.83. https://doi.org/10.1007/s00445-020-01423-2

Giuffrida, M., Viccaro, M. Three years (2011–2013) of eruptive activity at Mt. Etna: Working modes and timescales of the modern volcano plumbing system from micro-analytical studies

of crystals. Earth-Sci. Rev. 2017, 171, 289–322. https://doi.org/10.1016/j.earscirev.2017.06.003

Guest, J.E., 1982. Styles of eruptions and flow morphology on Mt. Etna (volcanological data). Mem Soc Geol It 23:49–73

Harris, A., 2013. Thermal Remote Sensing of Active Volcanoes: A User's Manual. Cambridge, MA: Cambridge university press. https://doi.org/10.1017/CBO9781139029346

Harris, A.J.L., Stevens, N.F., Maciejewski, A.J.H., Röllin, P.J., 1996. Thermal evidence for linked vents at Stromboli. Acta Vulcanologica, 8, 57–62.

Harris, A.J.L., Stevenson, D.S., 1997a. Magma budgets and steady-state activity of Vulcano and Stromboli volcanoes. Geophys. Res. Lett.24, 1043–1046. https://doi.org/10.1029/97GL00861

Harris, A.J.L., Stevenson, D.S., 1997b. Thermal observations of degassing open conduits and fumaroles at Stromboli and Vulcano using remotely sensed data. J. Volcanol. Geotherm. Res. 1997, 76, 175–198. https://doi.org/10.1016/S0377-0273(96)00097-2

Harris, A.J.L., Ripepe, M., 2007. Synergy of multiple geophysical approaches to unravel explosive eruption conduit and source dynamics – a case study from Stromboli. Geochem. 67, 1–35. https://doi.org/10.1016/j.chemer.2007.01.003

Harris, A.J.L., Steffke, A., Calvari, S., Spampinato, L., 2011. Thirty years of satellite-derived lava discharge rates at Etna: Implications for steady volumetric output. J. Geophys. Res., 116, B08204. https://doi.org/10.1029/2011JB008237

Houghton, B.F., Gonnermann, H.M., 2008. Basaltic explosive volcanism: constraints from deposits and models. Chem. der Erde 68, 117–140 (2008). https://doi.org/10.1016/j.chemer.2008.04.002

INGV-OE, 2020a. Bollettino settimanale sul monitoraggio vulcanico, geochimico e sismico del vulcano Etna. 23/11/2020–29/11/2020. Rep. N◦ 49/2020. Available at. https://www.ct.ingv.it/index.php/monitoraggio-e-sorveglianza/prodotti-del-monitoraggio/bollettini-settimanali-multidisciplinari/394-bollettino-settimanale-sul-monitoraggio-vulcanico-geochimico-e-sismico-del-vulcano-etna20201201/file

INGV-OE, 2020b. Bollettino settimanale sul monitoraggio vulcanico, geochimico e sismico del vulcano Etna. 08/06/2020 - 14/06/2020. Rep. N° 25/2020.

https://www.ct.ingv.it/index.php/monitoraggio-e-sorveglianza/prodotti-del-monitoraggio/bollettini-settimanali-multidisciplinari/342-bollettino-settimanale-sul-monitoraggio-vulcanico-geochimico-e-sismico-del-vulcano-etna20200616/file

INGV-OE, 2021a. Bollettino settimanale sul monitoraggio vulcanico, geochimico e sismico del vulcano Etna. 02/08/2021 - 08/08/2021. Rep. N° 32/2021. Available at. https://www.ct.ingv.it/index.php/monitoraggio-e-sorveglianza/prodotti-del-monitoraggio/bollettini-settimanali-multidisciplinari/527-bollettino-settimanale-sul-monitoraggio-vulcanico-geochimico-e-sismico-del-vulcano-etna20210810/file

INGV-OE, 2021b. Bollettino settimanale sul monitoraggio vulcanico, geochimico e sismico del vulcano Etna. 18/10/2021 - 24/10/2021. Rep. N° 43/2021. Available at. https://www.ct.ingv.it/index.php/monitoraggio-e-sorveglianza/prodotti-del-monitoraggio/bollettini-settimanali-multidisciplinari/550-bollettino-settimanale-sul-monitoraggio-vulcanico-geochimico-e-sismico-del-vulcano-etna20211026/file

INGV-OE, 2021c. Bollettino settimanale sul monitoraggio vulcanico, geochimico e sismico del vulcano Etna. 15/02/2021 - 21/02/2021. Rep. N° 08/2021. Available at. https://www.ct.ingv.it/index.php/monitoraggio-e-sorveglianza/prodotti-del-monitoraggio/bollettini-settimanali-multidisciplinari/473-bollettino-settimanale-sul-monitoraggio-vulcanico-geochimico-e-sismico-del-vulcano-etna20210223/file

Johnson, J.B., Watson, L.M., Palma, J.L., Dunham, E.M., Anderson, J.F., 2018. Forecasting the eruption of an open-vent volcano using resonant infrasound tones. Geophysical Research Letters, 45, 2213–2220. https://doi.org/10.1002/2017GL076506

Kazahaya, K., Shinohara, H., Saito, G., 1994. Excessive degassing of Izu-Oshima volcano: Magma convection in a conduit. Bull. Volcanol. 56, 207–216. https://doi.org/10.1007/BF00279605.

Laiolo, M., Ripepe, M., Cigolini, C., Coppola, D., Della Schiava, M., Genco, R., Innocenti, L., Lacanna, G., Marchetti, E., Massimetti, F., Silengo, M.C., 2019. Space- and Ground-Based Geophysical Data Tracking of Magma Migration in Shallow Feeding System of Mount Etna Volcano. Remote Sens., 11, 1182. https://doi.org/10.3390/rs11101182

Laiolo, M., Delle Donne, D., Coppola, D., Bitetto, M., Cigolini, C., Della Schiava, M., Innocenti, L., Lacanna, G., La Monica, F.P., Massimetti, F., Pistolesi, M., Silengo, M.C., Aiuppa, A., Ripepe, M., 2022. Shallow magma dynamics at open-vent volcanoes tracked by

coupled thermal and SO2 observations. Earth Planet. Sci. Lett., 594, 117726. https://doi.org/10.1016/j.epsl.2022.117726

Marchese, F., Neri, M., Falconieri, A., Lacava, T., Mazzeo, G., Pergola, N., Tramutoli, V., 2018. The Contribution of Multi-Sensor Infrared Satellite Observations to Monitor Mt. Etna (Italy) Activity during May to August 2016. Remote Sens., 10, 1948. https://doi.org/10.3390/rs10121948

Marchese, F., Genzano, N., Neri, M., Falconieri, A., Mazzeo, G., Pergola, N., 2019. A Multi-Channel Algorithm for Mapping Volcanic Thermal Anomalies by Means of Sentinel-2 MSI and Landsat-8 OLI Data. Remote Sens., 11, 2876. https://doi.org/10.3390/rs11232876

Marchese, F., Filizzola, C., Lacava, T., Falconieri, A., Faruolo, M., Genzano, N., Mazzeo, G., Pietrapertosa, C., Pergola, N., Tramutoli, V., et al., 2021. Mt. Etna Paroxysms of February–April 2021 Monitored and Quantified through a Multi-Platform Satellite Observing System. Remote Sens., 13, 3074. https://doi.org/10.3390/rs13163074

Marchetti, E., Ripepe, M., 2005. Stability of the seismic source during effusive and explosive activity at Stromboli Volcano. Geophys. Res. Lett. 32, 33-1-33–4, 2005. https://doi.org/10.1029/2004GL021406

Marchetti, E., Ripepe, M., Harris, A.J.L., Delle Donne, D., 2009. Tracing the differences between Vulcanian and Strombolian explosions using infrasonic and thermal radiation energy. Earth Planet. Sci. Lett. 279, 273–281. https://doi.org/10.1016/j.epsl.2009.01.004

Massimetti, F., Coppola, D., Laiolo, M., Valade, S., Cigolini, C., Ripepe, M., 2020. Volcanic Hot-Spot Detection Using SENTINEL-2: A Comparison with MODIS–MIROVA Thermal Data Series. Remote Sens 12: 820. https://doi.org/10.3390/rs12050820

McGreger, A.D., Lees J.M., 2004. Vent discrimination at Stromboli volcano, Italy, J. Volcanol. Geotherm. Res., 137, 169– 185. https://doi.org/10.1016/j.jvolgeores.2004.05.007

Mercalli, G. 1907. I vulcani attivi della Terra. Hoepli, Milan, Italy.

Mia, M.B., Fujimitsu, Y., Nishijima, J., 2018. Monitoring of Thermal Activity at the Hatchobaru–Otake Geothermal Area in Japan Using Multi-Source Satellite Images—With Comparisons of Methods, and Solar and Seasonal Effects. Remote Sens., 10, 1430. https://doi.org/10.3390/rs10091430

Neri, M., Acocella, V., Behncke, B., Giammanco, S., Mazzarini, F., Rust, D., 2011. Structural Analysis of the Eruptive Fissures at Mount Etna (Italy). Annals of Geophysics, 54, 5. https://doi.org/10.4401/ag-5332

Neri, M., Maio, M.D., Crepaldi, S., Suozzi, E., Lavy, M., Marchionatti, F., Calvari, S., Buongiorno, M.F., 2017. Topographic maps of Mount Etna's summit craters, updated to December 2015. J. Maps 13 (2), 674–683. https://doi.org/10.1080/17445647.2017.1352041.

Pallister, J., McNutt, S. R., 2015. "Synthesis of volcano monitoring," in The Encyclopedia of Volcanoes, 2nd Edn, ed. H. Sigurdsson, (Cambridge, MA: Academic Press), 1151–1171. doi: https://doi.org/10.1016/B978-0-12-385938-9.00066-3

Patanè, D., Aiuppa, A., Aloisi, M., Behncke, B., Cannata, A., Coltelli, M., Di Grazia, G., Gambino, S., Gurrieri, S., Mattia, M., Salerno, G., 2013. Insights into magma and fluid transfer at Mount Etna by a multiparametric approach: a model of the events leading to the 2011 eruptive cycle. J. Geophys. Res. 118, 7. https://doi.org/10.1002/jgrb.50248.

Pering, T.D., Liu, E.J., Wood, K., et al., 2020. Combined ground and aerial measurements resolve vent-specific gas fluxes from a multi-vent volcano. Nat Commun 11, 3039. https://doi.org/10.1038/s41467-020-16862-w

Phillipson, G., Sobradelo, R., Gottsmann, J., 2013. Global volcanic unrest in the 21st century: An analysis of the first decade. J. Volcanol. Geotherm. Res., 264, 183–196. https://doi.org/10.1016/j.jvolgeores.2013.08.004

Pioli, L., Pistolesi, M., Rosi, M., 2014. Transient explosions at open-vent volcanoes: The case of Stromboli (Italy). Geology; 42 (10): 863–866. doi: https://doi.org/10.1130/G35844.1

Plank, S., Marchese, F., Filizzola, C., Pergola, N., Neri, M., Nolde, M., Martinis, S., 2019. The July/August 2019 Lava Flows at the Sciara del Fuoco, Stromboli–Analysis from Multi-Sensor Infrared Satellite Imagery. Remote Sens., 11, 2879. https://doi.org/10.3390/rs11232879

Poland, M.P., Lopez, T., Wright, R. et al. 2020. Forecasting, Detecting, and Tracking Volcanic Eruptions from Space. Remote Sens Earth Syst Sci 3, 55–94. https://doi.org/10.1007/s41976-020-00034-x

Ramsey, M. S., Harris, A. J. L., 2013. Volcanology 2020: how will thermal remote sensing of volcanic surface activity evolve over the next decade? (invited review article). J. Volcanol. Geotherm. Res., 249, 217–233. https://doi.org/10.1016/j.jvolgeores.2012.05.011

Ramsey, M.S.; Harris, A.J.L.; Watson, I.M., 2022. Volcanology 2030: Will an orbital volcano observatory finally become a reality? Bull. Volcanol., 84, 6. https://doi.org/10.1007/s00445-021-01501-z

Reath, K., Pritchard, M., Poland, M., Delgado, F., Carn, S., Coppola, D., et al., 2019. Thermal, deformation, and degassing remote sensing time series (CE 2000–2017) at the 47 most active volcanoes in Latin America: Implications for volcanic systems. Journal of Geophysical Research: Solid Earth, 124, 195– 218. https://doi.org/10.1029/2018JB016199

Ripepe, M., Marchetti, E., 2002. Array tracking of infrasonic sources at Stromboli volcano. Geophys. Res. Lett., 29, 2076. https://doi.org/10.1029/2002GL015452

Ripepe, M., Harris, A.J.L., Marchetti, E., 2005. Coupled thermal oscillations in explosive activity at different craters of Stromboli volcano, Geophys. Res. Lett., 32, L17302, https://doi.org/10.1029/2005GL022711

Ripepe, M., Delle Donne, D., Harris, A.J.L., Marchetti, E., Ulivieri, G., 2008. Dynamics of Strombolian activity. In: Calvari, S., Inguaggiato, S., Puglisi, G., Ripepe, M., Rosi, M. (Eds.), Learning from Stromboli: An Integrated Study of the 2002-2003 Eruption. In: AGU Geophysics Monograph Series, vol.182, pp.39–48. https://doi.org/10.1029/182GM05

Ripepe, M., Delle Donne, D., Lacanna, G., Marchetti, E., Ulivieri, G., 2009. The onset of the 2007 Stromboli effusive eruption recorded by an integrated geophysical network. JVolcanol GeothermRes 182(3–4): 131–136. https://doi.org/10.1016/j.jvolgeores.2009.02.011

Ripepe, M., Pistolesi, M., Coppola, D. et al., 2017. Forecasting Effusive Dynamics and Decompression Rates by Magmastatic Model at Open-vent Volcanoes. Sci Rep 7, 3885. https://doi.org/10.1038/s41598-017-03833-3

Ripepe, M., Marchetti, E., Delle Donne, D., Genco, R., Innocenti, L., Lacanna, G., & Valade, S., 2018. Infrasonic early warning system for explosive eruptions. Journal of Geophysical Research: Solid Earth, 123. https://doi.org/10.1029/2018JB015561

Ripepe, M., Lacanna, G., Pistolesi, M., et al., 2021. Ground deformation reveals the scale-invariant conduit dynamics driving explosive basaltic eruptions. Nat Commun 12, 1683. https://doi.org/10.1038/s41467-021-21722-2

Rose, W.I., Palma, J.L., Delgado Granados, H., Varley, N., 2013. Open-vent volcanism and related hazards: overview. Spec. Pap., Geol. Soc. Am.498, vii–xiii. https://doi.org/10.1130/2013.2498(00)

Rosi, M., Bertagnini, A., Landi, P., 2000. Onset of persisting activity at Stromboli Volcano (Italy). Bulletin of Volcanology 62, 294–300. https://doi.org/10.1007/s004450000098

Rosi, M., Pistolesi, M., Bertagnini, A., Landi, P., Pompilio, M., Di Roberto, A., 2013. Stromboli volcano, Aeolian Islands (Italy): present eruptive activity and hazards. Mem. Geol. Soc. Lond.37, 473–490. https://doi.org/10.1144/M37.14. Ch. 14.

Salvatore, V., Silleni, A., Corneli, D. et al., 2018 Parameterizing multi-vent activity at Stromboli Volcano (Aeolian Islands, Italy). Bull Volcanol 80, 64. https://doi.org/10.1007/s00445-018-1239-8

Schmid, M., Kueppers, U., Civico, R., Ricci, T., Taddeucci, J., Dingwell, D.B., 2021. "Characterising vent and crater shape changes at Stromboli: implications for risk areas", Volcanica, 4(1), p. 87–105. https://doi.org/10.30909/vol.04.01.87105

Shevchenko, A.V., Dvigalo, V.N., Zorn, E.U., Vassileva, M.S., Massimetti, F., Walter, T.R., Svirid, I.Y., Chirkov, SA, Ozerov, A.Y., Tsvetkov, V.A., Borisov, I.A., 2021. Constructive and Destructive Processes During the 2018–2019 Eruption Episode at Shiveluch Volcano, Kamchatka, Studied From Satellite and Aerial Data. Front. Earth Sci. 9:680051. https://doi.org/10.3389/feart.2021.680051

Simons, B.C., Jolly, A.D., Eccles, J.D., Cronin, S.J., 2020. Spatiotemporal relationships between two closely-spaced Strombolian-style vents, Yasur, Vanuatu. Geophysical Research Letters, 47, e2019GL085687. https://doi.org/10.1029/2019GL085687

Sparks, R., 2003. Forecasting volcanic eruptions. Earth and Planetary Science Letters, 210(1-2), 1–15. https://doi.org/10.1016/S0012-821X(03)00124-9

Sparks, R.S.J., Biggs, J., Neuberg, J.W., 2012. Geophysics. Monitoring volcanoes. Science, 335, 1310–1311. https://doi.org/10.1126/science.1219485

Tamburello, G., Aiuppa, A., Kantzas, E.P., McGonigle, A.J.S., Ripepe, M., 2012. Passive vs. active degassing modes at an open-vent volcano (Stromboli, Italy). Earth Planet. Sci. Lett. 359–360, 106–116. https://doi.org/10.1016/j.epsl.2012.09.050

Tibaldi, A., Corazzato, C., Apuani, T., Pasquaré, F.A., Vezzoli, L., 2008. Geological-structural framework of Stromboli volcano, past collapses, and possible influence on the events of the 2002-2003 crisis. In: Calvari S, Inguaggiato S, Puglisi G, et al (eds) The Stromboli Volcano: an integrated study of the 2002-2003 eruption, Am Geophys Union Geophys Monogr 182:5–17 https://doi.org/10.1029/182GM03

Tilling, R. I., 2008. The critical role of volcano monitoring in risk reduction. Adv. Geosci. 14, 3–11. https://doi.org/10.5194/adgeo-14-3-2008

Urlaub, M., Petersen, F., Gross, F., Bonforte, A., Puglisi, G., Guglielmino, F., Krastel, S., Lange, D., Kopp, H., 2018. Gravitational collapse of Mount Etna's southeastern flank. Sci. Adv. 4, 1–8. https://doi.org/10.1126/sciadv.aat9700

Valade, S.; Lacanna, G.; Coppola, D.; Laiolo, M.; Pistolesi, M.; Delle Donne, D.; Genco, R.; Marchetti, E.; Ulivieri, G.; Allocca, C., et al., 2016. Tracking dynamics of magma migration in open-conduit systems. Bull. Volcanol., 78, 78. https://doi.org/10.1007/s00445-016-1072-x

Vergniolle, S., Métrich, N., 2021. Open-vent volcanoes: a preface to the special issue. Bull Volcanol 83, 29. https://doi.org/10.1007/s00445-021-01454-3

Wooster, M.J., Zhukov, B., Oertel, D., 2003. Fire radiative energy for quantitative study of biomass burning: Derivation from the BIRD experimental satellite and comparison to MODIS fire products. Remote Sens. Env., 86, 83–107. https://doi.org/10.1016/S0034-4257(03)00070-1

Wright, R., Flynn, L., Garbeil, H., Harris, A.J.L., Pilger, E., 2002. Automated volcanic eruption detection using MODIS. Remote Sens. Env., 82, 135–155. https://doi.org/10.1016/S0034-4257(02)00030-5

Wright, R., Pilger, E., 2008. Radiant flux from Earth's subaerially erupting volcanoes. International Journal of Remote Sensing 29 (22), 6443–6466. https://doi.org/10.1080/01431160802168210

Wright, R., Blackett, M., Hill-Butler, C., 2015. Some observations regarding the thermal flux from Earth's erupting volcanoes for the period of 2000 to 2014, Geophys. Res. Lett., 42, 282–289, https://doi.org/10.1002/2014GL061997

Yokoyama, I. Heat and mass transfer through volcanoes. Riv. Ital. Geofis. 1972, 21, 165–169.

Chapter 4

4. Thermal Signatures at Lava Domes: an overview comparison using multi-sensor and multi-spatial thermal IR satellites

Abstract

Lava dome eruptions represent hazardous volcanic phenomena, with possible collapses and explosions posing severe risks to local communities and difficulties in studying their activity in-depth. Lava domes are active thermal bodies, and thermal satellite remote sensing is a valuable tool to quantitively and qualitatively characterize their eruptive dynamics, particularly over long-term analysis. Understanding thermal signals during these eruptions provide insight into eruptive scenarios and is a crucial parameter for monitoring. A straightforward interpretation of what a thermal anomaly indicates at lava domes is a subtle issue, and long-term multisensory tracking of thermal behavior is a missing approach. Here, we study over a multiyear time scale the thermal activity of three dome-forming eruptions taken as illustrative case studies, which are Láscar (Chile), Sabancaya (Peru), and Shiveluch (Russia), all of those showing intense volcanic activity recently. We apply a multisensory satellite-based method, using moderate to high-spatial-resolution Infrared sensors, such as MODIS (Moderate Resolution Imaging Spectroradiometer), VIIRS (Visible Infrared Imaging Radiometer Suite), MultiSpectral Instrument on SENTINEL-2, and Operational Land Imager on LANDSAT-8, with a resolution spanning from 1 km to 20 meters. This approach allows to study thermally: i) the Láscar's cyclicity shown in 2013 – 2021, revealing an explosive event otherwise unnoticed, tracking the regular patterns and proposing a mechanism for the passive thermal behavior observed and ruled by explosion occurrence; ii) the Sabancaya's unrest and eruptive phases in 2012 -2020, characterizing the two stages and highlighting the opening of a new conduit and the extrusion of a new dome body; iii) the Shiveluch complex constructive and destructive process occurred in 2018 – 2019, showing the beginning of a new extrusive phase leading to two important explosions and revealing the presence of a major structural trend ruling the dome evolution. We focused our attention on constraining the thermal signatures in terms of intensity (Heat Flux, Thermal Index), persistence (duration over time), and spatial attributes (hot Area, dimensional evolution), trying to understand the volcanic source responsible for emission, often related to diverse processes such as magma extrusion, hot degassing, passive exposure of hot inner magmatic materials, and hot ejecta deposition. This information enlightens our understanding of the volcanic processes triggering a thermal anomaly and, consequently, a better interpretation of lava dome dynamics, opening pathways for future monitoring applications and upgrading hazard evaluation.

1. INTRODUCTION

Lava domes represent one of the most impulsive and dangerous volcanic-related phenomena on Earth, representing the 6% ca. of eruptions worldwide (Newhall & Melson, 1983; Calder et al., 2015). Around 200 dome-building volcanoes have been recognized as active during Holocene (Siebert et al., 2011), and of these, ca. 120 have erupted in the last 1000 years, and around 90 erupted in the last century (Ogburn et al., 2015). Dome-building eruptions show a wide variety of growth styles, from domes standing alone in volcanic craters or forming part of

a cluster or dome complex (Fink, 1990). Generally, dome-forming eruptions can last many months, years, or decades (Newhall & Melson, 1983; Sparks, 1997; Ogburn et al., 2015), but, even if volcanic activity can be viewed as continuous over historical timescales, it may also include abrupt or cyclic fluctuations in magnitude, duration, and style (Sheldrake et al., 2016). Lava domes form when the extruding lava, typically felsic, is too viscous to flow far from the volcanic conduit and thus accumulates up into a mound-shaped dome (Calder et al., 2015). They form under peculiar conditions, indicating underlying magmatic processes with specific characteristics: high viscosities (10^6 to 10^{11} Pa*s; Yokoyama, 2005), low eruption rates (~10^{-2} to 10^{-1} km^3 * $year^{-1}$), high groundmass crystallinity (Cashman, 1992) and noticeable yield strength (Calder et al., 2015; Walter et al., 2019). From a chemical point of view, dome lavas cover a wide compositional range from basaltic through to rhyolitic; however, most are of intermediate composition from andesitic to dacitic (Calder et al., 2015). Lava domes have been historically classified by using two main distinct growing dynamics as references: exogenous (extrusive growth, with magma apports extruding through the dome surface and forming various shapes of lava emplacements), and endogenous (intrusive growth, whereby magma embedded inside the dome causing internal swelling; see Fink, 1990; Hale et al., 2009; Calder et al., 2015). Nevertheless, lava dome eruptions can show marked differences in behavior, growth patterns, morphological features, and typology of explosive activity. Indeed, their dynamics can span from mild effusion and non-explosive growth and emplacement of lava bodies (Eichelberger et al., 1986) to unpredictable explosions, even with large-magnitude eruptions (e.g., Plinian) and collapses, producing pyroclastic currents, volcanic blasts (Calder et al., 2002), and triggering cascades of secondary processes such as lahars, rock avalanches and tsunamis (Ogburn et al., 2015). Often, dome eruptions can show a sudden transition from an "ordinary" extrusive behavior to a critical one due to several complex interactions between extrusion rate, dome permeability, lava degassing, cooling, and crystallization that can cause pressurization and gravitational instability (Sparks, 1997; Melnik & Sparks, 1999; Sparks & Young, 2002; Yokoyama, 2005; Boudon et al., 2015).

For these reasons, dome-forming eruptions and associated hazards have been studied over the past decades, based on the numerous eruptive events and, unfortunately, human and economic losses that these have produced (Calder et al., 2015 and references therein; Ogburn et al., 2015). Indeed, two-thirds of worldwide volcanic-associated fatalities since 1600 were related to dome-building activity (Auker et al., 2013). Collapses constitute the riskiest scenario in a dome evolution story, producing thousands of victims through Pyroclastic Density Currents (PDCs) and hitting vast surrounding areas (Witham, 2005). Famous examples of significant eruptions

at dome-building volcanoes in the last century occurred at Mt. Pelée in 1902 (Martinique, defined as the worst volcanic disaster of the twentieth century with ca. 30.000 estimated fatalities), Colima in 1913 (Mexico), Kelut in 1919 (Indonesia), Bezymianny in 1956 (Russia), Mount St. Helens in 1980 (USA), El Chichon (Mexico) in 1982, Pinatubo (Philippines) in 1991, Soufrière Hills in 1996-99 (Montserrat), Chaiten in 2008 (Chile), Merapi in 2010 (Indonesia), and Colima again in 2015 (see Calder et al., 2015; Walter et al., 2019), with most of these events ranging in Explosivity Index between VEI 4 up to VEI 6 (Ogburn et al., 2015). Understanding and monitoring the dynamics of growth and evolution of lava domes is one of the most critical tasks in volcanology. These volcanic phenomena can pose a severe threat to human lives and goods. Despite the importance of this understanding and the vast number of studies done on dynamics, frequencies, and impact of dome-forming eruptions, several processes remain still unclear: a detailed identification of the growth styles, if as internal and external extrusive growth (endogenous vs. exogenous), or on growing patterns, are limited (Zorn et al., 2019); relationships between rock strength, topography, and dome geometry is a matter of ongoing investigation (Harnett & Heap, 2021); external forcing effects, such as rains or earthquakes triggering explosions or collapses (Walter et al., 2007; Gaete et al., 2020) are still to explore; non-linear processes and cyclicity in extrusion rates, changing properties of magma, growth phases and degassing patterns, as well as their mutual interactions, are poorly understood (Costa et al., 2007; Melnik et al., 2009).

The role of volcanic monitoring is to have the most continuous and as homogenous as possible collection of geophysical, geochemical, deformation parameters and observational information about lava dome dynamics and activity, to then recognize and interpret conditions possibly leading to critical states such as collapses, failures, and sudden transition toward explosive styles (Sparks et al., 2012; Pallister & McNutt, 2015). Because of the hazardous nature of erupting lava domes and the severe environmental conditions and remote locations where they are often located, the installation of permanent ground-based monitoring networks could be arduous (Pallister & McNutt, 2015). In this view, remote satellite techniques offer a precious and safe tool to improve dome-eruption monitoring and are complementary to ground-based methods (Furtney et al., 2018; Reath et al., 2019; Coppola et al., 2022a).

Recent satellite remote sensing observations on dome dynamics commonly used optical (Krippner et al., 2018; Pallister et al., 2019), aerial (Darmawan et al., 2018; Zorn et al., 2020; Moussalam et al., 2021; Shevchenko et al., 2021), and radar (Wang et al., 2015; Mania et al., 2019; Walter et al., 2019) sensors. The Synthetic Aperture Radar (SAR) technique has been

increasingly used to record dome evolution (Pallister et al., 2013; Salzer et al., 2017; Walter et al., 2015; 2019) and summit volcanic deformation (Salzer et al., 2014; Mania et al., 2021), as radar microwaves could penetrate atmospheric clouds allowing imaging independently by cloud coverage.

Lava domes are active thermal bodies (Gaunt et al., 2016). They are typically considered to comprise a hot ductile core and a brittle carapace that can brecciate and form a blocky talus apron around the base of the dome itself (Wadge et al., 2009). The high viscosity nature of a lava dome, differentiating from a lava flow, is a consequence of several factors, including the volume fraction of crystals and a general relatively low temperature (ranging between 600 °C to 800 °C, depending on how and from which hot source is measured; Melnik et al., 2009; Calder et al., 2015; Tsepelev et al., 2020). Thus, surface temperature measurements are another fundamental aspect of studying dome dynamics (Oppenheimer et al., 1993a, Sahetapy-Engel & Harris, 2009; Coppola et al., 2020; Zorn et al., 2020). Thermal imaging investigation of volcanic lava domes is an especially valuable tool for monitoring their activity; for these purposes, several handheld, airborne, and satellite-based techniques have been applied in the last decade (Hutchison et al., 2013; Pallister et al., 2013; Thiele et al., 2017; Walter et al., 2013). Thermal images can be used qualitatively to detect thermal anomalies, reveal structural features, map areas, and quantitively to measure temperatures, cooling rates, and heat fluxes. Due to problems of safe access and technical maintenance of measuring equipment, a few studies applied an in-depth thermal characterization of dome-forming eruptions, particularly over prolonged periods (Hutchison et al., 2013). Some examples where quantitative and qualitative thermal approaches from remote were used to study dome-forming volcanoes include, among others: the evolution of the Láscar dome (Chile) was investigated by using long-term satellite thermal analysis, measuring spectral radiance and unveiling cycles of dome growth and explosive events (Oppenheimer et al., 1993a); thermal active structures have been characterized at Unzen (Japan) dome-forming eruption between 1991-1993, differentiating areas of active fumaroles, dome growth, and collapse deposition (Wooster et al., 2000); Santiaguito (Guatemala) revealed ring-shaped structural features highlighted by thermal anomalies observed around the dome top (Sahetapy-Engel & Harris, 2009; Hutchison et al., 2013), and fractures and high strain zones associated with thermal anomalies tracked by UAS-based techniques (Zorn et al., 2020); Vaughan et al., 2005 used airborne and space-based methods to measure dome surface temperature and radiant heat flux at Mount St. Helens (USA); thermal unrest has been characterized at Sant Ana volcano (El Salvador) by satellite remote analysis of fumarole field temperatures (Laiolo et al., 2017); at Sabancaya (Perù), a multisensory satellite thermal

approach was used to characterize the activity of the dome during the unrest and eruption phases (Coppola et al., 2022a). Nevertheless, a multiyear and multisensory continuous tracking of thermal behavior and features at dome-forming eruptions, in all their broad spectrum of activity and phases, is nowadays a still missing approach or at least is a goal possible to achieve just using by using space-based data (Coppola et al., 2020).

Space-based thermal data have also been primarily used to investigate several effusive and low-viscosity volcanic phenomena, such as lava flow-forming eruptions (Harris & Baloga, 2009), lava lakes dynamic (Francis et al., 1993; Aiuppa et al., 2018), and to calculate lava discharge rate (Coppola et al., 2019). This is possible because, for basaltic-effusive lava flow events, the heat radiated by the hot lava surface is related to the effusion rate which feeds the lava flow itself (Harris & Baloga, 2009). In other terms, the thermal signature (i.e., the intensity, dimension, spatial distribution, and temporal persistency of a thermal anomaly, see Oppenheimer et al., 1993b) of active lava flows, even if it may vary in space and time, is easier to interpret and characterize, because of the presence of higher temperatures, larger areas covered, more evident anomalies to detect. At dome-forming volcanoes, a clear and unique interpretation of what a thermal anomaly indicates, in terms of dynamics of source processes, is complicated by lower temperatures, smaller areas exposed, high variability in thermal source, and ultimately subtle anomalies to detect. For instance, a thermal anomaly detected on a growing lava dome can be related to a variety of processes such as (*i*) increase in extrusion rate, (*ii*) explosive disruption of the external carapace and exposure of the hot inner core, (*iii*) partial collapse of the dome and pyroclastic flows, (*iv*) higher temperature degassing within a permeable dome, (*v*) cracks and fractures exposing hotter material. Therefore, the basic equation *higher thermal anomalies = higher discharging/extrusive rates* at lava domes is not as straightforward as in the case of lava flows (Werner et al., 2017). Similar uncertainties can arise when a magma body at some depth but lacking a direct exposure at the surface, produces small and relatively cold thermal anomalies (i.e., fumaroles), which remains a challenging task to detect due to a cooler and smaller thermal signal if compared to lava flows (Laiolo et al., 2017). Moreover, changes in the distribution and intensity of thermal anomalies can also precede volcanic eruptions or changes in eruptive style (Thiele et al., 2017). So, even though thermal satellite remote sensing of volcanic activity has benefited from significant developments, the thermal signature associated with different volcanic phenomena brings information about the source processes, which must be interpreted accurately considering the appropriate volcanic context.

Here, we investigate the thermal signatures of lava-dome forming eruptions, taking some volcanoes as case studies that have recently shown remarkable volcanic activity: Láscar (Chile, Global Volcanism Program, 2013a), Sabancaya (Perù, Global Volcanism Program, 2013b), and Shiveluch (Russia, Global Volcanism Program, 2013c). We focused our attention on these three volcanoes, which have shown different processes in their recent eruptions in the range of lava dome activity, spanning from episodes of lava dome extrusion and destruction to gravity-driven collapses, large explosions, and cyclicities in explosivity. We apply a thermal-based approach employing satellite data, exploring the different features of thermal signals related to the ongoing volcanic processes, which can be declined into geochemical (i.e., degassing), magmatic (extrusion and explosive events), or structural (collapses, morphological changes) processes. In each of these case studies, we attempt at defining as much as possible the thermal signatures; as suggested by Oppenheimer et al., 1993b, how does one identify the cause of a thermal anomaly and its attribute to a volcano, and in this case on a lava dome eruption, from satellite data solely? Naturally, knowledge of the volcano's characters aids in interpretation. But there are clues in the remotely sensed data themselves, which are: *i*) the spatial attributes, so size, shape, and distribution of a thermal anomaly; *ii*) the context, such as where an anomaly is located in the volcano geography; *iii*) quantitative or spectral attributes, such as how intense is a thermal anomaly; *iv*) comparison with other a time-series of satellite data, to highlight temporal changes in spatial and spectral attributes of an anomaly that can also provide insights for interpretation (Oppenheimer et al., 1993b). By studying all these attributes, we can likely reach a major understanding of which process functions as the source of a thermal anomaly, that here we can resume like that:

1) magma reaching the surface, emitting heat by its exposing and cooling;
2) magma rising to the surface or to very shallow levels, which loses gas and heat before being recycled by returning to depth (convection);
3) outgassing and high-T fumarolic activity, related to the presence of magma at shallow depths;
4) destruction of the dome / unsealing process that continuously exposes hot material.

We used a long-term multi-satellite method to study the thermal signals at Láscar, Sabancaya, and Shiveluch volcanoes, integrating moderate to high-spatial resolution imagery such as MODIS in the Middle InfraRed analysis, and MSI SENTINEL-2 and OLI LANDSAT-8, in the Short Wave InfraRed, respectively. We explored both quantitively and qualitatively thermal magnitude trends, spatial variations, and visual observations of thermal images to show the

variety of information that analysis of satellite thermal signals can provide for understanding the eruptive and evolutionary mechanisms of a lava dome volcanic phenomena. The final aim is to enhance our understanding of dome-forming volcanoes and to strengthen future monitoring perspectives.

2. CASE STUDIES

In this chapter, we have chosen three case studies of dome-forming eruptions, such as Láscar (Chile), Sabancaya (Perù), and Shiveluch (Russia) volcanoes. The choice fell on these case studies for two main reasons: *i*) these three volcanoes have shown recently, in the last decade, a variety of exciting processes that can serve as a synopsis of some characteristic features and dynamics of lava domes, and on which space-based thermal analysis can be successfully applied to shed light on the underlying volcanic processes; *ii*) availability during the doctoral course to study these volcanoes through collaborations with colleagues, which led to the publication of papers as co-authors on these volcanoes: in particular, Sabancaya and Shiveluch have been subject of peer-reviewed scientific publications in which the Ph.D. candidate has been involved as co-author, while Láscar has been a theme of diverse abstracts and presentations at international conferences. Considering their activity, the Láscar volcano showed in the last decade an outstanding regular thermal cyclicity, not entirely understood, accompanied by Vulcanian explosions poorly constrained; Sabancaya volcano has been characterized in the last years by a dome-forming eruption, with the opening of a new conduit and the extrusion of a new dome body; Shiveluch volcano suffered repeated episodes of lava dome growth and destruction, accompanied by large explosions and collapses.

2.1 Láscar

Láscar is a composite andesite-dacitic stratovolcano (23.37°S; 67.73°W) with an altitude of 5592 m a.s.l., the most active of the Central Volcanic Zone (CVZ) in the north of Chile (Figure 1a; Gardeweg et al., 1998; 2011). It is located at the eastern edges of Salar de Atacama Desert, one of the driest areas in the world, with high atmospheric transparency and a sky almost cloudless, optimal for remote sensing observations (Fig. 1b; Bredemeyer et al., 2018). The closest inhabited center to the volcano is Talabre municipality, which is located 17 km west of the volcano, while the bigger town of San Pedro de Atacama is about 70 km far away; the most significant hazard is represented by ash falling dozens to hundreds of kilometers away (Glaze & Self, 1991). The Láscar volcanic edifice comprises two truncated western and eastern cones, hosting five aligned nested craters, where the deepest and central crater (800 m wide, 400 m deep) is the only current active vent (Fig. 1c/d; Gardeweg et al., 2011). The main magma

chamber is hypothesized to be around 10 – 17 km beneath the edifice (González et al., 2015), while an efficient hydrothermal system, feeding fumaroles in the active crater and influencing ascending of deep fluids, is assumed to be in the first 2-3 km of depth (Tassi et al., 2009). The present-day activity mainly consists of permanent fumarolic releases feeding a permanent gas plume and minor explosive events, often accompanied by ash emissions (Gardeweg et al., 1998; 2011). These frequent minor explosive eruptions (with Volcanic Explosivity Indexes 1–3; Siebert et al., 2011) occur on average every 2–3 years, with half of them during the springtime (Gaete et al., 2020). The last more energetic eruption occurred in April 1993, when a subplinian eruption (VEI 4) produced an eruptive column up to 25 km, and pyroclastic flow extended up to 8 km (Denniss et al., 1998). After the 1993 eruption, a new dome with an andesitic–dacitic composition grew inside the crater (González-Ferrán, 1995). This eruption was interpreted as the peak of a multiyear cyclicity of dome construction-destruction processes, started in 1984: each of these cycles, four in total, produced a dome extrusion accompanied by intense degassing, followed by subsidence into the conduit of both the dome and the crater floor, progressive inhibition of gas loss and pressure increase triggering explosive events (mainly Vulcanian eruptions; Matthews et al., 1997). This proposed theoretical model is the primary framework for interpreting the various evolutionary cycles of Láscar's dome.

Several studies reported a peculiar thermal behavior of Láscar with a short-term reduction of thermal emission before explosions, as numerous events in the last 40 years ca. showed, including the VEI 4 explosion of April 1993, suggesting the interpretation of thermal emissions as a precursor of the Láscar explosivity (Oppenheimer et al., 1993a; Matthews et al., 1997; Wooster & Rothery 1997; Wooster, 2001; González et al., 2015; Gaete et al., 2020). Moreover, according to several authors, the heat source is located mainly at the bottom of the active crater, where extensive fumarolic areas, having an average temperature estimated between 300 °C and 600 °C, have been observed (Francis & Rothery, 1987; Glaze et al., 1989; Oppenheimer et al., 1993a; Wooster & Rothery, 1997; Tassi et al., 2009; OVDAS, 2013b; González et al., 2015; Gaete et al., 2020)

Although between 1993 and 2015 at least 11 phreatic-to-Vulcanian eruptions have been recorded, Láscar's behavior has been less regularly studied and monitored in the last decades and after the 1993 eruption (Aguliera et al., 2006; Gaete et al., 2020). These common explosions usually occur without any clear precursor signs and have been poorly studied, leading to insufficient knowledge about their mechanisms (Gaete et al., 2020). The volcano's remoteness partly explain the lack of volcanological investigations and a proper monitoring network

installed (Tassi et al., 2009), even if Láscar enjoys a discrete influx of tourists (Erfurt-Cooper, 2014). Fortunately, since the end of 2010, a volcano monitoring network has been gradually arranged, providing a reliable geophysical and geochemical database, which allows more detailed monitoring actions (Gaete et al., 2020).

The last two main explosive events publicly reported were observed during April 2013, with an emission of a gray ash plume up to 320 meters above the crater preceded by days of crater glowing (VEI 1, OVDAS, 2013b), and in October 2015, when a 2.5 km greyish plume was emitted by a steam-driven explosion (VEI 2), associated with various seismicity and anticipated by a reduction in thermal emissions (Gaete et al., 2020; OVDAS, 2015).

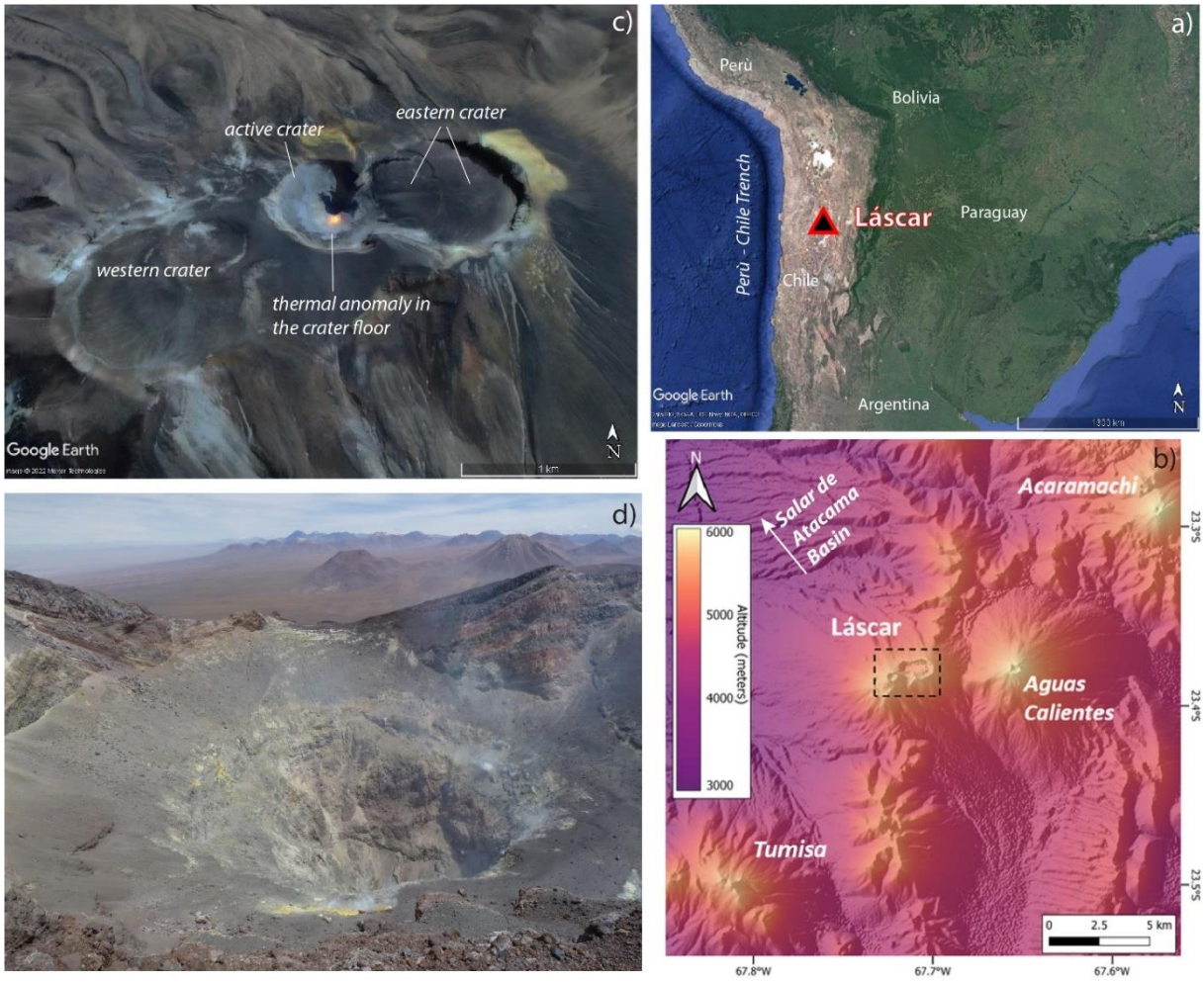

Figure 1 *– Láscar volcano localization (a). DEM of Láscar volcanic region; the black dotted box bounds the volcano's summit area (b). Summit area of Láscar, projection of MSI Sentinel 2 image (bands 12 11 8a, SWIR) over Google Earth terrain (c). Photography of Láscar active crater (view from SW), taken in January 2019, courtesy of Stefan Bredemeyer (d).*

2.2 Sabancaya

Sabancaya (15°47'S; 71°51'W; 5876 m a.s.l.) is a dacite to andesite stratovolcano in the south of Peru, located in the Central Volcanic Zone (CVZ) of Andes originated by the subduction of

the Nazca under the South American Plates (Figure 2a; Jay et al., 2015; Coppola et al., 2022a). It is located 75 km NW of Arequipa city and is considered the second most active volcano in Peru after Ubinas (INGEMMET, 2019). Eruptions present a hazard to the surrounding area through ashfall and possible contamination of the drinkable water supply (Rankin, 2012). The volcano is constituted by a succession of pyroclastic deposits and lava flows. It is the youngest of three edifices in a volcanic complex, with Hualca Hualca to the north and Ampato to the south (Fig. 2b; Jay et al., 2015; Samaniego et al., 2016). An active crater of 350 meters ca. in diameter at the top of the edifice is responsible for the Holocene eruptive activity characterizing the volcano. The eruptive history of Sabancaya has been punctuated by violent eruptions, mingled by periods of repose lasting years to centuries (Samaniego et al., 2016). The volcanic products petrochemically range from andesite to dacite (Gerbe & Thouret, 2004; Samaniego et al., 2016). Studies (Gerbe & Thouret, 2004, Jay et al., 2015, Boixart et al., 2020, MacQueen et al., 2020) suggest that the main magmatic reservoir is supplied by andesitic magma and is located not under the Sabancaya volcanic edifice but displaced 7 km NE under the Hualca Hualca volcano, at ca. 13 km depth. Nevertheless, during eruptions, a dacitic magma chamber under Sabancaya summit at 6 km depth is temporarily tapped and fed by the arrival of more mafic magmatic components from depth (Gerbe & Thouret, 2004). The thermal anomalies and the continuously elevated degassing is thought to be caused by heat and magmatic gases traveling from the dacitic chamber along permeable pathways inside the volcanic conduit (Moussalam et al., 2017; MacQueen et al., 2020).

After about 200 years of quiescence, Sabancaya entered a new eruptive phase in 1988 to 1997 (Global Volcanism Program, 1988; Coppola et al., 2022a). This eruptive phase was characterized by Vulcanian explosions (VEI 1-2) and small eruptive columns (5-7 km in height; Fig. 2c; Gerbe & Thouret, 2004). A gradual decrease in the activity was observed with a magma production rate of 0.001–0.01 km^3 per year. Notably, an open crater in the summit area was observed in this period, but no evidence of lava dome extrusion was noted (Gerbe & Thouret, 2004).

After a new long period of quiescence that lasted 15 years, fumarolic activity resumed in late 2012, accompanied by an increase in seismic and deformation activity (Jay et al., 2015, Boixart et al., 2020, Kern et al., 2017; MacQueen et al., 2020). Phreatic eruptions occurred in August 2014 and persistent degassing from the main crater, often producing whitish plumes up to 1500 meters above the vent, has been observed since June 2014 (Moussallam et al., 2017). In November 2016, eruptive activity dramatically increased, firstly changing from gas to ash-rich

plume emissions, then with the production of a series of Vulcanian explosions (VEI 2-3), signing the beginning of a new eruptive phase on November 6, 2016 (MacQueen et al., 2020), still ongoing at the time of writing. This change in activity was accompanied by a change in the thermal output, with thermal satellite measurements indicating high-temperature anomalies (Reath et al., 2019); the explosive eruption opened the magma path and led the magma to arrive at the surface, producing evident and persistent thermal anomalies (Coppola et al., 2022a). This new phase was followed by the extrusion of the first lava dome visible in the main crater in more than 300 years (Fig. 2c; Coppola et al., 2022a).

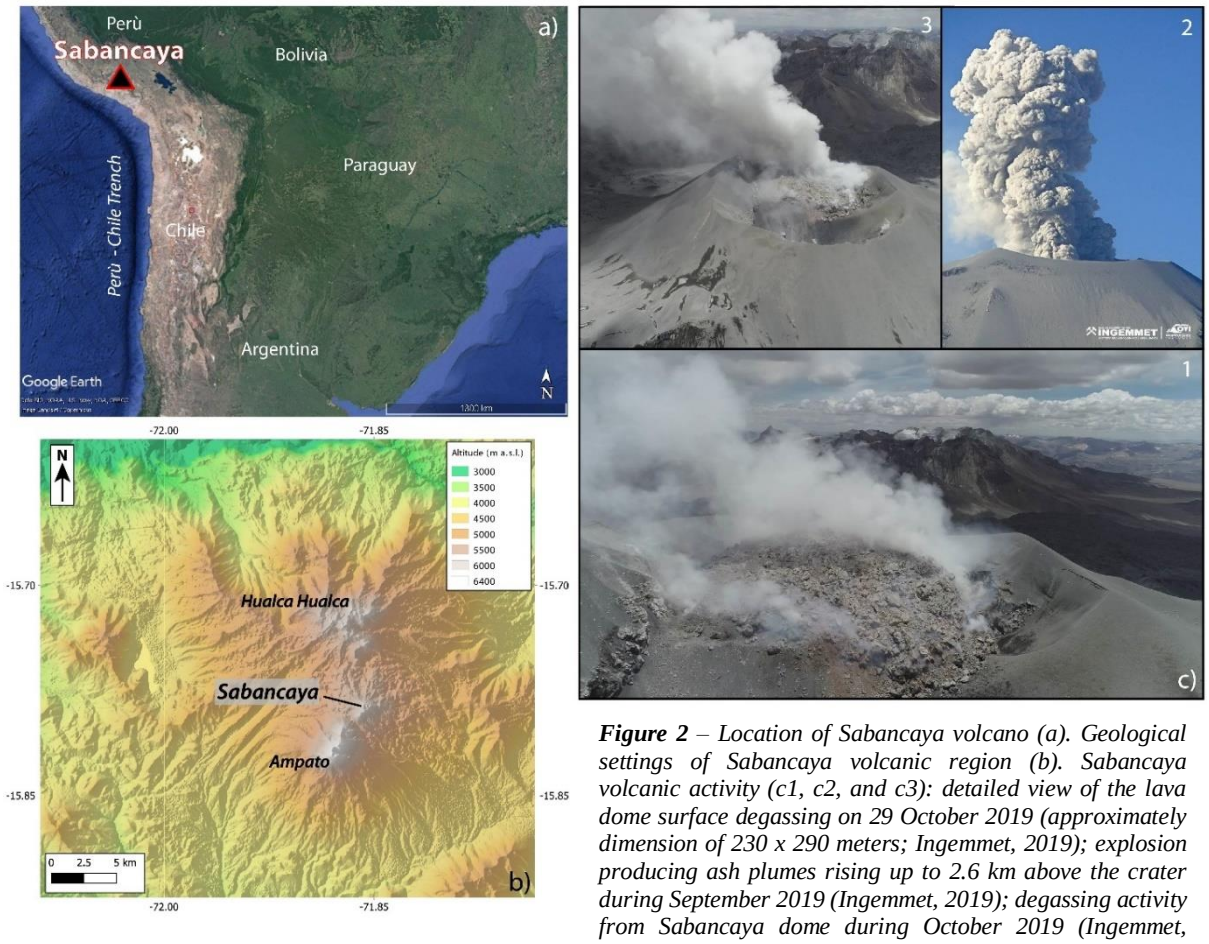

Figure 2 *– Location of Sabancaya volcano (a). Geological settings of Sabancaya volcanic region (b). Sabancaya volcanic activity (c1, c2, and c3): detailed view of the lava dome surface degassing on 29 October 2019 (approximately dimension of 230 x 290 meters; Ingemmet, 2019); explosion producing ash plumes rising up to 2.6 km above the crater during September 2019 (Ingemmet, 2019); degassing activity from Sabancaya dome during October 2019 (Ingemmet, 2019).*

2.3 Shiveluch

Shiveluch volcano (or more precisely, the current active cone named Young Shiveluch or Molodoy Shiveluch; 56°38′10″N, 161°18′54″E; 2763 meters of elevation) is the most active and hazardous andesitic volcano in the Kamchatka Peninsula, Russia (Figure 3a; Shevchenko et al., 2015). It is located in the northern part of the Central Kamchatka Depression (CKD), at the junction of the Aleutian and Kuril Kamchatka arcs, northern to the Klyuchevskaya volcanic group (KVG), and possibly associated with a structural regional trend SW-NE directed (Fig. 3a; Koulakov et al., 2020). Shiveluch has been very active during the Holocene, with tens of

tephra fall deposits identified, several lava andesitic dome extrusions, and signs of edifice collapse producing debris avalanches (Dirksen et al., 2006). Recently, a new stage of activity started in 1964 and was followed by three main episodes of lava dome extrusion until the present (Fig. 3b; Dirksen et al., 2006). The event that occurred in November 1964 (Fig. 3c; see Belousov, 1995) resulted in a lava dome failure, which led to the formation of a collapse caldera with an active northern part and an opening to SSW, producing a vast debris-avalanche deposit covering ca. 100 km^2, and a Plinian eruption triggered by decompression after the collapse (Shevchenko et al., 2021 and references therein).

Since August 1980, the growth of a new dome was observed inside the amphitheater, often punctuated by large explosions producing ash plumes up to 10 km and partial collapses of the dome (Dvigalo et al., 2011; Ozerov et al., 2020). The growth of the dome, composed of dacite with ~64% SiO_2 (Gorbarch, 2006), is distinguished into three main periods, during 1980-1918 and 1993-1995, with an endogenous evolution (Melekestsev et al., 2004), and 2001-present, which shifted into an exogenous growth mechanism (Shevchenko et al., 2015). The beginning of the volcano's activity and extrusive phase in 1980 seems not to have been preceded by any evident seismic events (Gorelchik et al., 1996). This constructive process was frequently interrupted by destructive events because of the instability of the growing dome, episodic endogenous phases, irregular distribution of extruded lava body, and the occurrence of several explosions (Shevchenko et al., 2015). Two main collapse events happened in 2005 and 2010, leaving scars opened toward SSW and SSE, PDCs deposits extended over ca. 15 km (Fig. 3c; Dvigalo et al., 2011; Ramsey et al., 2012), whose related large paroxysmal explosions produced columns with a height up to 15 km (Ozerov et al., 2020). This combination of explosive–extrusive–effusive behavior continued over the years, with several discrete explosive events; the most relevant occurred during July-October 2013 and in September 2016, hurling ash to ca. 10 km a.s.l. and producing partial collapse and consequent pyroclastic flow extending over 10 km in length (Fig. 3c; Ozerov et al., 2020).

In recent times, during the 2018 – 2019 period, the Kamchatka Volcanic Eruption Response Team (KVERT) (http://www.kscnet.ru/ivs/kvert/index?lang_en; Gordeev & Girina, 2014), which provides information on volcanic activity to international air navigation authorities, reported two-stage of pronounced activity of constructive and destructive episodes at Shiveluch volcano (Fig. 3b), additionally confirmed by seismic evidence reflecting a culminating activity reported by the regional seismic network of the Kamchatka Branch of the Unified Geophysical Service (http://www.emsd.ru; Chebrov et al., 2013).

Despite the recent intense activity, studies of the last dome-forming period of Shiveluch are fragmentary due to the high volcanic risk in case of direct observations and unpredictable activity; since 2008, no direct study has been performed on the lava dome (Shevchenko et al., 2021). In this view, remote sensing techniques are highly appropriate for inspecting the evolution of the Shiveluch dome in detail. Particularly thermal analysis by satellite, with opportune spatial resolution, could decrypt changes in temperature and surface texture, possibly revealing, for example, new additions of lava, changes in the eruptive state, and opening of fractures (Ramsey et al., 2012).

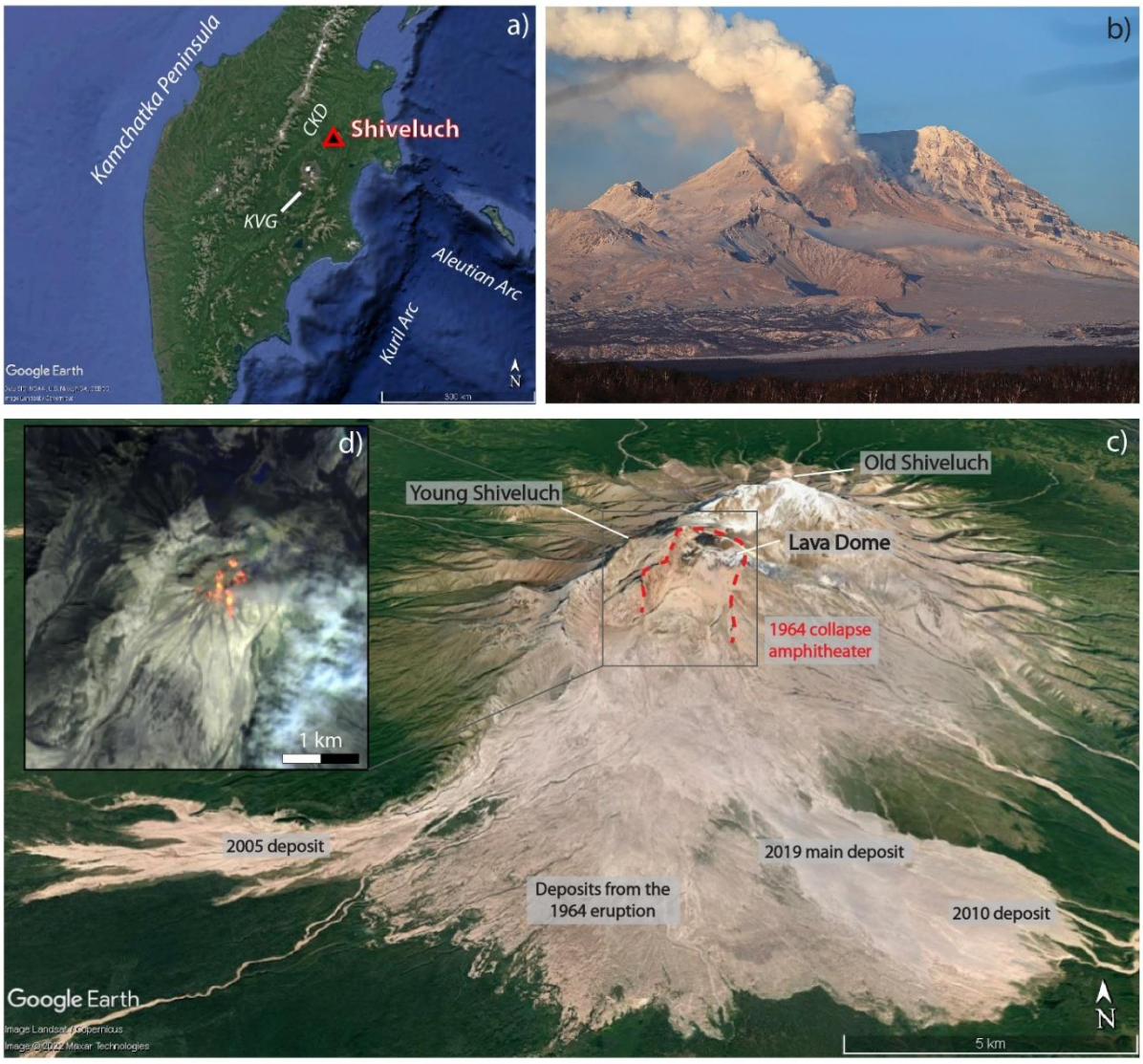

Figure 3 *– Geographic location of Shiveluch volcano (a); in CKD, the Central Kamchatka Depression; in KVG, the Klyuchevskoy volcanic group. Panoramic photography of Shiveluch volcano activity (from Ozerov et al., 2020, photo courtesy of Yu. Demyanchuk, taken on February 21, 2019; b). The edifice of Shiveluch volcano and its deposits (c); with a red dotted curve line, the 1964 collapse scar is highlighted; at the bottom of the edifice, the different PDC's deposits are signed. A particular of the Shiveluch lava dome in activity by MSI Sentinel-2 image (bands 12 11 8a, SWIR) of July 17, 2019, in which it is possible to observe several thermal anomalies on the top of the dome and a subtle greyish degassing plume (d).*

3. METHODS

To characterize the Láscar, Sabancaya, and Shiveluch volcanic activity from a thermal point of view, we used a combination of different but complementary Infrared satellite-based datasets in diverse periods. These satellites data consist of moderate resolution images such as Moderate Resolution Imaging Spectroradiometer (MODIS) and VIIRS (Visible Infrared Imaging Radiometer Suite) images, and the higher spatial resolution ones such as the Sentinel-2 (S2) Multispectral Instrument (MSI) and the Landsat 8 (L8) Operational Land Imager (OLI) images. The combined thermal datasets allow major hot volcanic thermal processes and their effects to be tracked. Following, the spans of studying are briefly explained, and the characteristics of thermal imagery and sensors used.

3.1 Time Periods of Investigation

The investigation periods change about different activities recently expressed by the three volcanoes. Notably:

- Láscar activity has been investigated during the period spanning between January 2013 – December 2020, in which the volcano experienced at least two reported explosions (in April 2013 VEI1, and October 2015 VEI 2) and showed regular cycles of rising and decreasing thermal emissions;
- Sabancaya activity has been studied in the period between January 2012 – December 2020, encompassing the reactivation of the volcano during both the unrest (2012-2016) and eruptive (2016-2020) phases;
- Shiveluch activity evolution was explored during January 2018 – December 2019, when a new extrusive phase began in late 2018, followed by a new extrusive phase of the lava dome and an explosive eruption in 2019, triggering a partial dome collapse.

3.2 Datasets

3.2.1 Volcanic Radiative Power MODIS and VIIRS

MIROVA (Middle InfraRed Observation of Volcanic Activity; www.mirovaweb.it; Coppola et al., 2016a) is an automatic volcano-dedicated hotspot detection system based on the analysis of MODIS satellite images in the Middle InfraRed spectral region (3.9 μm). MODIS sensor is mounted onboard *Terra* and *Aqua* NASA platforms. That imagery dataset, with a spatial resolution of 1 km^2 in the MIR bands and a revisit frequency of up to 4 images per day, is automatically processed by a hybrid algorithm whose main result is the detection and

quantification, via Volcanic Radiative Power (VRP, in Watt) calculation, of the heat flux radiated by exposure of hot lava bodies at targeted volcanoes (Wooster et al., 2003; Coppola et al., 2016a). The same MIROVA algorithm has been recently applied to the VIIRS imagery dataset (Campus et al., 2022), a multispectral sensor mounted onboard the Suomi-NPP (since January 2012), and on the NOAA-20 (since January 2018) satellites (Cao et al., 2017). Both platforms allow full daily coverage of planet Earth due to their polar track. VIIRS sensor hosts different Infrared bands, in MIR and TIR regions, with a spatial resolution of 750 meters (moderate-resolution bands or M-bands) and up to 350 meters in the Imaging bands (or I-bands; see Campus et al., 2022). The better spatial resolution of the VIIRS sensor allows to detect thermal anomalies with lower intensities than those trackable by MODIS (i.e., VRP < 1 MW) but suffers from saturation problems for more intense thermal anomalies (i.e., VRP > 10 MW per pixel); nevertheless, this achievement is a significant improvement to fully detect weak and subtle thermal anomalies, likely associated with high-temperature fumaroles and degassing activity (Campus et al., 2022), and to quantify their released heat flux and detect possible signs of thermal unrest (Coppola et al., 2022b).

Because thermal satellite data may be strongly limited by cloud coverage, such as by geometry of satellite acquisition, VRP data were filtered to include exclusively *i*) nighttime MODIS and VIIRS alerts; *ii*) MODIS and VIIRS image with a Zenith scanning angle < 50°; *iii*) alerts into a 5 km from the volcano summit, always fine to exclude any other unwanted and possible heat source.

3.2.2 Hot Pixels, Area, and spatial distribution of thermal anomalies (SENTINEL 2 & LANDSAT 8)

SENTINEL-2 MultiSpectral Instrument and LANDSAT-8 Operational Land Instrument InfraRed images were used to track thermal anomalies of the different dome case studies. These multispectral sensors, launched in 2015/2017 (S2A&S2B) by ESA and in 2013 (L8) by NASA/USGS, offer a high spatial resolution in the Short Wave InfraRed (SWIR) wavelengths (20 and 30 m/pixel, respectively), with a total revisit time from a few days to weeks, depending on the latitude of the target. These higher spatial resolution thermal satellite datasets have been investigated by applying a novel hotspot detection algorithm based on fixed ratios in the SWIR regions with a contextual threshold derived from a statistical distribution of hotspot pixel clusters (see Chapter 2; Massimetti et al., 2020). The algorithm works on the SWIR Top-Of-Atmosphere (TOA) reflectances for both data products, resampled for L8 data to 20 m spatial

resolution to obtain the same geometric grid for both imageries. The result is the detection of the number of "hot" pixels (S2-L8 number of pixels), where a hotter area is superficially exposed, with an overall estimate of 2–4% false alerts detected (Massimetti et al., 2020). From the number of "hot" pixels is possible to derive: *i*) the Hot Area exposed related to the lava dome inside the craters, simply multiplying the number of hot pixels by their dimension (Fig. 3c); *ii*) the evolution of the dimension of thermal anomaly field and the Thermal Profile, generated by summing and stacking together the Thermal Index of the hot spotted pixels (oriented north-south and west-east) of each S2 and L8 image (see Laiolo et al., 2019; Massimetti et al., 2020; Chapter 3); *iii*) qualitative information by observation of composite RGB SWIR images about localization and features of thermal anomalies over the dome surface and volcanic edifice (Shevchenko et al., 2021).

3.2.3 Limits and Errors

The MODIS, OLI-L8, and MSI-S2 satellite thermal datasets allowed us to derive important quantitative and qualitative information on the thermal activity of Láscar, Sabancaya, and Shiveluch dome-forming volcanoes. However, some satellite-related and methodological limits must be considered. *i*) The cloud coverage, especially in regions characterized by severe meteorological conditions (i.e., Shiveluch in Kamchatka), represents a limitation due to the masking of hotspots. *ii*) The S2 and L8 combined revisit frequency means one image every 2-3 days on average, which is an optimal compromise for the field of infrared satellite sensing (Coppola et al., 2020). Nonetheless, this temporal resolution might mean an undersampling of thermal phenomena for processes tending toward explosive behavior, such as dome-forming eruptions, which may exhibit rapid and short-lived events. *iii*) A spatial resolution of 20-30 m is sufficient to identify major thermal features in space but does not allow a highly detailed analysis of small hot emitting sources (scale of meters) or permit very accurate dimensional measurements. *iv*) For both S2 and L8, SWIR analysis detects only the parts of thermal features with a threshold temperature hotter than approximately 200°C (Massimetti et al., 2020), while all colder emissions are lost; for VRP from MODIS and VIIRS, algorithms detected only portion at magmatic temperatures (T > 500 K), with an error of ca. 30%. *v*) S2 MSI and L8 OLI data are daytime images; thus, the analysis of SWIR reflectances could partially include solar reflection effects, possibly leading to a minor but present enhancement of nonvolcanic thermal features.

4. RESULTS AND DISCUSSION

4.1 Láscar

Even if no evidence of an existing lava dome has been reported after 1993, Láscar was constantly active in the last decades, experiencing persistent degassing and fumarolic activity, emission of thermal anomalies, and several phreatic-to-Vulcanian (Gaete et al., 2020; Layana et al., 2020; Global Volcanism Program, 2017). This is evident if we look at the entire VRP dataset from 2000 to 2021 (Figure 4a). VRP's longtime multiyear dataset indicates a period of moderate (up to 20 MW), variable but persistent thermal activity between 2000 and 2007, where some VEI 2-3 eruptions occurred producing ash plumes up to 11 km and pyroclastic ejection (main explosions occurred: 16th October 2002, phreatic explosion, VEI 2; 4th May 2005, Vulcanian eruption, VEI 3; 18th April 2006, phreatic eruption VEI 2; see Gaete et al., 2020). Afterward, a long period of very weak thermal anomalies spans between October 2007 and March 2013, when no eruptions were recorded (Layana et al., 2020). Starting from April 2013, an evident thermal pattern defining three yearly-long cycles having a similar trend took place (Fig. 4a). Considering the similar trends and the regularity of the three cycles, to exclude any external source due environmental or satellite effects, a comparison with the maximum and environmental Brightness Temperature (BT), showing the seasonal variations of temperature within the summit area of Láscar volcano, is reported in Figure 4b. The pixel-integrated maximum BT at 4 μm, in the peak of MIR wavelengths, if compared with the minimum at BT 12 μm, that is, the minimum environmental temperature at TIR, marks a clear separation from the trend throughout the three VRP cycles, indicating an actual increase in temperature and letting a seasonal effect to be ruled out (cf. Coppola et al., 2016b).

The three thermal cycles observed in the last decade at Láscar are shown in Figure 5. Generally, VRP values show three prominent peaks that reach up to almost 10-15 MW. All cycles are coherent, characterized by a sudden rising phase followed by a slow waning phase generally lasting 2.5-3 years, with VRP values reaching values below 1 MW. Before these explosions, no evident rising in thermal activity is detected by satellite. In this picture, a phase of no thermal anomaly detected by MODIS occurs between February and July 2018, preceding November 2018.

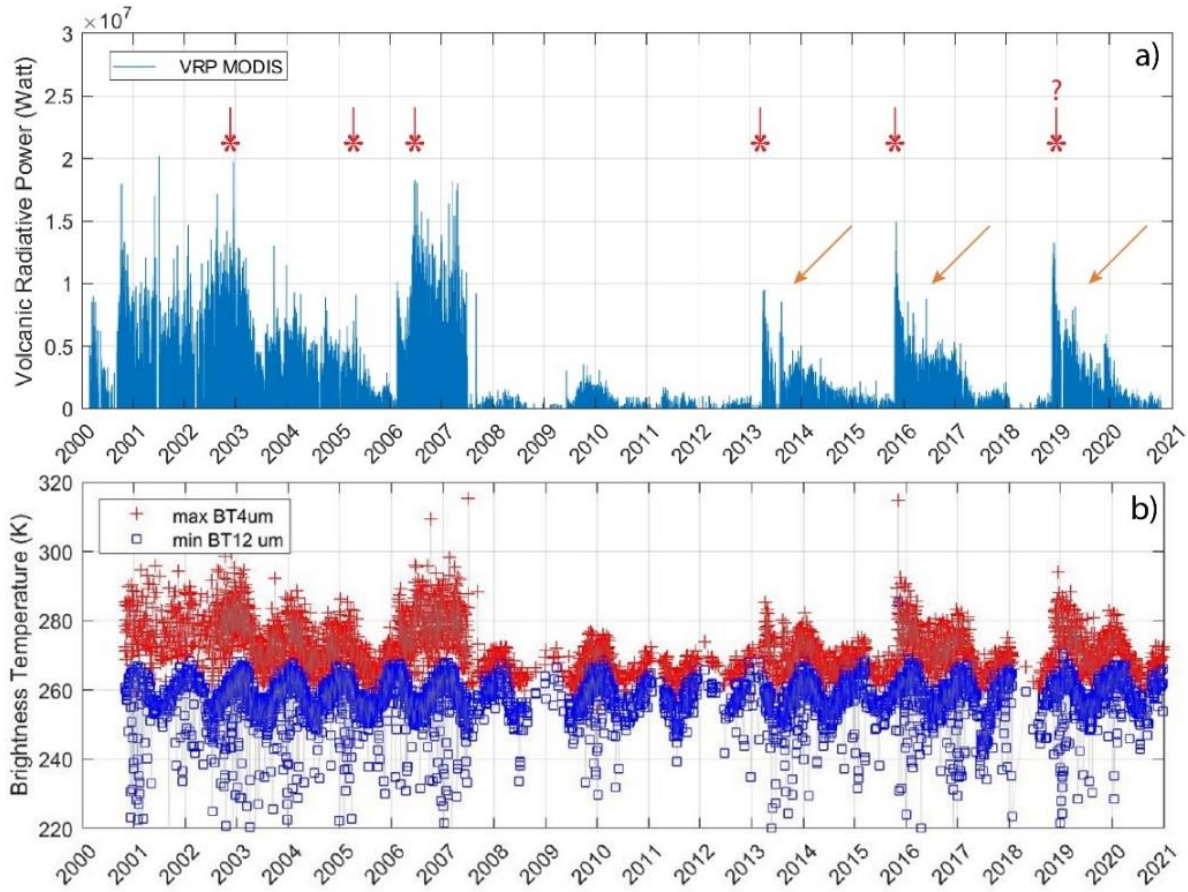

Figure 4 *– (a) Volcanic Radiative Power (VRP) of Láscar volcano, retrieved via the MIROVA algorithm. Red symbols mark the occurrence of reported explosions of VEI 2-3 (Gaete et al., 2020), with a question mark an unreported event. Orange arrows indicate the three thermal cycles. (b) Time series of nighttime brightness temperature (maximum temperature at 4 µm BT4 and minimum temperature at 12 µm BT12) recorded within a box of 5 km × 5 km, centered on Láscar volcano. A perturbation of the seasonal trend can be observed during all higher VRP periods and the three cycles starting in 2013.*

The two first peaks followed the reported explosive events, which occurred respectively on the 3rd of April 2013, with evidence of grey ash plume emission, glowing inside the crater and an increase in seismic LP events (Global Volcanism Program, 2013d; OVDAS, 2013a; González et al., 2016), and on the 30th of October 2015, with an explosion producing a 2.5 km height white-gray plume, a pronounced spike in SO_2 emission, incandescence inside the crater and preceded by increases in SO_2 flux and LP seismic signal (Gaete et al., 2020). The third thermal peak that occurred on the 22nd of November 2018 seems unrelated to any explosion (Layana et al., 2020). However, a report by local the local observatory OVDAS-SERNAGEOMIN observed a sudden intensification in the degassing activity, with a plume reaching 1.1 km above the crater rim and glowing evidence from the crater (OVDAS, 2018), while also other authors indicate a rapid increase in thermal emissions detected by MODIS, VIIRS, and Landsat-8 (Layana et al., 2020; Campus et al., 2022). In any case, a common feature of each stage is that before any explosive event, no rising in thermal activity is detected by the MODIS satellite;

instead, these events trigger and define a marked rise in thermal emissions, suggesting a direct relationship between the explosions and the exposure of heat emitting sources after blasting.

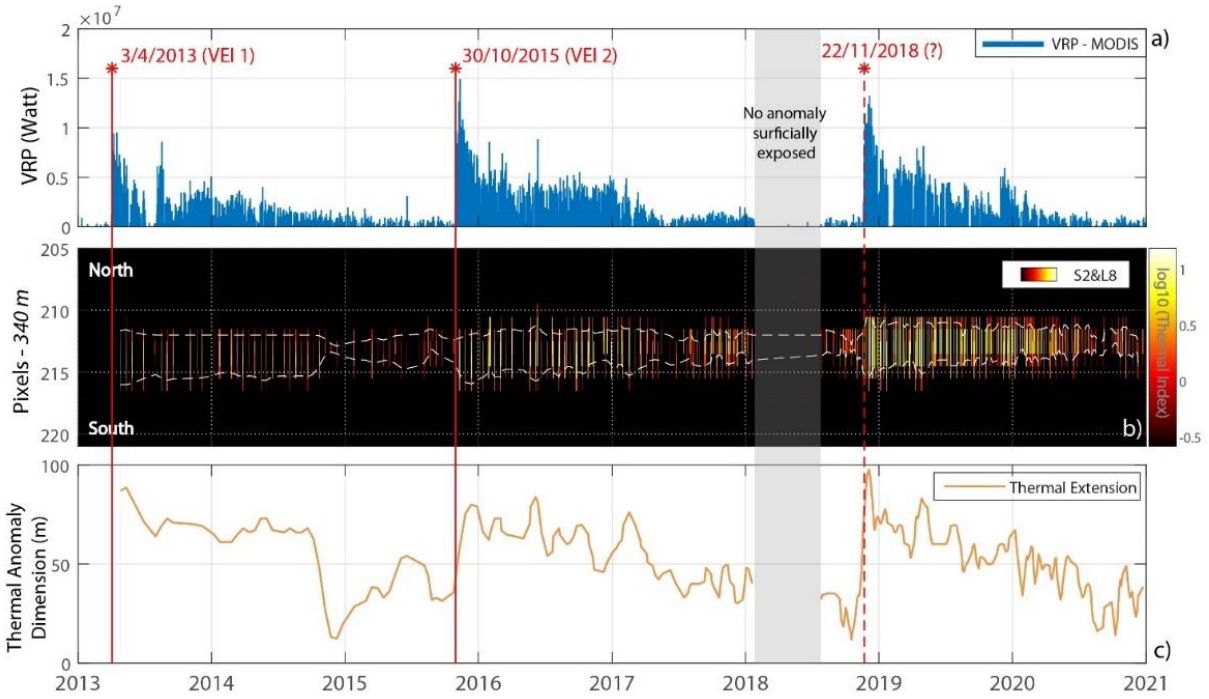

Figure 5 *– 2013 - 2021 Láscar thermal activity. (a) Volcanic Radiative Power (VRP), retrieved via the MIROVA algorithm. (b) Thermal profile of the log10 of Thermal Index parameter, N-S oriented over the Láscar crater (340 meters of dimension); the envelope of the thermal anomaly extension is marked with the white dotted line (c). Size of the thermal anomalies in longitude extension (one size, in meters).*

Meanwhile, thermal signals from high-resolution images (S2&L8) reveal a similar behavior. The Thermal Profile N-S oriented (Fig. 5b) shows cyclic trends in the Thermal Index value, with the three cycles producing an increase in Thermal Index values (colors brighter after VRP peaks) and an enlargement of the hot area exposed inside the Láscar crater, and then decreasing to weaker Thermal Index magnitude (darker colors). The thermal anomalies detected by MSI-S2 and OLI-L8 reflect the increasing and decreasing pattern shown by VRP MODIS data, with a clear association where the more intense the S2&L8 thermal anomaly, the higher the VRP detected. The absence of thermal signals during February – July 2018 is also traceable in the SWIR sensors. Notably, the apparent regularity of the cycles is represented even in the dimension reached by the anomalies: indeed, for each thermal stage, the thermal extension (Fig. 5c, in meters along one orientation) is confined within a maximum of 100 meters of longline extension.

Focusing on the event that occurred in November 2018, high-resolution composite SWIR-RGB images give a qualitative overview of the thermal processes that took place inside the crater

before and after the impulsive event (Fig. 6). Indeed, starting from ca. 20 days before the peak in thermal emission detected by MODIS, a subtle enlargement of the thermal anomaly is observable inside the active crater during November 2018 (Fig. 6a-c). This widening is evident one week before (15 November, Fig. 6d-e), with an expansion toward the southwest portion of the crater, with the anomaly showing still reddish color tones. Between 20 and 25 November (Fig. 6f-g), a sharp increase in dimension and intensity is noticeable, with the thermal anomaly occupying all crater floor with a bright color tone, continuing days later (Fig. 6h).

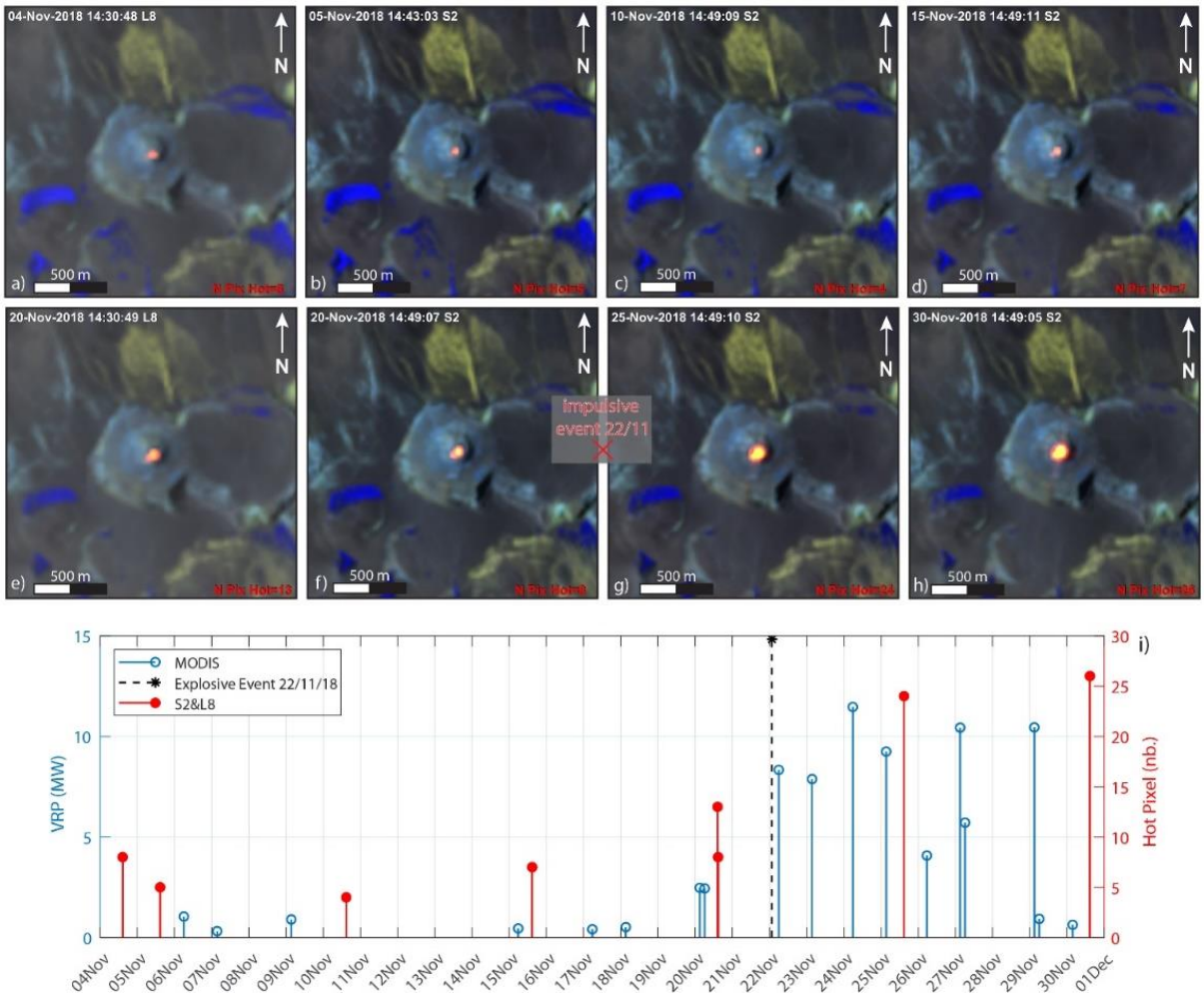

Figure 6 *– Composite RGB cloud-free MSI S2 and OLI L8 satellite images (2x2 km size, a) – h)) to track the evolution of Láscar thermal anomalies during November 2018. Images are obtained with band combination 12-11-8a (SWIR wavelengths at 20 m resolution). i) Timeseries of VRP (in blue, right axis) and Hot Pixels (in red, left axis) focused during November 2018.*

Thermal satellite detection thus allowed us to track and observe a unique cyclic pattern shown by Láscar's activity in the 2013 – 2021 period. In addition, thermal satellite data enable us to gain critical insight into the Láscar's recent volcanic behavior and dynamics preceding explosive events. Firstly, it appears clear how the occurrence of explosions, or more generally impulsive events (considering the uncertainties around the November 2018 episode; Fig. 5a/b),

governs the levels of thermal emissions from the active crater. There is a direct relationship between explosions and heat emission. This dynamic is highlighted by the lack of clear evidence of fresh magma arriving at the surface before explosions, indicating a "passive thermal behavior" of these cycles (see Layana et al., 2020), namely an enhanced thermal signal clearly visible only after the explosive events, without an explicit and appreciable long-time thermal increase before (cf. Fig. 5a with Fig. 6i). The long-term (years) lowering of heat flux preceding explosions is a recurrent and evident feature in the three cycles, that confirm the inhibition of thermal activity at shallow levels; this trait suggested Gaete et al., 2020 to invoke a phreatic character of explosive mechanisms. It is moreover interesting to observe that the second explosion during the investigated period on 30 October 2015 seems to have a more significant effect on "opening" the vent than those that occurred in 2013 and 2018, showing much more persistent thermal anomalies consequently and longer decay "thermal tail", including a phase of no evident thermal emissions. Tracking the three cycles during 2013 - 2021 highlights as the characteristic "thermal decreasing behavior", noticed by several authors at Láscar in the last 40 years of activity (cf. Oppenheimer et al., 1993a; Matthews et al., 1997; Wooster, 2001) is still active, even if there is no longer evidence of growing and emplacement of a lava dome morphology inside the crater.

The combination of MODIS and high-resolution SWIR images not only allows confirmation of thermal cycling otherwise recognized by only one sensor but enriches with important information the shallow system's dynamics of Láscar. Notable, any phase of increased thermal signals consists of an enlargement of thermal anomaly toward SW portions of the crater floor, always confined within 100 meters of extension (Fig. 5c). This pattern seems highly stable for the three cycles investigated. In addition, even if it is true that no explicit and appreciable long-time thermal increase is visible before explosions, focusing on high-resolution S2&L8 SWIR images shows a subtle but still present increase in the number of hot Pixels some days before the November 2018 event (Fig. 6), not visible in the 1 km MIR MODIS spatial resolution, questioning the phreatic explosive mechanism hypothesized by Geate et al. 2020, and suggesting an item for further study with the aim to improving monitoring of these impulsive explosive events.

Thermal satellite datasets alone are not enough to thoroughly investigate and understand the volcanological processes underlying the production of the three well-defined and outstanding thermal cycles shown by Láscar between 2013 - 2021. Nevertheless, some hypotheses may be here briefly proposed, focusing on the cycle patterns, such as the similar behavior of thermal

emissions before and after the beginning of a new cycle. Layana et al., 2020 proposed that this habitual behavior is related to deep processes, where an increase of magma supply triggered a fluid release at the surface, producing a discrete rise in degassing accompanied by minor explosions, or not accompanied at all by explosive activity but only by thermal anomalies. Gaete et al., 2020, suggested the role of precipitation as an external forcing factor for the 30 October 2015 eruption, which influenced the shallow degassing process, inhibiting degassing, resulting in overpressure of the system and consequently in a phreatic blast.

More generally, behavior at Láscar recorded by satellites indicates probably a progressive reduction of hot degassing and fluid movements (decrease in thermal emissions) before blasting, as if over time and at the end of each cycle, the portion of the superficial conduit suffers path sealing effects, and permeability changes or subsidence phenomena related to cooling (as suggested by Matthews et al., 1997 for past cycles at Láscar). This condition may produce inhibition of degassing activity and enhance local overpressure in the shallower portion of the conduit, leading to minor explosions (such as October 2015) or impulsive *"*exhalation" (November 2018), having the effect of "opening" the system and expose superficially hot material, reactivate of cracks and increasing fluids circulation, consequently producing an intense thermal signal after blasting events. Afterward, the cycle starts again with the slow but constant process (2.5 years ca.) of reducing fluids movement and "reclosing" the shallower system, finally inhibiting degassing and thermal anomalies.

Finally, it is important to emphasize the potentialities of the thermal satellite approach for studying a volcano such as Láscar. Multiple IR datasets here allowed us to detect and analyze the sharp deviation from the regular thermal activity of the volcano that occurred on the 22nd of November 2018, which was otherwise not detected by the local monitoring network. Although this volcano is not posing hazards directly to nearby property and human activities, several tourists and researchers arrive often reach its summit area: having a clear understanding of the thermal behavior of these recurrent cycles and the thermal precursors before the explosive events are of great relevance to reduce risks, strengthen monitoring capabilities and hazard assessments.

4.2 Sabancaya

Results and discussions presented here were published in a peer-reviewed paper which I co-authored: Coppola et al., 2022, "Shallow magma convection evidenced by excess degassing and thermal radiation during the dome-forming Sabancaya eruption (2012–2020)", published on Bulletin of Volcanology, 84, 16, https://doi.org/10.1007/s00445-022-01523-1

The analyzed multisensory parameters, comprising VRP from VIIRS-MODIS, Thermal Profile N-S, and hot Area exposed (by S2&L8), during Sabancaya 2012 – 2020 activity (Figure 7) are subdivided into two distinct main periods by the occurrence of a series of Vulcanian explosions, corresponding to the unrest (2014 - 6 November 2016; Figure 8) and the eruptive period (6 November 2016 – 31 December 2020; Figure 9). It is immediately evident that the sequence of explosions marks an evident change in the overall thermal output presented by the different sensors' detection, with persistent thermal anomalies spanning between VRP of 10^6 to 10^8 W and a stable persistence of S2&L8 hot spot detection after November 2016.

Starting from January 2012, thermal anomalies inside the Sabancaya crater started to be detected by VIIRS sensors with heat flux values spanning between 10^4 – 10^5 W(Fig. 7a), with slow but constant growth of VRP, reaching values above 1 MW in August 2014. This increase was pursued by two phreatic explosions on 9 and 25 August 2014 (Fig. 8), preceded by an intensification in fumarolic activity, grey ash emissions, and an increase in events per day of LP and hybrid seismic signals, as reported by the local Observatory (IGP-OVS, 2014; Global Volcanism Program, 2016). During this period, the first thermal anomaly was detected by the MODIS sensor (Fig. 7a). High-resolution images present the first signs of new activity too: indeed, on 26 August 2014, one day after the second phreatic explosion, the OLI Landsat 8 SWIR images detect the first hotspot inside the crater (Fig. 7a/c) and suggest the enlargement of high-temperature zones inside the crater (thermal anomaly has T > 200°C, see Massimetti et al., 2020). Notably, the high-resolution SWIR images show that these precursory thermal anomalies were not associated with the development new hot cracks or hot vents, but rather they were sourced by an almost diffuse uniform circular hot area (ca. 150 m in diameter) located on the southern part of the crater (Fig. 8a).

After the phreatic explosive events, heat flux continued to rise throughout 2015, then slightly decreased in late 2015 – 2016, and this trend is coupled with a minor increase and following reduction in the Hot Area detected by S2&L8 (Fig. 8b/c). This pattern reversed at the beginning of 2016, starting a new phase of increasing thermal flux and expansion of the hot area (Fig. 8b/c). New fumaroles opened external to the crater, located on the northern flank of the Sabancaya edifice. These new fumaroles are not detected as hotspots because their temperature is insufficient to be recognized as "hot" neither by the S2&L8 thermal algorithm nor by MIROVA (Coppola et al., 2022a). Nevertheless, on the high-resolution images, it is possible to observe the appearance and enlargement of these new degassing areas (bright zone in Fig. 8a), absent before late July 2015. An intensification of thermal anomalies accompanied the

northward expansion of thermal anomalies during September and October 2016, reaching the thermal maximum on 3 November with a VRP value higher than 1 MW that preluded the beginning of the eruptive phase.

On November 6, 2016, the eruptive phase was initiated with a series of explosions with columns reaching 1 to 3 km above the crater. The complex dome evolution encompassed the initial vent opening phase, episodes of dome growth and collapse, and recurrent occurrence of discrete Vulcanian explosions (VEI 2; Coppola et al., 2022a). The first weeks consisted of frequent explosions and ash emissions with eruptive columns up to 4.5 km above the crater; this period was purely explosive, no evidence of lava dome presence was observed, as well as thermal emissions remained essentially unchanged (Fig. 9a), possibly because detection was impossible by thick ash clouds.

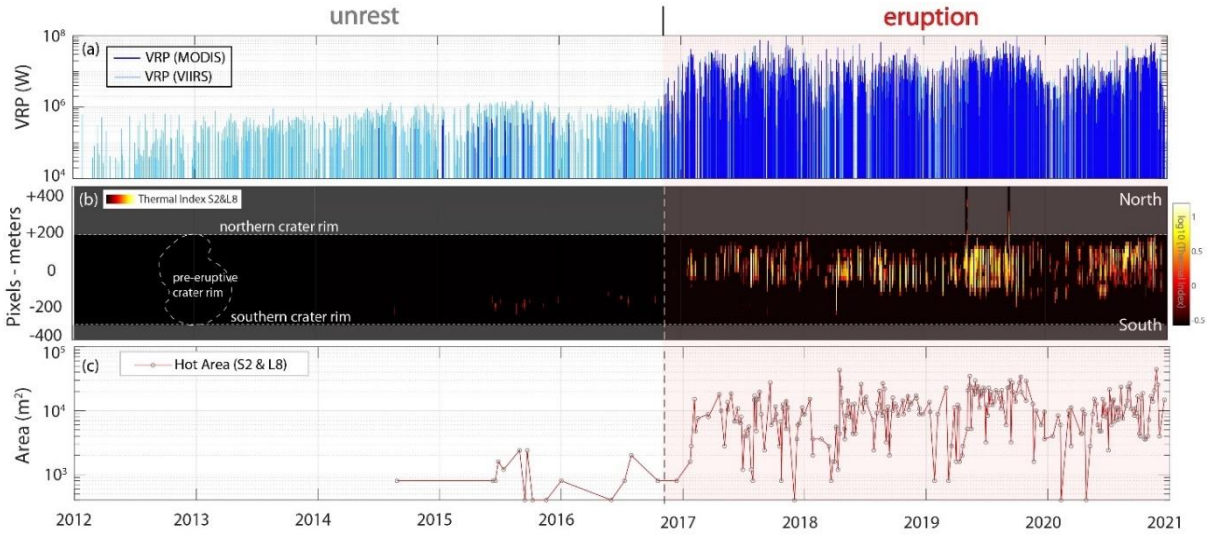

Figure 7 *– Plot of monitoring thermal multisensory satellite data during the unrest and eruptive stages at Sabancaya. (a) Volcanic Radiative Power VRP by MIROVA (Coppola et al., 2016a) retrieved from MODIS (blue) and VIIRS (cyan) sensors; (b) Thermal Profile N-S oriented along the crater area of Thermal Index parameter, from MSI S2 and OLI L8 sensors images; colors from red to bright yellow represent the increasing intensity of heat emission; pre-eruptive crater rim is shown on the left; (c) lava dome "Hot Area" (from S2&L8), obtained from the hot pixels detected by the thermal algorithm of Massimetti et al., 2020.*

Indeed, thermal anomalies started to increase in mid-December 2016 up to 20 MW, suggesting the exposure of hot magma at the surface (Fig. 9a). Consistently, MSI Sentinel-2 image showed on February 4, 2017, a clear thermal fingerprint of the new hot lava dome, of about 85 m in diameter, located in the northern sector of the crater (adjacent to the hot area detected during the unrest phase; Fig. 8a). Following, thermal signals by MODIS constantly accompanied the evolution of the dome (Fig. 9a), indicating a progressive emplacement inside the crater; this is particularly confirmed by the S2&L8 Hot Area enlargement (Fig. 9b), as the heat was sourced

by the whole dome surface, with some fluctuation in terms of location of the anomaly eventually affected by clouds covering. After that, from January 2018, a significant phase of stability of the dome took place, with persistent MODIS anomaly (VRP max 15 MW) and S2&L8 SWIR signals suggesting that the entire dome surface sourced thermal output (Fig. 9a/b), even displacing toward south (on 15 April 2018 an isolated thermal anomaly shows the presence of hot material in the southern part of the crater not occupied by the dome; Fig. 9b). From March 2019, a substantial increase in thermal emissions occurs, with VRP > 20 MW and hot anomalies detected by S2&L8; this phase coincides with reactivation of extrusive and explosive processes (Coppola et al., 2022a), and the rise in the explosive activity is evidenced by the detection of hot material outside the crater, on the northern flank of the volcano, likely related to pyroclastic flows deposition (on 11 May 2019 and 16 September 2019, OLI Landsat 8 images).

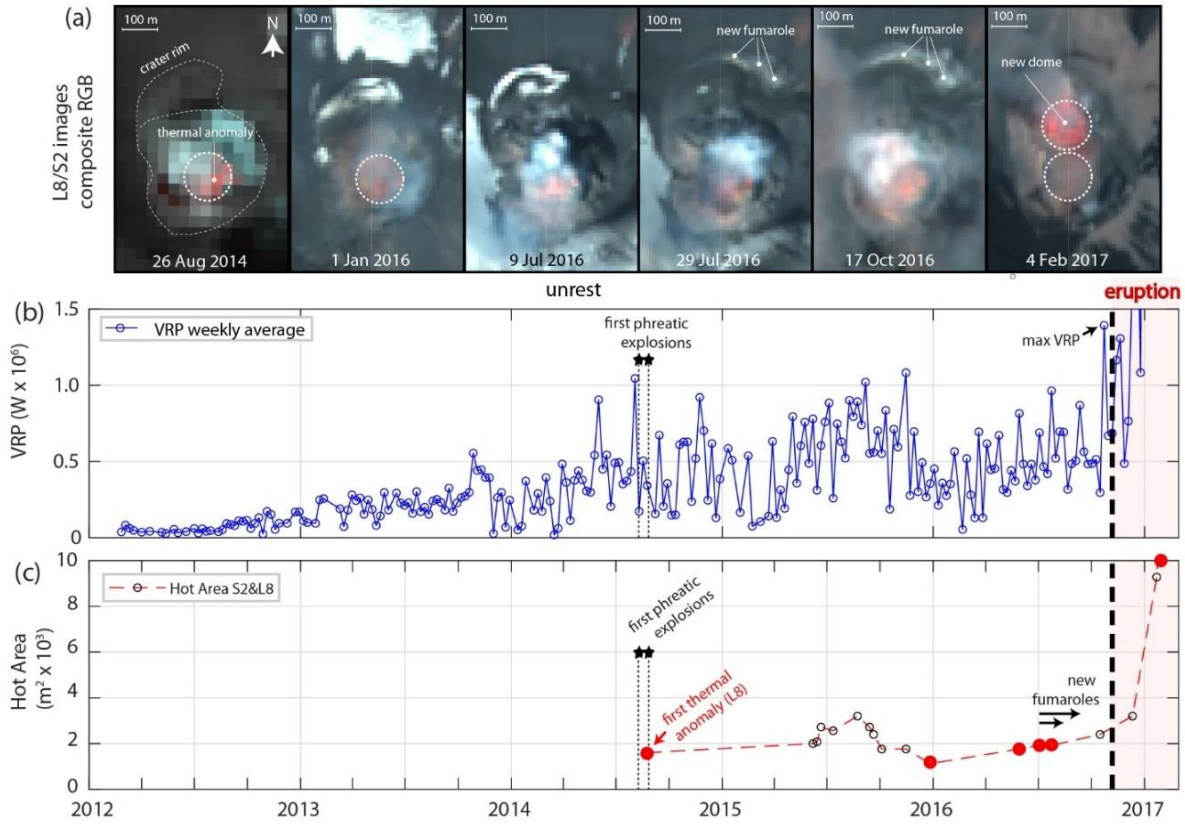

Figure 8 *– Evolution of thermal emissions from IR multiplatform during the 2012-2016 unrest phase at Sabancaya. Composite SWIR RGB OLI Landsat 8 and MSI Sentinel 2 images (band combination 12-11-8a) show the location of thermal anomalies on the southern portion of the crater. Image timings are indicated by red circles in the plot (c). Note the appearance of a new fumarolic zone on the northern crater rim in July and October 2016 images; (b) Time series of VRP (weekly average) from the combination of MODIS and VIIRS sensors; (c) "hot" area inside the crater as measured by MSI Sentinel2 and OLI Landsat8.*

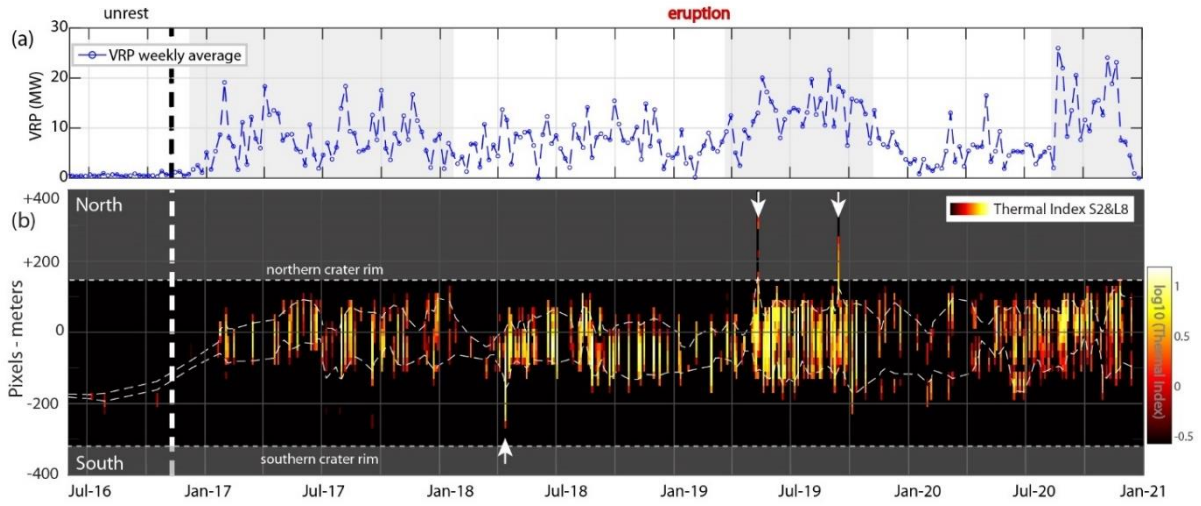

***Figure 9** - Evolution of thermal emissions from IR multiplatform during the 2016 - 2020 eruptive phase at Sabancaya. (a) Time series of VRP (weekly average) from the combination of MODIS and VIIRS sensors; (b Thermal Profile N-S oriented along the crater area of Thermal Index parameter, from MSI S2 and OLI L8 sensors images; colors from red to bright yellow represent the increasing intensity of heat emission; the white dashed line envelops the maximum extension of the thermal anomaly (moving average one month); the white arrows indicate the occurrence of pyroclastic flows outside the crater.*

A change in thermal emissions from previous phases started in November 2019, when the thermal anomalies dropped to a minimum (< 10 MW; Fig. 9a) and appeared spatially distributed at the edges of the dome, along a ring structure surrounding the crater center which seems cold (Fig. 9b), eventually indicating a dome subsidence phase. Anyway, this phase rapidly gives way to a new dome growth stage, with a quick resumption of thermal activity (VRP > 25 MW), and the hot SWIR thermal anomalies shifted northern where the new dome was growing (Fig. 9b).

In this evolution, thermal anomalies associated with the Sabancaya eruptive dynamics during 2012 - 2020 could be produced by a combination of different processes directly related to the emplacement and exposure of new hot magma arrived at the surface and to other heat sources, such as the transport of heat by gases, the explosive activity exposing hot materials of the dome, and shallow magma convection, carrying hot magma under the permeable lava plug (Shinohara, 2008; Coppola et al., 2022a). The jointing of various InfraRed sensors, such as MODIS and MSI-S2/OLI-L8, allows us to understand the underlying volcanic mechanisms.

The low thermal anomalies recorded during the unrest phase (VRP < 10 MW) were sourced by the southern part of the crater area (presumably occupied by the remains of the old conduit feeding the 1988-1997 eruption) and possible by a hot degassing flow through a permeable conduit, triggered by rising magma. The formation of new fumaroles in July 2016 on the northern flank of the crater could be viewed as a sign of ascending magmatic intrusion, progressively opening a new pathway, and moving toward the north to a position adjacent to

the old permeable plug (Coppola et al., 2022a). On the other hand, during the eruptive activity, thermal radiation, testified by variable heat flux (0.5 -25 MW), was sourced by the hot emplacing dome, continuously disrupted by the explosive activity. Its hot core was exposed superficially, producing thermal anomalies as testified by MODIS VRP and S2&L8 Thermal Index intensity and area correlation (Fig. 9a/b). In this phase, a sustained heat supply was necessary to keep the overall thermal output, even after explosions, indicating a convective magmatic process in the shallow portion of the Sabancaya volcanic system (Coppola et al., 2022a). In addition, still within the eruptive phase, the formation of annular thermal anomalies between November 2019 - July 2020, located around the crater's center, is compatible with degassing sources ad edges of the dome. This feature has been observed in other andesite domes dynamics (Oppenheimer et al. 1993b; Matthews et al., 1997; Werner et al., 2017; Walter et al., 2019) and has been interpreted as the consequence of a draining back mechanism of the dome, supporting the idea of a convective magma column at shallow levels (Matthews et al., 1997; Coppola et al., 2022a).

The high-resolution S2&L8 SWIR thermal images, in conjunction with the VRP MODIS data, were here used to: *i*) spatially distinguish the location of thermal anomalies during the unrest and eruptive phases, indicating the opening and emplacement of the new dome from late 2016 - 2017 in a position northern to the first anomalies; *ii*) tracking the evolution of hot area exposed; *iii*) recognize the opening of new fumaroles, indicating a possible new ongoing process (i.e., magmatic intrusion) and the transition to the eruptive phase; *iv*) constrain intensity and extension of the hot source in the different phase of dome evolution during 2017 – 2021, indicating, for example, high explosivity periods with evidence of deposition of hot materials outside the crater area, or stages of reduction of thermal activity and peripheral localization of hotspots during November 2019 – July 2020; *v*) highlight the occurrence of a new dome emplacement northern to the previous location after September 2020.

4.3 Shiveluch

Results and discussions presented here were published in a peer-reviewed paper which I co-authored: Shevchenko et al., 2021, "Constructive and Destructive Processes During the 2018–2019 Eruption Episode at Shiveluch Volcano, Kamchatka, Studied From Satellite and Aerial Data" published on Frontiers in Earth Sciences, 9, 680051, https://doi.org/10.3389/feart.2021.680051

Shiveluch thermal activity detected by satellites during the eruptive period 2018 – 2019 exhibits significant variabilities in terms of heat flux and hot area (Figure 10), and different heat sources

(Figure 11) related to several processes and eruptive products released by the constructive (extrusive dome phase) and destructive (collapse) dynamics began in late 2018 (Shevchenko et al., 2021). It is possible to observe a striking difference in heat flux (VRP MODIS) and the number of Hot Pixels (S2&L8) between 2018 and 2019. The 2018 thermal activity was extremely weak and discontinuous, consisting of low-power anomalies, with VRP values most below 1 MW (Fig. 10a); interestingly, even the thermal signature expressed by SWIR S2 and L8 show very sporadic anomalies detected during this phase on the dome top (Fig. 10b). These values indicate that hot exposed magmatic material was absent and that these anomalies were possibly related to moderate gas and steam (Shevchenko et al., 2021). In late December 2018, an explosive event was identified by KVERT, which issued a Volcano Observatory Notice for Aviation (VONA) on December 30, 2018 (VONA note 20201229/0050Z), producing an ash cloud that rose to 11 km altitude and drifted for 35 km to the north-east from the volcano (http://www.kscnet.ru/ivs/kvert/van/index?type=1&name=Sheveluch). This event marked the beginning of a new eruptive phase, thermally expressed by a sudden peak (VRP > 250 MW) recorded by MODIS, shortly after accompanied by an increase in the thermal area (1115 hot pixels on the 5th of January 2019) by MSI S2 and OLI L8 images. Immediately after that, the thermal flux and the number of hot pixels continued to be very high, with VRP values variating between 300 – 500 MW, with a peak of 750 MW on the 4th of January 2019, and the hot area reaching more than 1000 Hot Pixels (Fig. 10b). Interestingly, starting from mid-November 2018, one-half months before the explosion, S2&L8 imagery presents very weak anomalies.

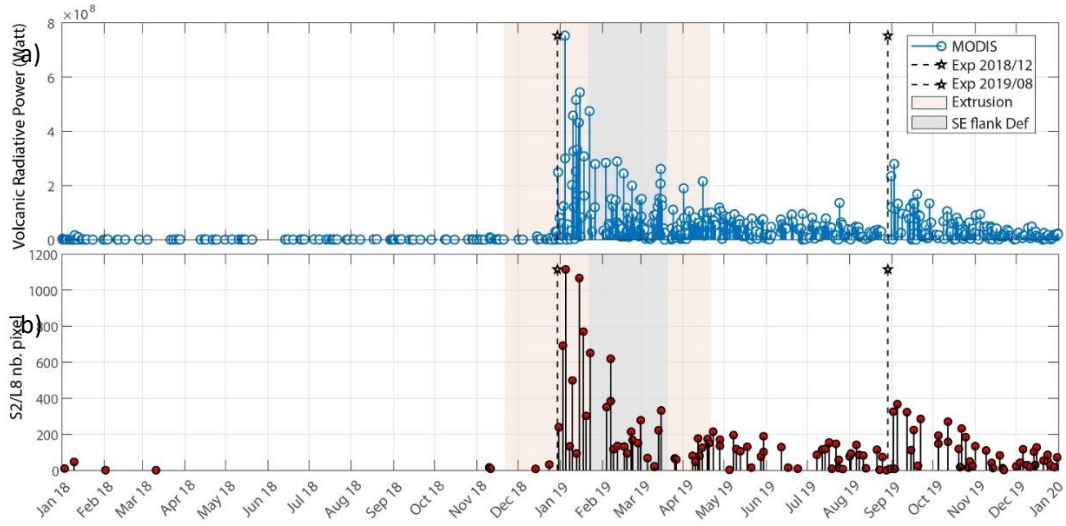

Figure 10 *– Thermal satellite-based linear scale data series at Shiveluch during 2018 – 2019. a) Volcanic Radiative Power (heat flux, in Watt) detected by MODIS via MIROVA algorithm, in blue. b) Number of Hot Pixels by MSI S2 and OLI L8 imagery, detected via Massimetti et al., 2020 algorithm. Black stars and dotted lines mark the occurrence of the two main explosions on December 30, 2018, and August 29, 2019. With pale yellow and gray fields, periods of dome extrusion, and south-east flank deformation of Shiveluch (see Shechenko et al., 2021), respectively.*

Looking at the composite RGB SWIR images (Figure 11), the trend shown by the VRP and Hot Pixels is traceable visually. Intense degassing activity is observable from the dome surface at the end of December 2018, mainly over the central and northern sectors (Fig. 11a). Following images reveal the signs of the explosion reported by KVERT, with an intense explosive and thermal activity sourced by hot ejecta emplacing radially over almost all volcano flanks (Fig. 11b-d). Hot avalanches move along the southern sector, and slumping and partial collapses occur, exposing hot surficial materials. A persistent degassing and white plume emissions are observable on the main crater in the north (Fig. 11d). In this period, a series of cloud-free images from March 2019 allows us to notice some morphological features (Fig. 11e-h). Several glowing hotspots represent a thermally active area in an elongated zone traversing the dome's summit in an SW-NE direction, with most of the hotspots distributed over the eastern dome flank. Small collapses of the lobe's front are observed to trigger hot PDCs that mainly travel towards the south and east (Fig. 11g). Moreover, the presence of a new crater in the northeastern portion is underlined by white steam emissions (Fig. 11h). In this phase, VRP and nb. Hot Pixels signals remain very dense, suggesting an ongoing shallow activity and the production of hot ejecta over the dome edifice, but gradually decrease during 2019, with sporadic peaks likely indicating minor explosive events. This trend was again interrupted on the 29th of August 2019, when a large explosive eruption occurred (VONA note 20190829/0339Z; KVERT, http://www.kscnet.ru/ivs/kvert/van/?n=2019-125), which led to a partial dome collapse (Shevchenko et al., 2021). This event marked a renewed increase in thermal heat flux (VRP > 250 MW) and hot area exposed (up to 370 nb. Hot Pixels). The explosion of August 2019 reshaped the summit morphology and the location of thermal emissions. The main summit crater turns out wider, cold, and filled with snow (Fig. 11i). In contrast, thermal anomalies appear structured around the summit crater and at the eastern edges of the dome, with hot avalanches and pyroclastic flows occurring. The new crater near the northeastern amphitheater rim hosts strong thermal emissions, likely evidence of an explosive event (Fig. 11i/j). Afterward, thermal emissions slowly declined again by the end of 2019 (Fig. 10), with anomalies localized on the eastern flank, mainly on the outer walls of the central crater, and in contrast with the new northern crater appearing cold (Fig. 11 k/l).

The overall thermal output detected by satellites at Shiveluch in the 2018 - 2019 eruptive episode reveals how the thermal emissions suffered abrupt changes after the main explosions and suggested an important role of explosive events. These explosions are inserted in a frame of constructive-destructive behavior that Shiveluch typically exhibits (Shevchenko et al., 2021). The investigated activity was one of the strongest in the recent history of Young Shiveluch

(since 1980) in erupted volume and morphological changes; indeed, a massive lava lobe developed during the extrusive period of December 2018 – April 2019, while the eruptive of 29th August 2019 formed an SW–NE oriented crater and produced a partial collapse of the eastern flank of the dome (Shevchenko et al., 2021). The intense thermal phase detected in late December 2018, and preceded by almost one year of very low thermal emissions, is related to the beginning of the extrusive phase, which started on the 27th of December 2018, when the new lava lobe extruded from the summit crater and spread laterally toward the SW flank (Shevchenko et al., 2021); anyway, the strong thermal rising detected by MODIS and S2&L8 satellites jointly, is instead directly produced by the occurrence of energetic thermal radiating processes such hot avalanches, pyroclastic flows, slumps exposing hot lava portions, new cracks opening and fumarolic activity. This is confirmed by the intensity and locations of thermal anomalies detected by SWIR sensors, visible in the Thermal Index profile (Fig. 12). Here, thermal emissions *i*) show their major intensities (brighter colors) mainly after the two major explosive events of December 2018 and August 2019, and *ii*) shift their main position over time, from northern and western sectors toward southern and eastern ones, indicating a migration of the dome active portion over time, with a reduction of the effects of large thermal anomalies due to hot ejecta deposition. The effects of the August 2019 explosions in reshaping the dome's shallow structural and morphological features is readable by the profile, where a novel hotspot became active to the north (the new crater in Fig. 11g/h). The emissions further concentrated toward east and south, along the SW-NE structural alignment highlighted in Fig. 11, leaving a black portion (i.e., cold summit crater) where before anomalies were present.

The thermal satellite multisensory and multi-spatial approach used gave important insights into understanding the complex constructive and destructive dynamics suffered by the Shiveluch. Indeed, the 2018 – 2019 episode was conceptually interpreted by Shevchenko et al., 2021 as a complex interplay between an extrusive phase that partially blocked the main vent and triggered a cascade of events, consisting of intrusion and lateral deformation of the SE flank, local instability of the dome, growing pressure buildup causing finally the August 2019 eruption and collapse of a portion of the eastern flank.

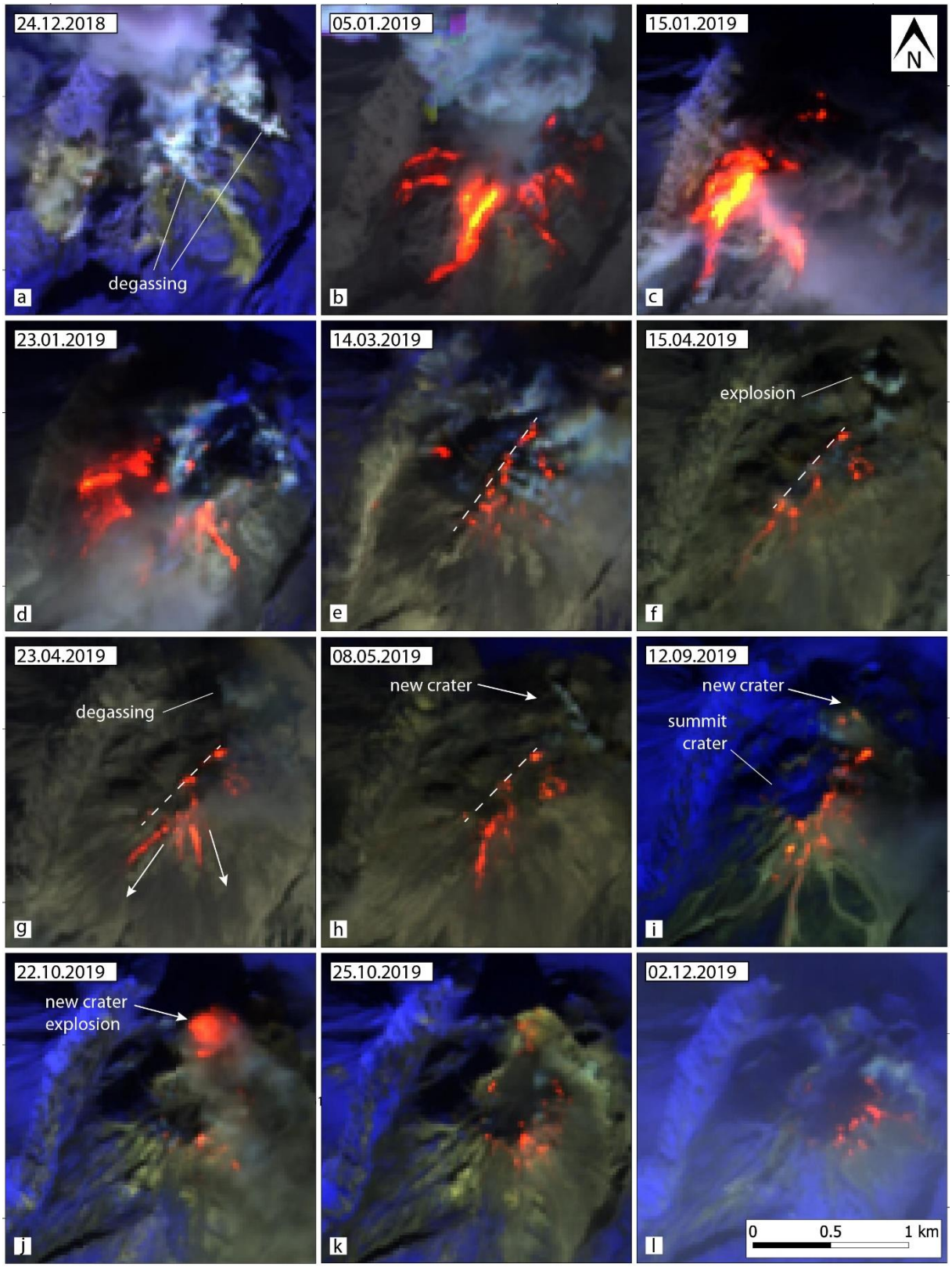

Figure 11 *- Selected composite RGB SWIR thermal imagery from MSI Sentinel-2, showing the evolution of the Shiveluch dome from December 2018 to December 2019. Brownish and grayish colors display cold deposits and bedrock. Blue indicates snow cover. Reddish to yellowish gradients represent hot magmatic ejecta and materials (see the text for details). Images are cropped over the Shiveluch dome top within an area of 2 km × 2 km. White dashed lines indicate morphological features of interest.*

In this picture, thermal space-based analysis allows us to precisely track the activity, highlighting periods of intense explosive behavior and dome extrusion, and indicating how explosion occurrence markedly rules the emission of thermal anomalies. The use of the MODIS sensor by the VRP trend fully prints the occurrence of the two explosions and the different stages of production of the various volcanic products and styles. On the other hand, the S2&L8 high-resolution thermal imagery revealed the presence of an SW-NE oriented (possibly regional) structure, governing the recent evolution of the Shiveluch dome since 2012 (see Shevchenko et al., 2015). Additionally, thermal analysis reveals the formation of a new crater on the dome top after the August 2019 eruption and records the shifting of the dome growth toward new directions, which is of great relevance to monitoring induced gravitational instability phenomena and collapses, and to precisely study where PDCs and hot avalanches deposits.

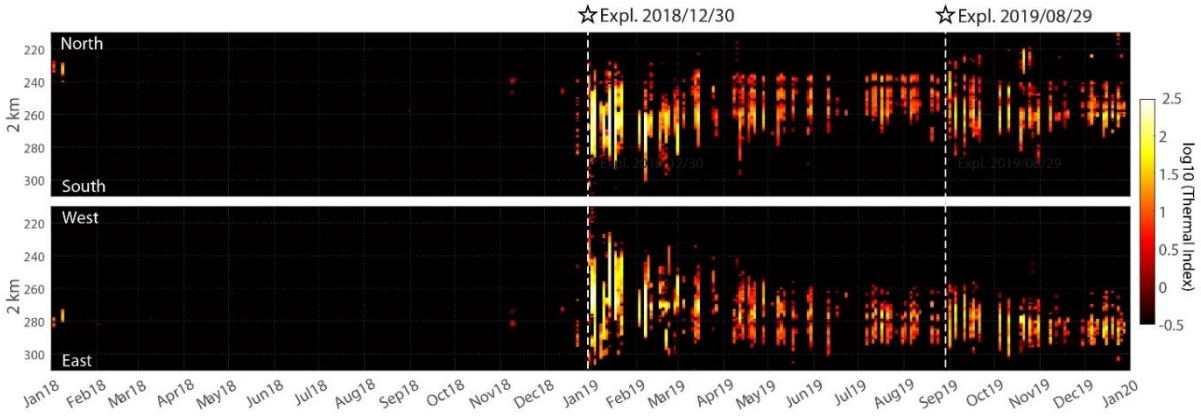

Figure 12 *- Thermal Profile of Thermal Index parameter (N-S and W-E oriented) along the summit area of Shiveluch, from MSI S2 and OLI L8 sensors images; colors from red to bright yellow represent the increasing intensity of heat emission; white dotted lines mark the occurrence of the two main explosions on December 30, 2018, and August 29, 2019.*

5. CONCLUSIONS

Lava dome activity represents one of the most unpredictable and hazardous volcanic phenomena, and their common occurrence worldwide makes an improved understanding of their mechanisms essential to reach, particularly applying a long-term, multiparameter, and multi-spatial analysis able to investigate these peculiar volcanic processes over the most significant number of research perspectives. Lava domes are active thermal bodies; thus, one of the possible approaches for studying their dynamics qualitatively and quantitively is thermal analysis, particularly by satellite methods that make the investigation safe and accessible.

Here, we chose to investigate and characterize the thermal signatures at three examples of active lava domes: the Láscar, Sabancaya, and Shiveluch volcanoes. These three contexts exhibit a

broad spectrum of different and illustrative processes and dynamics in their recent dome-forming eruptions. We studied the outstanding thermal cyclicity shown by Láscar activity during the 2013 – 2021 years ruled by the occurrence of minor explosive events, exploring trends and thermal precursors, defining a similar spatial pattern of the thermal anomalies for the stages, and revealing most likely an explosive event occurred in November 2019 otherwise undetected. Moreover, we hypothesized an underlying mechanism for the observed cyclicity, involving a reduction over time of the conduit permeability shallow portions and fluids circulation, leading to a decrease in thermal anomalies and a following overpressure producing weak explosions, exposing hot materials producing the observed thermal signals. At Sabancaya, the thermal satellite approach allows us to characterize the activity between 2012 – 2020 in two distinct phases of unrest (2012 – 2016) and eruption (2016 – 2020). The two periods have been constrained in terms of thermal emissions (heat flux) released by the fumarolic and degassing (unrest) and extrusive (eruption) activity, respectively. High-resolution images record the shifting of thermal activity in the summit area, indicating the opening of a new conduit for the extrusion of the lava dome and new fumaroles fields, as well as recognizing high explosivity periods producing PDCs outside the craters or stages of reduced thermal emissions. Important structural information has been collected at Shiveluch by thermal analysis of its constructive and destructive (new lobe extrusion and flank deformation *vs.* explosions and collapses) processes during the 2018 – 2019 years. Here the combination of moderate and high-spatial-resolution IR sensors reveals the beginning of a new extrusive phase in late 2018, leading to two important explosions ruling the emission of thermal anomalies and highlighting the presence of an SW-NE structural feature governing the Shiveluch dome evolution.

Joining different but complementary IR sensors such as MODIS, VIIRS, MSI S2, and OLI L8 drastically improve our capability to quantitively and qualitatively characterize thermal activity at lava domes in terms of intensity, spatial distribution, and temporal persistence, reaching significant insights into the sourcing processes of the thermal signals. This information increases our understanding of the eruptive and dynamics of dome-forming eruptions, strengthening future monitoring perspectives and enhancing hazard assessments.

6. BIBLIOGRAPHY

Aiuppa, A., de Moor, J., Arellano, S., et al., 2018. Tracking formation of a lava lake from ground and space: Masaya volcano (Nicaragua), 2014–2017. Geochem. Geophy. Geosy., 19:496–515. https://doi.org/10.1002/2017GC007227

Auker, M.R., Sparks, R.S.J., Siebert, L. et al., 2013. A statistical analysis of the global historical volcanic fatalities record. J Appl. Volcanol. 2, 2. https://doi.org/10.1186/2191-5040-2-2

Belousov, A. B., 1995. The Shiveluch Volcanic Eruption of 12 November 1964-explosive Eruption Provoked by Failure of the Edifice. J. Volcanology Geothermal Res. 66, 357–365. https://doi.org/10.1016/0377-0273(94)00072-O

Boixart, G., Cruz, L.F., Miranda Cruz, R., Euillades, P.A., Euillades, L.D., Battaglia, M., 2020. Source model for Sabancaya volcano constrained by dinsar and GNSS surface Deformation Observation. Remote Sensing 12:1852. https://doi.org/10.3390/rs121 11852

Boudon, G., Balcone-Boissard, H., Villemant, B., Morgan, D.J., 2015. What factors control superficial lava dome explosivity? Sci Rep 5. https://doi.org/10.1038/srep14551

Bredemeyer, S., Ulmer, F. G., Hansteen, T. H., & Walter, T. R., 2018. Radar path delay effects in volcanic gas plumes: the case of Láscar Volcano, Northern Chile. Remote Sensing, 10(10), 1514. https://doi.org/10.3390/rs10101514

Calder, E.S., Luckett, R., Sparks, R.S., Voight, B., 2002. Mechanisms of lava dome instability and generation of rockfalls and pyroclastic flows at Soufrière Hills Volcano, Montserrat. Geological Society, London, Memoirs 21:173–190. https://doi.org/10.1144/gsl.mem.2002.021.01.08

Calder, E.S., Lavallée, Y., Kendrick, J.E., Bernstein, M., 2015. Lava dome eruptions. In: H. Sigurdsson (Editor), The Encyclopedia of Volcanoes (Second Edition). Academic Press, Amsterdam, pp. 343-362. https://doi.org/10.1016/b978-0-12-385938-9.00018-3

Campus, A., Laiolo, M., Massimetti, F., Coppola, D., 2022. The Transition from MODIS to VIIRS for Global Volcano Thermal Monitoring. Sensors, 22, 1713. https://doi.org/10.3390/s22051713

Cao, C., Xiong, X., Wolfe, R., DeLuccia, F., Liu, Q., Blonski, S., Lin, G., Nishihama, M., Pogorzala, D., Oudrari, H., et al., 2017. Visible Infrared Imaging Radiometer Suite (VIIRS) Sensor Data Record (SDR) User's Guide, 2017, Version 1.3; NOAA Technical Report

NESDIS; NESDIS: College Park, MD, USA. https://ncc.nesdis.noaa.gov/documents/documentation/viirs-users-guide-tech-report-142a-v1.3.pdf

Cashman, K.V., 1992. Groundmass crystallization of Mount St. Helens dacite, 1980–1986: a tool for interpreting shallow magmatic processes. Contr. Mineral. and Petrol. 109, 431–449. https://doi.org/10.1007/BF00306547

Chebrov, V.N., Droznin, D.V., Kugaenko, Y.A. et al., 2013. The system of detailed seismological observations in Kamchatka in 2011. J. Volcanolog. Seismol. 7, 16–36. https://doi.org/10.1134/S0742046313010028

Coppola, D., Laiolo, M., Cigolini, C., Delle Donne, D., Ripepe, M., 2016a. Enhanced volcanic hot-spot detection using MODIS IR data: Results from the MIROVA system. Geol. Soc. Lond. Spec. Publ. 2016a, 426, 181–205. https://doi.org/10.1144/SP426.5

Coppola, D., Laiolo, M., Lara, L.E., Cigolini, C., Orozco, G., 2016b. The 2008 "silent" eruption of Nevados de Chillán (Chile) detected fromspace: effusive rates and trends from the MIROVA system. J. Volcanol. Geotherm. Res. 327:322–329. http://dx.doi.org/10.1016/j.jvolgeores.2016.08.016

Coppola, D., Barsotti, S., Cigolini, C., Laiolo, M., Pfeffer, M., Ripepe, M., 2019. Monitoring the time-averaged discharge rates, volumes and emplacement style of large lava flows by using MIROVA system: The case of the 2014-2015 eruption at Holuhraun (Iceland). Ann. Geophys., 61, 52. https://doi.org/10.4401/ag-7749

Coppola, D., Laiolo, M., Cigolini, C., Massimetti, F., Delle Donne, D., Ripepe, M., Arias, H., Barsotti, S., Parra, C.B., Centeno, R.G., Cevuard, S., Chigna, G., Chun, C., Garaebiti, E., González, D., Griswold, J., Juarez, J., Lara, L.E., López, C.M., Macedo, O., Mahinda, C., Ogburn, S., Prambada, O., Ramon, P., Ramos, D., Peltier, A., Saunders, S., de Zeeuw-van Dalfsen, E., Varley, N., William, R., 2020. Thermal remote sensing for global volcano monitoring experiences from the Mirova system. Front Earth Sci 7. https://doi.org/10.3389/feart.2019.00362

Coppola, D., Valade, S., Masias, P. et al., 2022a. Shallow magma convection evidenced by excess degassing and thermal radiation during the dome-forming Sabancaya eruption (2012–2020). Bull Volcanol 84, 16. https://doi.org/10.1007/s00445-022-01523-1

Coppola, D., Laiolo, M., Campus, A., Massimetti, F., 2022b. Thermal unrest of a fumarolic field tracked using VIIRS imaging bands: the case of La Fossa crater (Vulcano Island, Italy), Frontiers in Earth Science, accepted. doi: 10.3389/feart.2022.964372

Costa, A., Melnik, O., Sparks, R.S., Voight, B., 2007. Control of magma flow in dykes on cyclic lava dome extrusion. Geophys Res Lett 34. https://doi.org/10.1029/2006gl027466

Darmawan, H., Walter, T.R., Brotopuspito, K.S., Subandriyo, Nandaka, I.G.M.A., 2018. Morphological and structural changes at the Merapi lava dome monitored in 2012–15 using unmanned aerial vehicles (UAVs). J. Volcanol. Geotherm. Res. 349, 256–267. https://doi.org/10.1016/j.jvolgeores.2017.11.006

Denniss, A. M., Harris, A. J. L., Rothery, D. A., Francis, P. W., Carlton, R. W., 1998. Satellite observations of the April 1993 eruption of Láscar volcano, International Journal of Remote Sensing, 19:5, 801-821, DOI: 10.1080/014311698215739

Dirksen, O., Humphreys, M. C. S., Pletchov, P., Melnik, O., Demyanchuk, Y., Sparks, R. S. J., et al., 2006. The 2001-2004 Dome-Forming Eruption of Shiveluch Volcano, Kamchatka: Observation, Petrological Investigation and Numerical Modelling. J. Volcanology Geothermal Res. 155, 201–226. https://doi.org/10.1016/j.jvolgeores.2006.03.029

Dvigalo, V.N., Svirid, I.Y., Shevchenko, A.V., Sokorenko, A.V., Demyanchuk, Y.V., 2011. "Active Volcanoes of the north Kamchatka as Seen from Aerophotogrammetric Data in 2010," in Proceedings of Regional Conference "Volcanism and Associated Processes": abstracts book, 26–36. (In Russian).

Eichelberger, J., Carrigan, C., Westrich, H. et al., 1986. Non-explosive silicic volcanism. Nature 323, 598–602. https://doi.org/10.1038/323598a0

Erfurt-Cooper, P., 2014. Volcanic Tourist Destinations. Springer Verlag, Berlin, Heidelberg: Berlin. https://doi.org/10.1007/978-3-642-16191-9

Fink, J.H., 1990. Lava Flows and Domes. Springer, Berlin Heidelberg, New York. Fink, J.H., Griffiths. ISBN : 978-3-642-74381-8

Francis, P.W., Rothery, D.A., 1987. Using the Landsat Thematic Mapper to detect and monitor active volcanoes: An example from Láscar volcano, northern Chile. Geology, 15, 614–617. https://doi.org/10.1130/0091-7613(1987)15<614:UTLTMT>2.0.CO;2

Francis, P., Oppenheimer, C., Stevenson, D., 1993. Endogenous growth of persistently active volcanoes. Nature 366, 554–557. https://doi.org/10.1038/366554a0

Furtney, M.A., Pritchard, M.E., Biggs, J., Carn, S.A., Ebmeier, S.K., Jay, J.A., McCormick Kilbride, B.T., Reath, K.A., 2018. Synthesizing multisensor, multi-satellite, multi-decadal datasets for global volcano monitoring. J Volcanol Geoth Res 365:38–56. https://doi.org/10.1016/j.jvolgeores.2018.10.002

Gaete, A., Walter, T.R., Bredemeyer, S., Zimmer, M., Kujawa, C., Franco Marin, L., Bucarey Parra, C., 2020. Processes culminating in the 2015 phreatic explosion at Láscar volcano, Chile, evidenced by multiparametric data. Natural Hazards and Earth System Sciences (NHESS), 20(2), 377-397. https://doi.org/10.5194/nhess-20-377-2020

Gardeweg, M.C., Sparks, R.S.J., Matthews, S.J., 1998. Evolution of Láscar Volcano, Northern Chile, J. Geol. Soc. Lond., 155, 89– 104, https://doi.org/10.1144/gsjgs.155.1.0089

Gardeweg, M., Amigo, A., Matthews, S., Sparks, R., Clavero, J., 2011. Geología del volcán Láscar, Región de Antofagasta, Carta Geológica de Chile, Serie Geología Básica 131, p. 43, 1 mapa escala 1 V 50:000, Servicio Nacional de Geología y Minería, Santiago, 2011.

Gaunt, H.E., Sammonds, P.R., Meredith, P.G. et al., 2016. Effect of temperature on the permeability of lava dome rocks from the 2004–2008 eruption of Mount St. Helens. Bull Volcanol 78, 30. https://doi.org/10.1007/s00445-016-1024-5

Gerbe, M.C., Thouret, J.C., 2004. Role of magma mixing in the petrogenesis of tephra erupted during the 1990–98 explosive activity of Nevado Sabancaya, southern Peru. Bull. Volcanol., 66, 541–561. https://doi.org/10.1007/s00445-004-0340-3

Glaze, L., Francis, P.W., Rothery, D.A., 1989. Measuring thermal budgets of active volcanoes by satellite remote sensing. Nature, 338, 144–146. https://doi.org/10.1038/338144a0

Glaze, L.S., Self, S., 1991. Ashfall dispersal for the 16 September 1986, eruption of Láscar, Chile, calculated by a turbulent diffusion model. Geophys. Res. Lett., 18(7):1237–1240. https://doi.org/10.1029/91GL01501

Global Volcanism Program, 1988. Report on Sabancaya (Peru) (McClelland, L., ed.). Scientific Event Alert Network Bulletin, 136. Smithsonian Institution. https://doi.org/10.5479/si.GVP.SEAN1 98806- 354006

Global Volcanism Program, 2013a. [Láscar (355100)] *in* Volcanoes of the World, v. 4.11.0 (08 Jun 2022). Venzke, E (ed.). Smithsonian Institution. Downloaded 21 Jul 2022 ([https://volcano.si.edu/volcano.cfm?vn=355100]). https://doi.org/10.5479/si.GVP.VOTW4-2013

Global Volcanism Program, 2013b. [Sabancaya (354006)] *in* Volcanoes of the World, v. 4.11.0 (08 Jun 2022). Venzke, E (ed.). Smithsonian Institution. Downloaded 21 Jul 2022 ([https://volcano.si.edu/volcano.cfm?vn=354006]). https://doi.org/10.5479/si.GVP.VOTW4-2013

Global Volcanism Program, 2013c. [Sheveluch (300270)] *in* Volcanoes of the World, v. 4.11.0 (08 Jun 2022). Venzke, E (ed.). Smithsonian Institution. Downloaded 21 Jul 2022 ([https://volcano.si.edu/volcano.cfm?vn=300270]). https://doi.org/10.5479/si.GVP.VOTW4-2013

Global Volcanism Program, 2013d. Report on Láscar (Chile) (Wunderman, R., ed.). Bulletin of the Global Volcanism Network, 38:7. Smithsonian Institution. https://doi.org/10.5479/si.GVP.BGVN201307-355100

Global Volcanism Program, 2016. Report on Sabancaya (Peru) (Crafford, A.E., and Venzke, E., eds.). *Bulletin of the Global Volcanism Network*, 41:5. Smithsonian Institution. https://doi.org/10.5479/si.GVP.BGVN201605-354006

Global Volcanism Program, 2017. Report on Láscar (Chile); Crafford, A.E., Venzke, E., Eds.; Bulletin of the Global Volcanism Network; Smithsonian Institution: Washington, DC, USA, 2017; Volume 42. https://doi.org/10.5479/si.GVP.BGVN201707-355100.

González, C., Inostroza, M., Aguilera, F., González, R., Viramonte, J., Menzies, A., 2015. Heat and mass flux measurements using Landsat images from the 2000-2004 period, Láscar volcano, northern Chile. J. Volcanol. Geotherm. Res., 301, 277–292. https://doi.org/10.1016/j.jvolgeores.2015.05.009

González, D. M., Bataille, K., Eulenfeld, T., Franco, L. E., 2016. Temporal seismic wave velocity variations at Láscar volcano, Andean Geol., 43, 240–246, https://doi.org/10.5027/andgeoV43n2-a05.

González-Ferrán, O.: Volcanes de Chile, Instituto Geografico Militar, Santiago, Chile, 1995.

Gordeev, E.I., Girina, O.A., 2014. Volcanoes and their hazard to aviation. Her. Russ. Acad. Sci. 84, 1–8. https://doi.org/10.1134/S1019331614010079

Gorelchik, V.I., Garbuzova, V.T., Droznin, D.V., et al., 1996. The Shiveluch Volcano: deep structure and prediction of eruptions using detailed seismicity data, 1962–1994, Volcanology and Seismology, 17, no. 4-5, pp. 423–448. https://doi.org/10.1016/S0377-0273(96)00108-4

Hale, A.J., Calder, E.S., Loughlin, S.C., Wadge, G., Ryan, G.A., 2009. Modelling the lava dome extruded at Soufrière Hills Volcano, Montserrat, August 2005–May 2006: Part II: Rockfall activity and talus deformation. J. Volcanology Geothermal Res. 187, 69–84. https://doi.org/10.1016/j.jvolgeores.2009.08.014

Harnett, C.E., Heap, M.J., 2021. Mechanical and topographic factors influencing lava dome growth and collapse. J. Volcanol. Geotherm. Res. 420, 107398. https://doi.org/10.1016/j.jvolgeores.2021.107398

Harris, A., Baloga, S., 2009. Lava discharge rates from satellite-measured heat flux. Geophys. Res. Lett. 36, L19302. https://doi.org/10.1029/2009GL039717

Hutchison, W., Varley, N., Pyle, D.M., Mather, T.A., Stevenson, J. A., 2013. Airborne thermal remote sensing of the Volcán de Colima (Mexico) lava dome from 2007 to 2010. Geological Society, London, Special Publications 380, 203–228, https://doi.org/10.1144/sp380.8

IGP-OVS, 2014. Annual Report, Sabancaya. www.igp.gob.pe/servicios/centro-vulcanologico-nacional/sites/default/files/2020/reporte_sabancaya_201407.pdf

INGEMMET, 2019 - Instituto Geológico, Minero y Metalúrgico, Erupción del volcán Sabancaya 2016-2019: Emplazamiento de domo de lava en el cráter. Región Arequipa, provincia Caylloma, Informe técnico N° A6969, October 2019. https://hdl.handle.net/20.500.12544/2491

Jay, J.A., Delgado, F.J., Torres, J.L., Pritchard, M.E., Macedo, O., Aguilar, V., 2015. Deformation and seismicity near Sabancaya volcano, Southern Peru, from 2002 to 2015. Geophys Res Lett 42:2780–2788. https://doi.org/10.1002/2015GL063589

Koulakov, I., Shapiro, N.M., Sens-Schönfelder, C., Luehr, B.G., Gordeev, E.I., Jakovlev, A., et al., 2020. Mantle and Crustal Sources of Magmatic Activity of Klyuchevskoy and Surrounding Volcanoes in Kamchatka Inferred from Earthquake Tomography. J. Geophys. Res. Solid Earth 125, e2020JB020097. https://doi.org/10.1029/2020JB020097

Kern, C., Masias, P., Apaza, F., Reath, K., Platt, U., 2017. Remote measurement of high preeruptive water vapor emissions at Sabancaya volcano by passive differential optical absorption spectroscopy. Journal Geophysical Research Solid Earth 122:3540–3564. https://doi.org/10.1002/2017JB014020

Krippner, J.B., Belousov, A.B., Belousova, M.G., Ramsey, M. S., 2018. Parametric analysis of lava dome-collapse events and pyroclastic deposits at Shiveluch volcano, Kamchatka, using visible and infrared satellite data. J. Volcanol. Geotherm. Res. 354, 115–129. https://doi.org/10.1016/j.jvolgeores.2018.01.027

Laiolo, M., Coppola, D., Barahona, F., Benítez, J. E., Cigolini, C., Escobar, D., et al., 2017. Evidences of volcanic unrest on high-temperature fumaroles by satellite thermal monitoring: the case of Santa Ana volcano, El Salvador. J. Volcanol. Geotherm. Res. 340, 170–179. https://doi.org/10.1016/j.jvolgeores.2017.04.013

Laiolo, M., Ripepe, M., Cigolini, C., Coppola, D., Della Schiava, M., Genco, R., Innocenti, L., Lacanna, G., Marchetti, E., Massimetti, F., Silengo, M.C., 2019. Space- and Ground-Based Geophysical Data Tracking of Magma Migration in Shallow Feeding System of Mount Etna Volcano. Remote Sens., 11, 1182. https://doi.org/10.3390/rs11101182

Layana, S., Aguilera, F., Rojo, G., Vergara, Á., Salazar, P., Quispe, J., Urra, P., Urrutia, D., 2020. Volcanic Anomalies Monitoring System (VOLCANOMS), a Low-Cost Volcanic Monitoring System Based on Landsat Images. Remote Sens., 12, 1589. https://doi.org/10.3390/rs12101589.

MacQueen, P., Delgado, F., Reath, K.A., Pritchard, M.E., Bagnardi, M., Milillo, P., Lundgren, P.R., Macedo, O., Aguilar, V., Ortega, M., Anccasi, R., Lazarte Zerpa, I.A., Miranda, R., 2020. Volcanotectonic interactions at Sabancaya volcano, peru eruptions, magmatic inflation, moderate earthquakes, and fault creep. https://doi.org/10.1029/2019JB019281

Mania, R., Walter, T. R., Belousova, M., Belousov, A. & Senyukov, S. L., 2019. Deformations and Morphology Changes Associated with the 2016–2017 Eruption Sequence at Bezymianny Volcano, Kamchatka. Remote Sensing 11, 1278, https://doi.org/10.3390/rs11111278

Mania, R., Cesca, S., Walter, T.R., Koulakov, I. Senyukov. S.L., 2021. Inflating Shallow Plumbing System of Bezymianny Volcano, Kamchatka, Studied by InSAR and Seismicity Data Prior to the 20 December 2017 Eruption. Front. Earth Sci. 9:765668. https://doi.org/10.3389/feart.2021.765668

Massimetti, F., Coppola, D., Laiolo, M., Valade, S., Cigolini, C., Ripepe, M., 2020. Volcanic Hot-Spot Detection Using SENTINEL-2: A Comparison with MODIS–MIROVA Thermal Data Series. Remote Sens 12: 820. https://doi.org/10.3390/rs12050820

Matthews, S., Gardeweg, M., Sparks, R., 1997. The 1984 to 1996 cyclic activity of Láscar Volcano, northern Chile: cycles of dome growth, dome subsidence, degassing and explosive eruptions. Bull Volcanol 59, 72–82. https://doi.org/10.1007/s004450050176

Melekestsev, I.V., Dvigalo, V.N., Kirsanova, T.P., Ponomareva, V.V., Pevzner, M.M., 2004. The 300 Years of Kamchatka Volcanoes: the Young Shiveluch. An Analysis of the Dynamics and Impact of Eruptive Activity during the 17–20th Centuries. Part II. 1965–2000. Volcanol. Seism., 1, 5–24.

Melnik, O., Sparks, R.S., 1999. Nonlinear dynamics of lava dome extrusion. Nature 402:37–41. https://doi.org/10.1038/46950

Melnik, O, Sparks, R.S., Costa, A., Barmin, A., 2009. Volcanic Eruptions: Cyclicity During Lava Dome Growth. in Encyclopedia of Complexity and Systems Science, Editor in chief: R.A. Meyers, 10995 pp, vol. 11, pp. 9763– 9784, Springer, Berlin. doi:10.1007/978-0-387-30440-3_578.

Moussallam, Y., Tamburello, G., Peters, N., Apaza, F., Schipper, C.I., Curtis, A., Aiuppa, A., Masias, P., Boichu, M., Bauduin, S., Barnie, T., Bani, P., Giudice, G., Moussallam, M., 2017. Volcanic gas emissions and degassing dynamics at Ubinas and Sabancaya volcanoes; implications for the volatile budget of the central volcanic zone. J Volcanol Geoth Res 343:181–191. https://doi.org/10.1016/j.jvolgeores.2017.06.027

Moussallam, Y., Barnie, T., Amigo, A., Kelfoun, K., Flores, F., Franco, L., Cardona, C., Cordova,L., Toloza, V., 2021. Monitoring and forecasting hazards from a slow growing lava dome using aerial imagery, tri-stereo Pleiades-1A/B imagery and PDC numerical sim-ulation. Earth Planet. Sci. Lett. 564. https://doi.org/10.1016/j.epsl.2021.116906

Newhall, C.G., Melson, W.G., 1983. Explosive activity associated with the growth of volcanic domes. J Volcanol Geoth Res 17:111–131. https://doi.org/10.1016/0377-0273(83)90064-1

Ogburn, S.E., Loughlin, S.C., Calder, E.S., 2015. The association of lava dome growth with major explosive activity (VEI ≥ 4) Dome-Haz, a global dataset. Bull. Volcanol. 77. https://doi.org/10.1007/s00445-015-0919-x

Oppenheimer, C., Francis, P.W., Rothery, D.A., Carlton, R.W., Glaze, L.S., 1993a. Infrared image analysis of volcanic thermal features: Láscar Volcano, Chile, 1984–1992. J. Geophys. Res. Solid Earth, 98, 4269–4286. https://doi.org/10.1029/92JB02134

Oppenheimer, C., Rothery, D.A., Francis, P.W., 1993b. Thermal distributions at fumarole fields - implications for infrared remote-sensing of active volcanos. J. Volcanol. Geotherm. Res. 55 (1–2), 97–115. https://doi.org/10.1016/0377-0273(93)90092-6

OVDAS, O. V. de los A. del S.: Reporte Especial de Actividad Volcánica (REAV) 2013a No. 39 – Región de Antofagasta, Temuco, Servicio Nacional de Geología y Minería (SERNAGEOMIN), Temuco, 05 April 2013. https://rnvv.sernageomin.cl/rnvv/TI_Santiago_prod/reportes_LB/2013/_20130405043026329REAV_N39_Antofagasta_05042013.pdf

OVDAS, O. V. de los A. del S.: Reporte Especial de Actividad Volcánica (REAV) 2013b – Región de Antofagasta, Temuco, Servicio Nacional de Geología y Minería (SERNAGEOMIN), Temuco, 10 April 2013. https://rnvv.sernageomin.cl/rnvv/TI_Santiago_prod/reportes_LB/2013/_20130410030029305REAV_Antofagasta_2013_abril_10.pdf

OVDAS, O. V. de los A. del S.: Reporte Especial de Actividad Volcánica (REAV) 2015 – Región de Antofagasta, Temuco, Servicio Nacional de Geología y Minería (SERNAGEOMIN), Temuco, 30 October 2015. https://rnvv.sernageomin.cl/rnvv/TI_Santiago_prod/reportes_LB/2015/_20151030100023908REAV_Antofagasta_30-10-2015_LC3A1scar20.pdf

OVDAS, O. V. de los A. del S.: Reporte de Actividad Volcánica (RAV) 2018 N° 16 – Región de Antofagasta, Temuco, Servicio Nacional de Geología y Minería (SERNAGEOMIN), Temuco, 7 December 2018.

Ozerov, A.Y., Girina, O.A., Zharinov, N.A. et al., 2020. Eruptions in the Northern Group of Volcanoes, in Kamchatka, during the Early 21st Century. J. Volcanolog. Seismol. 14, 1–17. https://doi.org/10.1134/S0742046320010054

Pallister, J.S., Schneider, D.J., Griswold, J.P., Keeler, R.K., Burton, W.C., Noyles, C., Newhall, C.G., Ratdomopurbo, A., 2013. Merapi 2010 eruption—chronology and extrusion rates monitored with satellite radar and used in eruption forecasting. J. Volcanol. Geotherm. Res. 261, 144–152. https://doi.org/10.1016/j.jvolgeores.2012.07.012

Pallister, J., McNutt, S. R., 2015. "Synthesis of volcano monitoring," in The Encyclopedia of Volcanoes, 2nd Edn, ed. H. Sigurdsson, (Cambridge, MA: Academic Press), 1151–1171. doi: https://doi.org/10.1016/B978-0-12-385938-9.00066-3

Pallister, J., Wessels, R.L., Griswold, J., McCausland, W., Kartadinata, N., Gunawan, H., Budianto, A., Primulyana, S., 2019. Monitoring, forecasting collapse events, and mapping pyroclastic deposits at Sinabung volcano with satellite imagery. J. Volcanol. Geotherm. Res. 382, 149–163. https://doi.org/10.1016/j.jvolgeores.2018.05.012

Ramsey, M. S., Wessels, R. L., Anderson, S. W., 2012. Surface Textures and Dynamics of the 2005 Lava Dome at Shiveluch Volcano, Kamchatka. Geol. Soc. America Bull. 124, 678–689. https://doi.org/10.1130/B30580.1

Rankin, A.J., 2012. Predicted ash hazards from potential eruptions at Nevado Sabancaya, Peru: HYSPLIT and remote sensing (Master's thesis), State University of New York at Buffalo, United States—New York.

Reath, K., Pritchard, M., Poland, M., Delgado, F., Carn, S., Coppola, D., et al., 2019a. Thermal, deformation, and degassing remote sensing time series (CE 2000–2017) at the 47 most active volcanoes in Latin America: Implications for volcanic systems. Journal of Geophysical Research: Solid Earth, 124, 195– 218. https://doi.org/10.1029/2018JB016199

Sahetapy-Engel, S.T., Harris, A.J.L., 2009. Thermal structure and heat loss at the summit crater of an active lava dome. Bulletin of Volcanology 71, 15–28, https://doi.org/10.1007/s00445-008-0204-3

Salzer, J.T., Nikkhoo, M., Walter, T.R., Sudhaus, H., Reyes-Dávila, G., Bretón, M., Arámbula, R., 2014. Satellite radar data reveal short-term pre-explosive displacements and a complex conduit system at Volcán de Colima, Mexico. Front. Earth Sci. 2 (12). https://doi.org/10.3389/feart.2014.00012

Salzer, J.T., Milillo, P., Varley, N., Perissin, D., Pantaleo, M., Walter, T.R., 2017. Evaluating links between deformation, topography and surface temperature at volcanic domes: results from a multi-sensor study at Volcan de Colima, Mexico. Earth Planet. Sci. Lett. 479, 354–365. https://doi.org/10.1016/j.epsl.2017.09.027

Samaniego, P., Rivera, M., Mariño, J., Guillou, H., Liorzou, C., Zerathe, S., Delgado, R., Valderrama P,, Scao, V., 2016. The eruptive chronology of the Ampato-Sabancaya volcanic

COMPLEX (Southern Peru). J. Volcanol. Geoth. Res., 323:110–128. https://doi.org/10.1016/j.jvolg eores.2016.04.038

Sheldrake, T. E., Sparks, R. S. J., Cashman, K. V., Wadge, G. & Aspinall, W. P., 2016. Similarities and differences in the historical records of lava dome-building volcanoes: Implications for understanding magmatic processes and eruption forecasting. Earth-Science Reviews 160, 240–263, https://doi.org/10.1016/j.earscirev.2016.07.013

Shevchenko, A.V., Dvigalo, V.N., Svirid, I.Y., 2015. Airborne Photogrammetry and Geomorphological Analysis of the 2001-2012 Exogenous Dome Growth at Molodoy Shiveluch Volcano, Kamchatka. J. Volcanology Geothermal Res. 304, 94–107. https://doi.org/10.1016/j.jvolgeores.2015.08.013

Shevchenko, A.V., Dvigalo, V.N., Zorn, E.U., Vassileva, M.S., Massimetti, F., Walter, T.R., Svirid, I.Y., Chirkov, SA, Ozerov, A.Y., Tsvetkov, V.A., Borisov, I.A., 2021. Constructive and Destructive Processes During the 2018–2019 Eruption Episode at Shiveluch Volcano, Kamchatka, Studied From Satellite and Aerial Data. Front. Earth Sci. 9:680051. https://doi.org/10.3389/feart.2021.680051

Shinohara, H., 2008. Excess degassing from volcanoes and its role on eruptive and intrusive activity. Rev. Geophys. 46. https://doi.org/10.1029/2007rg000244

Siebert, L., Simkin, T., Kimberly, P., 2011. Volcanoes of the World, 3rd ed.; University of California Press: Berkley, CA, USA. ISBN: 9780520268777. https://www.ucpress.edu/book/9780520268777/volcanoes-of-the-world.

Sparks, R.S.J., 1997. Causes and consequences of pressurisation in lava dome eruptions. Earth Planet. Sci. Lett. 150, 177–189. https://doi.org/10.1016/S0012-821X(97)00109-X

Sparks, R.S.J., Young, S.R., 2002. The eruption of Soufrière Hills volcano, Montserrat (1995-1999): overview of scientific results. In: Druitt TH, Kokelaar BP (eds) The eruption of the Soufrière Hills Volcano, Montserrat from 1995 to 1999. Geological Society, London, Memoir No 21, pp 45-69.

Sparks, R.S.J., Biggs, J., Neuberg, J.W., 2012. Geophysics. Monitoring volcanoes. Science, 335, 1310–1311. https://doi.org/10.1126/science.1219485

Tassi, F., Aguilera, F., Vaselli, O. et al., 2009. The magmatic- and hydrothermal-dominated fumarolic system at the Active Crater of Láscar volcano, northern Chile. Bull Volcanol 71, 171–183. https://doi.org/10.1007/s00445-008-0216-z

Thiele, A.M., Liggett, R.S., Sant, G., Pilon, L., 2017. Simple thermal evaluation of building envelopes containing micro-encapsulated phase change materials using a modified admittance method. Energy Build. 145, 238–250. https://doi.org/10.1016/j.enbuild.2017.03.046

Tsepelev, I., Ismail-Zadeh, A., Melnik, O., 2020. Lava dome morphology inferred from numerical modelling- Geophys. J. Int., 223, 1597–1609, https://doi.org/10.1093/gji/ggaa395

Vaughan, R.G., Hook, S.J., Ramsey, M.S., Ralmuto, V.J., Schneider, D. J., 2005. Monitoring eruptive activity at Mount St. Helens with TIR image data. Geophysical Research Letters, 32, 2–5. https://doi.org/10.1029/2005GL024112

Wadge, G., Ryan, G., Calder, E.S., 2009. Clastic and core lava components of a silicic lava dome. Geology, 37 (6): 551–554. https://doi.org/10.1130/G25747A.1

Walter, T.R., Wang, R., Zimmer, M., Grosser, H., Lühr, B., Ratdomopurbo, A., 2007. Volcanic activity influenced by tectonic earthquakes static and dynamic stress triggering at Mt. Merapi. Geophysical Research Letters 34. https://doi.org/10.1029/2006gl028710

Walter, T.R., Ratdomopurbo, A., Subandriyo, Aisyah, N., Brotopuspito, K.S., Salzer, J., Lühr, B., 2013. Dome growth and coulée spreading controlled by surface morphology, as determined by pixel offsets in photographs of the 2006 Merapi eruption. Journal of Volcanology and Geothermal Research, 261: 121-129. https://doi.org/10.1016/j.jvolgeores.2013.02.004

Walter, T.R., Subandriyo, J., Kirbani, S., Bathke, H., Suryanto, W., Aisyah, N., Darmawan, H., Jousset, P., Luehr, B.G., Dahm, T., 2015. Volcano-tectonic control of Merapi's lava dome splitting: The November 2013 fracture observed from high resolution TerraSAR-X data. Tectonophysics, 639: 23-33. https://doi.org/10.1016/j.tecto.2014.11.007

Walter, T. R., Harnett, C. E., Varley, N., Bracamontes, D. V., Salzer, J., Zorn, E. U., et al., 2019. Imaging the 2013 explosive crater excavation and new dome formation at Volcán de Colima with TerraSAR-X, timelapse cameras and modelling. J. Volcanol. Geother. Res. 369, 224–237. https://doi.org/10.1016/j.jvolgeores.2018.11.016

Wang, T., Poland, M.P., Lu, Z., 2015. Dome growth at Mount Cleveland, Aleutian Arc, quantified by time series TerraSAR-X imagery. Geophysical Research Letters 42(10), 614–610, 621, https://doi.org/10.1002/2015GL066784

Watts, R.B., Herd, R.A., Sparks, R.S.J., Young, S.R., 2002. Growth patterns and emplacement of the andesitic lava dome at Soufrière Hills Volcano, Montserrat. Geological Society, London, Memoirs 21, 115–152, https://doi.org/10.1144/GSL.MEM.2002.021.01.06

Werner, C., Kern, C., Coppola, D., et al., 2017. Magmatic degassing, lava dome extrusion, and explosions from Mount Cleveland volcano, Alaska, 2011–2015: Insight into the continuous nature of volcanic activity over multi-year timescales. J. Volcanol. Geotherm. Res., 337, 98-110. https://doi.org/10.1016/j.jvolgeores.2017.03.001

Witham, C.S., 2005. Volcanic disasters and incidents: A new database. Journal of Volcanology and Geothermal Research 148, 191–233, https://doi.org/10.1016/j.jvolgeores.2005.04.017

Wooster, M., Rothery, D., 1997. Thermal monitoring of Láscar Volcano, Chile, using infrared data from the along-track scanning radiometer: a 1992–1995 time series. Bull Volcanol 58, 566–579. https://doi.org/10.1007/s004450050163

Wooster, M.J., Kaneko, T., Nakada, S., Shimizu, H., 2000. Discrimination of lava dome activity styles using satellite-derived thermal structures. J. Volcanol. Geotherm. Res. 102, 97–118. http://dx.doi.org/10.1016/S0377-0273(00)00183-9.

Wooster, M.J., 2001. Long-term infrared surveillance of Láscar Volcano: Contrasting activity cycles and cooling pyroclastics. Geophys. Res. Lett., 28, 847–850. https://doi.org/10.1029/2000GL011904

Wooster, M.J., Zhukov, B., Oertel, D. 2003. Fire radiative energy for quantitative study of biomass burning: derivation from the BIRD experimental satellite and comparison to MODIS fire products. Remote Sensing of Environments, 86, 83–107. https://doi.org/10.1016/S0034-4257(03)00070-1

Yokoyama, I., 2005. Growth rates of lava domes with respect to viscosity of magmas. Ann. Geophys. 48 (6), 957–971. https://doi.org/10.4401/ag-3246

Zorn, E.U., Le Corvec, N., Varley, N.R., Salzer, J.T., Walter, T.R., Navarro-Ochoa, C., Vargas-Bracamontes, D.M., Thiele, S.T., Arámbula Mendoza, R., 2019. Load stress controls on directional lava dome growth AT VOLCÁN de colima, mexico. Front Earth Sci 7. https://doi.org/10.3389/feart.2019.00084

Zorn, E.U., Walter, T.R., Johnson, J.B. et al., 2020. UAS-based tracking of the Santiaguito Lava Dome, Guatemala. Sci Rep 10, 8644. https://doi.org/10.1038/s41598-020-65386-2

Chapter 5

5. Monitoring applications and implementation of the Mirova system

Abstract

Space-based InfraRed observation enhances volcano surveillance, allowing monitoring of several active volcanoes toward a global strategy. The recent MSI SENTINEL-2 (MSI-S2) and OLI LANDSAT-8 (OLI-L8) SWIR (Short Wave InfraRed) high-spatial resolution (20-30 m/pixel) imagery enrich the quantity and quality of thermal information, particularly if integrated with widely used spatial moderate (1 km) products such as MODIS (Moderate Resolution Imaging Spectroradiometer). This method goes in the direction of implementing monitoring platforms with a multi-sensor approach, providing access to diverse but complementary thermal data. Here we firstly show how the SENTINEL-2 and LANDSAT-8 high-spatial-resolution thermal data have been used in case of eruptive crises, such as the December 2018 Etna and the Stromboli 2019 summer eruptions, to obtain as quickly and safely as possible relevant information to support civil protection agency and local authorities in the hazard assessment and risk management efforts. Following, we summarize the features of the automated monitoring process based on the SWIR SENTINEL-2 and LANDSAT-8 data and the implementations made to the MIROVA thermal global monitoring system based on MODIS-MIR data. These consist of new graphical output representing the last six high-resolution images, a searchable slideshow resuming VRP and the number of Hot Pixels trends, the last SWIR image on Google Earth, and the entire S2 and L8 thermal dataset freely accessible, with quantitative information about the hot area, intensity, and location of the thermal features. Using the SWIR high-spatial-resolution images upgrades the monitoring dissemination actions of MIROVA, adding new sensors with a larger scale of details and making the link between the heat flux and its thermal source visible. This information is accessible to observatories, monitoring centers, and local authorities for monitoring and hazard assessment needs, moving a step toward a modern thermal multisensory volcanic monitoring system.

1. INTRODUCTION

Volcano monitoring consists of the regular and real-time acquisition and processing of different data that portray the behavior of a volcano, with two main functions: *i*) providing basic scientific information to develop the comprehension of volcanic systems; *ii*) detecting any sign of unrest that may prelude an eruption (Pallister & McNutt, 2015; Newhall et al., 2017). These actions are crucial for hazard assessment, eruption forecasting and warnings, and risk mitigation (Tilling, 2008). Tracking volcanic thermal emissions can provide improved insight into volcanic behavior and eruptive scenarios, and represents a key parameter for monitoring applications. This is because variations in thermal features can accompany volcanic eruptions, in relation to changes in gas and ash emissions, lava flows and domes dynamics, fumaroles, and hydrothermal systems, in the temperature of crater lakes (Oppenheimer & Rothery, 1991; Blackett, 2017; Coppola et al., 2020; Poland et al., 2020).

Thermal satellite remote sensing techniques are increasingly used by the volcanological community (Harris, 2013), with the possibility of monitoring the thermal features of hundreds of volcanoes (Way et al., 2022). The development of new sensors for high-temporal coverage and accurate detection algorithms continues to evolve the discipline (Ramsey & Harris, 2013; Coppola et al., 2020). Important information such as detecting precursor anomalies, estimating mass erupted fluxes, and recognizing how a lava flow is evolving, can be assessed from the InfraRed remote sensed data (Harris et al., 2017; Coppola et al., 2020). Moreover, continuous long-term thermal measurements from space let to build a solid knowledge of the thermal state of a volcano and are crucial to define a thermal baseline for the background behavior (Reath et al., 2019). The different volcanic hot-spot detection systems developed in the last decade, working on a specific volcanic region or with a global perspective (Coppola et al., 2020), have different performance capacities concerning the spatial, spectral, and temporal resolutions of the InfraRed (IR) sensor used (Steffke & Harris, 2011; Blackett, 2017).

The MODIS (Moderate Resolution Imaging Spectroradiometer) sensor, with a moderate spatial resolution, data available on a global scale, and acquisitions several times per day, is widely used for monitoring volcanic thermal activity, for example by multiple operational global systems such as MIROVA, MODVOLC, and REALVOLC (see Coppola et al., 2020; Way et al., 2022 and references therein). However, this sensor is not adequate to precisely detect hot features. The question that often arises is: to which process or thermal source is related the thermal anomaly detected by the MODIS sensor at 1 km pixel resolution? Conversely, high-spatial-resolution images (<100m) such as Multispectral Instrument SENTINEL-2 (MSI-S2) and the LANDSAT 8 Operational Land Image (OLI-L8) ones, are critical for precise detection of thermal anomalies, but they provide images with a temporal resolution of several days, too high for near real-time monitoring needs (Blackett, 2017; Poland et al., 2020). Nevertheless, the thermal high-spatial-resolution dataset in the last years expressed all the potential in volcanological studies, providing analysis of thermal and morphometric features of heat sources and facilitating tracking of a series of volcanic processes, including lava flow advancements, lava lake evolution, extrusion of lava domes, fumarolic activity, thermal activity at multiple craters, and rise of magma column in open-vent volcanic systems (see Laiolo et al., 2019; Plank et al., 2019a,b; Marchese et al., 2021; 2022; Coppola et al., 2022). Therefore, even if the temporal-spatial-spectral resolution trade-off dictates several shortcomings, the integration between different sensors' capabilities, combining, for example, moderate to high-spatial-resolution thermal data, is one of the main current goals for volcanic space-based thermal remote sensing (Coppola et al., 2020; Ramsey et al., 2022).

MIROVA (Middle Infrared Observation of Volcanic Activity) is an automatic volcanic hot-spot detection system for thermal anomalies at high temperatures (T > 500K), born at the University of Torino, in collaboration with the LGS group at the University of Firenze and supported by Italian Civil Protection (Coppola et al., 2016). It analyses images by MODIS and uses the MIR (Middle Infrared) to measure the Volcanic Radiative Power (VRP, in Watt), providing near real-time monitoring of about 220 volcanoes (Coppola et al., 2020). These targets were gradually added to the MIROVA list based on scientific interest or following specific cases of need (unrest of a new volcano). MODIS data have been available since March 2000, allowing the investigation of more than 20 years of thermal volcanic activity worldwide, constituting an excellent source of information and allowing multi-decadal analysis of eruptive trends. In addition, compared to other global MODIS-based hotspot detection systems, it is highly efficient in detecting low-power thermal emissions (Coppola et al., 2016; 2020). The system disseminates thermal data mainly through a dedicated website continuously updated (http://www.mirovaweb.it/), with a series of tables and static graphical outputs for any monitored volcano, which are: *i*) the latest 10 MODIS acquisition, *ii*) the VRP time series (Log and Linear scale) in the previous month and year periods of acquisition, iii) the distance from the farthest hot pixel to the summit of the volcano, and *iv*) the last MODIS MIR processed image projected on Google Earth (see Coppola et al., 2020 for details).

Although MIROVA nowadays represents an invaluable instrument for monitoring requests and many volcanological research, some limits must be considered. Firstly, MODIS is at the end of its operativeness (Blackett, 2017); important preliminary results have already been reached to apply the MIROVA algorithm on the VIIRS (Visible Infrared Imaging Radiometer Suite) sensor, which is the ideal substitute for the MODIS in terms of spectral, spatial and revisit frequency (see Campus et al., 2022). Secondly, the coarse MODIS spatial resolution sets limits for detailing the thermal and morphometric features of volcanic heat sources. The spatial resolution of a satellite thermal detection is crucial in volcanic monitoring; it has been proved that the integration of high spatial resolution data in the TIR (Thermal Infrared, i.e., ASTER) as well as in the SWIR (Short Wave Infrared, i.e., MSI-S2 and OLI-L8), dramatically improves the ability to detect smaller or low-intensity anomalies (Reath et al., 2019b; Valade et al., 2019). This means, from an operational point of view, to have higher detection potentialities, tracking thermal precursors with respect to days/months earlier than moderate-resolution systems (see Chapter 2; Massimetti et al., 2020; Reath et al., 2019b). In this regard, the high-spatial-resolution MSI-S2 and OLI-L8 imagery, with a revisit frequency of 2 to 5 days, a spatial resolution of 20-30 meters/pixel in SWIR channels, and almost global coverage, show up as

excellent for retrieving useful spatial information on ongoing eruptive events (Marchese et al., 2019; Layana et al., 2020; Massimetti et al., 2020). The two high-resolution imageries are spectrally and spatially compatible in the SWIR region, allowing them to be used synergically to improve the revisit frequency of acquisitions and strengthen thermal investigations (Massimetti et al., 2020). Therefore, due to the satellite development, the more advanced monitoring requests, and the issues mentioned above, to make MIROVA up to the future global challenges, it has been necessary to update and restructure it as a multi-sensor detection system.

Here, we show a few examples of how the high-resolution SWIR dataset used and investigated in this Thesis has been used for operational support activity to eruptive crises at Stromboli and Etna (Italy) volcanoes during the 3-years Ph.D. course. Then, we explore how this dataset has been inserted inside the MIROVA system, implementing the number of released products, and improving the system's monitoring capabilities. For the first case, through a relationship with the Italian Department of Civil Protection (DPC) and the Laboratorio di Geofisica Sperimentale (LGS) of the University of Firenze, satellite thermal data processed by MIROVA data have been used for years to provide the DPC daily/weekly and monthly reports regarding the activity of Stromboli and Etna (Italy) volcanoes (Coppola et al., 2020). In this framework, the recent development and results achieved by using MSI-S2 and OLI-L8 were taken inside the communication and products furnished to support the risk management actions of DPC, particularly during eruptive crises. Secondly, results achieved by applying the hotspot detection algorithm presented in Chapter 2 have been structured inside the MIROVA architecture with a global monitoring perspective to increase the number of IR sensors used, moving steps toward a multisensory approach, and enlarge the type of thermal measurements and disseminated data.

2. SUPPORTING ERUPTIVE CRISIS MANAGEMENT

2.1 Etna December 2018 Eruption

In December 2018, the Etna volcano (Sicily, Italy) erupted, with a short-lived effusive episode that started on 24 December 2018 and lasted until 27 December. The event was characterized by the opening of an eruptive fissure at the base of the New South-East Crater on the western flank of Valle del Bove (INGV, 2019; Laiolo et al., 2017; Bonforte et al., 2019). The eruption produced gas and ash-rich plumes from summit vents and sustained Strombolian activity from the fissure, feeding small lava flow eastward directing in the Valle del Bove, with a total lava volume of 0.85 Mm^3 (Laiolo et al., 2019). The event was accompanied on 26 December by an Mw 4.9 earthquake with the epicenter between Lavinaio and Viagrande villages (CT), in correspondence with the Fiandaca-Pennisi Fault (Bonforte et al., 2019). The earthquake

affected several buildings and injured people close to the epicentral areas (Laiolo et al., 2019). The eruption was preceded by a gradual increase in explosive activity since November 2018, expressed by intense thermal activity, and by a monthly-long phase of low-level explosive activity from September 2018 from summit vents.

In relation to the ongoing eruptive crisis, on 28 December a "*National Commission for the forecast and preventions of Major Risks*" (Commissione Grandi Rischi) meeting was called by the Italian Civil Protection Agency, with all the local authorities and local DPC headquarters, and research institutions such as INGV (Istituto Nazionale di Geofisica e Vulcanologia), CNR-IREA (Istituto per il Rilevamento Elettromagnetico dell'Ambiente - Consiglio Nazionale delle Ricerche) and LGS from University of Firenze, among others. Here, thermal satellite results by MIROVA from MODIS and MSI SENTINEL-2 IR sensors have been presented to help understand the ongoing events and assess future eruptive scenarios. An example is shown in Figure 1 and Figure 2.

SENTINEL-2 MSI images (hereafter S2 or MSI-S2), processed in the SWIR bands (ρ12 – ρ11 – ρ8a, see Chapter 2), are illustrated from September to December 2018 to reconstruct the chronology of Etna activity preceding the unrest of the 24 December 2018 (Fig. 1a-l). In the images are highlighted the location of the Etna active summit craters, with other dimensional elements of interest, such as the length of overflow from the South-East crater and the area of the new eruptive fissure on the western flank of the Valle del Bove (see Fig. 1h and 1l). These pure observational products are presented in combination with the MODIS-derived Volcanic Radiative Power time series (divided for levels of intensity, see Coppola et al., 2016) over the same period, thus giving the possibility *i*) to link the heat flux with the thermal source responsible for those rising thermal emissions, and *ii*) looking at the evolution of intra-crater thermal features over time before effusion started. Focusing on the rapid eruptive episode during 24-27 December 2018, even for this short-lived event, the proper timing acquisition of SENTINEL-2 gave essential insights into the current eruptive processes (Figure 2). The image of 24 December was acquired some hours before the beginning of the opening of the effusive cracks, showing an interesting dark-grey plume coming from the base of the northwards side of Serra Giannicola Grande and possibly associated with a landslide generated in response to the ongoing fissure propagation and related to the intense seismic activity (Fig. 2a). The S2 image captured on 26 December, reveals critical information for volcanic hazard assessment. Firstly, the high resolution allows the flow length and path spatial analysis. Secondly, the SWIR image presents the lava body with black-reddish color tones, indicating that the lava flow is cooling (Laiolo et al., 2019).

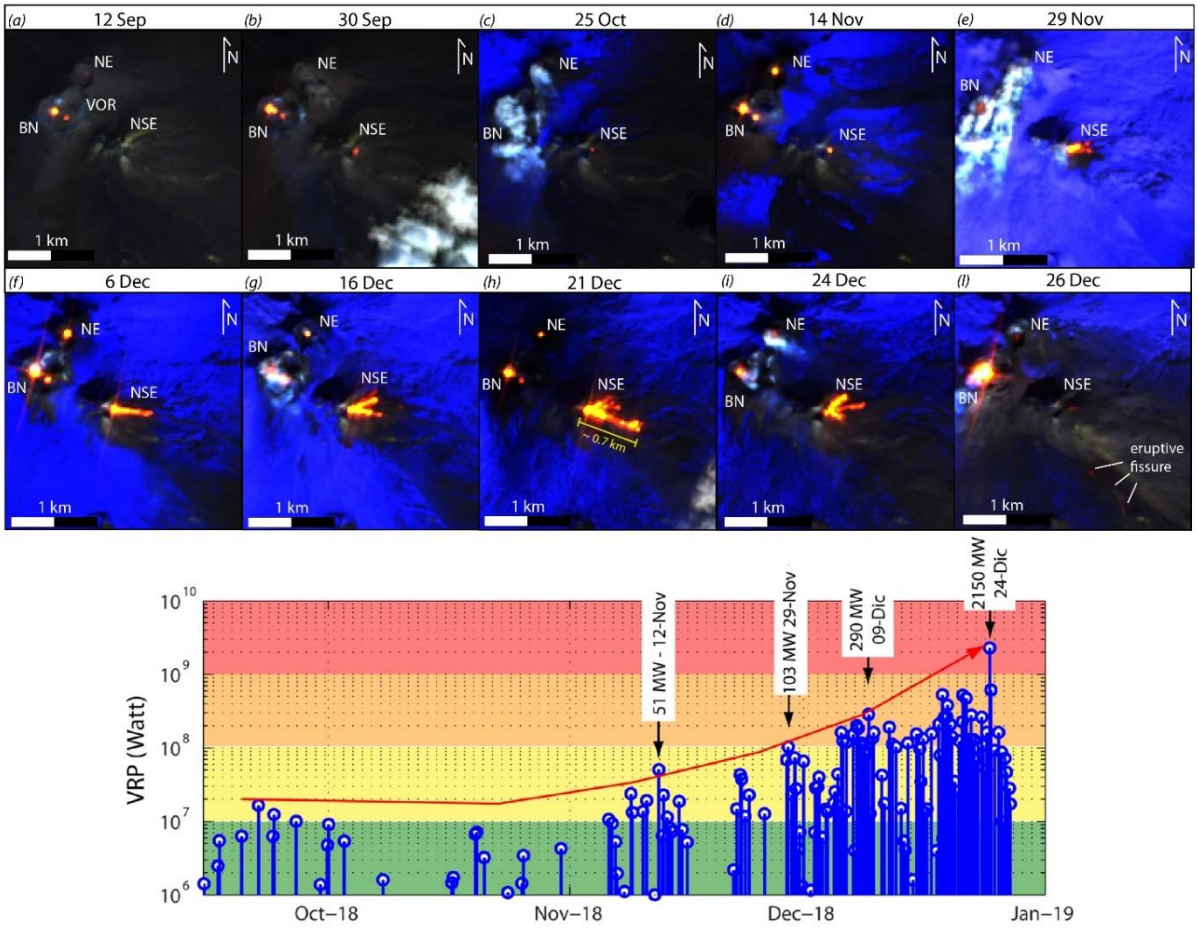

Figure 1 *– (below) September – December 2018 time-series of VRP (in Watt, blue stem) at the Etna volcano; in the background, green, yellow, orange, and red colors mark the five distinct thermal levels (low, moderate, high, very high). Date and VRP measurements in the white box indicate the main steps of thermal rising and values close to S2 MSI acquisitions. (above) SENTINEL-2 MSI class images acquired during Etna activity, with summit craters Bocca Nuova (BN), Voragine (VOR), New South-East (NSE), and North-East (NE) marked. Images represent the most representative shots (a–l) of the Etna volcano activity from September to December 2018.*

This evidence is of great relevance for the complete comprehension of the eruptive episode from a hazard management perspective, letting to understand that the effusion is approaching the end and that, most likely, the lava flow is no longer fed. Additionally, the last image allowed to reconstruct the path of the eruptive fissure, marked by subtle but still visible hotspots. In this case, for the short but intense eruptive event at Etna in December 2018, noteworthy information for civil protection aims was obtained through the contribution of MSI S2 images, which can be summarized as *i*) observing the eruptive state qualitatively, comparing the chronology of Etna activity with the visual inspection of satellite images and tracking the presence of emissions from summit crater; *ii*) evaluate length and precise location of the lava flow produced during the crisis; *iii*) having essential clues on the ending of effusive phase.

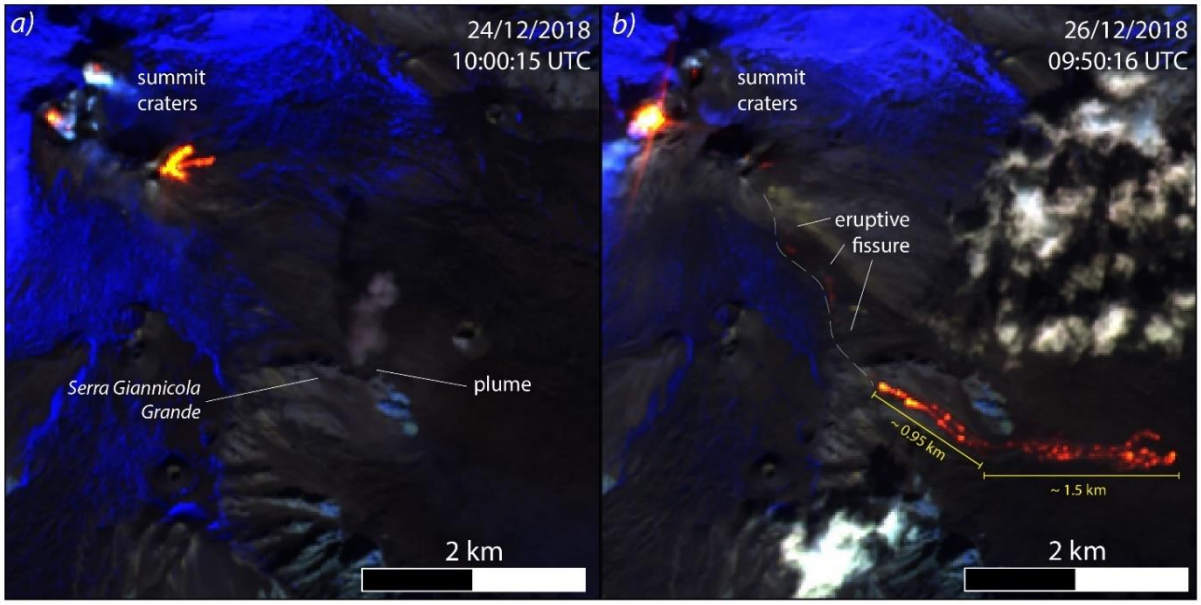

Figure 2 *- Focus on 24 (a) and 26 (b) December 2018, SENTINEL-2 MSI resumes the eastern summit portion of Etna edifice, covering from craters to the upper portion of Valle of the Bove.*

2.2 Stromboli eruptive crisis of summer 2019

During summer 2019, the Stromboli volcano (Sicily, Italy) exhibited a violent eruptive phase, marked by the occurrence of an unexpected paroxysmal explosion on July 3 (the strongest ever recorded at Stromboli of the instrumental era, Ripepe et al., 2021), followed by an intense explosive and intermittent effusive activity culminating in a second paroxysm on August 28 (Aiuppa et al., 2021; Giordano & De Astis, 2021; Ripepe et al., 2021). Both paroxysms occurred from the summit crater terrace, producing eruptive columns up to 8 km ca., which dense tephra fallout (ash, lapilli, and bombs) over the entire island, and pyroclastic density currents descending along the Sciara del Fuoco sector and entering the sea, triggering a small tsunamis wave (~2 meters; Lacanna & Ripepe, 2020). The eruptive crisis has represented a complex challenge to face for the volcanological Italian community and local civil protection authorities, posing considerable hazard implications for the villages and causing the loss of one life (Giordano & De Astis, 2021); if the first paroxysmal event, occurred at 14.45 UTC of 3 July, had happened a few hours later, hundreds of tourists usually reaching the summit of the volcano would have been affected (Giordano & De Astis, 2021; Ripepe et al., 2021).

The 3$^{rd\ of}$ July explosion caused a substantial morphological reshape of the summit crater terrace and, importantly, the partial breakout of the central-southwest crater's outer rim, enabling conduit lava to be drained out directly into the Sciara del Fuoco slope and feeding a lava flow reached the sea (Aiuppa et al., 2021; Laiolo et al., 2022). Following the explosion, an energetic explosive activity takes place at the summit vents, accompanying the nearly continuous effusive

activity sustained by the main effusive source located in the SW portion of the crater terrace (Laiolo et al., 2022). The presence of volcanologists and witnesses of local inhabitants on the island reported that days immediately after the 3rd of July paroxysm were dominated by very high-intensity Strombolian eruptions, with several tens of explosions per hour and very high fountains that could also be seen from Stromboli village, likely above ca. 300 m in elevation (Giordano & De Astis, 2021). The Regional Civil Protection closed the access to the volcano summit above 400 meters and sea navigation in front of the Sciara del Fuoco sector (DRPC, 2019). This evidence marks the prohibitive and unsafe conditions to safely reach the summit and make volcanological observations immediately after the explosion in a state of instability and high explosivity of the Stromboli system (LGS, 2019a). In this context, remote sensing techniques are crucial to getting information as quickly and safely as possible. During those days, several monitoring reports resuming the main geophysical, geochemical, and thermal parameter trends have been sent several times per day for all necessary updates to the Italian Civil Protection Agency by the LGS group, of which the MIROVA project is a part. Numerous online and in-presence meetings were held with local authorities, national and local Civil Protection Agency headquarters, and other research and monitoring institutions. Here, the thermal remote sensed dataset, by MODIS and SENTINEL-2 sensor, has been used to obtain information on the status of both effusive and explosive activity, especially in the inaccessible summit craters area (see Figure 3 and Figure 4).

The first usable MSI SENTINEL-2 satellite image arrived only on the 7th of July and gave important information (LGS, 2019b). Indeed, thermal anomalies' location on the Stromboli crater terrace depicted a new setting, in which the thermal signature related to the south-west crater was strongly off-centered by ca. 120 meters toward west (i.e., the Sciara del Fuoco sector) from the previous position of the SW if compared with image precedent to the 3rd of July paroxysm (Figure 3). This outcome not only covered a lack of information on the post-explosive condition of the crater terrace, given the impossibility during those days to perform direct observations but mainly provided information for assessing the risk of collapse of crater terrace portions seawards, considering the enlargement of the crater area outside its previous location. Indeed, with the new active crater moved toward the west and so toward the Sciara del Fuoco scar, the arrival of magma and current effusive activity could easily destabilize those portions already weakened by the July 3 explosion.

Having a database of the various SENTINEL-2 images from 2015 (see Chapter 2; Massimetti al., 2020), and thus background of the location of the thermal anomalies at Stromboli, made it possible to check that the thermal features at Stromboli and the position of the new southwest-

oriented anomaly were indeed anomalous with respect to ordinary activity and external to the limit of the terrace as shaped before the paroxysmal explosion (Figure 4).

Following, the effusive activity continued for the entire July – August 2019 and lasted until the 1st of September, some days after the occurrence of the second paroxysmal event, producing a total amount of ca. 2 Mm^3 with an average effusive rate of 0.4 m^3/s (Laiolo et al., 2022). Most of the effusive products were emplaced along the Sciara del Fuoco scar, with lava rarely reaching the sea and constantly moving its front (Plank et al., 2019a, because of the poor feeding rate and the occurrence of autobrecciation broken processes producing rolling and accumulation of lava debris at the base of the slope (Giordano & De Astis, 2021). This underlines the importance of monitoring the lava flow spatial evolution and migration of its front. For this task, high-resolution SWIR images had been of great help during the Stromboli crisis of summer 2019, such as the MSI S2 image of the 19th of July (Figure 5); in this case, it was possible to estimate the lava width, length, front location, and sourcing from the new South West active vent, as well as to observe the intense thermal activity occurring at the summit craters. This image, and others with the same spatial and spectral features, have been used routinely disseminated to Italian Civil Protection for the Stromboli activity monitoring July – August 2019 (see LGS, 2019c; 2019d), with other crucial information derived by the MIROVA system such as the VRP heat flux time series and the estimate of updated TADR (Time Averaged Discharge Rate, see Coppola et al., 2020) values, monitoring the feeding conditions to the lava flow.

Considering the complexity of the summer 2019 Stromboli crisis and the challenge that this event posed to local communities, authorities, Civil Protection Agency, and volcanologists, thermal high-spatial-resolution images such as the SENTINEL-2 ones demonstrate to be extremely useful for tracking the evolution of the eruptive event, to retrieve precious information of the effusive activity and, importantly, to give insights about the conditions on the crater terrace immediately after the occurrence of the strongest paroxysm event in the instrumental era at Stromboli, otherwise impossible to have safely.

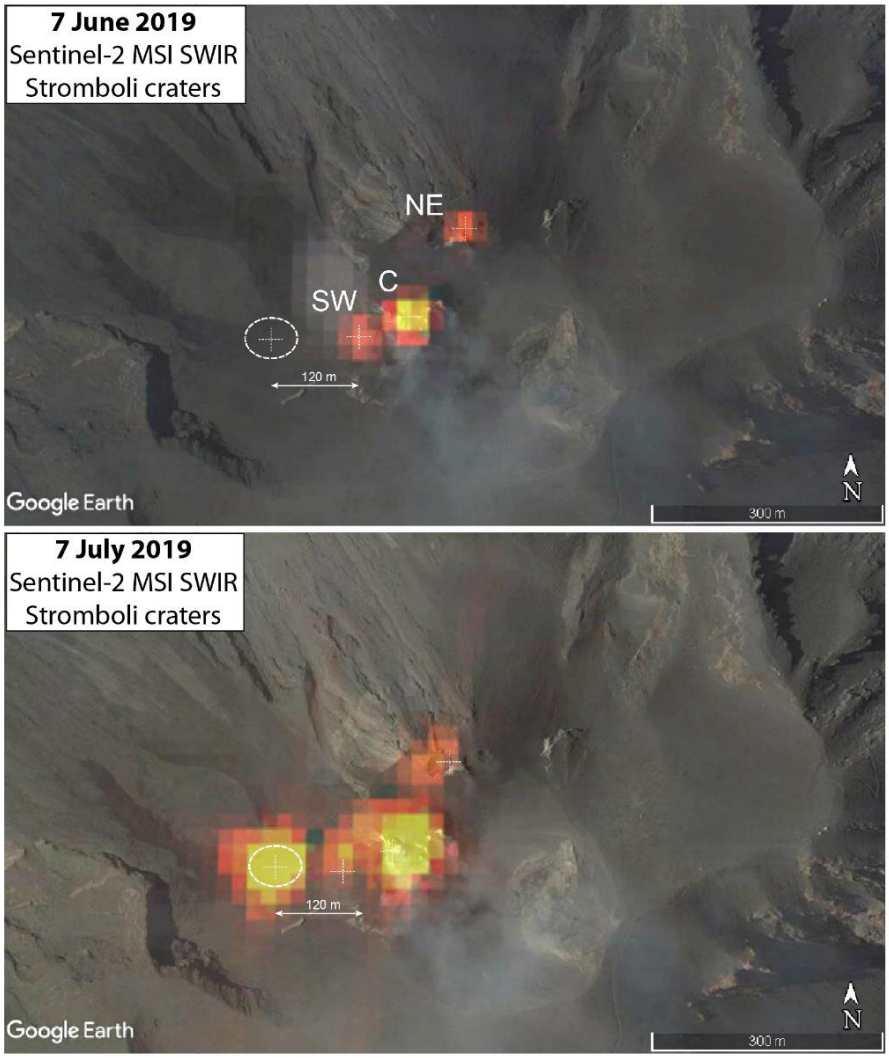

Figure 3 *- Comparison of composite RGB SWIR MSI SENTINEL -2 images taken over Stromboli crater terrace before (7 June 2019, above) and immediately after (7 June 2019, below) the beginning of summer 2019 eruptive crisis after the 3rd of July paroxysms. As is possible to observe, the thermal anomaly formerly associated with the South West crater shifted by ca. 120 meters towards the west.*

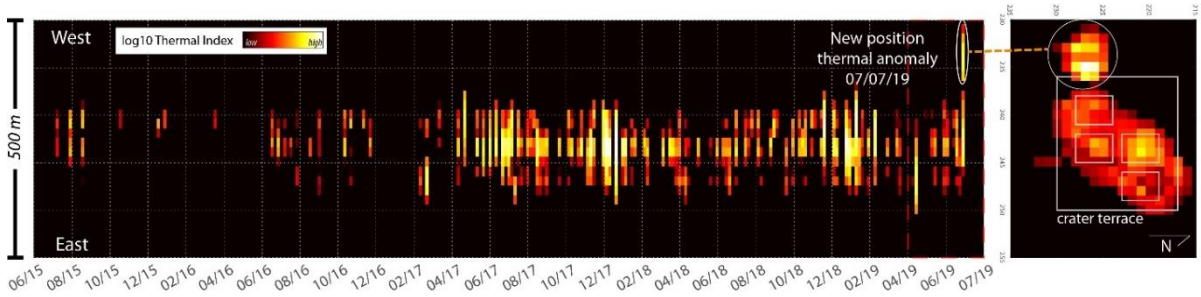

Figure 4 *– Thermal Profiles west-east oriented of the Thermal Index from MSI SENTINEL-2 images over the Stromboli summit area, between June 2015 – July 2019 (left). The location of the thermal anomaly of 7 July 2019 is highlighted with a white circle and compared to the sum of thermal anomalies in the time period 2015 – 2019 (right, north toward right), which represents the ordinary position of thermal anomalies on the crater terrace.*

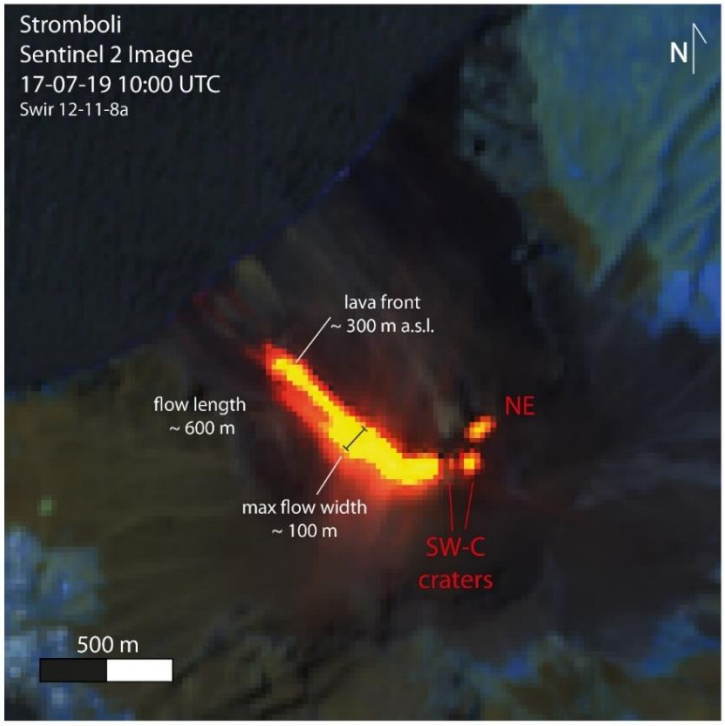

Figure 5 *– Satellite image of Stromboli acquired by SENTINEL-2 MSI sensor on July 17, 2019, in the SWIR bands, showing the July-August lava flow field at its maximum extension, and intense thermal emissions from the Central – South West (C-SW) and North East (NE) sectors, produced by Strombolian explosive activity.*

3. MONITORING APPLICATIONS AND IMPLEMENTATION OF THE MIROVA SYSTEM

One of the current limits of the MIROVA system is the use of just one sensor as MODIS, offering only a moderate spatial resolution (Coppola et al., 2020). Specifically, improving spatial resolution is one of the main issues presented by the system. Specifically, improving spatial resolution is one of the main issues presented by the system.

Here, we use the thermal hotspot algorithm presented in Chapter 2 with a global monitoring outlook, with three main improvements: *i*) the algorithm has also been applied to the Operational Land Instrument SWIR images of LANDSAT-8 satellite platforms, as already explained in the Method sections in Chapter 3 and Chapter 4, thus raising the number of acquired images; *ii*) the number of targeted volcanoes using both SENTINEL-2 and LANDSAT-8 imagery has been incremented to monitor a huger number of volcanoes; *iii*) the results have been structured inside the MIROVA systems and website architecture, creating a series of table and graphical output similar to those already based on MODIS images, and available on the www.mirovaweb.it for each volcano page. During the Ph.D. course, an automated system able to download, process, archive, extract and disseminate useful thermal information about the volcanic activity using S2-MSI and L8-OLI images has been architected

to be easily included inside the already existing MIROVA framework (see Chapter 2; Massimetti et al., 2020). The algorithm works operationally on MOUNTS (Monitoring Unrest from Space, http://www.mounts-project.com/home), a multiparametric monitoring satellite system combining SAR, UV, and IR analysis, using the SENTINEL ESA constellation (Valade et al., 2019).

Both SENTINEL-2 MSI and LANDSAT-8 OLI datasets are accessed by the AmazonWeb Service S3 (AWS S3, https://registry.opendata.aws/sentinel-2/, and https://registry.opendata.aws/usgs-landsat/), and processed by the conceptual flow presented in Chapter 2, applying fixed thresholds, spatial and statistical filters to the Thermal Index parameter for each altered SWIR MSI and OLI images (see section 2.3, Chapter 2). Based at the Department of Earth Sciences of the University of Torino, the processing system works routinely every day in near real-time, updating the acquisition and processing of the high-spatial-resolution images every 3 hours. To date, 118 volcanoes worldwide are daily thermally monitored by MSI SENTINEL-2 images, and 115 by using OLI LANDSAT-8 ones (Table 1 and Figure 6). This discrepancy is because a few volcanoes are not geographically covered by SENTINEL-2 platform overpasses (such as Nishinoshima, Japan), or vice-versa, not covered by LANDSAT-8 satellite (such as Erebus, Antarctica region), or because we decided not to add volcanic targets no longer in eruption to the LANDSAT-8 processing (such as Kilauea East, i.e., LERZ zone, Plank et al., 2021), or still we have to do (such as Fernandina volcano, Galapagosgos Island, Ecuador; Global Volcanism Program, 2013a).

VOLCANO	***COUNTRY***	**VOLCANO**	***COUNTRY***
Agung	*Indonesia*	Montagu Island	*United Kingdom*
Aira	*Japan*	Nabro	*Eritrea*
Alaid	*Russia*	Negra, Sierra	*Ecuador*
Ambrym	*Vanuatu*	Nishinoshima	*Japan*
Aoba	*Vanuatu*	Nyamuragira	*DR Congo*
Asamayama	*Japan*	Nyiragongo	*DR Congo*
Asosan	*Japan*	Ontakesan	*Japan*
Bagana	*Papua New Guinea*	Pacaya	*Guatemala*
Barren Island	*India*	Paluweh	*Indonesia*
Bezymianny	*Russia*	Pavlof	*United States*
Bristol Island	*United Kingdom*	Planchón-Peteroa	*Chile*
Campi Flegrei	*Italy*	Poás	*Costa Rica*
Chaitén	*Chile*	Popocatépetl	*Mexico*

Chillán, Nevados de	*Chile*	Puyehue-Cordón Caulle	*Chile*
Chirinkotan	*Russia*	Rabaul	*Papua New Guinea*
Chirpoi	*Russia*	Raung	*Indonesia*
Cleveland	*United States*	Reventador	*Ecuador*
Colima	*Mexico*	Rincón de la Vieja	*Costa Rica*
Copahue	*Chile-Argentina*	Rinjani	*Indonesia*
Cotopaxi	*Ecuador*	Ruapehu	*New Zealand*
Dukono	*Indonesia*	Ruiz, Nevado del	*Colombia*
Ebeko	*Russia*	Sabancaya	*Peru*
Erebus	*Antarctica*	SanCristóbal	*Nicaragua*
Erta Ale	*Ethiopia*	San Miguel	*El Salvador*
Etna	*Italy*	Sangay	*Ecuador*
Fernandina	*Ecuador*	Sangeang Api	*Indonesia*
Fournaise, Piton de la	*France*	Santa María	*Guatemala*
Fuego	*Guatemala*	Sarychev Peak	*Russia*
Galeras	*Colombia*	Semeru	*Indonesia*
Geldingadalur	*Iceland*	Semisopochnoi	*United States*
Great Sitkin	*United States*	Shishaldin	*United States*
Heard	*Australia*	Shiveluch	*Russia*
Hudson, Cerro	*Chile*	Sinabung	*Indonesia*
Huila, Nevado del	*Colombia*	Sirung	*Indonesia*
Ibu	*Indonesia*	Slamet	*Indonesia*
Ijen	*Indonesia*	Soputan	*Indonesia*
Kadovar	*Papua New Guinea*	Soufrière Hills	*United Kingdom*
Karangetang (Api Siau)	*Indonesia*	Soufrière St. Vincent	*Saint Vincent and the Grenadines*
Karymsky	*Russia*	Stromboli	*Italy*
Kelut	*Indonesia*	Suwanosejima	*Japan*
Kilauea	*United States*	Taal	*Philippines*
KilaueaEast	*United States*	Tara, Batu	*Indonesia*
Kirishimayama	*Japan*	Telica	*Nicaragua*
Kizimen	*Russia*	Tengger Caldera	*Indonesia*
Kliuchevskoi	*Russia*	Tinakula	*Solomon Islands*
Krakatau	*Indonesia*	Tofua	*Tonga*

La Palma	*Spain*	Tungurahua	*Ecuador*
Langila	*Papua New Guinea*	Turrialba	*Costa Rica*
Láscar	*Chile*	Ubinas	*Peru*
Lastarria	*Chile-Argentina*	Ulawun	*Papua New Guinea*
Lengai, Ol Doinyo	*Tanzania*	Unzendake	*Japan*
Lewotolo	*Indonesia*	Veniaminof	*United States*
Lopevi	*Vanuatu*	Vesuvius	*Italy*
Manam	*Papua New Guinea*	Villarrica	*Chile*
Masaya	*Nicaragua*	Vulcano	*Italy*
Mayon	*Philippines*	White Island	*New Zealand*
Merapi	*Indonesia*	Wolf	*Ecuador*
Michael	*United Kingdom*	Yasur	*Vanuatu*
Momotombo	*Nicaragua*	Zavodovski	*United Kingdom*

Table 1 *– List of the near-real-time monitored volcanoes using SENTINEL-2 MSI and LANDSAT-8 OLI SWIR thermal images developed during this Ph.D. course. Volcanoes are nominated as the Global Volcanism Program provides the list of 1,337 volcanoes with eruptions during the Holocene period (approximately the last 10,000 years; Global Volcanism Program, 2013b). In red are marked volcanoes only monitored by MSI S2 images, in blue those by using OLI L8 ones.*

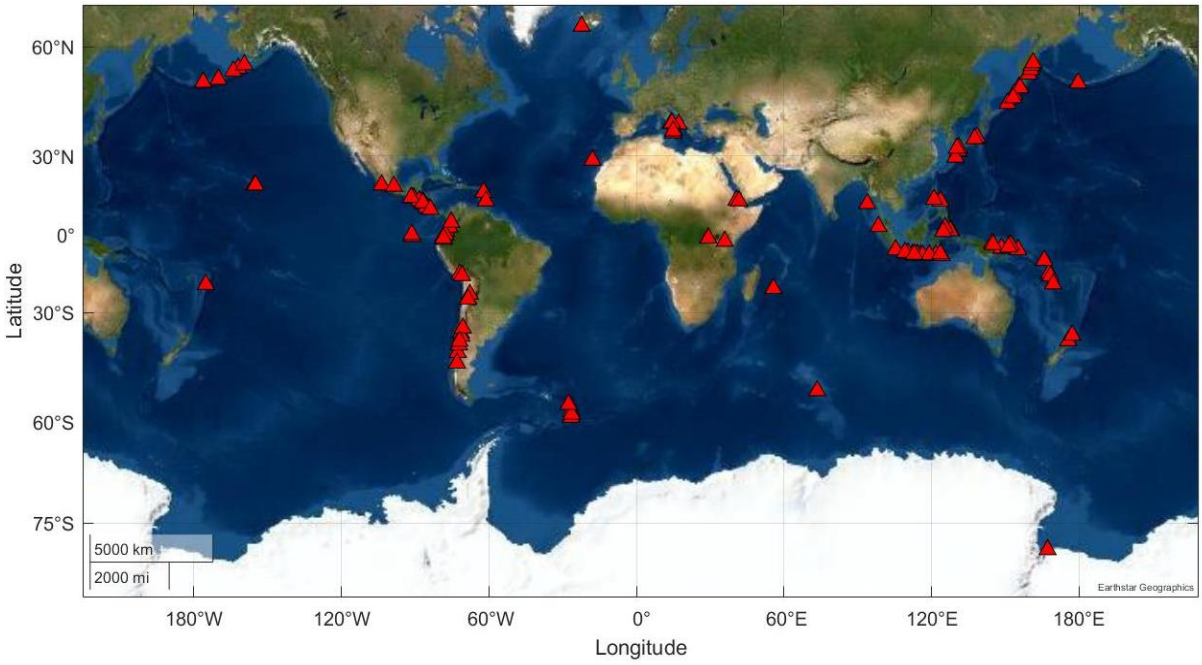

Figure 6 *– Geographical location of the volcanoes monitored using SENTINEL-2 MSI and LANDSAT-8 OLI SWIR thermal images developed during this Ph.D. course.*

All new acquisitions are listed in two different tables for SENTINEL-2 and LANDSAT-8 images, indicating the last anomaly detected and the nb. of Hot Pixels (Figure 7a/b), colored

with the same alert level used for the VRP MODIS dataset: green, yellow, orange, and red colors for the five distinct thermal levels (low, moderate, high, very high; see Coppola et al., 2020). Indeed, we defined five thermal levels based on the nb. Hot Pixels parameter, as follows: LOW (1-10 nb. HotPixels, green), MODERATE (10-100 nb. HotPixels, yellow), HIGH (100-1000 nb. HotPixels, orange), VERY HIGH (1000 - 10000 nb.HotPixels, red) and EXTREME (nb. HotPixels > 10000). The tables, letting to check the list of new anomalies detected, are available online (https://www.mirovaweb.it/SENTINEL2/S2_Latest_Update.html;https://www.mirovaweb.it/LANDSAT8/L8_Latest_Update.html). By clicking on the volcano name you are directed to the individual volcano page on the Mirova website.

Volcanic Sentinel2 HotSpot - Last Update 26-Jul-2022 09:14:49 a)

Volcano	Last S2 Anomaly (UTC)	N.HotPixel
Shiveluch	26-Jul-2022 00:41:12	226
Tinakula	25-Jul-2022 23:19:30	6
Pavlof	25-Jul-2022 22:10:20	14
Telica	25-Jul-2022 16:30:11	3
Slamet	25-Jul-2022 03:10:04	1
CamplFlegrei	24-Jul-2022 10:09:28	1
Heard	24-Jul-2022 04:43:44	20
Semeru	24-Jul-2022 02:50:07	33
TenggerCaldera	24-Jul-2022 02:50:07	2
Raung	24-Jul-2022 02:50:03	3
Dukono	24-Jul-2022 01:57:20	9
Ibu	24-Jul-2022 01:57:20	8
Sabancaya	23-Jul-2022 15:07:28	31
Geldingadalur	23-Jul-2022 13:04:16	4
Etna	23-Jul-2022 09:50:28	16
Manam	23-Jul-2022 00:48:20	25
Lascar	22-Jul-2022 14:49:29	9
LengaiOlDoinyo	22-Jul-2022 08:01:07	7
ErtaAle	22-Jul-2022 07:56:16	3
Sirung	22-Jul-2022 02:10:01	1
Karangetang	22-Jul-2022 02:06:49	3
Tofua	21-Jul-2022 22:01:27	29
Kilauea	21-Jul-2022 21:00:08	344
Vulcano	21-Jul-2022 10:00:16	1
Stromboli	21-Jul-2022 10:00:12	12
Vesuvius	21-Jul-2022 09:59:33	5
Nyamuragira	21-Jul-2022 08:30:48	164
Nyiragongo	21-Jul-2022 08:30:48	61
Pacaya	18-Jul-2022 16:39:56	1
Erebus	08-Mar-2022 20:37:42	7

Volcanic Landsat8 HotSpot - Last Update 26-Jul-2022 07:16:54 b)

Volcano	Last L8 Anomaly (UTC)	N.HotPixel
Shiveluch	25-Jul-2022 00:14:58	91
Krakatau	24-Jul-2022 03:06:36	6
Tinakula	22-Jul-2022 23:06:45	13
Fuego	22-Jul-2022 16:24:26	11
Sabancaya	22-Jul-2022 14:53:55	52
Stromboli	22-Jul-2022 09:42:07	13
Nyamuragira	22-Jul-2022 08:14:24	239
Nyiragongo	22-Jul-2022 08:14:24	82
Ulawun	22-Jul-2022 00:01:10	6
Semeru	21-Jul-2022 02:36:27	33
Lewotolo	20-Jul-2022 01:53:11	14
Sirung	20-Jul-2022 01:53:11	16
Kilauea	19-Jul-2022 20:48:57	310
ErtaAle	19-Jul-2022 07:39:28	2
Merapi	19-Jul-2022 02:48:23	4
Masaya	17-Jul-2022 16:06:37	9
Momotombo	17-Jul-2022 16:06:13	4
Ibu	13-Jul-2022 01:44:09	29
LengaiOlDoinyo	10-Jul-2022 07:50:00	9

Figure 7 *– Last Update tables for new alerted images acquired by SENTINEL-2 (a) and LANDSAT-8 (b) satellites. With different colors, the diverse thermal levels are based on the nb. HotPixels are marked.*

New graphical outputs based on SENTINEL-2 and LANDSAT-8 imagery have been produced and set inside the existing MIROVA website (see, for example, these links on Stromboli volcano for MSI-S2 and OLI-L8 images,https://www.mirovaweb.it/?action=volcanoDetails_S2&volcano_id=211040; https://www.mirovaweb.it/?action=volcanoDetails_L8&volcano_id=211040). Each volcano page has been implemented with new buttons for each sensor, allowing one to observe what thermal information is obtained from the different sensors and shift from one webpage to another. Specifically, the additional output for the MSI S2 and OLI L8 are: *i*) the last six images acquired (Figure 8); *ii*) the slideshow of the graphical output summarizing the VRP – Nb. Hot Pixels time-series and the SWIR RGB images (Figure 9); *iii*) the last image acquired projected on Google Earth software (Figure 9); *iv*) the entire high-spatial resolution thermal dataset open to be downloaded (Table 2). All these products are freely available and accessible on the MIROVA website.

The first implementation consists of a statical image resuming the last six SENTINEL-2 or LANDSAT-8 RGB (in SWIR bands, Fig. 8) images acquired in chronological order, from newest to oldest, in the original dimension of 50x50 km size, with the number of Hot Pixels detected in each image signed (see Chapter 2). Depending on the geographical location of the volcano, the last six images could cover a period of ca. 12 days for SENTINEL-2 acquisition and one month for LANDSAT-8. This product serves to give a first general overlook for anyone who is interested in a specific volcano investigation and offers the possibility to visually check the atmospheric (clouds presence), environmental (snow or ice presence), and satellite geometry (i.e., cut images, stripe sensor artifacts) conditions of the image, having a direct assessment of the quality of the thermal sensing. The wide geographic scale of 50 km per side inevitably reduces the detail of observation for small or anomalies at crater scale but allows to visualize distant and spatially huge thermal signals in the case of an effusive eruption.

The slideshow visualization provides a rich graphical output containing several quantitative and qualitative information (Fig. 9): the MSI-S2 or OLI-L8 RGB images in SWIR images with the double zoom visualization of 2x2 km and 10x10 km, the estimate of the nb. of Hot Pixels located in the summit area and in the whole image, and two plots on short (two months) and long (two years) period jointing MODIS-VRP and nb. Hot Pixels dataseries. The thermal information in the single graphic product offers a direct characterization of the thermal activity of the investigated volcano, indicating the location of thermal hotspots and measurement of the related thermal signal in terms of heat flux resealed and hot area exposed. Changes in the hot feature's position, area, and temperature can be easily tracked and compared between the

different MODIS, MSI, and OLI InfraRed sensors. Thanks to the slideshow application, users can friendly explore the entire thermal activity history (*Play* button or sliding over dates of images), from the first MSI-S2 (2015/2016) or OLI-L8 (2013) image acquired, having an overview of the evolution of the volcanic thermal activity over the years. Each graphical output can be selected and downloaded as a single image *.png* file.

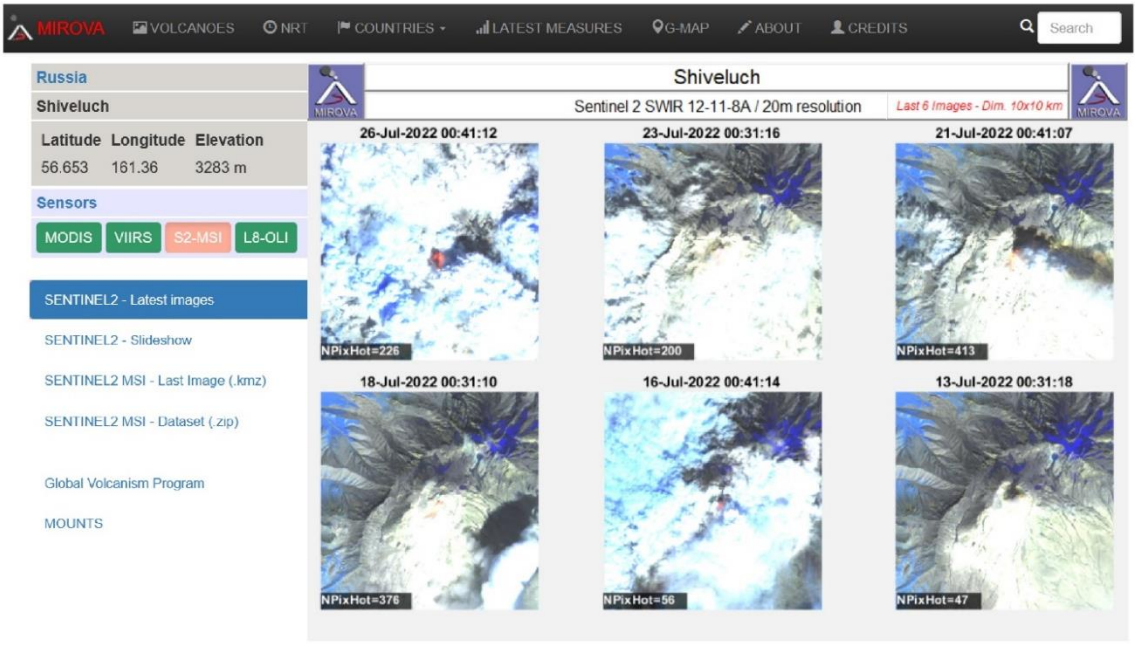

Figure 8 *– Latest SWIR images (here for the SENTINEL-2 MSI sensor) on Shiveluch volcano (Kamchatka, Russia) on the MIROVA website. The last six MSI images cover 13 July to 26 July 2022.*

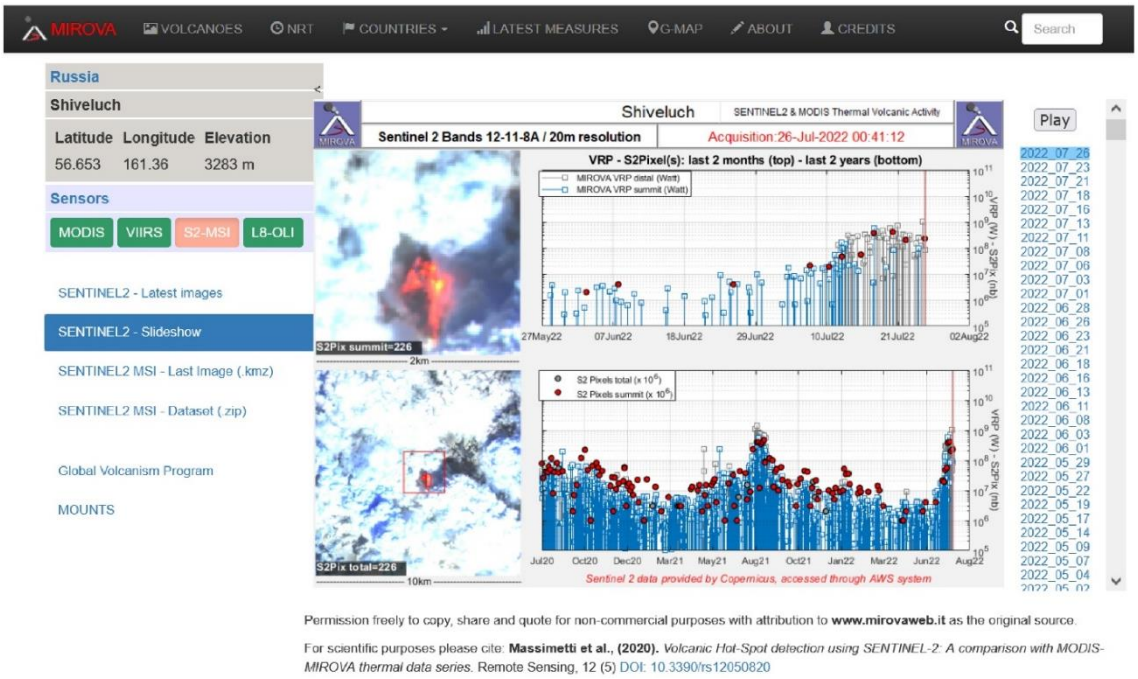

Figure 9 *– Slideshow application of the SENTINEL-2 MSI images at the Shiveluch volcano (Kamchatka, Russia) on the MIROVA website. Look on the right at the series of different dates for each acquired image and the rising thermal trend in VRP and nb. HotPixel from June 2022.*

The last image in *.kmz* format offers the last processed SWIR high-spatial resolution image projected on the Google Earth map to be downloaded (Fig. 10). This product allows to locate the SWIR thermal anomaly, verify where precisely it is, for example, inside or outside a crater or the position over the volcano edifice, make dimensional analysis on thermal extension, useful for hazard evaluation of the ongoing activity. All the above outputs are exclusively made up of static graphs overwritten as newer data are processed.

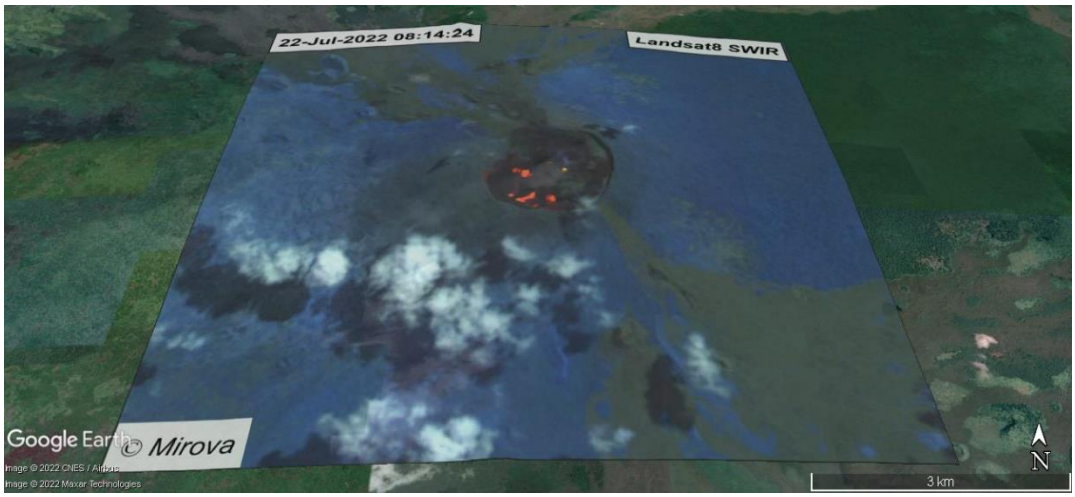

Figure 10 *– LANDSAT-8 OLI SWIR images projection on Google Earth, on the Nyamuragira volcano (DR Congo), downloaded by the MIROVA website. The image was acquired on 22 July 2022 at 08:14 UTC, and shows the presence of hotspots inside the summit crater related to the dynamics of the lava lake.*

The last implementation consists of the publication of the entire MSI-S2 and OLI-L8 thermal dataset, continuously updated as soon as a new image arrives, in *.zip* format. A file named *S2_HotSpot_volcanoname* or *L8_HotSpot_volcanoname* could be freely downloaded and contains a *ReadMe* instruction and a table in .csv format with thermal, spatial, and quantitative information about hot spot detection at the volcano of interest. The dataset is structured in 8 columns as follows (Table 2):

1) Date of MSI-S2 or OLI-L8 Image's acquisition (UTC Time);
2) Number of Hot Pixel(s) detected in the image (10 x 10 km) (nb.);
3) Thermal Index of Hot Pixel(s) (Mean Value, adimensional);
4) Thermal Index of Hot Pixel(s) (Max Value, adimensional);
5) Distance Max of Hot Pixel(s) from volcano summit (meters);
6) Distance Max of Hot Pixel(s) in a box of 2x2 km around the volcano summit (meters);
7) Number of Hot Pixel(s) in a box of 2x2 km around the volcano summit (nb.);
8) Number of Cluster(s) of Hot Pixel(s) (nb.)

Table 2 *– Contents of the SWIR SENTINEL-2 or LANDSAT-8 thermal downloadable dataset in .csv by the implemented MIROVA website.*

The dataset offers a unique series of complementary information, not only related to the number of Hot Pixels and the extension of the hot area exposed but also giving the quantification of thermal signals through the Thermal Index parameter (see Chapter 2), or the measure of the distance of hot pixels location from volcano summit, for example. This improvement represents an outstanding achievement in terms of data dissemination for several reasons. It is the first thermal dataset freely and autonomously downloadable on the MIROVA website; at the moment, the MODIS and VIIRS MIR thermal satellite datasets are still not accessible but only viewed as static graphic data (see Coppola et al., 2020). This means that for the whole volcanological community, composed of various stakeholders, users working in civil protection, monitoring observatories, researchers, authorities, or just people interested in volcanic themes, a complete thermal dataset over most of the thermally active volcanoes worldwide is available to any kind of research, monitoring, or informative purposes. Secondly, as far as we know, this step makes the MIROVA system the first woIrldwide volcanic monitoring tool which integrates thermal analysis at MIR, at 1 km pixel resolution, and SWIR, at 20-30 meters, with free access to the SWIR high-spatial-resolution dataset on a sub-global scale.

4. CONCLUSIONS

In this Chapter, we showed how SENTINEL-2 and LANDSAT-8 high-spatial-resolution thermal satellite data could be effective in providing to the whole volcanological community, and particular to civil protection agencies and observatories, a tool to better understand the evolution of volcanic episodes and their associated hazards, evaluating the presence and size of active hot spots, tracking the spatial development of thermal active volcanic areas, offering a method to make observations in unsafe or unreachable contexts, as shown in the two case studies of Etna December 2018 and Stromboli summer 2019 eruptions. An automated and near real-time system has been built to make the SWIR thermal dataset used as a monitoring tool for global volcanic activity. The results have been put into practice improving the already monitoring system of MIROVA. The new available graphical outputs based on SENTINEL-2 and LANDSAT-8 and the entire thermal dataset ready for use at the most active volcanoes worldwide highly contribute to enhancing the thermal surveillance offered by the MIROVA project to observatories, monitoring centers, and local authorities that everyday use thermal space-based data for their monitoring and management needs, moving toward the multisensory approach whose importance is increasingly evident and in demand.

5. BIBLIOGRAPHY

Aiuppa, A., Bitetto, M., Delle Donne, D., La Monica, F., Tamburello, G., Coppola, D., Della Schiava, M., Innocenti, L., Lacanna, G., Laiolo, M., Massimetti, F., Pistolesi, M., Silengo, C., Ripepe, M., 2021. Volcanic CO2 tracks the incubation period of basaltic paroxysms. Sci. Adv.17 (7(38)). https://doi.org/10.1126/sciadv.abh0191

AWS S3. Registry of Open Data on AWS. Available online: https://registry.opendata.aws/ (accessed on July 2022).

Blackett M. An Overview of Infrared Remote Sensing of Volcanic Activity, 2017. Journal of Imaging, 3(2):13. https://doi.org/10.3390/jimaging3020013

Bonforte, A., Guglielmino, F., Puglisi G., 2019. Large dyke intrusion and small eruption: the December 24, 2018 Mt. Etna eruption imaged by Sentinel-1 data. Terra Nova 31:405–412. https://doi.org/10.1111/ter.12403

Coppola, D., Laiolo, M., Cigolini, C., Delle Donne, D., Ripepe, M. 2016. Enhanced volcanic hot-spot detection using MODIS IR data: Results from the MIROVA system. Geol. Soc. Lond. Spec. Publ. 2016, 426, 181–205. https://doi.org/10.1144/SP426.5

Coppola, D., Laiolo, M., Cigolini, C., Massimetti, F., Delle Donne, D., Ripepe, M., Arias, H., Barsotti, S., Parra, C.B., Centeno, R.G., Cevuard, S., Chigna, G., Chun, C., Garaebiti, E., González, D., Griswold, J., Juarez, J., Lara, L.E., López, C.M., Macedo, O., Mahinda, C., Ogburn, S., Prambada, O., Ramon, P., Ramos, D., Peltier, A., Saunders, S., de Zeeuw-van Dalfsen, E., Varley, N., William, R., 2020. Thermal remote sensing for global volcano monitoring experiences from the Mirova system. Front Earth Sci 7. https://doi.org/10.3389/feart.2019.00362

Coppola, D., Valade, S., Masias, P. et al., 2022. Shallow magma convection evidenced by excess degassing and thermal radiation during the dome-forming Sabancaya eruption (2012–2020). Bull Volcanol 84, 16. https://doi.org/10.1007/s00445-022-01523-1

DRPC, 2019. Avviso Regionale di Protezione Civile per Eventi Vulcanici di Impatto Locale a Stromboli n. 3 del 3 luglio 2019. Regione Siciliana – Presidenza – Dipartimento della Protezione Civile, Servizi Rischi Sismico e Vulcanico, accessible at https://www.protezionecivilesicilia.it/avvisi/Avviso_Stromboli_03_03072019.pdf, last access 24 July 2022

Giordano, G., De Astis, G., 2021. The summer 2019 basaltic Vulcanian eruptions (paroxysms) of Stromboli. Bull Volcanol 83, 1. https://doi.org/10.1007/s00445-020-01423-2

Global Volcanism Program, 2013a. [Fernandina (353010)] *in* Volcanoes of the World, v. 4.11.0 (08 Jun 2022). Venzke, E (ed.). Smithsonian Institution. Downloaded 24 Jul 2022 ([https://volcano.si.edu/volcano.cfm?vn=353010]). https://volcano.si.edu/volcano.cfm?vn=353010

Global Volcanism Program, 2013b. Volcanoes of the World, v. 4.11.0. Venzke, E (ed.). Smithsonian Institution. Downloaded 25 Jul 2022. https://doi.org/10.5479/si.GVP.VOTW4-2013

Harris, A., 2013. Thermal Remote Sensing of Active Volcanoes: A User's Manual. Cambridge, MA: Cambridge university press. https://doi.org/10.1017/CBO9781139029346

Harris, A.J.L., Villeneuve, N., Di Muro, A. et al., 2017. Effusive crises at Piton de la Fournaise 2014–2015: a review of a multi-national response model. J Appl. Volcanol. 6, 11. https://doi.org/10.1186/s13617-017-0062-9

Istituto Nazionale di Geofisica e Vulcanologia. Bollettino Settimanale, Rep. N° 01/2019. Available online: http://www.ct.ingv.it/it/rapporti/multidisciplinari.html (accessed on 26 December 2018).

Lacanna, G., Ripepe, M., 2020. Genesis of tsunami waves generated by pyroclas-tic flows and the early-warning system. In 4th Rittmann conference Abstract volume (Miscellanea INGV, 52, 2020), Catania, 12 to 14 February 2020.

Laiolo, M., Coppola, D., Barahona, F., Benítez, J. E., Cigolini, C., Escobar, D., et al., 2017. Evidences of volcanic unrest on high-temperature fumaroles by satellite thermal monitoring: the case of Santa Ana volcano, El Salvador. J. Volcanol. Geotherm. Res. 340, 170–179. https://doi.org/10.1016/j.jvolgeores.2017.04.013

Laiolo, M., Ripepe, M., Cigolini, C., Coppola, D., Della Schiava, M., Genco, R., Innocenti, L., Lacanna, G., Marchetti, E., Massimetti, F., Silengo, M.C., 2019. Space- and Ground-Based Geophysical Data Tracking of Magma Migration in Shallow Feeding System of Mount Etna Volcano. Remote Sens., 11, 1182. https://doi.org/10.3390/rs11101182

Laiolo, M., Delle Donne, D., Coppola, D., Bitetto, M., Cigolini, C., Della Schiava, M., Innocenti, L., Lacanna, G., La Monica, F.P., Massimetti, F., Pistolesi, M., Silengo, M.C., Aiuppa, A., Ripepe, M., 2022. Shallow magma dynamics at open-vent volcanoes tracked by

coupled thermal and SO2 observations. Earth Planet. Sci. Lett., 594, 117726. https://doi.org/10.1016/j.epsl.2022.117726

Layana, S., Aguilera, F., Rojo, G., Vergara, Á., Salazar, P., Quispe, J., Urra, P., Urrutia, D., 2020. Volcanic Anomalies Monitoring System (VOLCANOMS), a Low-Cost Volcanic Monitoring System Based on Landsat Images. Remote Sens., 12, 1589. https://doi.org/10.3390/rs12101589.

LGS, 2019a. ESPLOSIONE PAROSSISTICA A STROMBOLI DEL 03/07/2019 14:45 GMT http://lgs.geo.unifi.it/index.php/blog/esplosione-parossistica-stromboli-3-luglio-2019, Last access 24 July, 2022

LGS, 2019b. IMMAGINI SATELLITARI SENTINEL 2 DOPO L'EVENTO PAROSSISTICO DEL 03/07/2019 http://lgs.geo.unifi.it/index.php/blog/immagini-sentinel2-stromboli-3-luglio-2019 , Last access 24 July, 2022

LGS, 2019c. STROMBOLI: IMMAGINI SATELLITARI SENTINEL 2 DEL 12/07/2019 http://lgs.geo.unifi.it/index.php/blog/immagini-sentinel2-stromboli-12-luglio-2019, Last access 24 July, 2022

LGS, 2019d. COMUNICATO N.15 ATTIVITA' VULCANO STROMBOLI DELLE 21:30 (ORA LOCALE) DEL 17/07/2019 http://lgs.geo.unifi.it/index.php/blog/comunicato-stromboli-17-luglio-h2130, Last access 24 July, 2022

Marchese, F., Genzano, N., Neri, M., Falconieri, A., Mazzeo, G., Pergola, N., 2019. A Multi-Channel Algorithm for Mapping Volcanic Thermal Anomalies by Means of Sentinel-2 MSI and Landsat-8 OLI Data. Remote Sens., 11, 2876. https://doi.org/10.3390/rs11232876

Marchese, F., Filizzola, C., Lacava, T., Falconieri, A., Faruolo, M., Genzano, N., Mazzeo, G., Pietrapertosa, C., Pergola, N., Tramutoli, V., et al., 2021. Mt. Etna Paroxysms of February–April 2021 Monitored and Quantified through a Multi-Platform Satellite Observing System. Remote Sens., 13, 3074. https://doi.org/10.3390/rs13163074

Marchese, F., Genzano, N., Nolde, M., Falconieri, A., Pergola, N., Plank, S., 2022. Mapping and characterizing the Kīlauea (Hawai‘i) lava lake through Sentinel-2 MSI and Landsat-8 OLI observations of December 2020–February 2021. Environ. Model. Softw., 148, 105273. https://doi.org/10.1016/j.envsoft.2021.105273

Massimetti, F., Coppola, D., Laiolo, M., Valade, S., Cigolini, C., Ripepe, M., 2020. Volcanic Hot-Spot Detection Using SENTINEL-2: A Comparison with MODIS–MIROVA Thermal Data Series. Remote Sens 12: 820. https://doi.org/10.3390/rs12050820

Newhall, C. G., Costa, F., Ratdomopurbo, A., Venezky, D. Y., Widiwijayanti, C., Win, N. T. Z., et al., 2017. WOVOdat – an online, growing library of worldwide volcanic unrest. J. Volcanol. nd Geotherm. Res. 345, 184–199. https://doi.org/10.1016/j.jvolgeores.2017.08.003

Oppenheimer, C.M.M., Rothery, D.A., 1991. Infrared monitoring of volcanoes by satellite. J. Geol. Soc. 148 (3), 563–569. https://doi.org/10.1144/gsjgs.148.3.0563

Pallister, J., McNutt, S. R., 2015. "Synthesis of volcano monitoring," in The Encyclopedia of Volcanoes, 2nd Edn, ed. H. Sigurdsson, (Cambridge, MA: Academic Press), 1151–1171. doi: https://doi.org/10.1016/B978-0-12-385938-9.00066-3

Plank, S., Marchese, F., Filizzola, C., Pergola, N., Neri, M., Nolde, M., Martinis, S., 2019a. The July/August 2019 Lava Flows at the Sciara del Fuoco, Stromboli–Analysis from Multi-Sensor Infrared Satellite Imagery. Remote Sens., 11, 2879. https://doi.org/10.3390/rs11232879

Plank, S., Walter, T.R., Martinis, S., Cesca, S., 2019b. Growth and collapse of a littoral lava dome during the 2018/19 eruption of Kadovar Volcano, Papua New Guinea, analyzed by multi-sensor satellite imagery. J. Volcanol. Geotherm. Res., 388, 106704. https://doi.org/10.1016/j.jvolgeores.2019.106704

Plank, S., Massimetti, F., Soldati, A., Hess, K., Nolde, M., Martinis S., Dingwell, D.B., 2021. Estimates of lava discharge rate of 2018 Kīlauea Volcano, Hawai'i eruption using multi-sensor satellite and laboratory measurements, International Journal of Remote Sensing, 42:4, 1492-1511, https://doi.org/10.1080/01431161.2020.1834165

Poland, M.P., Lopez, T., Wright, R. et al. 2020. Forecasting, Detecting, and Tracking Volcanic Eruptions from Space. Remote Sens Earth Syst Sci 3, 55–94. https://doi.org/10.1007/s41976-020-00034-x

Ramsey, M. S., Harris, A. J. L., 2013. Volcanology 2020: how will thermal remote sensing of volcanic surface activity evolve over the next decade? (invited review article). J. Volcanol. Geotherm. Res., 249, 217–233. https://doi.org/10.1016/j.jvolgeores.2012.05.011

Ramsey, M.S.; Harris, A.J.L.; Watson, I.M., 2022. Volcanology 2030: Will an orbital volcano observatory finally become a reality? Bull. Volcanol., 84, 6. https://doi.org/10.1007/s00445-021-01501-z

Reath, K., Pritchard, M., Poland, M., Delgado, F., Carn, S., Coppola, D., et al., 2019a. Thermal, deformation, and degassing remote sensing time series (CE 2000–2017) at the 47 most active volcanoes in Latin America: Implications for volcanic systems. Journal of Geophysical Research: Solid Earth, 124, 195– 218. https://doi.org/10.1029/2018JB016199

Reath, K., Pritchard, M., Moruzzi, S., Alcott, A., Coppola, D., Pieri, D., 2019b. The AVTOD (ASTER Volcanic Thermal Output Database) Latin America archive. J. Volcanol. Geotherm. Res. 376, 62–76. https://doi.org/10.1016/j.jvolgeores.2019.03.019

Ripepe, M., Lacanna, G., Pistolesi, M., Silengo, M.C., Aiuppa, A., Laiolo, M., Massimetti, F., Innocenti, L., Della Schiava, M., Bitetto, M., La Monica, F.P., Nishimura, T., Rosi, M., Mangione, D., Ricciardi, A., Genco, R., Coppola, D., Marchetti, E., Delle Donne, D., 2021. Ground deformation reveals the scale-invariant conduit dy-namics driving explosive basaltic eruptions. Nat. Commun.12, 1683. https://doi.org/10.1038/s41467-021-21722 -2

Shevchenko, A.V., Dvigalo, V.N., Zorn, E.U., Vassileva, M.S., Massimetti, F., Walter, T.R., Svirid, I.Y., Chirkov, SA, Ozerov, A.Y., Tsvetkov, V.A., Borisov, I.A., 2021. Constructive and Destructive Processes During the 2018–2019 Eruption Episode at Shiveluch Volcano, Kamchatka, Studied From Satellite and Aerial Data. Front. Earth Sci. 9:680051. https://doi.org/10.3389/feart.2021.680051

Steffke, A.M., Harris, A.J.L., 2011. A review of algorithms for detecting volcanic hot spots in satellite infrared data. Bull. Volcanol. 73, 1109–1137. https://doi.org/10.1007/s00445-011-0487-7

Tilling, R. I., 2008. The critical role of volcano monitoring in risk reduction. Adv. Geosci. 14, 3–11. https://doi.org/10.5194/adgeo-14-3-2008

Valade, S., Ley, A., Massimetti, F., D'Hondt, O., Laiolo, M., Coppola, D., Loibl, D., Hellwich, O., Walter, T.R., 2019. Towards Global Volcano Monitoring Using Multisensor Sentinel Missions and Artificial Intelligence: The MOUNTS Monitoring System. Remote Sens., 11, 1528. https://doi.org/10.3390/rs11131528

Way, L., Pritchard, W.E., Wike, L., Reath, K., Gunawan, H., Prambada, O., Syahbana, S., 2022. Detection of thermal features from space at Indonesian volcanoes from 2000 to 2020 using ASTER. J. Volcanol. Geotherm. Res., 430, 107627. https://doi.org/10.1016/j.jvolgeores.2022.107627

Chapter 6

6. Conclusions and Perspectives

1. SUMMARY OF CONCLUSIONS

In this thesis, I explored the potential of using Short Wave Infrared high-spatial-resolution images to study and monitor thermal activity produced by active volcanoes in comparison with moderate MODIS (Moderate Resolution Imaging Spectroradiometer) data, starting from the MIROVA project experience. The MultiSpectral Instrument SENTINEL-2 (MSI-S2) and Operational Land Imager LANDSAT-8 (OLI-L8) images have been used to detect hotspots and study several volcanic activities through a new algorithm able to robustly work with a global perspective by constructing a near real-time monitoring system currently operating on ca. 120 volcanoes worldwide. The results have important implications to both enlarge our knowledge of thermal processes revealing volcanic dynamics and improve thermal satellite monitoring applications, starting from the MIROVA system. The whole research represents an important step toward a multisensory approach in the thermal satellite remote sensing field, considering the increasing demands for developed monitoring tools and the lack of operational multisensory systems on a global scale.

In Chapter 2, the most methodological of the thesis, a new algorithm was developed for detecting, locating, and measuring the exposed hot area at magmatic temperatures (T > 200 °C) using high-spatial-resolution imagery of MSI SENTINEL-2 and OLI LANDSAT-8 with a global applicability purpose. The process of enhancing hotspot presence is based on a multispectral hybrid approach, analyzing the Short Wave Infrared bands (0.8 – 2.2 μm) with a series of spectral, spatial, and statistical filters. The algorithm results, in terms of the number of Hot Pixel(s), have been tested in comparison to the Volcanic Radiative Power VRP recorded by the MODIS-MIROVA thermal images based on Middle InfraRed analysis, on eight volcanic contexts with different thermal features and temperatures involved. The outcomes are extremely coherent, matching the two thermal satellite-based metrics. This proves that the moderate- and high-spatial-resolution thermal datasets can be joined to give complementary information about the volcanic status. The algorithm presented is one of the few multispectral-based hotspot detection methods to work on SWIR high-spatial-resolution images to be tested on various volcanic settings with a solid “thermal reference” such as the MODIS-MIROVA dataset. The overall result gives the possibility to characterize and monitor volcanic activity with a high level of detail on a global scale.

In Chapter 3, the integration of MODIS, MSI-S2, and OLI-L8 sensors is proposed to study thermal emissions emitted by open vents activity in the two persistent-active volcanic case studies of Stromboli and Etna. The investigation results of eight years of thermal activity allow us to compare the thermal emissions detected by the different sensors and to study at the scale of a single crater the thermal signals produced. The analysis displays a linear relationship between the SWIR Thermal Index parameter (by S2 and L8), and the Thermal Energy (by MODIS) emitted during ordinary activity. For the first time, a multiyear quantification of heat fluxes from every single crater is shown on these volcanoes, depicting the diverse thermal behavior of each sector, and opening the door of a dedicated space-based algorithm monitoring the heat flux produced by vents and the thermal budget on multicraters contexts. Thermal outputs are in close accord with the occurrence of higher intensities events such as effusions, explosions, and paroxysms. At Stromboli, a remarkable change in the thermal budget from the crater terrace since 2017 is observed, in connection with the increase of explosivity suffered by the shallow magmatic system in the last years. The conjunction of InfraRed moderate and higher spatial analysis offers a precise and denser analysis of how thermal emissions variate over time and space at open vents volcanoes.

In Chapter 4, an overview of thermal features at lava domes is offered by applying a multisensory (MODIS, VIIRS, MSI-S2, and OLI-L8) and multiyear investigation of thermal activities in three illustrative dome-forming eruptions at Láscar (Chile), Sabancaya (Peru), and Shiveluch (Russia) volcanoes. Satellite observations characterize the thermal signatures related to volcanic processes and phenomena typically occurring at lava domes. The volcanic cyclicity shown by Láscar in 2013 - 2012 was thermally constrained, showing the ruling behavior of weak explosive events (VEI 1-2), defining thermal cycles of rapid waxing phase, partially preceded by subtle thermal precursors, and long-term waning phase, lasting ca. 2.5 years on average. An explosive event in November 2019 was recorded by thermal SWIR and MIR sensors, otherwise not noted by ground-based methods. At Sabancaya, unrest to eruptive phase transition in 2012 - 2020 has been thermally characterized, with the two periods distinguished by degassing and extrusive activity, respectively. High-spatial-resolution images tracked the opening of a new conduit for the extrusion of the lava dome and new fumaroles fields, as well as recognized high explosivity periods and stages of reduced thermal emissions. The Shiveluch 2018 – 2019 constructive and destructive episode, characterized by the extrusion of a lava dome and collapse event, was accompanied by two important explosions detected by IR satellite detections, with the emission of intense thermal signals related to hot avalanches, cracks, and partial exposure of inner dome materials. The lava dome dynamic here seems to be ruled by an

SW-NE-directed structural feature, whose presence was highlighted by hotspots detected by SWIR images. The results of the overview, achieved by using complementary IR sensors, demonstrate how space-based methods allow to characterize the thermal activity at lava domes in terms of intensity, spatial distribution, and temporal persistence and enhance the hazard assessments of these dangerous and impulsive types of eruptions.

In Chapter 5, we show how the high-spatial-resolution thermal imagery used for research purposes of the Thesis could be crucial, particularly for monitoring applications and during eruptive crises. The multisensory approach proposed, with the combination of SENTINEL-2 and LANDSAT-8, provides valuable information to civil protection agencies and volcanological observatories in understanding the evolution of eruptions, allowing them to evaluate the presence of hotspots, tracking dimensions and changes of thermal active areas, and offering a method to make safe and low-cost observations, as shown in the Etna December 2018 and Stromboli July-August 2019 eruptions. The analysis process of SWIR high-spatial-resolution images has been inserted in a fully automated near real-time monitoring architecture, from the algorithm to web data dissemination, built up specifically to be joined with the MIROVA system. About 120 active volcanoes worldwide are thermally monitored daily by MSI SENTINEL-2 and OLI LANDSAT-8 images, whose data and results are freely accessible and downloadable by anyone on the MIROVA website. These improvements highly contribute to qualitatively and quantitively enriching the thermal surveillance offered by the MIROVA project, contributing to developing a modern and multisensory volcano-devoted thermal monitoring system.

2. FUTURE PERSPECTIVES

Looking at the significant improvements shown in this Ph.D. Thesis by using SWIR high-spatial-resolution in today's volcanic studies, spanning from the quality of the research on volcanic systems and behaviors, up to operative monitoring applications, ideas and proposals for new forthcoming steps come up spontaneously, particularly looking carefully at developments in the field of Earth Observation.

Starting from the outcomes presented in this manuscript, the perspectives would certainly consider new technical steps for integrating other high-spatial-resolution Infrared sensors. Indeed, the recent launch in September 2021 of the LANDSAT-9 platform from NASA (https://landsat.gsfc.nasa.gov/satellites/landsat-9/), boarding the sensor Operational Land Imager 2 (OLI-2), with the same spectral, temporal, and spatial features of the OLI sensor of LANDSAT-8 platform, allows improving with little efforts the number of images acquired and

to make denser the thermal observations. The same applies to the upcoming launch of two other satellites of the ESA SENTINEL family, specifically the SENTINEL-2C and –2D, slated for launch at the beginning of 2024 and 2025, respectively, and with the same MultiSpectral Instrument sensor onboard the -2A and -2B platforms. The more data, the greater our coverage of volcanic activity, particularly for short-timing events such as explosions or precursors detection.

Another further perspective to put into practice is to analyze the heat flux from single craters, as explained in Chapter 3, a near real-time product available on the MIROVA website and automatically transmitted to the competence and monitoring centers such as the Department of Civil Protection, the Laboratory of Experimental Geophysics (LGS) of the University of Firenze and the Istituto Nazionale di Geofisica e Vulcanologia (INGV), for Stromboli and Etna monitoring. Considering the recent intense eruptive phase suffered by the two volcanoes, the possibility of automatically monitoring every 2-3 days (assuming the overlapping frequency of SENTINEL-2 and LANDSAT-8 platforms) the heat flux and volume output rate released by the crater terrace or the singles craters, could represent a great research and monitoring achievement.

But, of course, this application is not only limited to Italian volcanoes. The following research steps want to explore the high-spatial-resolution potentialities in terms of dimensional analysis of single volcanic features and analysis of thermal emissions sourced by single sectors in other multicraters active volcanoes, such as, to name a few, the Yasur (Vanuatu), Tofua (Tonga), and Erta Ale (Ethiopia) volcanic case studies. The combination of MODIS, SENTINEL-2, and LANDSAT-8 to study thermal budgets of different volcanic features is one of the more exciting research applications deriving from the multisensory approach.

Finally, the near-real-time monitoring system based on the SWIR Sentinel-2 and LANDSAT-8 imagery needs constant technical improvement and maintenance, particularly to add as rapidly as possible and without issues, volcanoes still lacking to the monitoring list and entering an unrest phase or with impending eruption. Thus, the technical improvement of the monitoring system is one of the upcoming goals arising from this doctoral Thesis.

Considering the future perspective, opportunities are plain: satellite thermal data provide a clear and synoptic view of volcanic activity, that in lots of cases is not otherwise possible due to remote location, hazards, costs, or environmental conditions (Harris, 2013; Coppola et al., 2020; Poland et al., 2020). Thermal data support meaningful action for societies dealing with volcanoes, recognizing eruptive precursors, assessing variations of ongoing eruptions, and

offering measurement of dangerous phenomena such as the rate at which a lava flow is fed. These key advantages are even more precious in context with a limited or lacking ground-based monitoring network, a common condition (Sparks et al., 2012; Brown et al., 2015; Pallister & McNutt, 2015). Despite these advantages, satellite thermal monitoring involves significant efforts and barriers to the acquisition and analysis of remote sensing data, such as financial and technological resources to manage a noteworthy amount of digital data or human costs, which are not easily overcome by small research groups or monitoring experience, such as MIROVA project was (Coppola et al., 2016; 2020). The absence of a volcano surveillance devoted satellite mission represents an enormous obstacle for volcano monitoring in wider terms and for thermal satellite remote sensing too (Poland et al., 2020; Ramsey et al., 2022).

Unlike these limitations, issues can be overcome. For example, the use of open data that facilitate free access to satellite imagery, such as SENTINEL and LANDSAT missions, especially in support of natural hazards research and mitigation, is becoming common practice (Delgado et al., 2019; Reath et al., 2019; Poland et al., 2020). The sharing of technical and research knowledge and the rising number of collaborations between volcano observatories is a great achievement to possibly in-depth monitor hundreds of volcanoes worldwide (Lowenstern et al., 2022). The lack of satellites designed with specific volcano surveillance aims certainly represents a limitation, but also a spur to explore approaches using different sensors to improve our ability to understand and monitor volcanic systems. That’s precisely what this Thesis represents in the field of thermal satellite remote sensing and related to the MIROVA existing project.

3. BIBLIOGRAPHY

Brown, S.K., Loughlin, S.C., Sparks, R.S.J., Vye-Brown, C., Barclay, J., Caldera, E., Cottrell, E., Jolly, G., Komorowski, J.-C., Mandeville, C., Newhall, C.G., Palma, J.L., Potter, S., Valentine, G., 2015. Global volcanic hazard and risk. In: Loughlin SC, Sparks RSJ, Brown SK, Jenkins SF, Vye-Brown C (eds) Global Volcanic Hazards and Risk. Cambridge University Press, pp. 81–172. https://doi.org/10.1017/CBO9781316276273.004

Coppola, D., Laiolo, M., Cigolini, C., Delle Donne, D., Ripepe, M. 2016. Enhanced volcanic hot-spot detection using MODIS IR data: Results from the MIROVA system. Geol. Soc. Lond. Spec. Publ. 2016, 426, 181–205. https://doi.org/10.1144/SP426.5

Coppola, D., Laiolo, M., Cigolini, C., Massimetti, F., Delle Donne, D., Ripepe, M., Arias, H., Barsotti, S., Parra, C.B., Centeno, R.G., Cevuard, S., Chigna, G., Chun, C., Garaebiti, E., González, D., Griswold, J., Juarez, J., Lara, L.E., López, C.M., Macedo, O., Mahinda, C., Ogburn, S., Prambada, O., Ramon, P., Ramos, D., Peltier, A., Saunders, S., de Zeeuw-van Dalfsen, E., Varley, N., William, R., 2020. Thermal remote sensing for global volcano monitoring experiences from the Mirova system. Front Earth Sci 7. https://doi.org/10.3389/feart.2019.00362

Delgado, F., Poland, M., Biggs, J., Ebmeier, S., Sansosti, E., Lundgren, P., et al., 2019. lessons learned from the ceos volcano pilot in latin american and the ongoing volcano demonstrator project. Geophys. Res. Abstr. 21, EGU2019 – EGU14981.

Harris, A., 2013. Thermal Remote Sensing of Active Volcanoes: A User's Manual. Cambridge, MA: Cambridge university press. https://doi.org/10.1017/CBO9781139029346

Lowenstern, J.B., Ewert, J.W., Lockhart, A.B., 2022. Strengthening local volcano observatories through global collaborations. Bull Volcanol 84, 10. https://doi.org/10.1007/s00445-021-01512-w

Pallister, J., McNutt, S. R., 2015. "Synthesis of volcano monitoring," in The Encyclopedia of Volcanoes, 2nd Edn, ed. H. Sigurdsson, (Cambridge, MA: Academic Press), 1151–1171. doi: https://doi.org/10.1016/B978-0-12-385938-9.00066-3

Poland, M.P., Lopez, T., Wright, R. et al. 2020. Forecasting, Detecting, and Tracking Volcanic Eruptions from Space. Remote Sens Earth Syst Sci 3, 55–94. https://doi.org/10.1007/s41976-020-00034-x

Ramsey, M.S., Harris, A.J.L., Watson, I.M., 2022. Volcanology 2030: Will an orbital volcano observatory finally become a reality? Bull. Volcanol., 84, 6. https://doi.org/10.1007/s00445-021-01501-z

Reath, K., Pritchard, M., Poland, M., Delgado, F., Carn, S., Coppola, D., et al., 2019a. Thermal, deformation, and degassing remote sensing time series (CE 2000–2017) at the 47 most active volcanoes in Latin America: Implications for volcanic systems. Journal of Geophysical Research: Solid Earth, 124, 195– 218. https://doi.org/10.1029/2018JB016199

Sparks, R.S.J., Biggs, J., Neuberg, J.W., 2012. Geophysics. Monitoring volcanoes. Science, 335, 1310–1311. https://doi.org/10.1126/science.1219485

Acknowledgements

Volcanoes have always fascinated me, ever since I was a child. I remember, flipping through a book on active volcanoes around the world, one of the many books on the geography of planet Earth in which I would immerse myself, dreaming of distant lands and traveling with my head, every night before falling asleep. A book that I still remember to this day, with fabulous photos of eruptions and lava flows. Perhaps there, the dream of studying and traveling inside these spectacular phenomena began. I always had an attraction to the most dynamic, global, evident processes in the Earth Sciences, and volcanology is one of them. A renewing and destructive force at the same time, so iconic and primordial, so profound and magnetic, metaphor for the difference between what lies on the surface and what lies beneath.

Thanks to this doctorate, I have had the opportunity to study volcanoes, albeit in a small way and often from a distance, these beauties of heat and fire. I am grateful to all the people who, in different ways, have accompanied and supported me on this journey.

Particularly, I want to strongly acknowledge my supervisors and mentors Diego Coppola and Marco Laiolo, for the constant human and scientific guidance, closeness, and assistance throughout the study. I would never have started this journey without their precious presence, and for certain, it would not have gone the same way without their trust and support.

I want to acknowledge too other scientific mentors who partially accompanied me, advised and taught me a lot on this Ph.D. path, in particular Maurizio Ripepe, Corrado Cigolini, Thomas Walter and Dario Delle Donne.

I want to thank all my Ph.D. and office mates at the Department of Earth Sciences, as well as the people from over the world I met during my time at the GFZ in Potsdam, and the colleagues and friends of field works at Stromboli and Etna, of the LGS group from Florence to Palermo.

I would like to give a big thank you and hug to all my families, newer and older, in Italy, in Berlin, in Torino, in Susa Valley, and abroad, both those made up of parental ties, my parents and sister overall, and those made up of complicity, friendship, and care, who have put up with me and supported me, listened to me, cleared my mind, kept me company during tedious afternoons and sleepless nights, gave me love, and been there for me when I needed them and during difficult times during this intense journey.

I would like to thank the endless stars and geckos above my head during the nights in Stromboli.

And finally, for my precious little victories, I want to thank most of all myself, for all the strength and tenacity I put in and that came out.